

AD693246

PROCEEDINGS

THIRD CAL/AVLABS SYMPOSIUM



Aerodynamics of Rotary Wing and V/STOL Aircraft

VOLUME I

Rotor/Propeller Aerodynamics
Rotor Noise

18-20 June 1969
Buffalo, New York

Reproduced by the
CLEARINGHOUSE
for Federal Scientific & Technical
Information Springfield Va. 22151

236



CAL/AVLABS

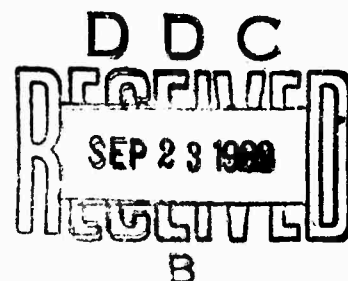


SYMPOSIUM PROCEEDINGS

Aerodynamics of Rotary Wing
and V/STOL Aircraft.

Published in three Volumes as follows:

- | | |
|------------|--|
| Volume I | Rotor/Propeller Aerodynamics
Rotor Noise |
| Volume II | Wind Tunnel Testing
New Concepts in Rotor Control |
| Volume III | Panel Session on Recommendations
for Future Aerodynamic Research,
Panel Summaries and Featured
Speakers |



This document has been approved
for public release and sale; its
distribution is unlimited

Statements and opinions contained herein are those of the authors and are not to be construed as reflecting the views of the Department of the Army nor the cosponsors of this Symposium - The U.S. Army Aviation Materiel Laboratories and Cornell Aeronautical Laboratory, Inc.

FOREWORD

Within the past six years, the U. S. Army Aviation Materiel Laboratories (AVLABS) and the Cornell Aeronautical Laboratory, Inc. (CAL) have co-sponsored two symposia as a means for direct exchange of information regarding technical problems of relevance to Army aviation. The first, in 1963, addressed itself to dynamic load problems associated with helicopters and V/STOL aircraft while the second, in 1966, focused on aerodynamic problems associated with V/STOL aircraft. In the spirit of continuing this interchange among technical specialists from industry, the universities and government laboratories, we have planned the Third CAL/AVLABS Symposium. The theme of the symposium is "Aerodynamics of Rotary Wing and V/STOL Aircraft" and, at this time, we feel it is appropriate to cast a critical eye upon the technical progress that has been made in the years subsequent to the two previous symposia. It is important to identify those research problems wherein solutions have and can be reduced to engineering practice as well as to identify those areas wherein additional research and development is required.

Five technical sessions have been planned in an attempt to provide coherent presentations of current developments in rotor/propeller aerodynamics, rotor noise, wind-tunnel testing and new concepts in rotor control. In addition, a panel session has been organized to draw upon the experience of the helicopter and V/STOL industry in discussing current problems still needing solution, future problems that are beginning to show up on the horizon and, finally, to recommend areas for future aerodynamic research.

These proceedings consist of three volumes, the formal papers being presented in the first two. This format was chosen in view of the inter-relationship between several sessions, in particular, those on rotor/propeller aerodynamics and rotor noise. Hence, at the risk of producing a slightly oversized volume, it was felt that in the interest of continuity, it would be more beneficial to include all the rotor aerodynamics and noise papers in Volume I. The papers on wind-tunnel testing and rotor control appear in Volume II. Volume III is devoted principally to the formal presentations of the panel session. Moreover, this session was tape recorded and an account of the verbal interchange between the panelists and the audience is also presented.

The Co-Chairmen want to acknowledge with thanks the cooperation of many people who have contributed to this symposium. Specifically, our thanks go to Colonel Eduardo Soler, Commanding Officer of the U. S. Army Aviation Materiel Laboratories, and Mr. Waldemar O. Breuhaus, Director of the Flight Dynamics Division of Cornell Aeronautical Laboratory, who opened this meeting; Mr. Alfred Gessow, Assistant Director of Research, Office of Advanced Research and Technology, NASA, whose keynote address,

contained in Volume III, served to set the tone for the technical sessions; and to our Banquet Speaker, Mr. A. Scott Crossfield, Division Vice President, Flight Research and Development, Eastern Airlines. We want to acknowledge the contributions of the five session chairmen — Barnes W. McCormick, Paul Yaggy, Robert G. Loewy, Mark Kelly and Dean C. Lauver — whose cooperation and counsel helped to shape the technical program. Our thanks also go to the authors and panelists for their cooperation in preparing manuscripts in a form that could be reproduced directly. This material was neither checked nor edited by CAL or AVLABS.

In conclusion, we wish to make special mention of the contributions of Mr. Patrick Cancre, Aeromechanics Division, AVLABS, whose efficient handling of countless administrative details guaranteed a smooth and coordinated effort between AVLABS and CAL.

SYMPOSIUM TECHNICAL CHAIRMEN

Alfred Ritter (CAL)

John E. Yeates (AVLABS)

CONTENTS

ROTOR/PROPELLER AERODYNAMICS I (Wake Structure)

A CONTINUOUS VORTEX SHEET REPRESENTATION OF DEFORMED WAKES OF HOVERING PROPELLERS

John C. Erickson, Jr.
Cornell Aeronautical Laboratory, Inc.
Buffalo, New York

PROPELLER WAKE DEFORMATION DUE TO INSTABILITY OF A TRAILING VORTEX SHEET

D. E. Cummings and J. E. Kerwin
Massachusetts Institute of Technology
Cambridge, Massachusetts

EXPERIMENTS ON ROTOR WAKE CONTRACTION*

M. Noak and J. P. Jones
University of Southampton
Southampton, England

ROTOR/PROPELLER AERODYNAMICS II (Other Effects)

VORTEX FIELD, TIP VORTEX, AND SHOCK FORMATION ON A MODEL PROPELLER

W. H. Tanner and R. M. Wohlfeld
Bell Helicopter Company
Forth Worth, Texas

AN EXPERIMENTAL INVESTIGATION OF AN OSCILLATING TWO-DIMENSIONAL AIRFOIL IN REVERSE FLOW

Richard F. Child
Boeing Company - Vertol Division
Morton, Pennsylvania

DESIGN OF AIRFOILS FOR ROTORS

F. X. Wortmann
University of Stuttgart, Germany
and Consultant to Bell Helicopter Company
and
Jan M. Drees
Bell Helicopter Company
Fort Worth, Texas

* Although not available at the time of publication of this volume, this paper will be found in Volume III of these Proceedings.

A HOVER PERFORMANCE ANALYSIS COMBINING THE STRIP-MOMENTUM AND PRESCRIBED
WAKE THEORIES

James B. Rorke and Clifford D. Wells
Sikorsky Aircraft
Stratford, Connecticut

ROTOR NOISE

HELICOPTER ROTOR NOISE GENERATION

S. E. Wright and J. W. Leverton
Institute of Sound and Vibration Research
University of Southampton, England

THE IMPORTANCE OF VORTEX SHEDDING EFFECTS ON HELICOPTER ROTOR NOISE WITH AND
WITHOUT BLADE SLAP

S. G. Sadler
Rochester Applied Science Associates, Inc.
and
R. G. Loewy
University of Rochester
Rochester, New York

PREDICTION METHODS AND TRENDS FOR HELICOPTER ROTOR NOISE

Robert J. King and Ronald G. Schlegel
Sikorsky Aircraft
Stratford, Connecticut

ROTOR NOISE MEASUREMENTS IN WIND TUNNELS

C. R. Cox
Bell Helicopter Company
Fort Worth, Texas

SESSION I

**Rotor/Propeller Aerodynamics I
(Wake Structure)**

*Chairman: Barnes W. McCormick
Pennsylvania State University
State College, Pennsylvania*

**WEDNESDAY MORNING
18 JUNE 1969**

**A CONTINUOUS VORTEX SHEET REPRESENTATION OF
DEFORMED WAKES OF HOVERING PROPELLERS**

John C. Erickson, Jr.
CORNELL AERONAUTICAL LABORATORY, INC.
Buffalo, New York

A CONTINUOUS VORTEX SHEET REPRESENTATION OF DEFORMED WAKES OF HOVERING PROPELLERS*

by

John C. Erickson, Jr.
Cornell Aeronautical Laboratory, Inc.
Buffalo, New York, USA

ABSTRACT

The trailing vortex system of a hovering propeller must undergo significant deformations if it is to remain force-free. The axial, radial and tangential deformations involved have to be represented adequately if one hopes to predict the performance to a high degree of accuracy. A lifting-line theory based on a continuous vortex-sheet representation of the wake has been considered with emphasis on determining a satisfactory force-free approximation to the effective pitch of the trailing vortex sheets, but with the contraction pattern fixed according to a heavily loaded actuator disk theory. Numerical solutions to the governing equations were found by a double iteration scheme consisting of an iterative loop for the inflow within an iterative loop on the assumed pitch variations. Computer programs were developed to evaluate the velocity induced along the deformed trailing vortex sheets as well as the inflow induced at the blades.

In an experimental portion of this investigation, the feasibility of measuring the instantaneous velocity components in propeller wakes by means of hot-wire anemometry was established. Measurements made for two cases displayed large regions of the flow field behind the propeller in which the velocity data were random in nature and did not repeat with blade passage.

*Based on work performed for the U. S. Army Aviation Materiel Laboratories and for the U. S. Army Research Office-Durham.

Computations were carried out for eight cases with either the propeller geometry or the blade circulation distribution specified. When the detailed characteristics of the computational results were examined, these cases could be grouped into three ranges of propeller operation. In the first range, at high pitch settings corresponding to thrust coefficients above about 0.15, the double iteration provided fair agreement between the assumed and computed pitch but the prescribed contraction was too great. In the second range, at pitch settings corresponding to thrust coefficients between about 0.10 and 0.15, the prescribed contraction was apparently too small as determined by iteration with respect to the inflow only. In the third range, at pitch settings near zero degrees at the tip and corresponding to thrust coefficients below about 0.10, successful iteration could not be carried out even for the inflow. This was due, in part, to the negative induced axial inflow near the tip. The cases for which wake measurements were made fell in the third range.

Calculations of the induced velocity between the blades in the propeller disk plane were carried out for a total of three typical cases in the first two propeller operating ranges. The azimuthal variation of the induced axial velocity component had a generally characteristic shape marked by rapid changes in magnitude in the vicinity of the blades. The average axial inflow at radii near the tip was negative despite positive values at the blades themselves. The average radial inflow was considerably larger in magnitude than the values at the blades.

Although detailed flow measurements were not available for comparisons with theoretical results in those cases which could be iterated successfully, overall performance data did exist. The predicted performance did not agree favorably with the data in the first range of propeller operation (overpredictions in figure of merit of from 5 to 10%) and agreed even less favorably at lower pitch settings (overpredictions of up to 20%). However, in the latter cases, extrapolations of the predicted performance based on modified pitch distributions showed a

reduction in the degree of overprediction. These modifications to the pitch distributions were indicated by theoretical computations of the induced velocities along the trailing vortex sheets.

INTRODUCTION

The requirement to develop accurate theoretical methods for the performance prediction and design of V/STOL propellers operating in hover has been well established in recent years. Such methods could complement existing techniques for treating propellers in axial forward flight and thus lead to a means of achieving improved V/STOL propeller design in a more systematic manner than has previously been possible. These same theoretical methods would be adaptable as well to helicopter rotors in hover.

The principal requisites for developing a theory for hovering propellers have been, first, a fundamental understanding of the deformations which the trailing vortex sheets must undergo to remain force-free and, second, representation of this physical reality sufficiently well in a mathematical model. The trailing vortex sheets deform, in general, by an axial stretching together with a radial contraction and a small tangential distortion. Moreover, the edges of the sheets are locally unstable and tend to roll up as for a finite wing. Although these deformations are of secondary importance in axial flight, they are of considerably greater magnitude and occur much closer to the propeller in hover since there is no free stream to convect away the trailing vortex sheets.

Various aspects of the hovering propeller and helicopter rotor have received considerable attention in recent years as evidenced by References 1 through 12, for example, as well as in papers at the recent 25th Annual Forum of the American Helicopter Society and at this Third CAL/AVLABS Symposium. Furthermore, there is other related literature on the trailing vortex system characteristics for helicopter rotors in forward flight.

This paper presents the most recently obtained results in the series of investigations reported in References 13 through 21. The initial studies of References 13 through 16 were based upon a simple model which assumed a discontinuous deformation of the trailing vortex system into discrete, rolled-up vortices at specified locations downstream of the propeller. The results pointed out not only the lack of knowledge of the roll-up process for propellers but also the need for modeling the continuous axial and radial deformation immediately aft of the propeller. Attention was concentrated subsequently on this continuous deformation of the trailing vortex sheets. In References 17 and 18, an initial and then a refined wake hypothesis were put forward to relate the velocities along elements of the trailing vortex sheets simply and generally to the corresponding inflow values at the blades. Computed results for several cases indicated the necessity for performing actual calculations of the velocity components along the trailing vortex sheets, as well as the requirement for obtaining corresponding experimental velocity data, to check and improve the hypothesized values. Development of the continuous deformation model was continued further along these lines, as reported in References 19 through 21, and these references form the basis for this paper.

In the present paper, the basic formulation of a lifting line model for the hovering propeller is outlined followed by a description of the steps taken to develop a representation of the wake deformation. Next, highlights are given of an exploratory experimental program in which the feasibility of measuring the instantaneous velocity components in propeller wakes by means of hot-wire anemometry was established. Then the numerical results of the theoretical development are presented and discussed. Finally, conclusions of the investigation are drawn.

BASIC FORMULATION

We consider a rigid propeller rotating at a constant angular speed Ω in a uniform, inviscid fluid that is otherwise at rest at infinity. The classical lifting-line formulation is assumed wherein each propeller blade

is represented by a radial bound vortex line. Each bound lifting-line vortex is accompanied, in turn, by a trailing vortex sheet which must drift force-free with the flow.

A propeller-fixed coordinate system (x, r, θ) is chosen with the axis of rotation as the x -axis (see Figure 1). In these coordinates, the flow field is reduced to a steady one. The lifting lines representing the blades are arranged symmetrically in the propeller plane $x = 0$ and each is assumed to have a radially varying bound circulation strength Γ . The strength of the incremental element of the vortex sheet trailing from the point $(0, r_p, \theta_p)$ along the lifting line is $-d\Gamma$.

The induced velocity at any point in the propeller field can be found by integrating the Biot-Savart law over all the vortex elements comprising the system in terms of their strength, orientation and distance to the field point. The resulting kinematic equations for the axial u , radial v and tangential w velocity components can be written operationally as

$$u = \mathcal{O}_u(\Gamma, -d\Gamma/dr_p; u_v, v_v, w_v) \quad (\text{Eq. 1})$$

$$v = \mathcal{O}_v(\Gamma, -d\Gamma/dr_p; u_v, v_v, w_v) \quad (\text{Eq. 2})$$

$$w = \mathcal{O}_w(\Gamma, -d\Gamma/dr_p; u_v, v_v, w_v) \quad (\text{Eq. 3})$$

The three integral operators $\mathcal{O}_u, \mathcal{O}_v, \mathcal{O}_w$ are a shorthand notation expressing the functional relationships that are given in any of References 17 through 19. These operators act not only on the bound and trailing vortex strengths but also on the velocity components u_v, v_v, w_v at all points (x_v, r_v, θ_v) along the trailing vortex sheets.

A fourth equation is needed to complete the set. It can be found by using the Kutta-Joukowski formula to relate the blade circulation and the induced velocity field in terms of the propeller geometry; namely,

$$\Gamma = b W_p C_L / 2 \quad (\text{Eq. 4})$$

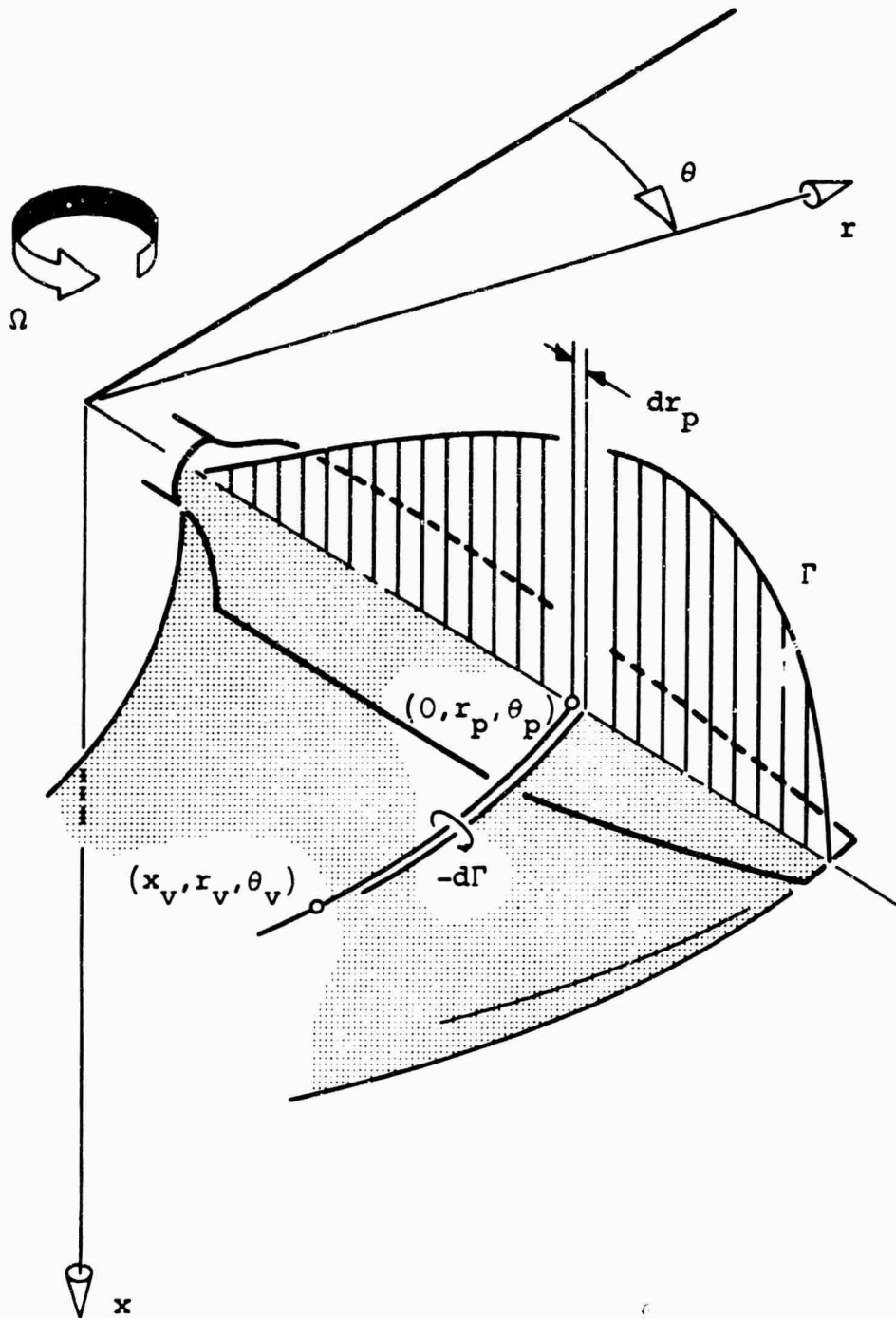


Figure 1 PROPELLER COORDINATES AND VORTEX REPRESENTATION

where b is the blade chord, w_p is the total local velocity evaluated at the propeller plane normal to the blade section and C_L is the lift coefficient of the blade section. The sectional lift coefficient is assumed to be known as a function of the induced angle of attack α at approximately the local Mach and Reynolds numbers. Equation (4) is a dynamic equation that holds on the blade surfaces which, of course, can support forces. On the trailing vortex surfaces, which cannot support forces, there are also dynamic equations which state that the surfaces must be force-free. These equations will be satisfied if the trailing vortex elements making up the system are all aligned with streamlines of the flow.

When the propeller geometry is specified, the propeller performance can be predicted if the inflow velocity components u_p and w_p are known at the propeller plane along with r and the sectional characteristics, as shown in any of References 17 through 19. In order to solve for these quantities, though, the velocity components must be known everywhere along the trailing vortex sheets as indicated by the form of Equations (1) through (3). Therefore, a solution for the performance necessitates simultaneous solution of Equations (1) through (3) everywhere on the trailing vortex sheets as well as at the lifting lines, Equation (4) at the lifting line, and the force-free condition.

When the blade circulation distribution Γ is specified, only Equations (1) through (3) along with force-free condition need be solved simultaneously, again everywhere on the trailing vortex sheets as well as at the lifting lines. The propeller geometry can then be found from the solution and Equation (4); i. e., the blade chord b , the blade pitch distribution β and the airfoil section characteristics would be determined consistent with the inflow and circulation.

Approximate numerical solutions of the set of equations described above can be carried out by means of an iteration scheme. To iterate, it is convenient to rewrite Equations (1) through (3) in the following form,

$$u^n = u^{n-1} - K_u \{ u^{n-1} - \mathcal{O}_u (r^{n-1}, -dr^{n-1}/dr_p, u_v^{n-1}, v_v^{n-1}, w_v^{n-1}) \} \quad (\text{Eq. 5})$$

$$v^n = v^{n-1} - K_v \{ v^{n-1} - O_v(r^{n-1}, -dr^{n-1}/dr_p; u_v^{n-1}, v_v^{n-1}, w_v^{n-1}) \} \quad (\text{Eq. 6})$$

$$w^n = w^{n-1} - K_w \{ w^{n-1} - O_w(r^{n-1}, -dr^{n-1}/dr_p; u_v^{n-1}, v_v^{n-1}, w_v^{n-1}) \} \quad (\text{Eq. 7})$$

The quantities K_u , K_v , K_w are "iteration factors" chosen as necessary to achieve convergence of the iteration. Generally, they have been chosen empirically.

When the propeller geometry is given, iteration begins by finding an initial approximation to the blade circulation distribution and the velocity components at the lifting lines and on the trailing vortex sheets. The first approximation to each velocity component then is found by operating with Equations (5) through (7). With these determined, the first approximation to the circulation follows from Equation (4). The iteration continues by operating as before on the first approximation to determine the second, and so forth. Once convergence is achieved to within a prescribed accuracy, the propeller performance can be evaluated. When the blade circulation is given, iteration proceeds similarly except that the circulation does not change at each step.

Implementation of the iterative solution outlined above necessitated development of a series of computer programs for evaluating the integral operators in Equations (1) through (3). Originally, a very general computer program was developed for calculating these operators for points located at the lifting lines or anywhere else in the field, except on the trailing vortex sheets themselves (see References 17 and 18). Later, two separate, specialized programs were developed; one which evaluates these operators for field points along the lifting line only, and one which evaluates them for field points along the trailing vortex sheets only (see Reference 19). Full details of the numerical techniques used for these programs are given in the references cited. It should be mentioned here, though, that the radial integration over the trailing vortex sheets, which is implied by the operators in Equations (1) through (3), is carried out by considering them as continuous sheets instead of as a series of discrete

trailing vortices. This required that proper account be taken of the singularities which occur when field points coincide with points along the trailing vortex sheets.

DEVELOPMENT OF WAKE REPRESENTATION

The iteration approach described above requires, at each step, calculation of the induced velocity components at a sufficient number of points along the trailing vortex sheets to define accurately the local streamlines and so the force-free location of the sheets. The number of calculations thus required is very large so we looked for a way of reducing this number while retaining an approximation to the force-free condition that would be adequate for predicting the propeller performance for design purposes. We found such a way by recognizing that, since the instantaneous inflow components at the lifting line must be computed in all cases in order to determine the performance, we should seek to link the velocity components along the trailing vortex sheets in some general fashion to the inflow.

In an early investigation (see References 13 through 16), attention was concentrated on a simple model of the vortex sheet deformation. In the model chosen, there was no axial or radial deformation of each sheet until specified locations downstream were reached. Then the inboard and outboard portions of the sheet were assumed to contract discontinuously; i. e., to roll up instantaneously into a pair of concentrated vortices. Results of a series of computations indicated that the initial axial and radial deformation immediately behind the blades must be represented, especially near the blade tip. Moreover, there was at that time a lack of fundamental knowledge of the basic nature of the roll-up process for the trailing vortex sheets of propellers.

Consequently, we concentrated our attention thereafter (in References 17 through 19) on the continuous axial and radial deformation of the trailing vortex sheets without an explicit representation of the roll-up process. To represent this continuous deformation, yet relate the velocity

components along the trailing vortex sheets to the inflow at the lifting lines, the results from the lightly-loaded generalized actuator disk model of References 22 through 24 for propellers in axial flight were considered initially. In that basic analysis, it was found that along the element of the vortex sheet trailing from a given radius, the θ -averages of the induced velocity components varied from their inflow values to their asymptotic values for large x , in a manner that was not strongly dependent upon the pitch of the trailing vortex system or upon the blade circulation distribution.

As an initial wake hypothesis for satisfying the force-free condition, then, it was assumed in References 17 and 18 that the induced velocity components along the trailing vortex sheets at a constant radius varied according to the results of Reference 22. Iterative computations for the inflow and performance of two different propellers indicated that the predicted performance was excessively optimistic compared with test data. Also, preliminary wake velocity test data (see References 3 and 17) showed that, although the predicted contraction pattern of the trailing vortex sheets was realistic, the predicted effective pitch variations of the elements of the trailing vortex sheets were not. A refined wake hypothesis was developed accordingly (also in References 17 and 18) to improve the approximation to the effective pitch. It was based upon the contraction pattern predicted by the initial hypothesis but the axial velocity variations outboard of the 0.5 radial station were applied along streamlines instead of along constant radii; i. e., along the trajectories of the elements of the trailing vortex sheets. The first calculations carried out on the basis of the refined wake hypothesis gave encouragement so far as agreement with test data was concerned. However, subsequent computations for two other propeller designs led not only to poor performance predictions but also to an excessive amount of contraction.

The results of all computations with both the initial and refined wake hypotheses led to the conclusion that, whatever wake representation was chosen, it would be necessary to check the velocity components assumed along the trailing vortex sheets by direct computations and, where feasible,

by test data. This eliminated our initial hopes for a simple, yet general, wake representation that would apply to a wide range of propeller designs over the entire static operating range. Furthermore, the effective pitch of the trailing vortex sheets had emerged as a significant and poorly understood feature of the wake, provided that the contraction pattern was reasonable compared to flow visualization results.

A new wake representation was then formulated to provide an improved basis for the systematic development of a performance prediction method, recognizing these wake characteristics. It was based, in part, upon theoretical results obtained meanwhile by M. D. Greenberg and A. L. Kaskel for a force-free actuator disk model of a propeller or rotor in static operation out of ground effect (Reference 10). Their model leads to determination of the flow-field quantities numerically for the case of an infinite number of blades with constant blade circulation distribution. One important result is that the contraction pattern is virtually independent, numerically, of total blade loading and agrees well generally with flow visualization results. Therefore, in the new representation, the contraction pattern was established by assuming that the envelopes of the elements of the trailing vortex sheets were fixed according to the results of Reference 10. This promised to provide a reasonable approximation except inboard of about the 0.4 radial station where the effect of the differences is of minor importance. The variations of the tangential velocity component with axial distance along the trailing vortex sheets were fixed at different radii according to previously computed values. This left the radial distribution of the variations of the axial velocity component along the trailing vortex sheets from their inflow values to their asymptotic values as the principal variables remaining. Since these variations determine the effective pitch along the trailing vortex sheets, attention was therefore concentrated on this aspect. For the purposes of this study, only the trailing vortex contributions to the axial variations were considered.

The iteration scheme described earlier thus became a double iteration scheme with this wake representation. First, a radial distribution of variations of the axial velocity component with axial distance along the trajectories of the trailing vortex sheets is assumed. Then an iteration to find the inflow and blade circulation is carried out as before. Next, the axial velocity component is computed at several representative points along the trailing vortex sheets to compare assumed and computed variations. On the basis of these comparisons, a new radial distribution of the axial velocity variations is assumed and the iteration is continued until convergence is obtained. Of course, at any point in the iteration, the validity of the assumed contraction pattern and the assumed tangential velocity variations could be examined by computations as well, and modified as necessary.

Before describing the results of the numerical computations made using this wake representation, an experimental investigation of the instantaneous induced velocity components in the propeller wake will be discussed. The tests took place chronologically before the numerical calculations and so influenced them.

EXPERIMENTAL INVESTIGATION

The objective of the experimental investigation was the measurement of the instantaneous velocity components in the propeller wake; in particular, at the locations of the trailing vortex sheets. The data obtained could then be used to check the theoretical predictions of the velocity components along the trailing vortex sheets since these components determine the position of the vortex sheets and so the magnitude of the induced inflow to the propeller blades. Moreover, determination of the θ -variations of the velocity components between the blades would add to the physical understanding of the wake and could provide another basis for checking the theoretical representation.

The test program was carried out on the Canadair, Ltd. propeller test rig. A description of this rig is given in Reference 4. Hot-wire

anemometry was selected as a suitable means for measuring the instantaneous velocity components and equipment was made available by McGill University. The actual program was performed by Canadair personnel working in conjunction with Dr. I. S. Gartshore and Mr. D. C. Gilmore, then at McGill. Messrs. Gartshore and Gilmore handled the calibration and operation of the hot-wire equipment. Complete details of the hot-wire measurement and data reduction procedures are described in Reference 20, while the principal results are discussed and the final, reduced data are plotted in Reference 19.

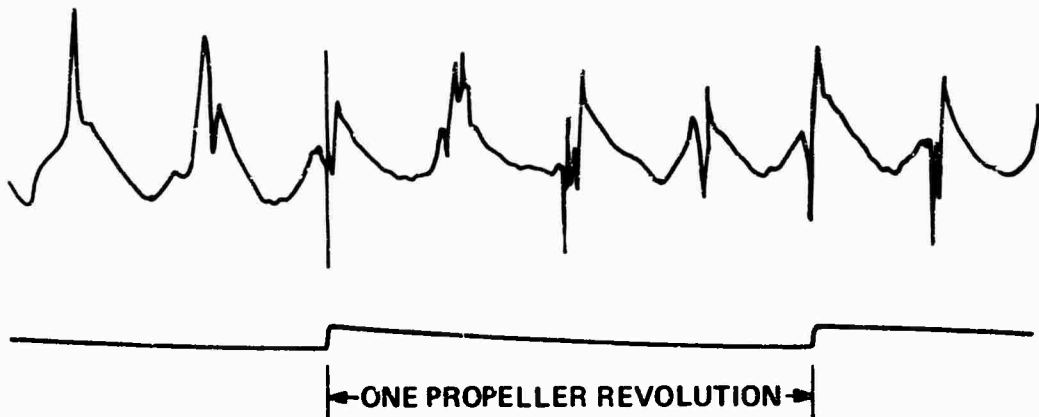
Since a single hot wire was used in these tests, data at three different hot-wire orientations, at least, were required to permit resolution of the three mutually perpendicular velocity components. Generally, data were taken at five different hot-wire orientations and a least-squares method was used in the reduction.

Calibration of the particular type of hot-wire probe used was a critical aspect of the test program and four effects were considered. The first effect is the basic velocity-voltage calibration with the flow velocity normal to the hot wire. The empirical relationship established by D. C. Collis and M. J. Williams in Reference 25 was used for this as well as for the ambient temperature calibration which constitutes the second effect. The third effect concerned the yaw response of a hot wire; i. e., its response not only to the velocity component normal to it but also to the velocity component along its length, as discussed by C. A. G. Webster in Reference 26. The fourth effect also concerns directionality and is not so well known. It is the dependency of the hot-wire response to the angle that the flow velocity makes with the axis of the probe stem and is due to aerodynamic interference of the probe. This effect has been described by B. J. Hoole and J. R. Calvert in Reference 27 and by D. C. Gilmore in Reference 28. Once calibrations for these four effects had been made and expressed in suitable mathematical form, equations were formulated that permitted an iterative resolution of the data into the three instantaneous velocity components.

Measurements were carried out for two propellers; namely, the four-bladed, seven-foot diameter Canadair 65 Activity Factor (AF) propeller at the 8.2° pitch setting, as measured at the 0.7 radial station, and the four-bladed, seven-foot diameter Canadair 120 AF propeller at 10.0° . These particular settings were chosen because they were in an operating regime at low thrust coefficients where the greatest difficulties had arisen in our previous theoretical computations for other propellers (see References 17 and 18).

The first important result of the tests concerned the nature of the flow field. Over the middle part of the blade at axial positions close behind the propeller, the hot-wire signals were repeatable with blade passage [see Figure 2(a), for example]. Near the hub, however, and especially near the tip, the hot-wire signals did not repeat with blade passage but were apparently random [see Figure 2(b), for example]. The extent of these regions grew rapidly with distance downstream of the propeller until the entire flow field had this character at a distance of about one propeller radius (see Figure 3). Beyond the outer radial limit of these regions and upstream of the propeller, a repeatable signal was obtained. The randomness precluded a meaningful resolution of the hot-wire data into the instantaneous velocity components. Therefore, no useful data for the trailing vortex sheet transport velocity could be found in the important tip region.

In hot-wire measurements of the wake of a helicopter rotor, H. H. Heyson found a similar and perhaps related phenomenon (Reference 29). His measurements covered a broad range of pitch settings at a fixed location of $r/R_p = 0.67$ and $x/R_p = 0.145$. When the blades were set such that the blade tips were at positive pitch angles, repeatable signals, much like those of Figure 2(a), were found. When the blade tips were at near-zero or negative pitch angles, however, the hot-wire signals were random and resemble those of Figure 2(b).



(a) REPEATABLE WITH BLADE PASSAGE



(b) NONREPEATABLE WITH BLADE PASSAGE

Figure 2 TYPICAL HOT-WIRE SIGNALS - 65 AF PROPELLER, $\beta_{0.7 R_p} = 8.2^\circ$

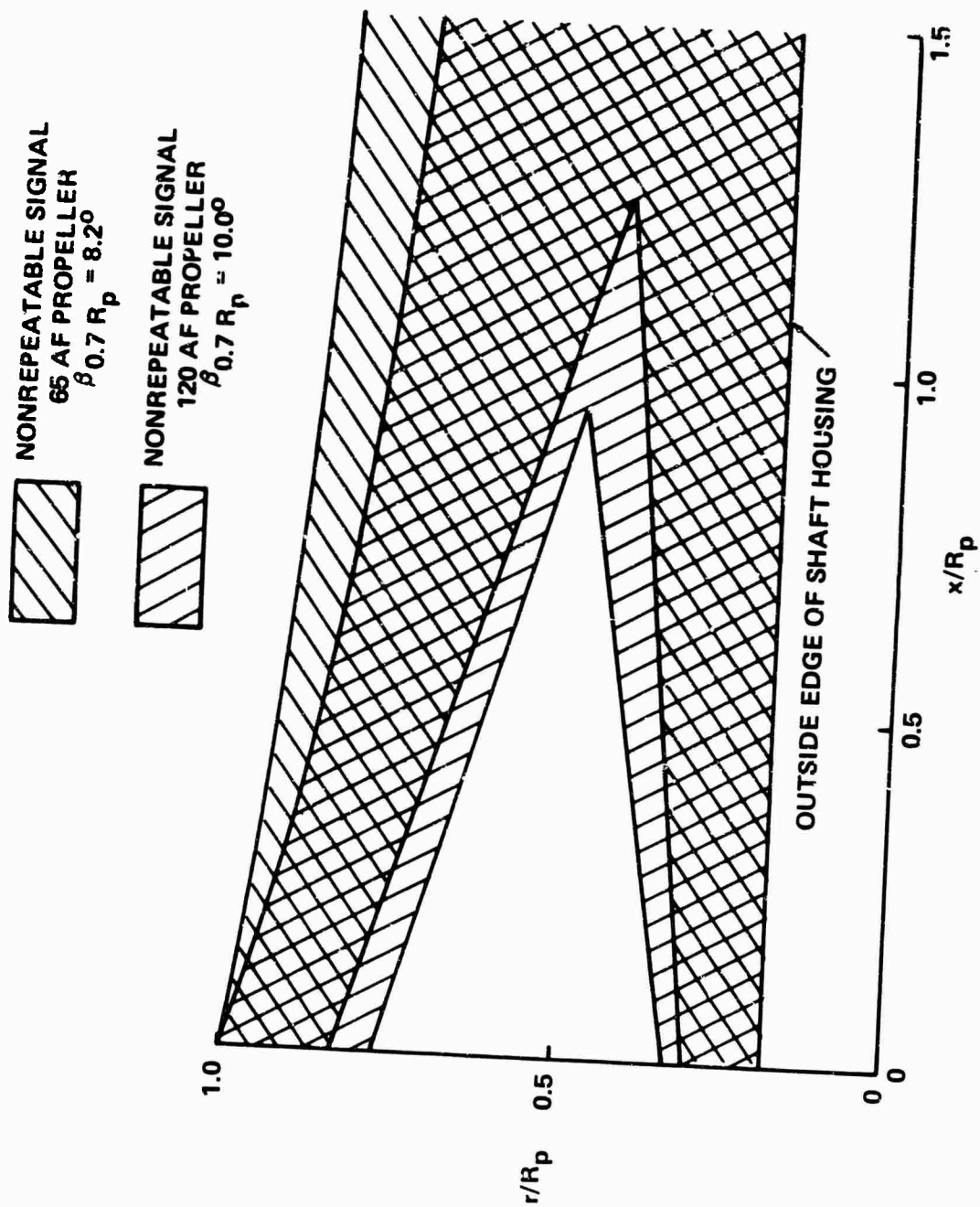


Figure 3 EXTENT OF REGIONS OF NONREPEATABLE HOT-WIRE SIGNALS FOR TWO PROPELLERS

In the region of the flow field where the hot-wire signals were repeatable with blade passage, the data were resolved into the three components. By transforming from space-fixed coordinates to blade-fixed coordinates, the time variation of the velocity components as measured can be related to their θ -variation, and it is in this latter form that the data are presented in Reference 19. The harmonic content of the velocity components was small (of the order of 10%) at most stations where the data could be resolved. Unfortunately, the measured velocities were extremely sensitive to the basic velocity-voltage calibration. Consequently, the resulting experimental errors were of the same magnitude as the harmonic content, and so the azimuthal variation is suspect.

NUMERICAL RESULTS AND DISCUSSION

Numerical computations were carried out for a total of eight cases. The wake representation used was based upon the fixed contraction pattern but iterates on the effective pitch by changing the assumed variations of the axial velocity component with distance downstream along the trailing vortex sheets. Pertinent features of the calculations for these cases are presented in Table I.

Six of the cases are for existing propeller designs, namely, the Canadair 65 AF and 120 AF propellers which were tested in the experimental program and the three-bladed, fifteen-foot-diameter Curtiss-Wright 3(109652) propeller. Blade characteristics of all three are described in Reference 19. The other two cases, called Representative Blade Loadings One and Two (RBL 1 and RBL 2), treat, respectively, four-bladed and three-bladed fixed-blade circulation distributions. Both of these Γ distributions were chosen by extrapolating axial flight distributions of Reference 30 to zero rate of advance, neglecting contraction. The particular distributions were selected to give three- and four-bladed cases with comparable induced thrust coefficients (as found by neglecting profile drag). The principal advantage of computations for these Representative Blade Loadings is that Γ remains fixed throughout the iteration so that only Equations (5) through (8) must be iterated. Equation (4) is needed only if a propeller design is desired at the end. Practically, this is a major simplification that permitted efficient investigation of the nature of the approximate solutions to the equations. The degree of experience gained with these cases led to greater ease of calculation when the six specified propeller design cases were treated.

Although not all of the eight cases were carried to the same degree of completion as regards iteration toward the ultimate satisfaction of the condition of a force-free wake, still an examination of all the results indicates that they can be separated into three ranges of operation with respect to this wake representation. The first range is characterized by high thrust coefficients, i. e., above about 0.15 and encompasses RBL 1, RBL 2, the 120 AF propeller at the 17.0° pitch setting and the 3(109652) propeller at

Table 1
CASES COMPUTED

CASE	NO. OF BLADES	ACTIVITY FACTOR	DIAMETER (feet)	$\beta_{0.7 R_p}$ (deg)	$\beta_{0.975 R_p}$ (deg)	TIP SPEED (fps)	RANGE	APPROXIMATION	NO. OF ITERATIONS REQUIRED	C_T^*	C_P^*	F/M^* %	$u_{\theta} 0.975 R_p$ $\div \Omega R_p$
RBL 1	4	-	-	-	-	-	1	1st 2nd 3rd	4	0.151	0.0476	108	0.0615
									2	0.161	0.0434	119	0.0617
									3	0.161	0.0355	145	0.0644
RBL 2	3	-	-	-	-	-	1	1st 2nd	3	0.154	0.0406	119	0.0719
									2	0.154	0.0357	135	0.0733
120 AF	4	120	7.0	17.0	7.4	700	1	1st 2nd	7	0.214	0.1029	77	0.0651
								EXPERIMENTAL	4	0.230	0.1096	80	0.0637
								**	-	0.180	0.0870	70	-
120 AF	4	120	7.0	10.0	0.4	700	3	EXPERIMENTAL	2	-	-	-	-
									-	0.099	0.0360	70	-
65 AF	4	65	7.0	12.6	4.8	800	2	1st EXPERIMENTAL	10	0.115	0.0377	83	0.0272
									-	0.120	0.0520	63	-
65 AF	4	65	7.0	8.2	0.4	800	3	** EXPERIMENTAL	2	-	-	-	-
									-	0.088	0.0280	76	-
3(109652)	3	115	15.0	16.0	7.4	785	1	1st EXPERIMENTAL	7	0.186	0.0791	81	0.0923
									-	0.161	0.0680	77	-
3(109652)	3	115	15.0	10.0	1.4	785	2	1st EXPERIMENTAL	8	0.122	0.0391	87	0.0241
									-	0.100	0.0360	73	-

- NOT APPLICABLE

* THESE ARE INDUCED QUANTITIES (NEGLECTING PROFILE DRAG) FOR RBL 1 AND RBL 2

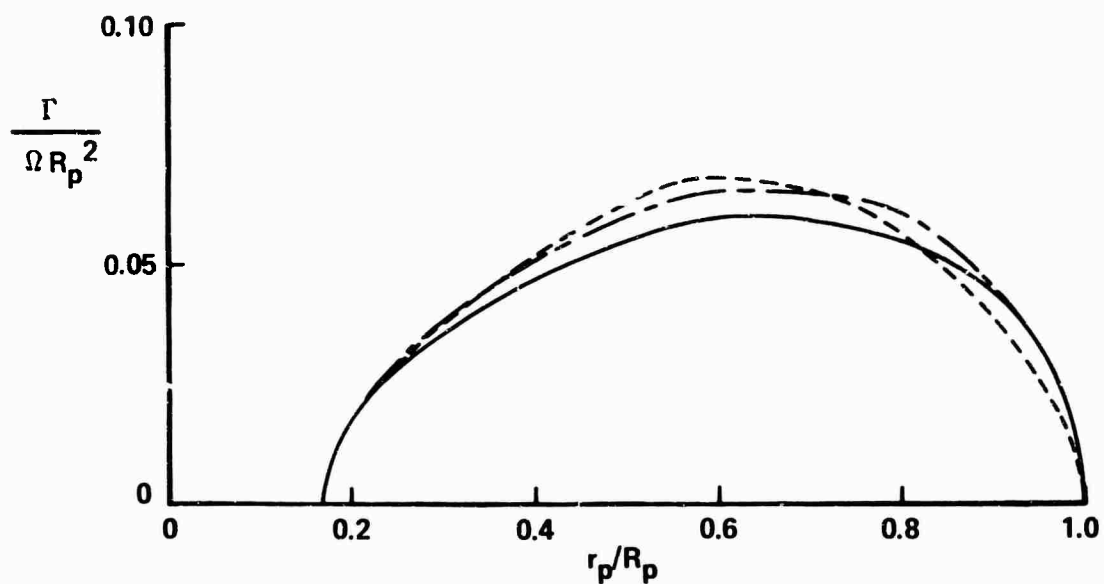
** SUCCESSFUL ITERATION COULD NOT BE ACHIEVED

the 16.0° pitch setting. (All pitch settings are measured at the 0.7 radial station.) The second range is characterized by thrust coefficients between about 0.10 and 0.15 and includes the 65 AF propeller at the 12.6° pitch setting and the 3(109652) propeller at the 10.0° pitch setting. Finally, the third range is characterized by low thrust coefficients below about 0.10 and includes the 65 AF propeller at the 8.2° pitch setting and the 120 AF propeller at the 10.0° pitch setting.

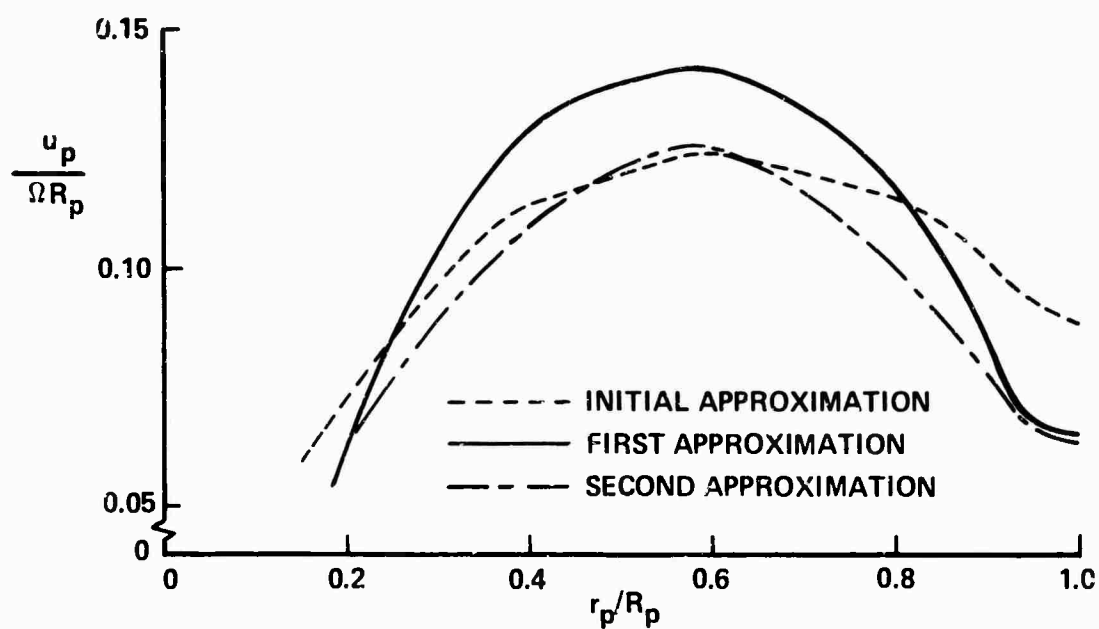
Three of the four cases computed in the first range were carried through at least one iteration on the assumed variations of the axial velocity component with distance downstream, i. e., on the effective pitch. There is every reason to believe that the remaining case that was not iterated on the effective pitch would exhibit the same characteristics. The 120 AF propeller at 17.0° is typical of these computations, and this case is described below.

Iteration was started by determining initial approximations to both the blade circulation distribution Γ and the axial inflow u_p by means of the Curtiss-Wright method of References 31 and 32 (see Figure 4 where these quantities are presented in appropriate nondimensional form). The initial tangential inflow w_p was found from this circulation distribution by the generalized actuator disk value of $-\Gamma/4\pi r_p$ which had been found, in References 17 and 18, to be a useful approximation. The assumed axial velocity variations u_v/u_p , based on previous calculations, increased with x_v at rates consistent with results for propellers in axial flight and reached asymptotic values of exactly 2.0 times the inflow values at all radii (see Figure 5 for the 0.975 radial station).

Seven successive iterations to the inflow and Γ were required to achieve convergence of u_p to within $\pm 2.6\%$ everywhere along the blade. The seventh iteration to both Γ and u_p , denoted here as the first approximations in the sense of iteration on the axial velocity variations, are presented in Figure 4. The assumed and computed values of radial inflow v_p are shown in Figure 6(a) for the first approximation. Overall, they are in good agreement, except inboard where we did not expect agreement for the



(a) BLADE CIRCULATION



(b) AXIAL INFLOW

Figure 4 COMPUTED RADIAL VARIATIONS OF FLOW QUANTITIES -
120 AF PROPELLER, $\beta_{0.7 R_p} = 17.0^\circ$

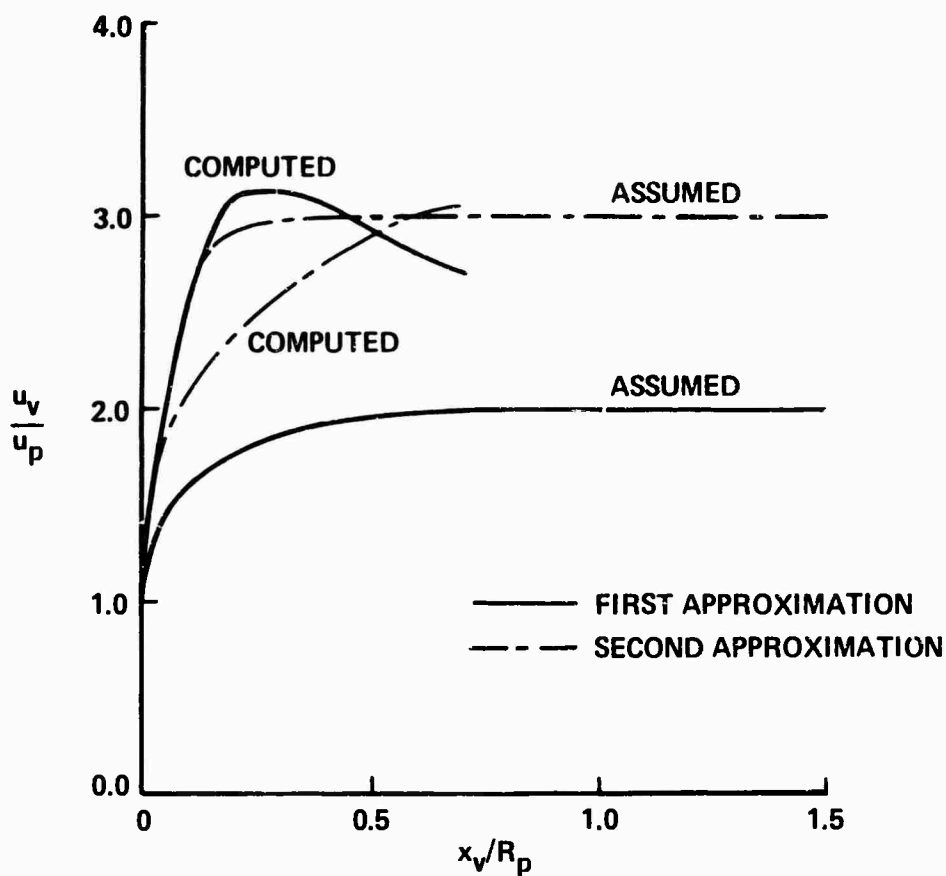
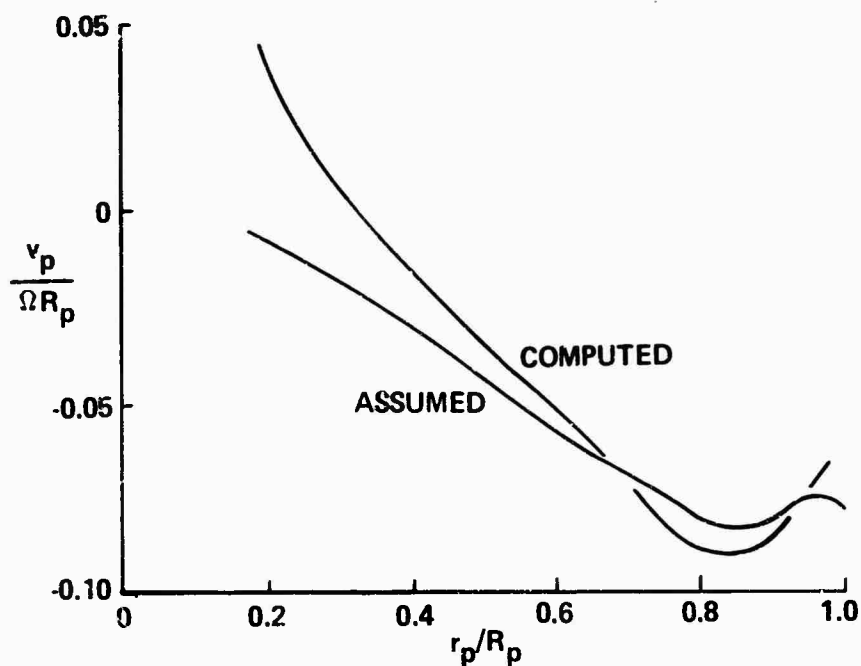
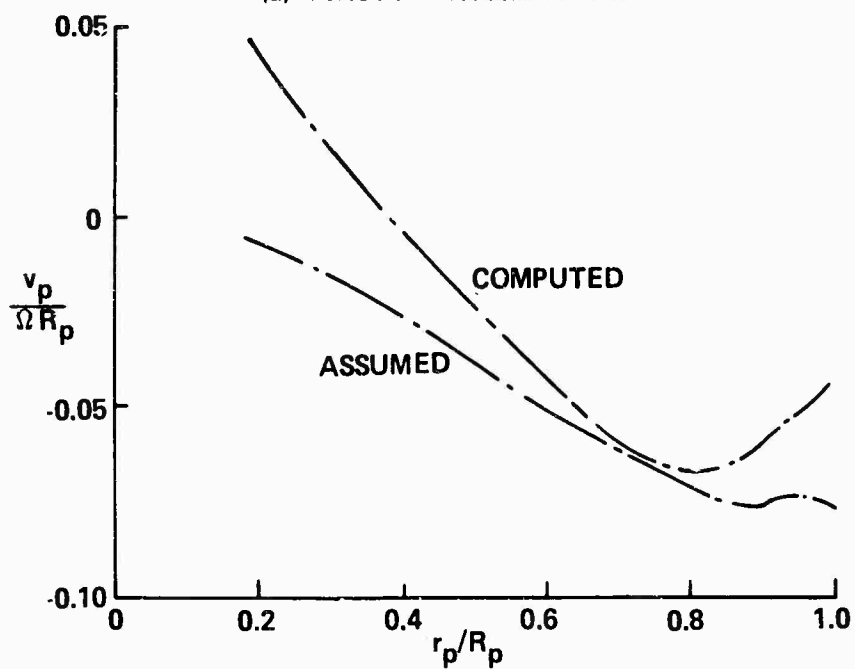


Figure 5 VARIATIONS OF AXIAL VELOCITY COMPONENT ALONG VORTEX ELEMENT TRAILING FROM $r_p/R_p = 0.975 - 120$ AF PROPELLER, $\beta_{0.7 R_p} = 17.0^\circ$



(a) FIRST APPROXIMATION



(b) SECOND APPROXIMATION

Figure 6 COMPARISONS OF ASSUMED AND COMPUTED RADIAL INFLOW -
120 AF PROPELLER, $\beta_{0.7 R_p} = 17.0^\circ$

present fixed contraction pattern. Next, the corresponding first approximations to the axial velocity variations were computed at several points along the elements of the vortex sheets trailing from the 0.4, 0.7, 0.9 and 0.975 radial stations. At the inboard two stations, the computed variations increased somewhat less rapidly than assumed, while at 0.9 the assumed and computed variations were in close agreement. At the 0.975 station, however, the computed variation increased much more rapidly than assumed but reached a maximum value and then decreased (see Figure 5).

Based upon these computed values of u_v / u_p , a new set of variations was assumed. However, the peak and subsequent decrease which appeared at the 0.975 station were ignored (see Figure 5). Four successive iterations to the inflow and r were then computed to achieve convergence of u_p to within $\pm 1.8\%$. The resulting second approximations to r and u_p are given in Figure 4. The assumed and computed radial inflow comparison was much less favorable, as can be seen in Figure 6(b). Here, the indication is that less contraction, initially at least, was needed than was being assumed. Moreover, the second approximations to the performance parameters were in poorer agreement with test data than the first, as shown in Table I. The corresponding second approximations to the axial velocity variations were computed at the same locations as before. Excellent agreement was achieved at the 0.4 and 0.7 radial stations. At the 0.9 station, the computed variation increased more rapidly initially but then reached a maximum and decreased. At the 0.975 station (see Figure 5), the computed variation increased less rapidly initially but did not reach a maximum, at least to the largest x_v at which computations were made. This was the extent of computations for this case, although further iterations with changes in the assumed contraction patterns as well as in the axial velocity variations are certainly required.

The results described above are typical for all the cases in the first range. That is, as the assumed and computed axial velocity variations approached agreement with the contraction pattern fixed, the predicted performance became less realistic (see Table I) and the indications were that less contraction was needed.

Before moving to a discussion of the other ranges, three observations should be made because they are typical of the results in all ranges. First, convergence of the inflow iteration for an assumed set of axial velocity variations began at the tip and moved inboard with successive iterative steps. This follows from the general property that the axial velocity induced by a helical vortex, even a distorted one, is much larger at radii smaller than its own initial radius than at larger radii. Moreover, the rate of convergence and the inboard progression of convergence are much more rapid for the RBL where β is fixed throughout the iteration. Second, although u_v / u_p at the 0.975 radial station was changed greatly between the first and second approximations (see Figure 5), there was only a small difference in the resulting values of u_p outboard of the 0.9 station (see Figure 4). On the other hand, the change had a profound effect on u_p at stations inboard of 0.9. This effect has been observed throughout the computations, namely, that a change in the axial velocity variation at a given radius has only a small effect locally, practically none outboard, but a large effect inboard. This, too, follows from the above-mentioned property of helical vortices. Third, maxima and subsequent decreases in the computed axial velocity variations occurred frequently during the computations, but often, as in the case described, disappeared from one approximation to the next. These decreases result from a stretching deformation of the trailing vortex sheet which reduces the local trailing vortex strength and so the local self-induced velocity.

Turning to the second range of operation, neither of the two cases were iterated on the assumed axial velocity variations, although first approximations to β and the inflow were found for the initially assumed variations. The 3(109652) propeller at the 10.0° pitch setting is typical of these two cases. Iteration was initiated exactly as for the 120 AF propeller at the 17.0° pitch setting, except that the axial velocity variations were selected by extrapolating the best previous experience and were assumed to reach asymptotic values greater than 2.0 outboard of the 0.8 radial station (see Figure 7, for example).

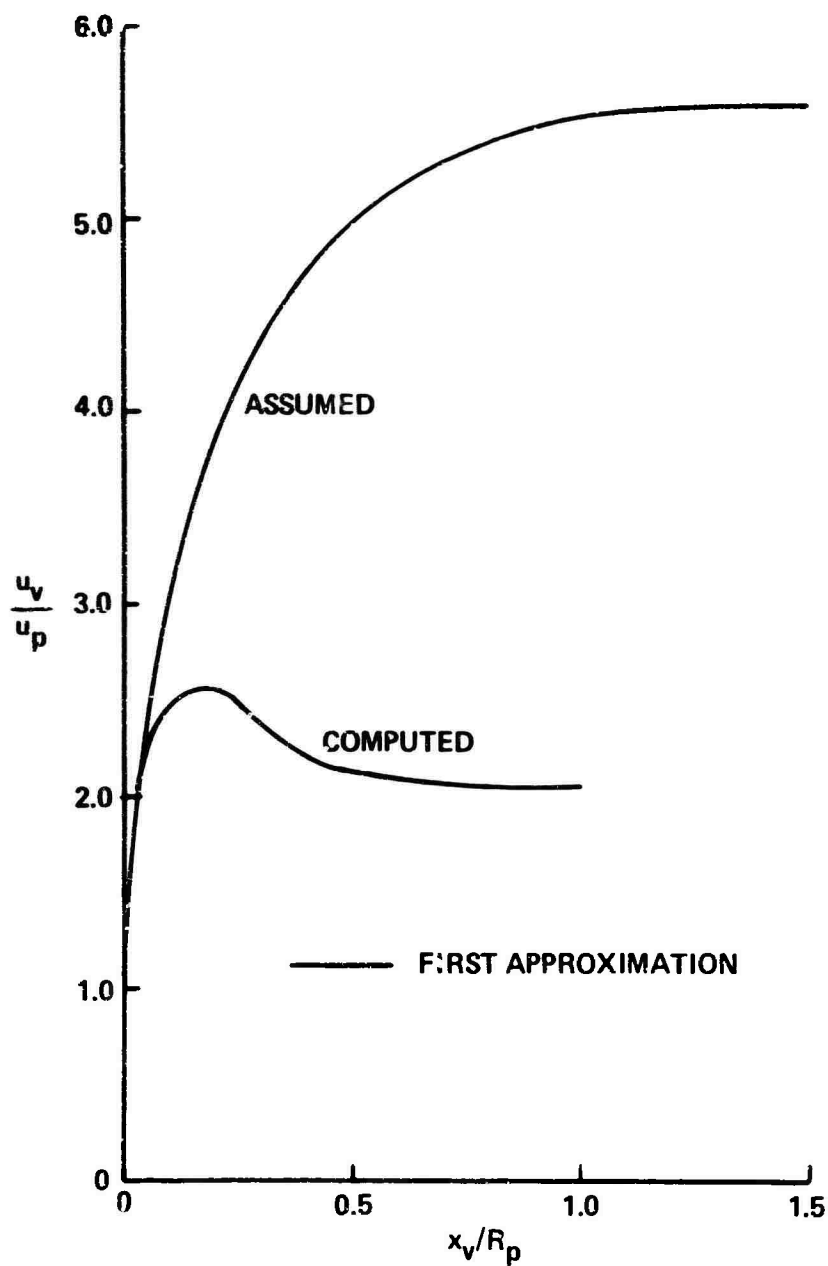


Figure 7 VARIATIONS OF AXIAL VELOCITY COMPONENT ALONG VORTEX ELEMENT TRAILING FROM $r_p/R_p = 0.975 - 3(109652)$ PROPELLER, $\beta_{0.7 R_p} = 10.0^\circ$

Eight successive iterations to the inflow and r' were required to achieve convergence of u_p to within $\pm 2.0\%$ inboard of the 0.9 station. Outboard, the differences were as large as $\pm 6.1\%$, although the absolute differences were of the same size as inboard because u_p near the tip is quite small in this case (see Table I). A less rapid rate of convergence also ensued because, as discussed previously, small changes in u_p near the tip can have a large effect inboard. An important feature of this case and this range is that the assumed and computed first approximations to the radial inflow indicated that, in contrast to the first range, initially at least, more contraction was needed than was being assumed (see Figure 8). Next, the corresponding first approximations to the axial velocity variations along the trailing vortex sheets were computed. At the 0.4 and 0.7 radial stations, the computed variations were slightly less than those assumed, while at 0.9 the computed variation increased more rapidly, reached a maximum that was larger than the assumed asymptotic value and then decreased. At 0.975, however, the computed variation increased initially at the assumed rate but reached a maximum less than one-half as large as the assumed asymptote and then decreased slightly (see Figure 7). The calculations were concluded at this point, although further iterations should certainly be made for changes in both the contraction pattern and the axial velocity variations.

The results described are typical of this second range, namely, the computed axial velocity variations outboard of the 0.9 radial station fell below the assumed values, and the indications were that more contraction was needed. Simple extrapolations based upon modified axial velocity variations, for the same fixed contraction pattern, show that the predicted performance would be distinctly improved so far as agreement with test data is concerned. This is in contrast to similar extrapolations for the first range which indicated progressively poorer agreement.

In the third range of operation, neither of the two cases attempted could be iterated successfully. The iteration was begun in each case as usual with a best guess at the assumed axial velocity variations. However, the computed axial inflow after the first iterative step in each case was

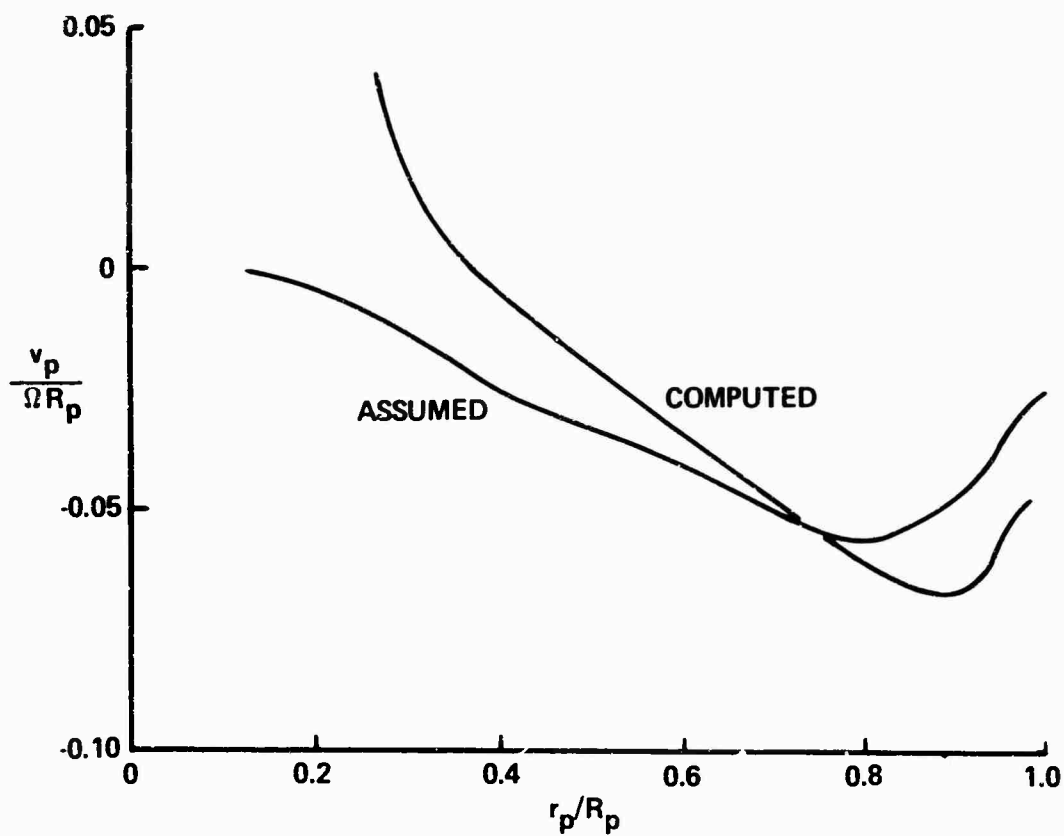


Figure 8 COMPARISON OF ASSUMED AND COMPUTED RADIAL INFLOW -
3(109652) PROPELLER, $\beta_{0.7 R_p} = 10.0^\circ$, FIRST APPROXIMATION

negative outboard of approximately the 0.93 radius. In the wake representation used in the calculations, negative axial inflow could not be handled. Moreover, experience in Reference 17 showed the extreme sensitivity of the computed inflow to small changes in the trajectories of the elements of the trailing vortex sheets if these elements moved ahead of the propeller a short distance in the negative x direction before turning and moving aft. Two different steps were taken here in attempts to overcome this difficulty. First, the assumed axial velocity variations were modified outboard of the 0.95 radial station. This led to substantial changes in the induced axial inflow inboard of 0.95 after a single iterative step but small changes outboard. This is consistent with the behavior observed in Figure 4. Second, based upon differences observed between previous initial and first approximations, modified initial approximations to the axial inflow and r' outboard of the 0.7 radial station were assumed. This change, too, led to results that were qualitatively the same as before and so this change also held little promise.

A successful iteration, then, could not be carried out in either case. Moreover, the wake data for these cases were nonrepeatable near the propeller tip and so could not be of help in determining the effective pitch of the trailing vortex sheets at that location. However, the data could have provided a check over the middle part of the blade if we had been able to iterate successfully.

Although this marked the total extent of our attempts to find iterative solutions for these eight cases, the induced velocity components in the propeller disk plane at points other than along the lifting lines were investigated subsequently. Numerical computations were carried out for three of the above cases, namely, the RBL 1 and RBL 2 from the first range of operation, and the 3(109652) propeller at the 10.0° pitch setting from the second range of operation. The complete results are given in Reference 21, but several key features bear description here since they help focus attention on some problem areas of our theoretical development.

An example of the variation with azimuth θ of the bound and trailing vortex contributions to the total induced axial velocity u_o at the 0.975 radial station in the propeller plane for RBL 1 is presented in Figure 9. The bound contribution in a lifting-line model is symmetrical about a θ half-way between lifting lines (here $\theta = 45^\circ$) and so its θ -average is zero. Further, it is not a valid approximation in the immediate vicinity of the blades, even becoming singular as the lifting line is approached. It is taken to be zero at the lifting line, i.e., at $\theta = 0^\circ$, for performance purposes. The results here for the θ -variation of the trailing vortex sheet contribution are typical of all three cases computed with regard to the basic shape, although detailed differences do arise, in large measure from the rate of contraction of the trailing vortex sheets with respect to azimuth. As the radius decreased, the magnitude of the harmonic fluctuations of the trailing contributions decreased rapidly so that at the 0.7 station the fluctuations about the average are less than $\pm 0.01 \Omega R_p$. The θ -average value of the total axial velocity for RBL 1 at 0.975 (Figure 9) is -0.0015; in fact, in all three cases treated, the axial velocity component at the 0.975 radius was positive at the lifting lines but was sufficiently negative at values of θ between them so that the average was negative. Therefore, although it is possible for the instantaneous axial inflow at the lifting line to be negative, as indicated in the third operating range, still it is possible to have cases in the first and second ranges where mean flow measurements or flow visualization results might indicate negative axial velocities at the propeller disk but where the inflow at an effective lifting-line position is actually positive.

Continuing our discussions in this regard, consider the ratios of the average to instantaneous axial $\langle u_o \rangle / u_p$ and radial $\langle v_o \rangle / v_p$ inflow as a function of radius in Figures 10(a) and 10(b), respectively, for the same three cases for which computations were made in the propeller disk plane. Computations were only made outboard of the 0.7 radial station because there appeared to be negligible differences farther inboard. The qualitative relationships displayed by these ratios with respect to one another are like the corresponding ratios for propellers in lightly loaded axial flight (see Reference 33, for example). That is, a comparison of the three-bladed cases

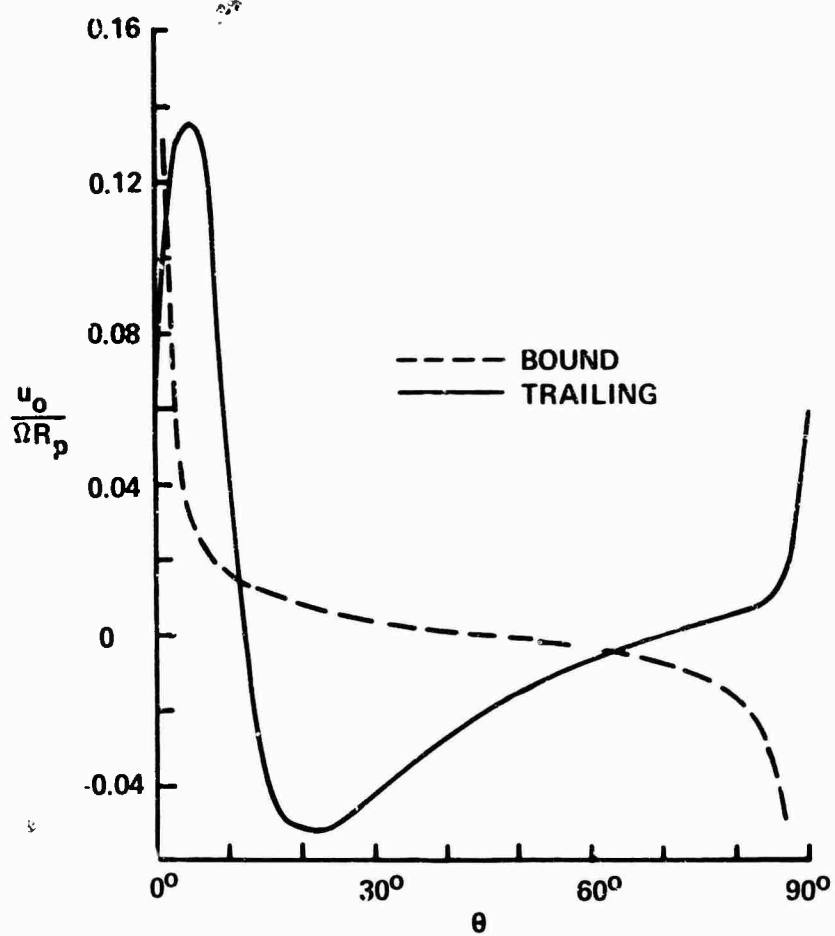


Figure 9 BOUND AND TRAILING VORTEX CONTRIBUTIONS TO AXIAL INDUCED VELOCITY IN PROPELLER PLANE - REPRESENTATIVE BLADE LOADING ONE, $r_p/R_p = 0.975$

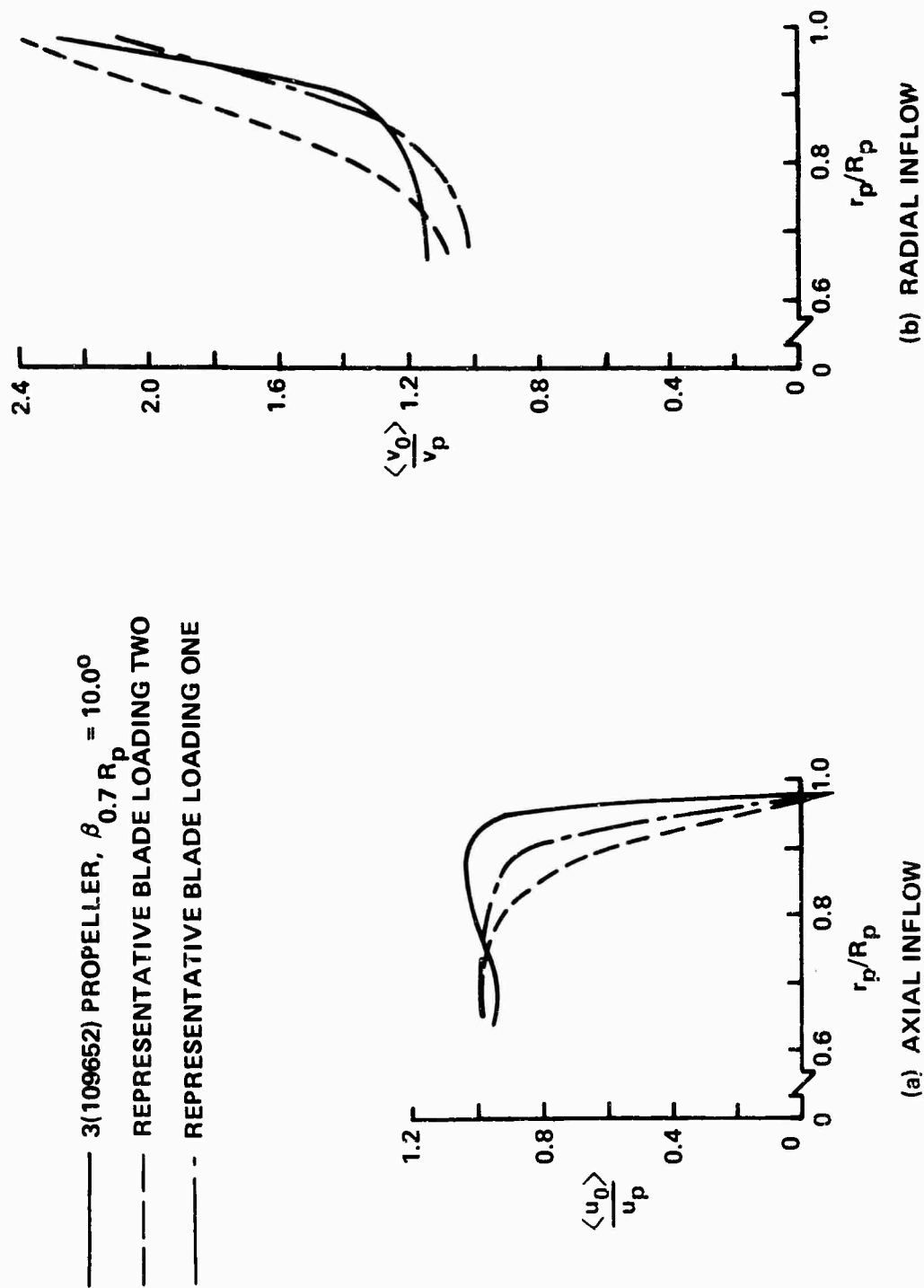


Figure 10 RATIOS OF AVERAGE INFLOW IN PROPELLER PLANE TO INSTANTANEOUS INFLOW AT PROPELLER BLADES FOR FIRST APPROXIMATIONS TO THREE CASES

indicated that, at a given radius, both average inflow components are closer to the instantaneous values for the 3(109652) propeller at 10.0° than for the RBL 2 because the former has a lower effective pitch. Also, for roughly comparable effective pitch, the average inflow components are closer to the instantaneous for RBL 1 than for RBL 2 because the former has a larger number of blades. The ratios of the average to instantaneous tangential inflow as a function of radius look qualitatively like the 3(109652) axial inflow in Figure 10(a).

Since the average radial inflow is greater than the instantaneous, while the average axial inflow is less than the instantaneous (and may be negative as shown), the θ -average streamline pattern (i.e., $\langle v \rangle / \langle u \rangle$) that is implied may be quite different from the instantaneous streamline pattern. Moreover, equivalence between infinite-blade-number models and the θ -average of finite-blade-number models has not been established in hover as it has been for axial flight (see Reference 22). Therefore, the contraction pattern predicted by Greenberg and Kaskel in Reference 10 may not be directly applicable to the present finite-bladed theory as we have assumed. The comparisons of assumed and computed radial inflow for the numerical cases discussed above certainly reinforce this observation.

Examination of the θ -variations of the trailing contribution to the axial induced velocity in the propeller plane (as in Figure 9, for example), shows that the magnitude of the axial induced velocity component changes significantly over distances as small as a blade chord length. The rapid increase of the computed variations of the axial component with distance downstream along the trailing vortex sheets (as in Figures 5 and 7, for example) also shows this effect. Estimates based on these results show that there may be an induced camber effect, especially near the propeller tip, which is of roughly the same size as, and which tends to reduce, the design camber. A more precise evaluation of the magnitude of the effect should be made because induced camber is implicitly assumed to be zero in the lifting-line model.

It should be recalled, too, that in the manner that we have applied our wake representation in these computations, the bound vortex contribution to the axial induced velocity component along the trailing vortex sheets has not been considered. Instead, its θ -average value of zero has been taken. Computations have shown that the neglected bound contribution is small compared to the trailing contribution for x_v / R_p values greater than about 0.2 propeller radii. However, the bound contribution may be very significant in the immediate vicinity of the lifting line, especially when the trailing vortex contribution is very small, or negative, as in the third range of operation. In particular, it may be important in establishing the position of the trailing vortex sheets in the immediate vicinity of the blades. That is, it appears that finite chord, lifting surface effects must be introduced in some fashion, even in what is basically a lifting-line theory, in order to be able to predict the axial inflow and performance successfully. A possible approach to an improved model might be to constrain the trajectories of the elements of the trailing vortex sheets to follow the mean chord line while these elements are still on the blades and to permit them to become force free only when the trailing edge is reached. At that distance from a lifting line located at the quarter chord, the bound vortex contribution to the axial velocity is a fairly reasonable estimate to the lifting surface value, at least on the basis of two-dimensional airfoil theory. Similar considerations of the trailing vortex locations have been made for the spanwise flow effects of side-slipping wings (Reference 34) and for helicopter rotors under certain conditions of low rotational speeds (Reference 35). In both these cases, as in the present problem, the location of the trailing vortex system cannot be clearly specified in advance as in the usual linearized models. An approach such as indicated above appears to give hope for achieving successful iterations in the third range of operation without completely abandoning the lifting-line model.

CONCLUSIONS

The refined wake hypothesis developed previously for predicting the hovering performance of a V/STOL propeller is inadequate for the systematic development of a performance prediction and design method. A new wake representation, utilizing results of heavily loaded actuator disk theory to fix the basic contraction pattern, is proposed. Attention was then focused on the determination of good approximations to the force-free effective pitch of the trailing vortex sheets for eight specific cases.

To provide data for checking details of the wake representation, a limited experimental program was carried out on the Canadair, Ltd. propeller test rig. It was demonstrated that it is experimentally feasible to make hot-wire measurements of the instantaneous values of the three velocity components in the wake of a hovering propeller, but extreme care is required in the basic hot-wire calibrations. For two propellers investigated at one blade pitch setting each, a hot-wire signal that is repeatable with blade passage could be obtained aft of the propeller only behind the middle part of the blade. Near the hub and tip, nonrepeatable, apparently random, signals were measured.

The results of numerical computations for the eight cases indicate three distinct ranges of propeller operation with respect to the wake representation used. In terms of thrust coefficient, the first range is above about 0.15, the second between about 0.10 and 0.15, and the third below about 0.10. As the effective pitch is iterated to approach the force-free condition of the wake in the first range, the predicted performance becomes poorer with respect to test data and the assumed contraction appears to be too great. In the second range, the effective pitch was not iterated but extrapolations show that the predicted performance should come into better agreement with the test data, although the assumed contraction appears to be too small. In the third range, where the hot-wire data were taken, successful iterations could not be achieved for the inflow and blade circulation with the present wake representation because of negative induced axial inflow near the tip. The effective pitch of the elements of the trailing vortex sheets outboard of

the 0.9 radial station, in all three ranges, has a large influence on the magnitude of the axial inflow at radii inboard but has only a small influence locally.

Computed velocity components in the propeller plane show harmonic fluctuations that increase rapidly in magnitude outboard of the 0.7 radial station. The ratios of the average inflow components to their instantaneous values behave qualitatively much like their axial flight counterparts. However, the average axial inflow for cases in the first and second operating ranges are negative outboard of about the 0.97 radial station despite a positive instantaneous axial inflow at the lifting lines there.

Detailed considerations of the flow in the vicinity of the blade (i. e., lifting surface effects) require examination to provide a better approximation to the bound blade vortex system for purposes of determining the location of the trailing vortex sheets immediately aft of the lifting lines. This is especially so in the third range of operation where the axial inflow induced by the trailing vortex sheets is very small or negative. There are also indications that the axial induced velocity component changes sufficiently in magnitude over the extent of the blade chord that significant induced camber effects exist and should be taken into account by an appropriate lifting surface approximation.

ACKNOWLEDGMENTS

The author wishes to acknowledge the support of the U. S. Army Aviation Materiel Laboratories, Fort Eustis, Virginia, under Contract DA44-177-AMC-379(T) with Mr. W.E. Sickles as project monitor, for the basic development of the theory, the experimental investigation and all the iterative computations. That portion of the investigation was performed at Therm Advanced Research, Inc., Ithaca, New York. Acknowledgment also is given to the support of the U. S. Army Research Office-Durham, Durham, North Carolina, under Contract DAHC04-68-C-0039 with Dr. S. Kumar as project monitor, for the computations of the flow field in the propeller disk plane. That portion was carried out at Cornell Aeronautical Laboratory, Inc., Buffalo, New York. Many people contributed in various ways during the performance of this investigation, and the author wishes to thank his past and present colleagues, Dr. I. S. Gartshore, Mr. D. C. Gilmore, Dr. M. D. Greenberg, Mr. G. R. Hough, Mr. A. L. Kaskel, Dr. G. Kurylowich, Dr. L. E. Ordway, Dr. A. Ritter, Dr. I. C. Statler and Mr. F. A. DuWaldt.

REFERENCES

1. Gray, R. B., "An Aerodynamic Analysis of a Single-Bladed Rotor in Hovering and Low-Speed Forward Flight as Determined from Smoke Studies of the Vorticity Distribution in the Wake", Princeton University, Aeronautical Engineering Department Report 356, September 1956.
2. Tararine, S., "Experimental and Theoretical Study of Local Induced Velocities Over a Rotor Disc", Proceedings, CAL/TRECOM Symposium on Dynamic Load Problems Associated with Helicopters and V/STOL Aircraft, Vol. I, Cornell Aeronautical Laboratory, Inc., Buffalo, New York, June 1963.
3. Borst, H. V. and Ladden, R. M., "Propeller Testing at Zero Velocity", Proceedings, CAL/USAAVLABS Symposium on Aerodynamic Problems Associated with V/STOL Aircraft, Vol. I, Technical Session 1, Cornell Aeronautical Laboratory, Inc., Buffalo, New York, June 1966.
4. Adams, G. N., "Propeller Research at Canadair Limited", Proceedings, CAL/USAAVLABS Symposium on Aerodynamic Problems Associated with V/STOL Aircraft, Vol. I, Technical Session 1, Cornell Aeronautical Laboratory, Inc., Buffalo, New York, June 1966.
5. Trenka, A. R., "Prediction of the Performance and Stress Characteristics of VTOL Propellers", Proceedings, CAL/USAAVLABS Symposium on Aerodynamic Problems Associated with V/STOL Aircraft, Vol. I, Technical Session 1, Cornell Aeronautical Laboratory, Inc., Buffalo, New York, June 1966.
6. Crimi, P., "Prediction of Rotor Wake Flows", Proceedings, CAL/USAAVLABS Symposium on Aerodynamic Problems Associated with V/STOL Aircraft, Vol. I, Technical Session 2, Cornell Aeronautical Laboratory, Inc., Buffalo, New York, June 1966.
7. Simons, I. A., Pacifico, R. E. and Jones, J. P., "The Movement, Structure and Breakdown of Trailing Vortices from a Rotor Blade", Proceedings, CAL/USAAVLABS Symposium on Aerodynamic Problems Associated with V/STOL Aircraft, Vol. I, Technical Session 2, Cornell Aeronautical Laboratory, Inc., Buffalo, New York, June 1966.
8. Gartshore, I. S., "An Application of Vortex Theory to Propellers Operating at Zero Advance Ratio", McGill University, Mechanical Engineering Research Laboratories Technical Note 66-3, June 1966.
9. Jenney, D. S., Olson, J. R. and Landgrebe, A. J., "A Reassessment of Rotor Hovering Performance Prediction Methods", Journal of the American Helicopter Society, Vol. 13, No. 2, April 1968.

10. Greenberg, M.D. and Kaskel, A.L., "Inviscid Flow Field Induced by a Rotor in Ground Effect", National Aeronautics and Space Administration CR-1027, May 1968.
11. Iwasaki, M., Sasaki, R., Shiki, T. and Himori, A., "Theoretical and Experimental Investigations of a Propeller Working at Static Condition", Reports of Research Institute for Applied Mechanics, Kyushu University, Vol. 16, No. 52, 1968.
12. Lehman, A.F., "Model Studies of Helicopter Rotor Flow Patterns in a Water Tunnel", American Helicopter Society Paper 207, 24th Annual Forum, Washington, D. C., May 1968.
13. Ordway, D.E. and Erickson, J.C., Jr., "A New Approach to the Static Thrust Problem, Phase I, Formulation and Preliminary Assessment of Mathematical Model", Therm, Inc. TAR-TR 631, March 1963.
14. Erickson, J.C., Jr. and Ordway, D.E., "A New Approach to the Static Thrust Problem, Phase II, Calculation of Thrust and Torque, Model X-100 Propeller, $\beta @ 0.7R_p = 10.0^\circ$ ", Therm, Inc. TAR-TR 632, May 1963.
15. Erickson, J.C., Jr. and Ordway, D.E., "A New Approach to the Static Thrust Problem, Phase III, Further Inflow Calculations with Extensions to Partially Negative Γ Distributions", Therm, Inc. TAR-TR 635, August 1963.
16. Erickson, J.C., Jr. and Ordway, D.E., "A New Approach to the Static Thrust Problem, Phase IV, Further Development of Performance Calculation Method", Therm, Inc. TAR-TR 638, December 1963.
17. Erickson, J.C., Jr., Ladden, R.M., Borst, H.V. and Ordway, D.E., "A Theory for VTOL Propeller Operation in a Static Condition", U. S. Army Aviation Materiel Laboratories Technical Report 65-69, October 1965.
18. Erickson, J.C., Jr. and Ordway, D.E., "A Theory for Static Propeller Performance", Proceedings, CAL/USAAVLABS Symposium on Aerodynamic Problems Associated with V/STOL Aircraft, Vol. I, Technical Session 1, Cornell Aeronautical Laboratory, Inc., Buffalo, New York, June 1966.
19. Erickson, J.C., Jr., "Theoretical and Experimental Investigations of V/STOL Propeller Operation in a Static Condition", U. S. Army Aviation Materiel Laboratories Technical Report (to be published).
20. Gilmore, D.C. and Gartshore, I.S., "Measurements of the Instantaneous Velocities in the Wake of Two Propellers Operating at Zero Advance Ratio", McGill University, Department of Mechanical Engineering, Final Report submitted to Therm Advanced Research, Inc., 11 January 1967.

21. Erickson, J. C., Jr. and Hough, G. R., "On the Fluctuating Flow Field of Propellers in Cruise and Static Operation", Paper submitted to the Journal of Aircraft for publication.
22. Hough, G. R. and Ordway, D. E., "The Generalized Actuator Disk", Developments in Theoretical and Applied Mechanics, Vol. 2, Pergamon Press, Oxford, 1965.
23. Hough, G. R. and Ordway, D. E., "The Steady Velocity Field of a Propeller with Constant Circulation Distribution", Journal of the American Helicopter Society, Vol. 10, No. 2, April 1965.
24. Hough, G. R. and Ordway, D. E., "Mean Flow Streamlines of a Finite-Bladed Propeller", Journal of Aircraft, Vol. 4, No. 6, November-December 1967.
25. Collis, D. C. and Williams, M. J., "Two-Dimensional Forced Convection from Cylinders at Low Reynolds Numbers", Government of Australia, Department of Supply, ARL Report A105, November 1957.
26. Webster, C. A. G., "A Note on the Sensitivity to Yaw of a Hot-Wire Anemometer", Journal of Fluid Mechanics, Vol. 13, 1962.
27. Hoole, B. J. and Calvert, J. R., "The Use of a Hot-Wire Anemometer in Turbulent Flow", Journal of the Royal Aeronautical Society, Vol. 71, July 1967.
28. Gilmore, D. C., "The Probe Interference Effect of Hot-Wire Anemometers", McGill University, Mechanical Engineering Research Laboratories Technical Note 67-3, July 1967.
29. Heyson, H. H., "Measurements of the Time-Averaged and Instantaneous Induced Velocities in the Wake of a Helicopter Rotor Hovering at High Tip Speeds", National Aeronautics and Space Administration TN D-393, July 1960.
30. Theodorsen, T., Theory of Propellers, McGraw-Hill, New York, New York, 1948.
31. Foss, R. L., "Strip Analysis Method for Evaluating Static Thrust", Curtiss-Wright Corporation, Propeller Division, Caldwell, New Jersey, Report C-2402, 19 November 1952.
32. Enos, L. H. and Borst, H. V., "Propeller Performance Analysis Aerodynamic Characteristics, NACA 16 Series Airfoils", Curtiss-Wright Corporation, Propeller Division, Caldwell, New Jersey, Report C-2000, 2 December 1948.

33. Hough, G.R., "A Numerical Study of the Fluctuating Flow Field of a Uniformly Loaded Propeller", Journal of Aircraft, Vol. 4, No. 1, January-February 1967.
34. Queijo, M.J., "Theoretical Span Load Distributions and Rolling Moments for Sideslipping Wings of Arbitrary Plan Form in Incompressible Flow", National Advisory Committee for Aeronautics Technical Report 1269, 1956.
35. Segel, L., "Air Loadings on a Rotor Blade as Caused by Transient Inputs of Collective Pitch", U. S. Army Aviation Materiel Laboratories Technical Report 65-65, October 1965.

**PROPELLER WAKE DEFORMATION DUE TO INSTABILITY OF
A TRAILING VORTEX SHEET**

*D.E. Cummings and J.E. Kerwin
MASSACHUSETTS INSTITUTE OF TECHNOLOGY
Cambridge, Massachusetts*

PROPELLER WAKE DEFORMATION DUE TO INSTABILITY OF
A TRAILING VORTEX SHEET*

by

D. E. Cummings and J. E. Kerwin
Department of Naval Architecture and
Marine Engineering
Massachusetts Institute of Technology
Cambridge, Massachusetts

ABSTRACT

The nature and effect of propeller vortex sheet deformation for wide-bladed propellers at finite advance speeds is demonstrated. A method is developed for determining the geometry of deformed trailing vortex sheets including a finite-core representation of the tip vortex. The effect of wake deformation on computed blade section pitch and camber is investigated. Comparative effect of several wake approximations on blade section geometry is shown for a specific example.

*This research was carried out under the Naval Ship Systems Command General Hydromechanics Research Program SR 009 01 01, Administered by the Naval Ship Research and Development Center. Prepared under the Office of Naval Research Contract. Nonr-1841(63)

Introduction

It has been a matter of practical necessity in the past to neglect the deformation of the trailing vortex sheet shed from a lifting-surface. Fortunately, this simplification does not appear to introduce significant errors in the determination of pressure distribution, lift and induced drag on most types of lifting-surfaces. However, there are important exceptions. It is now well known, for example, that the presence of a leading-edge vortex sheet in the flow around a highly swept wing at large incidence significantly alters its aerodynamic characteristics.

This paper is concerned with a somewhat less drastic situation, namely, the nature and effect of propeller vortex sheet deformation for wide-bladed marine propellers at finite advance speeds. Some of the reasons for looking into this problem at the present time are as follows:

1. The propeller design problem, i.e. the determination of blade section pitch and camber for a prescribed pressure distribution, is influenced by the assumed position of the trailing vortex wake. One would expect, intuitatively, that propellers with heavy loading, low pitch, large numbers of blades, or any combination thereof would be most affected, since significant deformation would occur relatively close to the blades. This, of course, is in contrast to a normal wing, whose wake disappears from sight much more rapidly.

2. The onset of tip-vortex cavitation for marine propellers cannot be predicted at all using the classical "linearized undeformed inviscid" wake model.

3. Determining the influence of the propeller on surrounding surfaces, of primary importance in ship vibration analysis, for example, may require a more realistic representation of the propeller wake.

4. The analysis of counter-rotating or tandem propellers, when one propeller is operating in the wake of another, requires a better understanding of the true behavior of wake shed from the upstream propeller.

In this paper, we shall restrict our attention to the problems of predicting the deformation of the wake of a propeller with a prescribed pressure distribution, and of determining the influence of the deformed wake on blade section pitch and camber.

Background

Before describing the general approach, it would seem advisable to review briefly the essential features of "more-or-less undeformed wake" marine propeller lifting surface theory, in widespread use at the present time. The basic coordinate system and nomenclature is illustrated in Fig. 1. The propeller is represented by K thin, symmetrically arranged, identical lifting-surfaces orbiting around a common axis with rotational speed ω . Both inner and outer extremities of each blade are treated as wing-tips, the presence of the hub being entirely neglected. The approach flow to the propeller is assumed axisymmetric in order to limit the problem to one steady flow. However, an arbitrary shear flow profile $V_A(r)$ is permitted in order to account, in at least an approximate way, for the characteristics of the flow around the ship in the vicinity of the propeller.

Following the usual linearization procedure, one would next represent the blades and wake by a suitable distribution

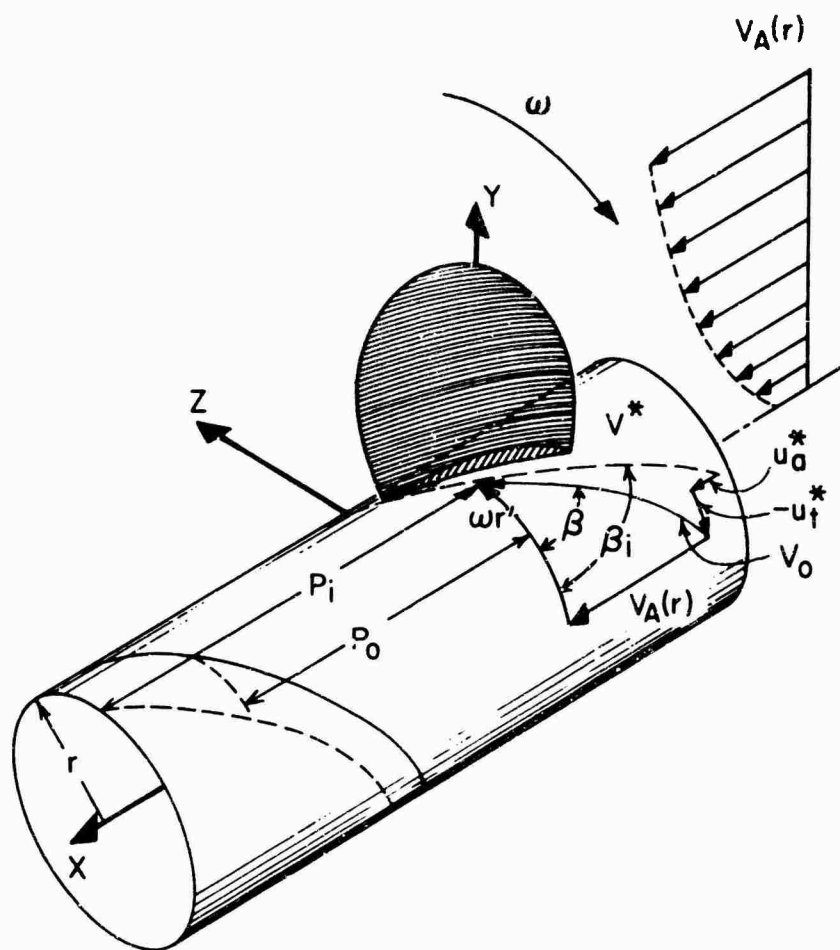


FIG. 1 APPROACH FLOW VELOCITY DIAGRAM

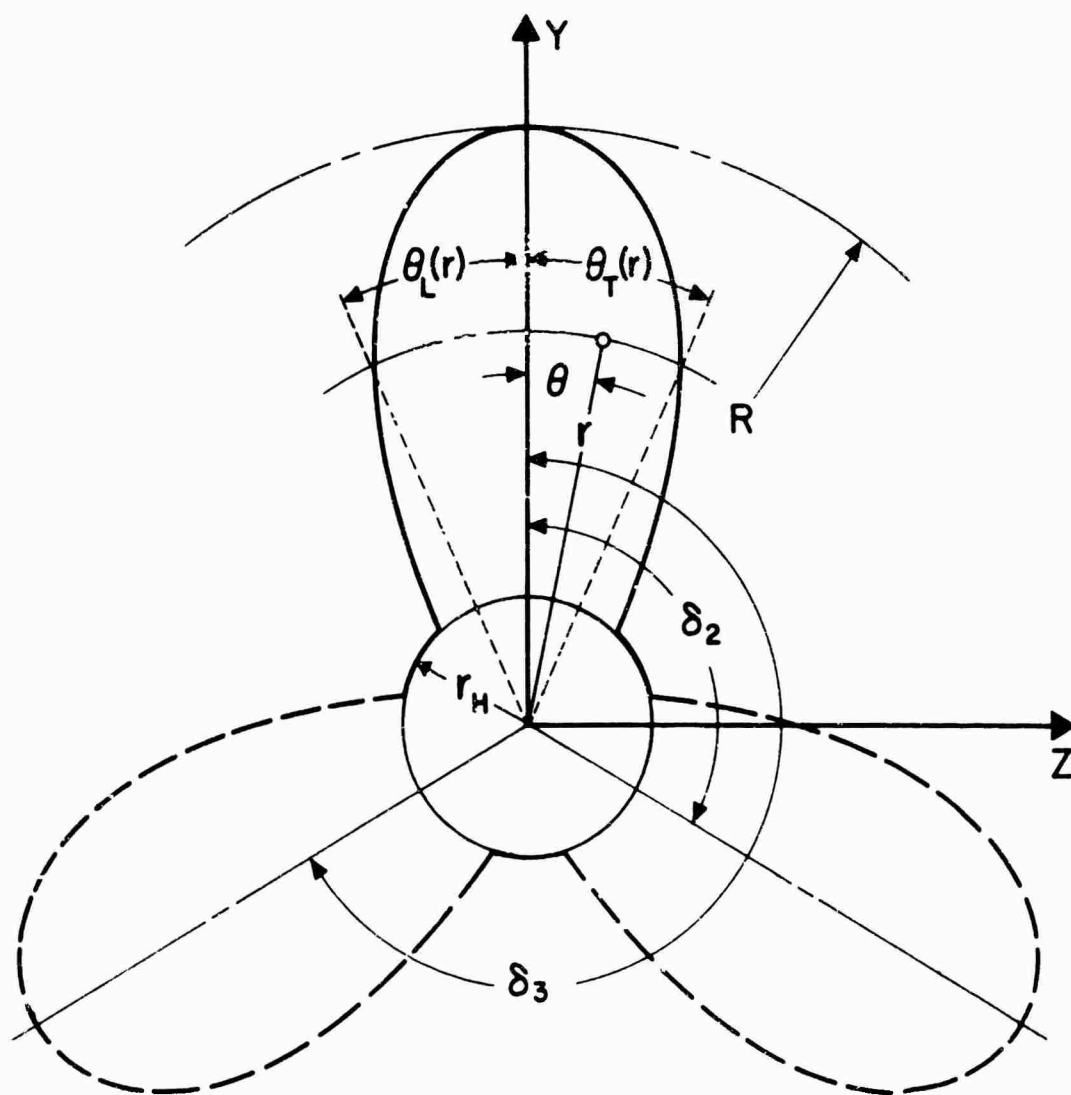


FIG. 2 PROJECTED BLADE OUTLINES

of singularities projected onto stream surfaces of the undisturbed flow. The intersection of a cylinder of radius r with each of these surfaces would be a helix of pitch angle

$$\beta(r) = \tan^{-1} \left[\frac{V_A(r)}{\omega r} \right] \quad (1)$$

as shown in Fig. 1.

However, a refinement is almost universally employed in an attempt to locate the singularities on surfaces which are closer to the actual positions of the blades and wake. This is carried out by first solving the lifting-line problem with the wake singularities projected onto helicoidal surfaces with pitch angle

$$\beta_i(r) = \tan^{-1} \left[\frac{V_A(r) + u_a^*(r)}{\omega r + u_t^*(r)} \right] \quad (2)$$

where u_a^* and u_t^* are the axial and tangential velocities induced at the lifting-line. This, of course, is an iterative process, since the induced velocities depend on the pitch angle β_i . However, convergence is rapid, so that a solution is easily obtained. Fig. 3 shows a comparison of the lifting-line induced velocities obtained from linear theory, where the wake singularities are projected onto a surface of pitch angle β , and the corresponding velocities obtained after the surface has converged to a new pitch angle β_i . The difference in downwash angle is approximately 1.8 degrees, with linear theory yielding the higher value.

The determination of blade section pitch and camber may next be determined by projecting the singularities representing the blades and wake onto the new reference helicoidal surface with pitch angle $\beta_i(r)$. The lifting-surface problem is then still a linear one, with an artificially altered inflow velocity and angle.

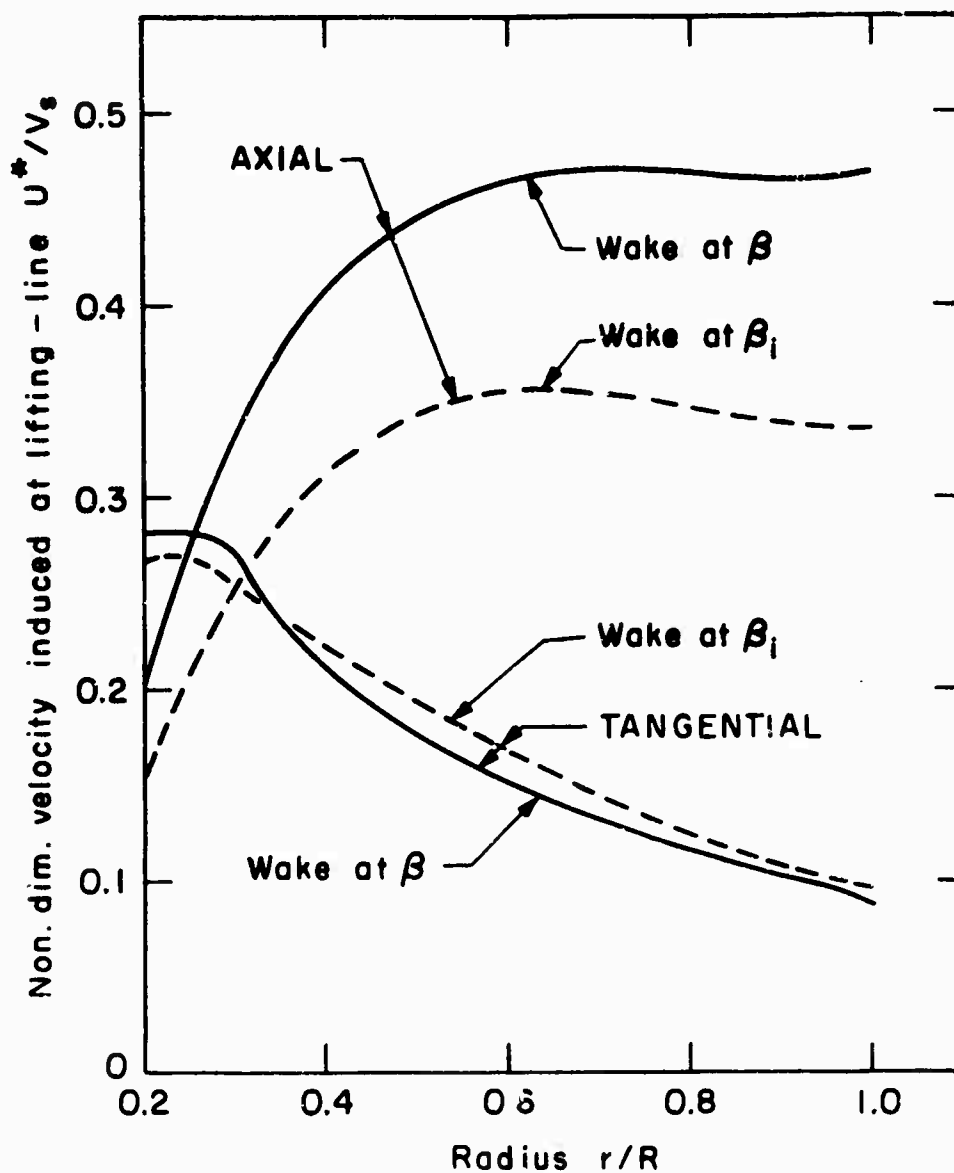


Fig. 3 Comparison of velocities induced at lifting-line for propeller R-2.

Blade loading is represented in the usual way by a distribution of bound and trailing vortices on the blades, and trailing vortices in the wake. Thickness is represented by a source-sink distribution with strength proportional to the slope of the thickness form.

Expressions for the downwash velocity induced at points on the blade by these singularity distributions are given in Table 1, and are developed in greater detail in Ref. 1. The angle of attack and blade section shape at each radius may then be obtained, in principle, from an integration of the downwash over the chord. In the actual numerical method employed, a curve-fitting procedure, which will be described subsequently, is used for this last step.

Representation of Propeller with Deformed Wake

It is assumed that the preceding representation is still valid for the flow on the blades, up to the trailing edge. Radial deformation of the streamlines is ignored, and the blade singularities are projected onto a reference helix of pitch angle $\beta_i(r)$. Downstream of the trailing edge, the wake is permitted to deform in accordance with the wake model described in the next section. Downwash velocities induced at points on the blade by the singularities representing the blade are therefore exactly the same as before, while those due to the trailing vortices in the wake are influenced by the wake deformation.

Trailing Vortex Sheet Position and Tip Vortex Dynamics

The calculations required to determine the configuration and dynamics of the vortex sheets shed in a propeller wake

TABLE I

BOUND VORTICES

$$\text{AXIAL: } u_a(r, \theta) = -\frac{1}{4\pi} \int_{r_H}^{r_0} \int_{\theta_L(\rho)}^{\theta_T(\rho)} \gamma_r(\rho, \varphi) \sum_{k=1}^K \frac{r \sin(\varphi + \delta_k - \theta) \sqrt{\rho^2 + \lambda_i^2(\rho)}}{D_k^3} d\varphi d\rho$$

$$\text{TANGENTIAL: } u_t(r, \theta) = -\frac{1}{4\pi} \int_{r_H}^{r_0} \int_{\theta_L(\rho)}^{\theta_T(\rho)} \gamma_r(\rho, \varphi) \sum_{k=1}^K \frac{(x - \xi) \cos(\varphi + \delta_k - \theta) \sqrt{\rho^2 + \lambda_i^2(\rho)}}{D_k^3} d\varphi d\rho$$

TRAILERS

$$\text{AXIAL: } u_a(r, \theta) = \frac{1}{4\pi} \int_{r_H}^{r_0} \int_{\theta_L(\rho)}^{\theta_T(\rho)} \gamma_s(\rho, \varphi) \sum_{k=1}^K \left\{ \frac{\rho^2 - \rho r \cos(\varphi + \delta_k - \theta)}{D_k^3} \right\} \sqrt{\rho^2 + \lambda_i^2(\rho)} d\varphi d\rho$$

$$\text{TANG. } u_t(r, \theta) = \frac{1}{4\pi} \int_{r_H}^{r_0} \int_{\theta_L(\rho)}^{\theta_T(\rho)} \gamma_s(\rho, \varphi) \sum_{k=1}^K \left\{ \frac{\lambda_i(\rho) \rho \sin(\varphi + \delta_k - \theta) + (x - \xi) \cos(\varphi + \delta_k - \theta)}{D_k^3} \right\} \cdot \sqrt{\rho^2 + \lambda_i^2(\rho)} d\varphi d\rho$$

SOURCES

$$\text{AXIAL: } u_a(r, \theta) = \frac{1}{4\pi} \int_{r_H}^{r_0} \int_{\theta_L}^{\theta_T} \sigma(\rho, \varphi) \sum_{k=1}^K \frac{(x - \xi) \sqrt{\rho^2 + \lambda_i^2(\rho)}}{D_k^3} d\varphi d\rho$$

$$\text{TANG: } u_t(r, \theta) = -\frac{1}{4\pi} \int_{r_H}^{r_0} \int_{\theta_L}^{\theta_T} \sigma(\rho, \varphi) \sum_{k=1}^K \frac{\rho \sin(\varphi + \delta_k - \theta) \sqrt{\rho^2 + \lambda_i^2(\rho)}}{D_k^3} d\varphi d\rho$$

WHERE:

$$D_k(x, r, \theta, \xi, \rho, \varphi) = \sqrt{(x - \xi)^2 + r^2 + \rho^2 - 2 r \rho \cos(\varphi + \delta_k - \theta)}$$

$$\delta_k = \frac{2\pi(k-1)}{K} \quad \lambda_i = r \tan \beta_i(r)$$

$$x = \lambda_i(r) \theta \quad \xi = \lambda_i(\rho) \varphi$$

$$\gamma_s(\rho, \varphi) = \gamma_r(\rho, \theta_L) \sqrt{\rho^2 + \lambda_i^2(\rho)} \frac{d\theta_L}{d\rho} - \int_{\theta_L(\rho)}^{\varphi} \frac{\partial}{\partial \rho} \left\{ \gamma_r(\rho, \nu) \sqrt{\rho^2 + \lambda_i^2(\rho)} \right\} d\nu$$

are most easily treated by first considering a lifting line wing model. This model can then be rotated to represent a lifting line propeller.

The treatment of the lifting line wing wake divides into two major parts, the configuration of the trailing vortex sheets, and the details of the tip vortex region. There is, as will be shown, interaction between these two parts of the problem.

The approach to the sheet kinematics problem is to separate the sheet of vorticity into discrete trailing vortices. These trailers are first assumed to pass directly down stream (the linear theory assumption) from the lifting line. The velocities induced at the lifting line by the trailing vortices are then calculated as shown in Fig. 4 with $N = 0$. These induced velocities are then used to obtain a new position for a cross section of the trailing vortex sheet at a distance ΔX downstream from the lifting line. The trailers are then assumed to have these same Y, Z positions from $X = 0$ to $X = \infty$ downstream and a new induced velocity field is calculated at the down stream section $X = \Delta X$. These velocities are then used to extend the sheet another interval downstream. This process is continued until the sheet is far enough downstream to have no measurable effect on downwash at the wing.

This procedure will inevitably give a rollup of the vortex sheet, but the details of the motion, particularly in the tip region, will depend on the discrete vortex spacing used. This fact is inescapable in the discrete vortex model as can be shown assuming an elliptical bound circulation distribution. The last vortex represents a distribution of vorticity over the last interval of the trailing sheet of vorticity. Since this vorticity is larger in the outer half of the interval than the inner half, and in fact becomes infinite at the tip, the last vortex always concentrates the vorticity from the last interval inside of its proper position.

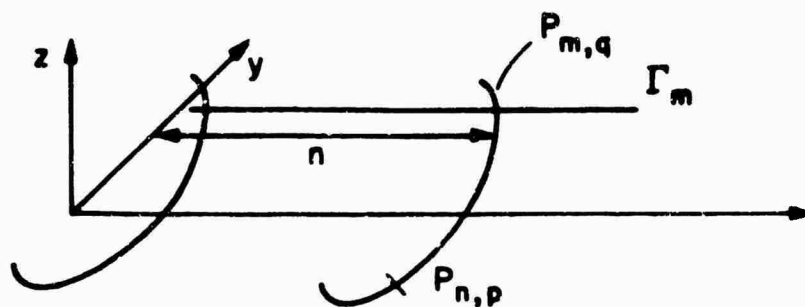


Fig.4 Line vortex induced velocities.

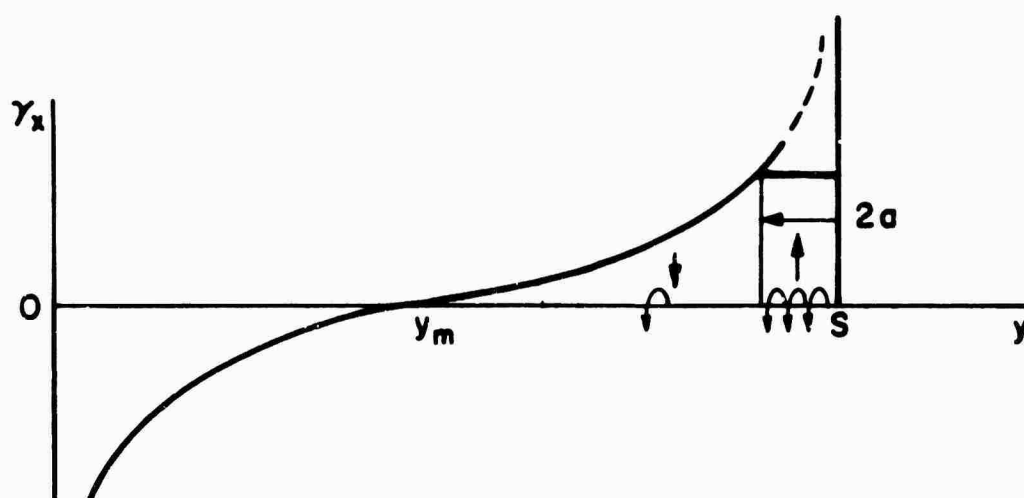


Fig.5 Tip vortex vorticity distribution.

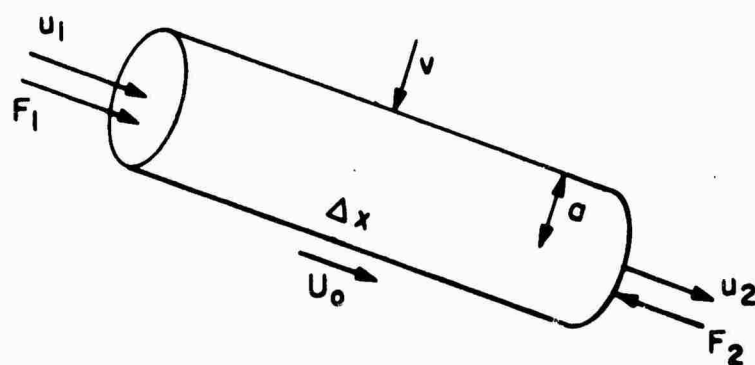


Fig.8 Tip vortex core model.

The tip vortex will always experience an upwash from the rest of the sheet and the downwash will be slightly exaggerated over the rest of the span. This artificial roll-up triggering mechanism can be compensated for as shown in Ref.2 , but rollup still takes place due to the basic instability of the configuration.

The question arises, however, if indeed the trailing vorticity can become infinite in a real fluid and, if not, over what region should it be spread. If a finite region can be defined over which the high vorticity at the tip is diffused and essentially constant, the finite vortex model becomes appropriate and the spacing problem is solved as shown in Fig. 5.

The fluid which contains the vorticity shed from the tip region comes off the tip of the wing and an appropriate dimension for the size of the fluid region in which the shear is high can be assumed to be the boundary layer thickness on the pressure side of the wing as suggested by Mc Cormick³. The vorticity is then assumed constant in this tip vortex region and the calculation proceeds as before. The results using this model show very little dependence on vortex spacing. (Fig. 6 and 7)

One of the reasons for working on a tip vortex core model for marine applications is to predict the minimum pressures and the velocity field in the core region. Cavitation commonly occurs first in the tip vortex core. This analysis requires some study of the dynamics of the core region itself. The strip model developed thus far with a rankine vortex of diameter equal to the boundary layer thickness and all trailing vorticity within a boundary layer thickness of the tip included in the core circulation gives the minimum pressure shown in equation 3 if the effect of the rest of the vortex sheet on the pressure is neglected. The increase of core radius due to diffusion is so slow that

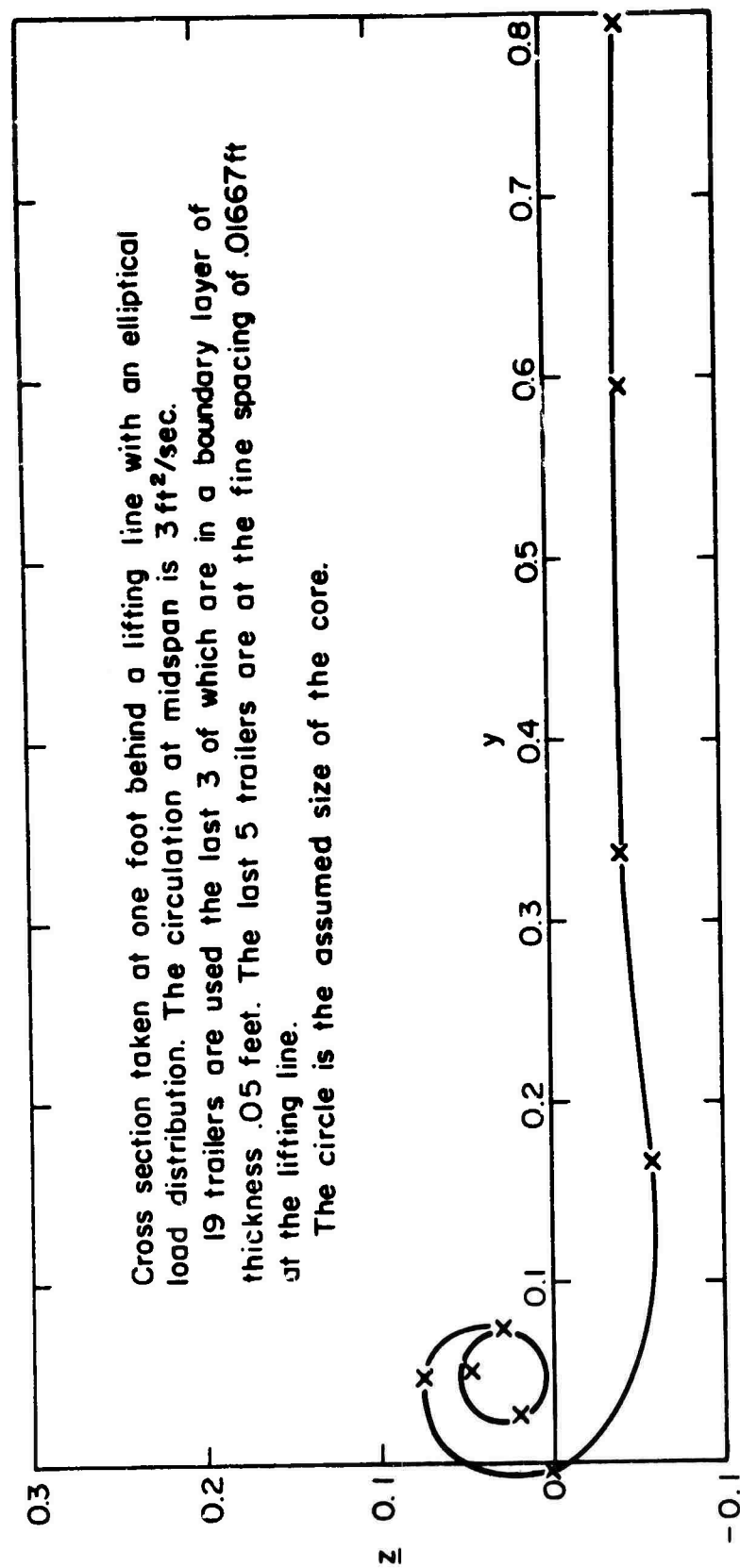


Fig.6 Rolled up wake with 19 trailers.

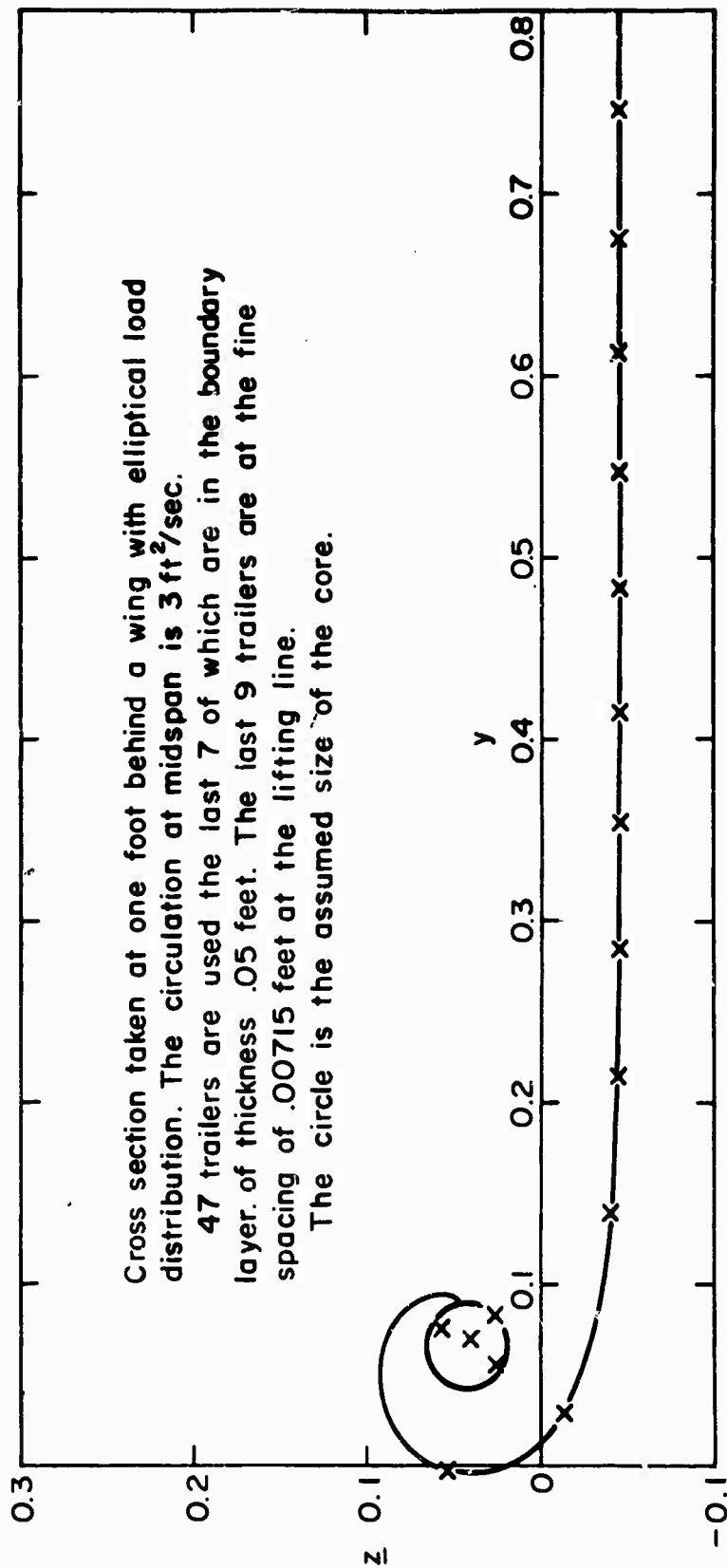


Fig. 7 Rolled up wake with 47 trailers.

it is negligible in the region of interest.²

However, two factors act to decrease the core pressure downstream. The rollup of the vortex sheet increases the circulation surrounding the core and any flow into the core region brings in vorticity from the rest of the sheet. The first effect, that of the sheet rollup, is small (Ref.2), but that of absorption of sheet vorticity into the core region may be large. Of course, this concentration of vorticity and fluid in the core region implies a sink at the vortex core in the strip theory model to satisfy continuity. In a three dimensional model, an increase of streamwise velocity in the core region disposes of the excess fluid. The vortex core model is shown in Fig. 8.

The forces due to differences in pressure on the upstream and downstream ends of a core element of length ΔX must be balanced by changes in momentum, and, therefore, velocity of the fluid assuming incompressible flow. Any inward flow V will bring vorticity into the core from the surrounding sheet and thereby decrease the pressure on the downstream face. The axial velocity then increases which again increases the sink strength. The process is repeated at each downstream position until convergence is obtained. The vorticity pulled into the core is added to the core circulation and subtracted from the outside sheet and the calculation continues to the next point downstream.

Calculations were made using this procedure with a water speed of 25 feet per second, boundary layer thickness of .01 feet and an elliptical loading with maximum circulation of 3 feet²/sec. on a 2 foot span. The results are shown in Fig. 9. Both calculations and water tunnel tests were done on a rudder model of these approximate dimensions². The results indicated that the tip vortex, after an initial

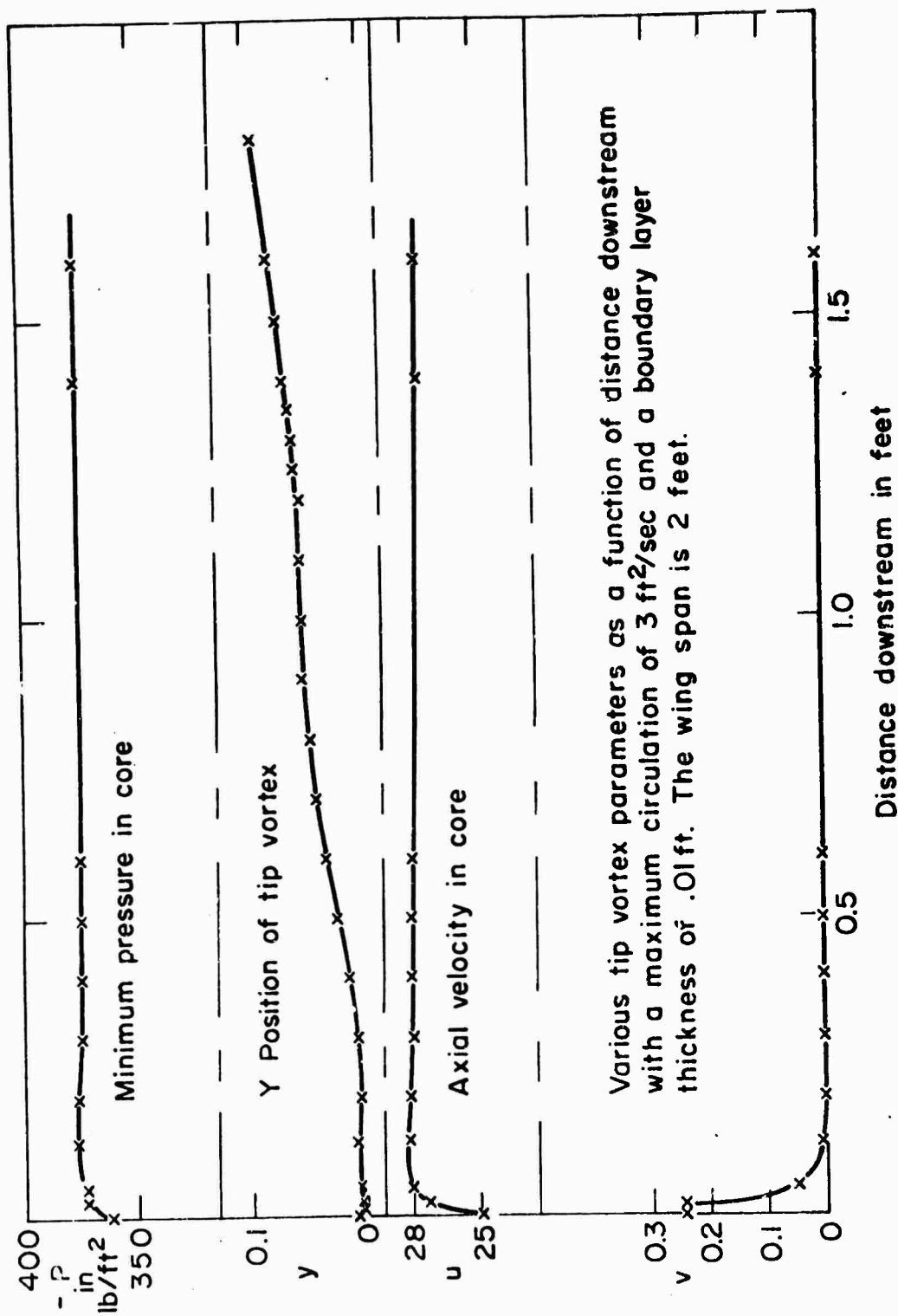


Fig. 9 Tip vortex parameters

roll above the plane of the foil, continues in the free stream direction. This is confirmed by pictures taken in the water tunnel and is logical since, if most of the trailing vorticity is concentrated in the tip vortex core, there is little left to induce velocities on it. The tip vortex also moves inward the calculated amount from the tip.

Cavitation begins when predicted and at the critical point can be seen to start slightly downstream of the foil.

When applied to a lifting line propeller, the procedures are essentially the same as for a wing. An equivalent strip model is used with discrete constant pitch helical vortices instead of straight line vortices. The equations for the induced velocity are given in Table 1. Calculated results for a sample lifting line propeller are shown in Fig. 10. The tip vortex again moves in the free stream direction rather than the free stream altered by induced velocities after an initial roll up out of the plane of the propeller pitch. This would indicate that the wake might better be assumed to lie on the undistorted $(\tan \beta)$ helicoidal surfaces rather than at $\tan \beta_i$ when doing lifting surface design calculations.

A comparison of measured and calculated tip vortex contraction using this method is shown in Fig. 11. The rollup of the tip vortex makes the outside boundary of the shipstream appear ⁴inside that calculated by actuator disk or linear theory.

The calculated position of a trailing vortex sheet from a 10 foot radius 4 bladed propeller.

The hub radius is 2 feet

The loading is elliptical ($G=Q.l \sin$)

The rotational velocity is 10 rad./sec.

The boundary layer thickness is assumed to be .05 ft.

The circles represent vortex positions. 19 are used with 5 in the fine spacing at the end and three in the core. Only the center of the core is plotted.

The forward velocity is 25 ft/sec

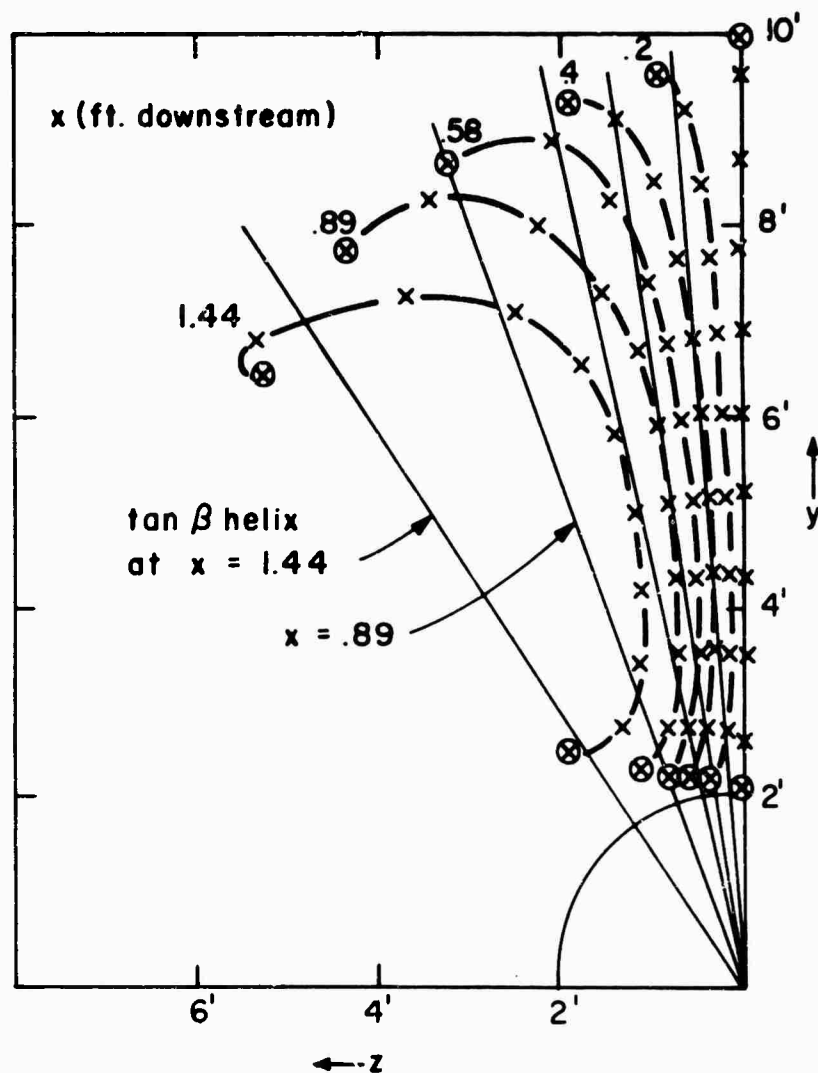


Fig. 10 Propeller vortex rollup

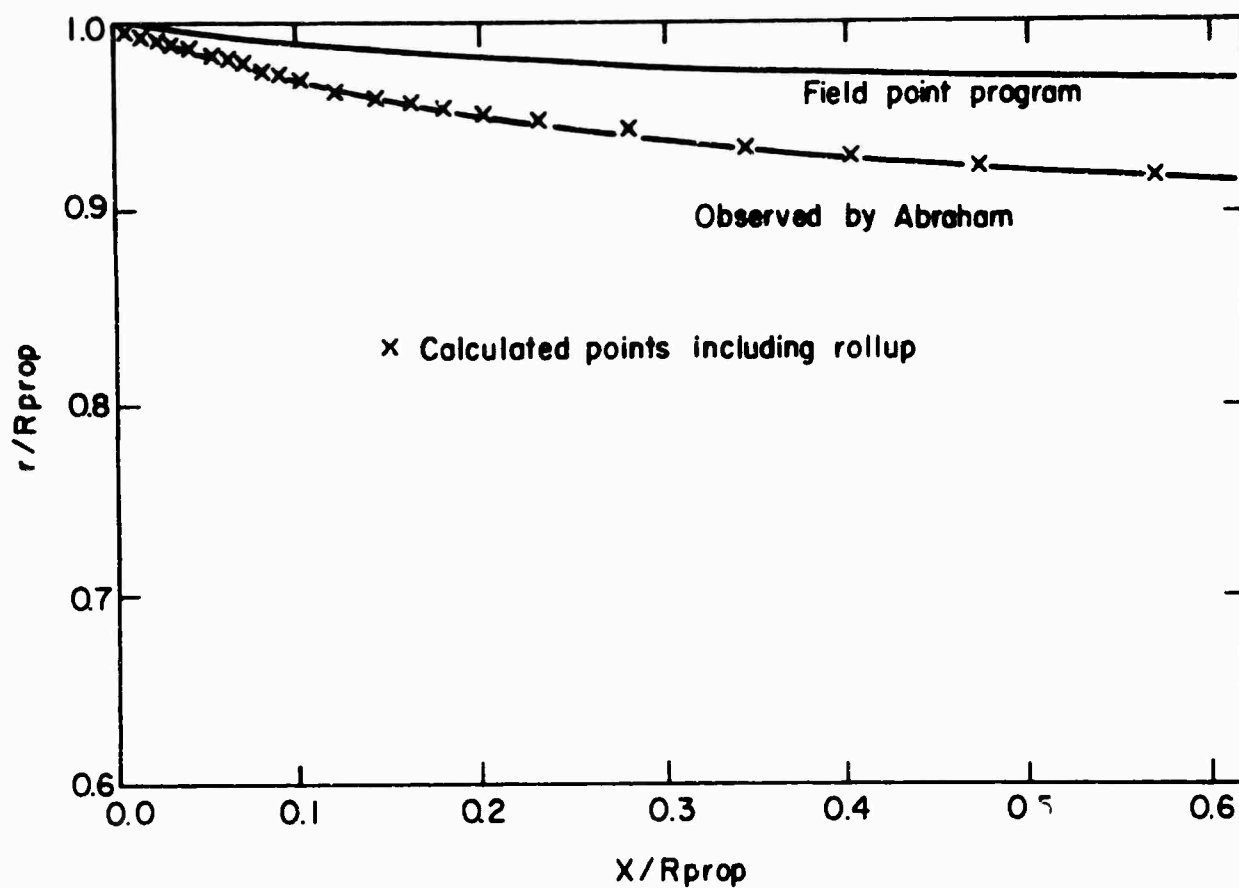


Fig. II A comparison of results for the contraction of a tip vortex shed from a model propeller

Numerical Methods

Singularities on Blades

As a first step in obtaining the blade section shape and pitch angle at each radius, one must be able to compute the downwash at any given point on the blade. This can be accomplished by evaluating the singular integrals given in Table 1 by a suitable numerical procedure.

A cylindrical grid arrangement, as shown in Fig. 12 is employed, with uniform angular intervals $\delta\theta$ and M uniform radial intervals δr . The angular interval $\delta\theta$ is selected in such a way that the blade outline just fits within the grid as shown in Fig. 12, and may be found from the expression

$$\delta\theta = \frac{2|\theta_{L,T}|_{\max}}{N} \quad (3)$$

where

$$\theta_{L,T} = \frac{s_{L,T}(r)}{r\sqrt{1+\tan^2\beta(r)}} \quad (4)$$

is the angular coordinate of either the leading or trailing edge. The grid is chosen to be symmetrical about $\theta = 0$ in order to minimize subsequent computations of trigonometric functions even though this wastes some computer storage for propellers with asymmetrical blade outlines.

The downwash induced by the sources and bound vortices and by the trailing vortices can be considered separately, and we will consider now the computation of the former.

The cylindrical grid elements divide the blade surface into a sequence of strips. We will assume that the pitch of the blade reference surface is constant within each strip, with a value matching the true value at mid-radius of the strip. With this simplification, each strip is a portion

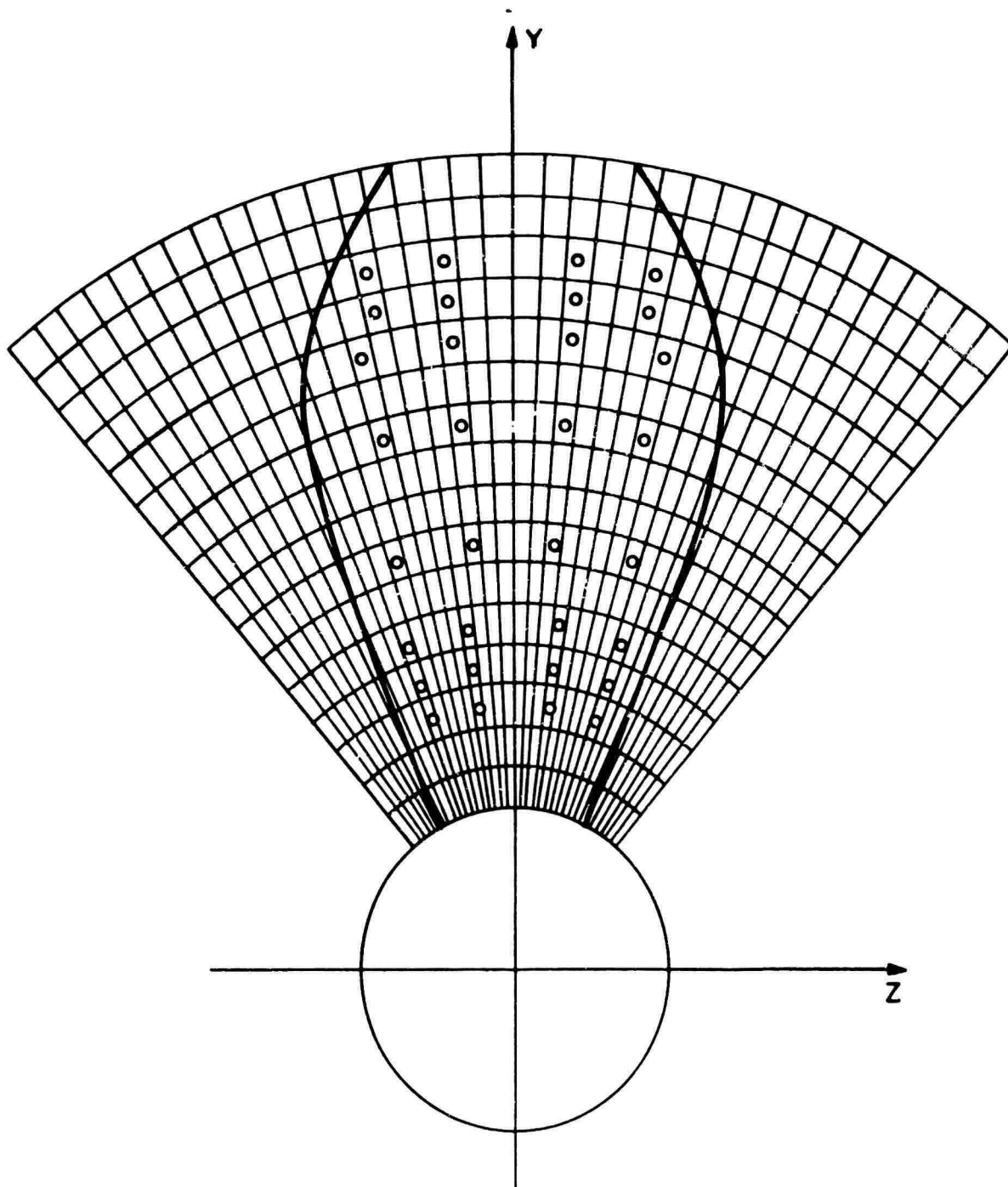


Fig. 12 Grid arrangement for propeller R-2.
 16 spanwise intervals - 36 chordwise intervals
 angular spacing - 2.23 degrees.
 Circles indicate locations of the 32
 points on the blade where the
 downwash is computed.

of a true helical surface, so that the intersections of the radial grid surfaces with the blade surfaces are all straight lines normal to the propeller axis. If this simplification were not made, these intersections would become progressively more curved for increasing values of $|\theta|$.

We assume, furthermore, that the source strength $\sigma(r, \theta)$ and bound vortex strength $\gamma(r, \theta)$ is independent of r within each strip, with a value matching the true value at the mid-radius of the strip.

With these approximations, the expressions for the downwash can be integrated analytically in the radial direction within each strip.

Evaluation of the chordwise integrals is carried out by concentrating the bound vortex and source strength contained within $\pm \frac{1}{2} \delta \theta$ of each radial grid line on the grid line itself and summing the integrands. This treats the Cauchy singularity properly provided, of course, that velocities are computed only at mid-points of the grid. A total of about 32 chordwise elements seems to be sufficient, there being an insignificant difference in the answer obtained with 32 and 64 elements.

We now come to the computation of downwash due to the trailing vortices. Since the bound circulation is approximated by a stepped radial distribution, it would seem reasonable by the same logic to replace the continuous trailing vortex distribution on the blades with

a set of $M+1$ concentrated helical vortex lines forming at the discontinuities of the bound circulation distribution. If we denote $\gamma_r^{m-1}(\theta)$ and $\gamma_r^m(\theta)$ as the chordwise distribution of bound circulation in the strips immediately below and above the m^{th} helical vortex line, the strength of the trailing vortex must be

$$\gamma_s^m(\theta) = \int_{\theta_L}^{\theta} [\gamma_r^{m-1}(\varphi) - \gamma_r^m(\varphi)] d\varphi \quad \text{for } m=2,3 \dots M+1 \quad (5)$$

$$\gamma_s^1(\theta) = - \int_{\theta_L}^{\theta} \gamma_r(\varphi) d\varphi \quad \text{for } m=1 \quad (6)$$

These integrations may be carried out analytically for flat-plate, elliptical or NACA a-Series chord loads, and are "built-in" to the computer program as options. With the trailing vortex strengths known, the velocity is obtained by summation of the integrand, with the last (trailing-edge) contribution multiplied by 0.5 in commemoration of the trapezoidal rule. As with the bound vortices and sources, results obtained with 32 and 64 chordwise elements are nearly identical.

Singularities in the Wake

The trailing vortices are assumed to begin at the closest grid point to the trailing edge of the propeller blade. Their trajectories downstream can be calculated in several alternative ways. They can be assumed to travel helicoidal paths of pitch angle $\beta_p(r)$ in which case the result for angle of attack and camber should agree with normal moderately loaded propeller theory. They can also

be assumed to travel at pitch $\beta(r)$, or they can be rolled up.

Given that the trajectories are defined, the velocity induced by the trailers on control points on the blades are calculated from the law of Biot-Savart using 65 straight line segments to approximate each trailing vortex. The lengths of the segments correspond initially to one half degree of angle and increase gradually to increments of sixty degrees.

In the case of the rolled up wake, the trajectories are assumed to be as indicated by Fig. 10 modified by the particular propeller's loading, pitch, and ship wake characteristics at 16% of the propeller radius downstream. The trajectories are interpolated between the trailing edge and this plane. From this point on, the vortices are assumed to move on constant radius helices at $\beta(r)$.

Numerical Computation of Camber and Pitch

The direct way to obtain the camber line shape and angle of attack is to integrate the total downwash divided by the local approach velocity from the leading edge to the point in question. The problem is that one needs the downwash at a large number of points, particularly near the leading and trailing edge. This leads to possible computational inaccuracies particularly for chord loads with square-root or logarithmic singularities in downwash. The scheme employed here is to compute the downwash at four points over the chord, at approximately the 1/4, 3/8, 5/8, and 3/4 chord positions, and to

fit a suitable continuous chordwise function by least-squares through these points. The function chosen is the corresponding two-dimensional mean line shape, which has two parameters; camber ratio and angle of attack. (Since a flat-plate chord load only has one parameter, a parabolic mean line is assumed for both elliptical and flat-plate loadings.) Values of angle of attack and camber are obtained in this way at eight spanwise locations, and the results fitted in the spanwise direction by four term polynomials in a least-squares approximation. The final pitch at each radius is then obtained by adding the section angle of attack to the inflow angle $\phi(r)$.

The Effect of Downwash on Pitch and Camber

Computations were performed on a typical five bladed heavily loaded low pitch marine propeller as shown in Fig. 12. The pitch and camber characteristics were found using four different wake geometries. The results for hydrodynamic pitch angle and camber at three radii are shown in Table 2 below. The four geometries are:

1. Trailing vortices at β ;
2. Trailing vortices at β
3. 2 Trailing vortices at $.25R$ and $.95R - \tan\beta$
4. Rolled up wake

TABLE 2

	$r=.3$	$r=.6$	$r=.9$
β	19.7°	13.0	12.0
1	73.5"	98.1"	101.7"
<u>1: Wake</u>			
ϕ	34.9°	21.5	17.0
Co	2.73"	2.00	1.90
<u>2: Wake</u>			
ϕ	36.3°	23.8	17.9
Co	2.75"	2.42	2.03
<u>2 Vortex</u>			
ϕ	38.5°	24.1	18.1
Co	3.54"	2.43	1.98
<u>Rolled Up</u>			
ϕ	36.0°	23.8	17.8
Co	2.79"	2.47	2.07

DEFINITIONS

- r non dimensional radius
 β incoming flow pitch angle in degrees
1 chord length in inches
 ϕ total hydrodynamic pitch angle
 C_o camber at mid chord in inches

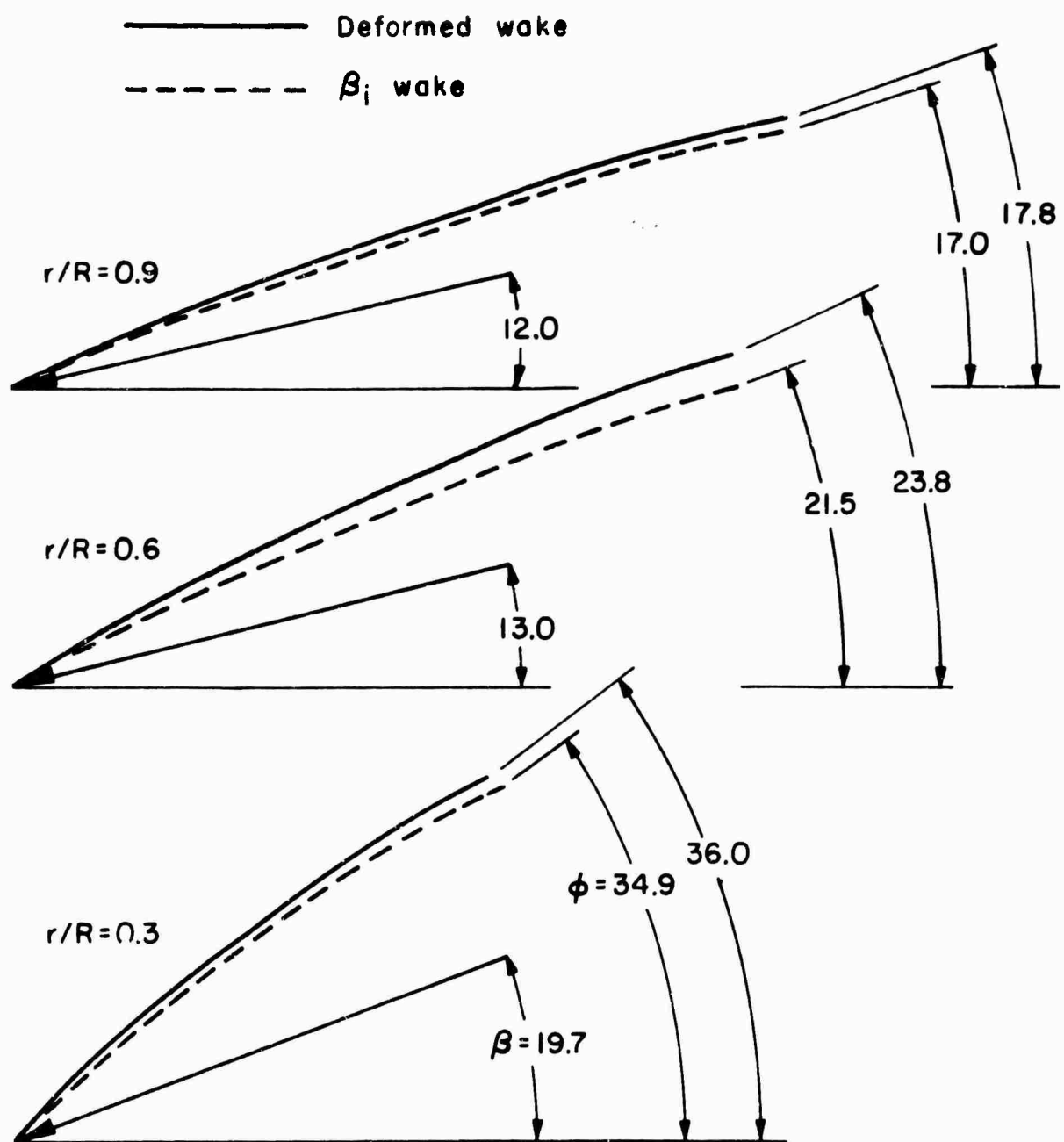


Fig. 13 Comparison of computed pitch and camber for propeller R-2 with deformed and β_i wake.

The results in pitch and camber are lowest for the β_i wake model, the one most frequently used. Those for the rolled up wake are very similar to the β or strictly linearized wake, reflecting the fact that the tip vortex tends to run in the free stream direction. The effect is exaggerated as might be expected by a single hub and tip vortex model. The resulting pitch and camber lines for the normally used β_i helices and the rolled up wake are shown in Fig. 13.

References

1. Kerwin, J. E., and Leopold, R., A Design Theory for Subcavitating Propellers, Transactions of the Society of Naval Architects and Marine Engineers, Vol. 72, 1964
2. Cummings, D. E., Vortex Interactions in a Propeller Wake, Massachusetts Institute of Technology, Department of Naval Architecture and Marine Engineering, Report Number 68-12, June 1968
3. McCormick, B. W., On Cavitation Produced by a Vortex Trailing from a Lifting Surface, Journal of Basic Engineering, Sept. 1962, pp. 369
4. Abraham, M., Theoretical and Experimental Correction of Streamlines in the Race of a Marine Propeller, SM Thesis, Department of Naval Architecture and Marine Engineering, Massachusetts Institute of Technology, 1965

EXPERIMENTS ON ROTOR WAKE CONTRACTION *

M. Nook and J.P. Jones
UNIVERSITY OF SOUTHAMPTON
Southampton, England

**Although not available at the time of publication of this volume, this paper
will be found in Volume III of these Proceedings.*

SESSION II

**Rotor/Propeller Aerodynamics II
(Other Effects)**

Chairman: Paul Yaggy
U.S. Army Aeronautical Research Laboratory
Moffett Field, California

WEDNESDAY AFTERNOON
18 JUNE 1969

VORTEX FIELD, TIP VORTEX,
AND SHOCK FORMATION ON A MODEL PROPELLER

By

W. H. TANNER,
Supervisor, R&D Aerodynamics

R. M. WOHLFELD,
Research Engineer

Bell Helicopter Company
Fort Worth, Texas

ABSTRACT

A Schlieren system for photographing the flow field of a rotating static thrust propeller or hovering rotor has been developed. The presently operating pilot system uses rotors or propellers up to 14-inches in diameter and has a maximum tip speed of Mach .85. This paper serves to acquaint the rotorcraft designer with details of the system and its potential uses. Among the results presented are details on the contraction of the stream tube of a model propeller. Displacement of the vortex core path has been measured at small time intervals and these have been converted to velocity components. Results for several number of blades are presented. Another topic discussed is the formation of the tip vortex. Photographs of the airflow around the blade tip are presented along with a discussion of the basic mechanisms of tip loss. The last topic briefly discussed is the formation of shock waves on a propeller.

INTRODUCTION

Many experimental techniques have been developed for visualization of the flow field of a rotor and/or propeller. Dust, smoke, condensation of water vapor and water tunnels are familiar techniques to the aerodynamicists (References 1-4). The disadvantage of the first two techniques is that foreign elements are being put into the flow field introducing unknown

Paper presented at the CAL/AVLABS 1969 Symposium on Aerodynamics of Rotary Wing and VTOL aircraft.

entities. Water introduces an entirely different test medium than air. The most acceptable technique of the four is condensation of the water vapor. With this technique, a density change of the flow field is avoided. However, this method as it has been used, necessitates the proper combination of atmospheric conditions which are obtained by chance and cannot be predicted or controlled. Because of the shortcomings of these techniques, it was decided that a new approach to the propeller/rotor flow visualization was needed.

One of the most common flow visualization techniques of the high speed aerodynamicist is the Schlieren. The Schlieren technique involves an optical system which gives a picture or an image representative of the variation of density throughout a flow field. In general, a Schlieren has been a tool for the supersonic wind tunnel engineer. In theory, the actual density gradients of a flow field can be measured; in practice, they are commonly used for qualitative analysis. Historically, the questions answered by the Schlieren technique have been:

- 1) Where are shocks located?
- 2) Is the shock weak or strong?
- 3) Where is the boundary layer transition?
- 4) Does separation occur and where?

Recently, the Bell Helicopter Company has extended Schlieren techniques to photograph the flow field of rotating propellers and hovering rotors. This new application of a classical technique provides a tool to study experimentally many rotorcraft/propeller areas in detail. Some of the possible fields of study are:

1. Accurate measurement of the tip vortex path.
2. Formation of the tip vortex.

3. Effects of tip shape on the forming vortex and wake.
4. Roll-up of the vortex sheet into a concentrated vortex.
5. Boundary layer transition and flow separation.
6. Shock formation.
7. Interaction between a shock and a forming vortex.
8. Shock induced separation.
9. Effect of shock on the vortex sheet and its roll-up.
10. Vortex field effects on wings and other bodies.

The Bell Helicopter Company has accomplished work in some of the above areas. Presently operating is a pilot system which used up to 14-inch diameter propellers or rotors. The small scale system has been used to develop the required techniques while acquiring useful information. First results are now available and are given in the following sections of this paper.

THE SCHLIEREN FOR ROTATING AIRFOILS (SCRAF)

Figure 1 is a sketch of the Schlieren system developed (see Reference 5 for a complete explanation of the Schlieren principle). The system of lenses and knife edges is conventional; the development by the Bell Helicopter Company has been in designing the electronic system to control the light source required by a rotating system. The control is shown schematically in Figure 2. The contactor (1) on the shaft produces a one-per-revolution signal. The signal from the contactor is fed into a sampler to obtain the RMS period at (2); this signal is then used to drive a sine wave generator (3). The purpose for this part of the loop is to eliminate shaft vibration effects which cause erratic firing of the light source. The sine wave is fed into a phase control circuit (4) which is used to control the firing of the light source (5). By setting the

connector at a specified location, the light source can be fired at any azimuth position by an adjustment of the phase delay control. Figure 3 shows the sign convention used for the velocities which will be discussed later. The blade azimuth is defined as zero when the blade span axis is perpendicular to the parallel light beam, and the angle is positive when the rotation is in a counterclockwise direction when viewed from above the disc.

Schlieren observations are made in three ways. First, visual observation on a ground glass screen; second, still photographs; and third, with a motion picture camera.

The present operating system is capable of rotational tip Mach numbers of 0.85 with a 14-inch diameter propeller/rotor. At tip Mach numbers above 0.25 the vortex core is visible and can be tracked for several revolutions below the propeller. Best details are seen, however, when a small amount of heat is introduced into the field to create an artificial density change. The density-change has been generated by placing a heating element, as illustrated in Figure 4, in the low pressure side of the flow field. The warm air is drawn locally into the stream tube and is not blown or forced into the flow field.

TECHNICAL DISCUSSION

Interpretation of the Photographs

Figure 5 shows two photographs of a two-bladed model propeller at 0.5 tip Mach number with propeller indexed at $\Psi = 30$ degrees. The density charge about the core is sufficient for clear visibility of the vortex core path in Figure 5a. The blade is visible on the right-hand side of the photograph. Two sections of the vortex core path are seen; the upper (1) is from the blade tip in view, and the lower (2) is from the previous

blade. A significant azimuthal distance of the path is seen; however, only the extreme left-hand side of the core path is in focus (tip of arrow). The reason for the general lack of clarity of the core path in the photograph is that for the present apparatus the depth of focus is approximately one-half inch.

Much greater details of the flow characteristics are shown in Figure 5b for the same condition as 5a; however, heat has been added locally as explained in a previous section. The core path is still visible, and with the introduction of heat in the plane of focus, the entire vortex is visible from the two blades. Also, as indicated in the figure, the vortex sheet or turbulent boundary layer from the inboard portion of the blade is shown as well as the vortex mutual interaction. Details of individual characteristics will be discussed in future sections.

The grid system used in making detailed measurement was left on these photographs to: first, show the type of grid used; and second, as an aid to show the effects of the addition of small amounts of heat on the flow field. Inspection of the comparative photographs shows that the tip on free vortex core from the blade in view is in the identical location on both photographs in both the y (horizontal) and z (vertical) directions indicating that heat does not affect its location. The exact amount of increase in air temperature above ambient is difficult to measure, but for the case shown in Figure 5, it is about 30°F. Delta temperatures as high as 150°F. have been used, and no effect on vortex core location could be measured with this system.

Examining the vortex (2) from the previous blade, it is seen that the y coordinate is essentially identical in both photographs, but the z coordinate is different. In Figure 5a, z (vertical displacement) is greater than in 5b. This difference is not due to the addition of heat and requires a somewhat detailed discussion which will be given in the next section.

To summarize:

- The density change in the region of the tip vortex core is sufficient for Schlieren photography for several revolutions of the wake for tip Mach numbers greater than 0.25.
- Introduction of small amounts of heat, with the present system, makes details of the entire vortex, vortex sheet roll-up and vortex intermixing visible.

Vortex Core-Displacements and Velocities

Figures 6, 7, and 8 are composite photographs with a seven-inch diameter square tip propeller of two, four, and six blades respectively. From the photographs, the displacement of the vortex core with time ($t = f(\Psi)$) is evident in the y-z plane (see Figure 3 for the sign conventions). When displacements are measured, the fixed grid is used (as in Figure 5) which is oriented to the center of rotation of the shaft, and all measurements are made in the focal plane of the lens system. With the displacement as a function of Ψ known, both velocity and acceleration in the y-z plane can be obtained by numerical integration. To obtain measurements in the x-z plane, an orthogonal axis to those of the presented photography must be used. To accomplish the latter, special equipment must be designed to keep the propeller and drive system hardware from blocking the focal plane and as yet this has not been done.

Figures 9, 10, and 11 are the vortex core displacements and velocities corresponding to the photographs of Figures 6 through 8. Figure 9 is a graph of the vortex path displacements and velocities in the y-z plane for a two-bladed rotor versus azimuth (Ψ). Figures 10 and 11 are for four and six blades,

respectively. It will be noted that both RPM and thrust vary on these graphs; therefore, comparisons between numbers of blades cannot be directly made. However, several observations are possible.

On Figure 9 the downward displacement z increases in a smooth manner until about $\Psi = 200$ degrees at which point there is a "bump" in the curve. The horizontal component y shows a similar characteristic with the y displacement tending to reach its maximum contraction value. The velocities calculated from the displacement curve are in the lower part of the figure. The y and z velocity components are shown along with the total velocity in the y - z plane, V , (where $V^2 = \frac{\delta y^2}{\delta t} + \frac{\delta z^2}{\delta t}$). The dashed line is the simple momentum induced velocity for a reference where the actual contraction values were used to obtain an increase in velocity with z . The points of inflection in velocity curves can also be seen and these appear at an azimuth of about 180 degrees or at blade passage frequency. The same phenomenon is even more clearly shown on the four- and six-bladed curves of Figures 10 and 11.

This phenomenon has been investigated and the motion of the vortex core was found to be more complex than inferred by Figures 9 through 11. Returning to Figure 5, it was stated that the core of the lower vortex (2) is not exactly in the same location on the grid in both photographs in the z direction. If numerous photographs are taken at the same propeller operating conditions, one finds that in the y direction the core path is quite steady, but in the z direction the motion resembles that of a vibrating spring of high frequency and low amplitude at the high RPM investigated. The motion can be visualized by using an analogy to a coil spring. Assume that a coil spring of constant diameter represents the vortex field from a propeller. Think of the tip vortex being shed as a pressure wave that inputs a motion in the downward (z) direction; there is no damping present and with ideal propagation; the spring will deflect some

constant amount. Now start the system rotating as in Figure 12. For this case, half a revolution later the pressure wave in the z direction will pass over a vortex which is 180 degrees old, and the 180 degree old vortex will now feel an impulse in the z direction. All coils of the spring below the first will begin to vibrate at b (number of blades) per revolution as illustrated in the figure. This type of motion of a propeller wake is evident when the wake from a rotating propeller is studied visually or with a motion picture camera but the motion cannot be captured in still photographs such as shown in this paper.

Because the wake motion is vibration, Figures 9 through 11 have been labeled mean displacement and velocity. The displacement and velocity can be measured to a high degree of accuracy with the Schlieren for $2\pi/b$ revolutions where b is the number of blades, then the vibrating amplitude must be accounted for, and for the data presented, the approximate mean displacement was used.

From the work accomplished to date, the wake beneath the static thrust model two-bladed propellers appears to be stable for four to five revolutions which is a sufficient distance for engineering solutions. From the theoretical work that has been done, (Reference 6) the indications are that computation for a wake more than five revolutions old are interesting but academic for rotor design and performance considerations. As yet the work has not progressed to the point where a firm statement can be made about the wake stability for propellers with more than two blades.

Although the wake for the pure static thrust two-bladed model propeller is stable for several revolutions, a few observations on the degree of the wake stability and comments on the conclusions which may be drawn under laboratory conditions are in order. Experience with the SCRAF has shown that the wake is on the very "ragged" edge of stability. To illustrate,

the experiments are being carried out with small propellers in a very large room under laboratory conditions. The propeller wake becomes unstable if a man walks at a normal pace six feet away, if a door to the room is opened, if the heating and ventilating system is turned on. From these observations a conclusion can be drawn. Since VTOL aircraft do not operate under laboratory conditions, the wake of a static thrust propeller/hovering rotor when examined in detail may be unstable in the free atmosphere. The complexity of an explicit mathematical model of a stable vibrating wake is great. Even with an order of magnitude increase in the power of computing machines, an explicit model of an unstable wake with atmospheric disturbances properly accounted for is probably impractical. Therefore, an engineering solution is required which combines a reasonable mathematical model in combination with the necessary empiricisms. Many mathematical models have been offered (References 7 through 9 are some of them) but the experimental empiricism for engineering solutions is lacking. Much work needs to be done.

Study of the Forming Tip Vortex

In addition to studying the vortex field, the Schlieren system developed is also useful for studying the vortex formation at the blade tip. Figure 13 shows some photographs from the initial studies of blade tip aerodynamics. Figures 13a, b, and c show airflow around the tip from lower to upper surface. Figures 13d and e are head-on views of the leading edge of the blade showing the forming tip vortex. Figure 12f shows a planform view of the upper surfaces. The flow at the tip can be seen clearly at the tip of the arrow. Also, the vortex core path is visible in this photograph.

Study of these photographs in comparison with Figure 6 lead to the formation of hypotheses about the mechanism of a tip vortex on a propeller and analogies to what is normally thought of in fixed wing terminology as induced drag or aspect ratio effect.

A Hypothesis of the Mechanism of Rotor/Propeller Hovering Tip Vortex Formation and Its Effects - Rotary Wing Induced Drag

It is believed that the clearest explanation of the mechanism of the formation of the tip vortex of a static thrust propeller/hovering rotor is best accomplished by showing the difference between a three-dimensional fixed wing of finite aspect ratio and a rotating wing. The following is a brief review of the basic concepts of finite fixed wing theory.

For lifting wings of finite span, a pressure difference between the upper and lower surfaces exists. The pressure difference must vanish at the wing tip and, because the pressure is lower on the wing upper surface, the air will flow from the bottom to the top around the wing tips. Therefore, spanwise currents exist on the wing surfaces causing a surface of discontinuity in the air leaving the wing which ultimately rolls up into two distinct vortices. Another explanation is the familiar one that the bound vortex cannot end at the wing tips but must continue to infinity as a free vortex. These free vortices give rise to a kinetic energy loss, which has been termed the induced drag of the wing. Mathematically, this can be expressed by the formula,

$$D_i = \frac{\rho}{4\pi} \int_{-b/2}^{b/2} \int_{-b/2}^{b/2} \Gamma(x') \frac{2\Gamma(x)}{2x} dx \frac{dx'}{x'-x} \quad (1)$$

where the notation of Reference 10 is used. Since, for all things being equal, the lift is proportional to the span and the induced drag is only dependent upon the kinetic energy of the free vortex, this gives rise to the familiar aspect ratio effect.

Study of Figures 6 and 12 show that the propeller has the same free vortex as the fixed wing and that the roll-up

process is similar. However, there is a significant difference in that the propeller must operate in its own wake and not in clean air as does a fixed wing. Figure 14 is a photograph of a vortex which is one-half a revolution old ($\Psi = 180$ degrees on Figure 6). Defining the stream tube as the vortex core path, air is still being drawn into the vortex from outside the stream tube when the second blade enters the flow field. Examining a particle of air (solid square), this particle will have a velocity in the direction shown. Study of Figures 13a, b, and c lead to the hypothesis that the particles of air which are flowing around the blade tip come from the flow field about the vortex from the previous blade. The dashed particles in the figure represent this air flow entering the forming vortex.

If this hypothesis is true, this means that in addition to the kinetic energy of the tip vortex, energy must be expended to decelerate the air particles from the previous vortex to zero and then accelerate them in the opposite direction for the particles to get into the forming vortex of the next blade. Also, energy is being subtracted from the formed vortex. Therefore, the propeller is doing work (a rotating wing induced drag) which is not being accounted for by any theoretical techniques known to the authors, and the power required may be large.

At this time the authors of this paper have not developed a suitable mathematical model for this proposed phenomenon. However, there are some unknowns in experimental data which this phenomenon could help to explain.

First, in Bell's experience with two-bladed rotors with large differences in aspect ratio, no adverse aspect ratio effect has been isolated, as would be anticipated with a fixed wing. A possible explanation for this is that the magnitude of the rotating wing induced drag is large compared to the fixed wing

type induced drag and the conventional induced drag is not an obvious measurement in normal experimental practices.

Secondly, reported in the literature such as Reference 3, is that hovering efficiency decreases with solidity or it is felt more likely with number of blades and operating lift coefficient. Figures 6 through 8 have shown that as expected, as the number of blades is increased the vortex from the first blade travels less before it is encountered by the second blade. Thus the particles of air encountered by the second blade are closer to the vortex core of the first blade and have a higher velocity for a four-bladed propeller than for the two, as an example. Therefore, more power will be dissipated in decelerating the air with increased number of blades if this rotating wing induced drag hypothesis is correct. Similarly, for increased operating lift coefficient the vortex velocities as a function of distance from the core will increase with lift and the associated losses will increase proportionally as they would do with number of blades.

Clearly, much study is needed to determine the validity of the hypothesis offered, and if it is valid, the magnitude of its importance must be ascertained. If the hypothesis is correct and the losses are of the first order of magnitude in importance, then some practical design rules would be established for hovering rotors/static thrust propellers.

- The number of blades should be minimized for a given configuration.
- The total vorticity should be spread out over as large an area as possible. Tip shape is important.
- Large pressure differential between the upper and lower surfaces should not be permitted.
- The tip chord should be minimized.

- An increase in the twist rate near the blade tip should be beneficial (i.e. reduce the local angle of attack).

The Vortex Sheet Roll-Up

The Schlieren is also a useful tool in studying the roll-up of the vortex sheet. Figure 15 shows the tip vortex path and the vortex sheet from an elliptical planform tip propeller. The view is from the bottom surface of the propeller. Another view for a square tip propeller is seen in Figure 13. Figures 13d and e show views from the leading edge of the blade and the turbulent boundary layer leaving the upper surface.

Part of the sheet can be seen rolling up into the tip vortex in Figures 6, 7, and 8. First looking at the two-bladed propeller, Figure 6, at $\Psi = 30$ degrees the area which looks similar to turbulence to the right of the uppermost vortex is the sheet. The roll-up process, as a function of Ψ , can be followed on the figure. Two details can be seen on Figure 6. First (see $\Psi = 50$ degrees) in the roll-up process the sheet seems to intermix with both vortex 1 and 2 where 1 is from the blade in view and vortex 2 is from the previous blade. The roll-up process is not "clean" as it is with fixed wing. Second, for the two-bladed propeller the roll-up is complete in one-half a revolution. The degree of intermixing increases rapidly with increased number of blades, Figures 7 and 8. Full roll-up distance has not yet been determined for more than two blades.

Much work is left to be done. However some conclusions can be reached with regard to the roll-up process of a propeller/rotor.

- For the two-bladed propeller/rotor the roll-up process is essentially complete within one-half a revolution.

- There is a high degree of intermixing of the sheet between adjacent vortices.
- The degree of overall vortex mixing, both the sheet and the concentrated, increased rapidly with number of blades.

The Study of Shock Formation

Study of the formation and effects of a shock on the flow characteristics of a propeller/rotor is in the embryonic stage. Thus far, only the feasibility has been demonstrated with the Schlieren and reduction to an engineering tool remains to be accomplished.

Figure 16 shows a shock at the tip of an untwisted propeller at flat pitch (thrust = zero). This configuration was selected to minimize tip vortex effects. The airfoil profile is approximately an NACA 0020. The view shown was taken from below the tip path plane at about a 30 degree angle, and the upper surface is visible. To insure printability the shock wave shown has been touched up. The tip Mach number was 0.82; the shock is approximately at the blade quarter chord with the boundary layer separation behind the shock which is indicative of shock stall.

Much effort will be required to develop the Schlieren techniques to the point where a detailed study of shock formation, intensity and their effect on the overall flow field can be made. The work so far has proven the feasibility of the method.

CONCLUDING REMARKS

The preceding discussion is believed to have shown that the Schlieren system for rotating airfoils is a powerful tool for use by both the aerodynamicist and the designer. The Schlieren system, coupled with modern electronic controls, makes possible the

detailed visualization of the flow characteristics at the propeller/rotor surface and the flow field. The theoretician can photograph the flow field he is trying to model, and the designer can see if his final articles fulfill his objectives.

The results presented are from a pilot system using small diameter blades, and the authors realize that effects such as Reynold number on the vorticity and others have been ignored. The purpose of this paper has been to acquaint the engineering community with the fact that a technique exists and to demonstrate its potential. In the course of accomplishing these objectives some speculations have been offered which, it is hoped, give some new insight into what is one of the most complex problems in all aerodynamics, the static thrust propeller/hovering rotor.

REFERENCES

1. Taylor, M. K., A Balsa-Dust Technique for Air-Flow Visualization and Its Application to Flow Through Model Helicopter Rotors in Static Thrust, NACA Technical Note 2220, November 1950.
2. Fradenburgh, E. A., Flow Field Measurements for a Hovering Rotor Near the Ground, paper presented before the Fifth Annual Western Forum of the American Helicopter Society, September 25-26, 1958.
3. Jenney, D. S., Olson, J. R. and Landgrebe, A. J., A Reassessment of Rotor Hovering Performance Prediction Methods, Journal of the American Helicopter Society, Vol. 13, No. 2, April 1968.
4. Lehman, A. F., Model Studies of Helicopter Rotor Flow Patterns, USAAVLABS Technical Report 68-17, U. S. Army Aviation Materiel Laboratories, Fort Eustis, Virginia, April 1968.
5. Reid, W. T. and Cornell Aerodynamic Laboratory, Schlieren Photography, Pamphlet P-11, Copyright 1968, Eastman Kodak.
6. Tanner, W. H. and Buettiker, P., The Boundary Layer of the Hovering Rotor, CAL/USAAVLABS Symposium Proceedings, Vol. III, June 22-24, 1966.
7. Piziali, R. A., A Method for Predicting the Aerodynamic Loads and Dynamic Response of Rotor Blades, USAAVLABS Technical Report 65-74, U. S. Army Aviation Materiel Laboratories, Fort Eustis, Virginia, January 1966.
8. Erickson, Jr., J. C. and Ordway, D. E., A Theory for Static Propeller Performance, Sponsored by U. S. Army Aviation Materiel Laboratories under Contracts DA 44-177-AMC-165(T) and DA 44-177-AMC-379(T).
9. Landgrebe, A. J., An Analytical Method for Predicting Rotor Wake Geometry, AIAA Paper No. 69-196, presented at AIAA/AHS VTOL Research, Design, and Operations Meeting, February 17-19, 1969.
10. Tietjens, O. G., Applied Hydro- and Aerodynamics, Dover Publications Inc., New York, 1934.

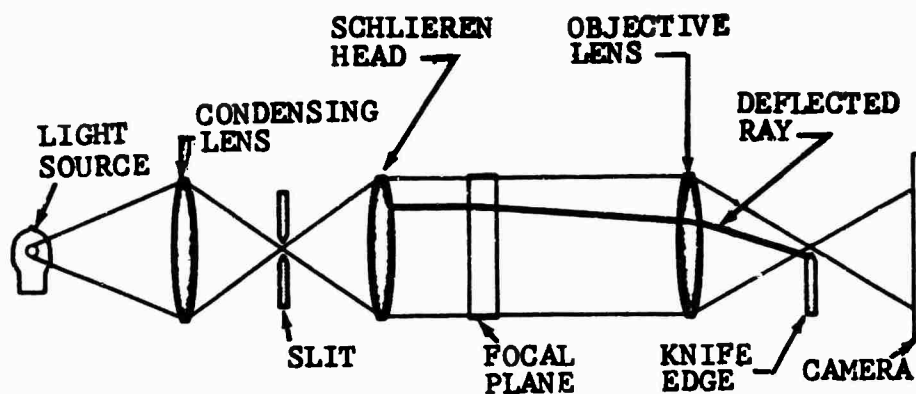


FIGURE 1. SKETCH OF SCHLIEREN SYSTEM.

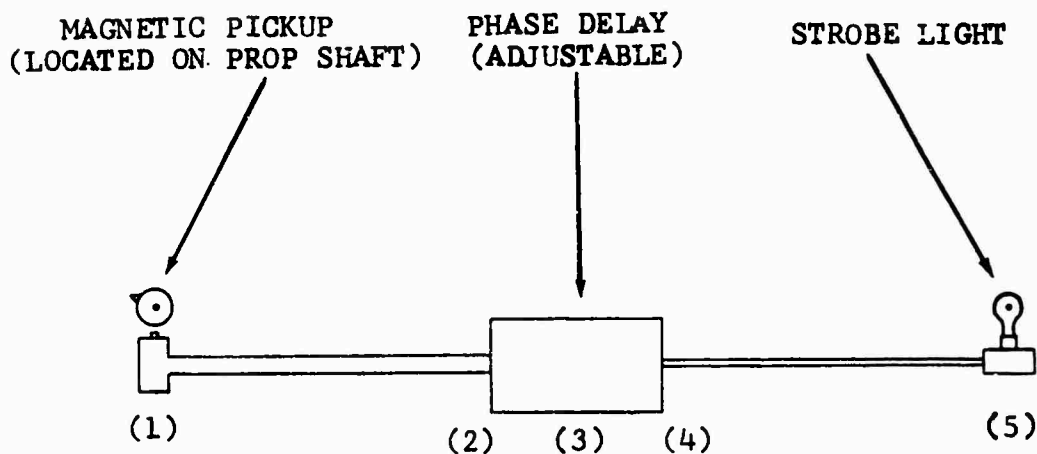


FIGURE 2. SKETCH OF LIGHT CONTROL SYSTEM.

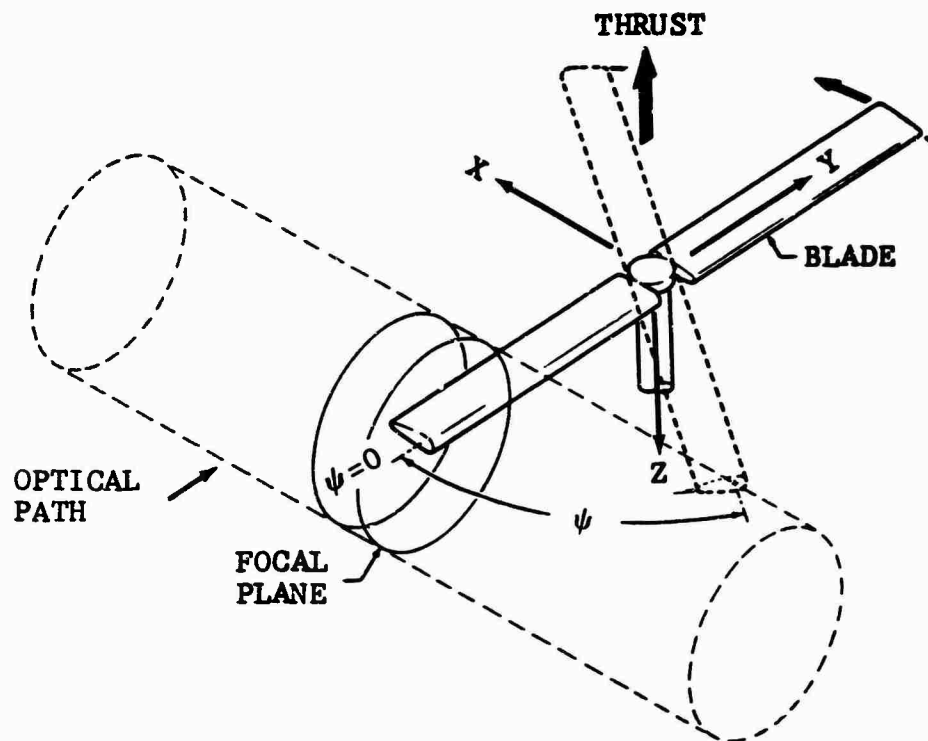


FIGURE 3. SKETCH OF SIGN CONVENTION, VALUES POSITIVE AS SHOWN.

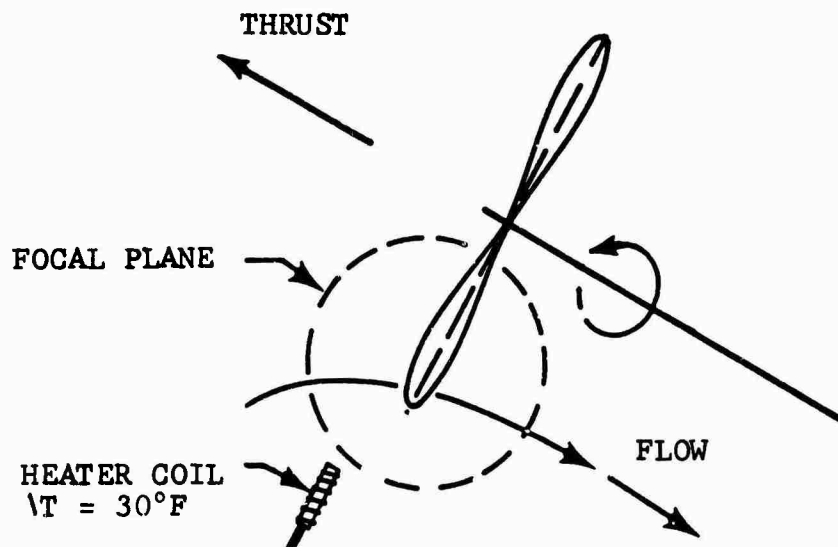


FIGURE 4. SKETCH OF PROPELLER WITH HEATING ELEMENT.

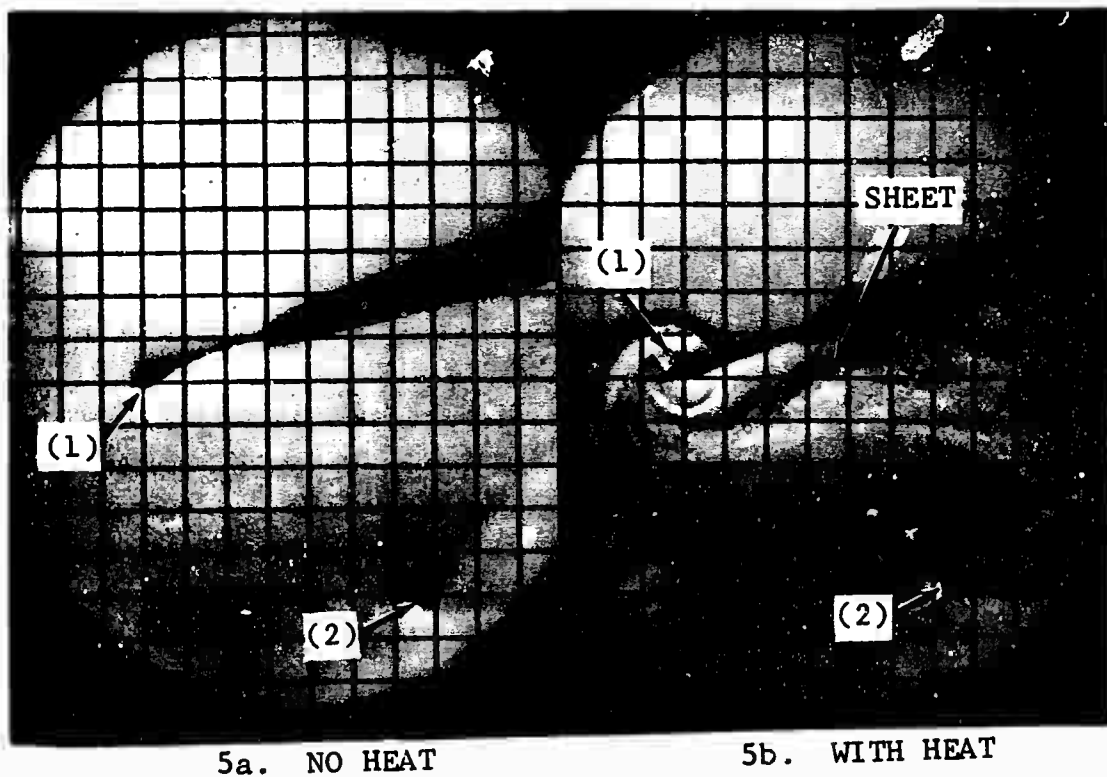


FIGURE 5. SCHLIEREN PHOTOGRAPHS OF
MODEL PROPELLER AT $M_T = 0.5$,
 $\Psi \approx 30$ DEGREES.



FIGURE 6.
SCHLIEREN
PHOTOGRAPHS OF
TWO-BLADED MODEL
PROPELLER AT
4000 RPM.



FIGURE 7. SCHLIEREN PHOTOGRAPHS
OF FOUR-BLADED MODEL
PROPELLER AT 6500 RPM.



FIGURE 8.
SCHLIEREN PHOTOGRAPHS OF
SIX-BLADED MODEL PROPRTOR
AT 5000 RPM

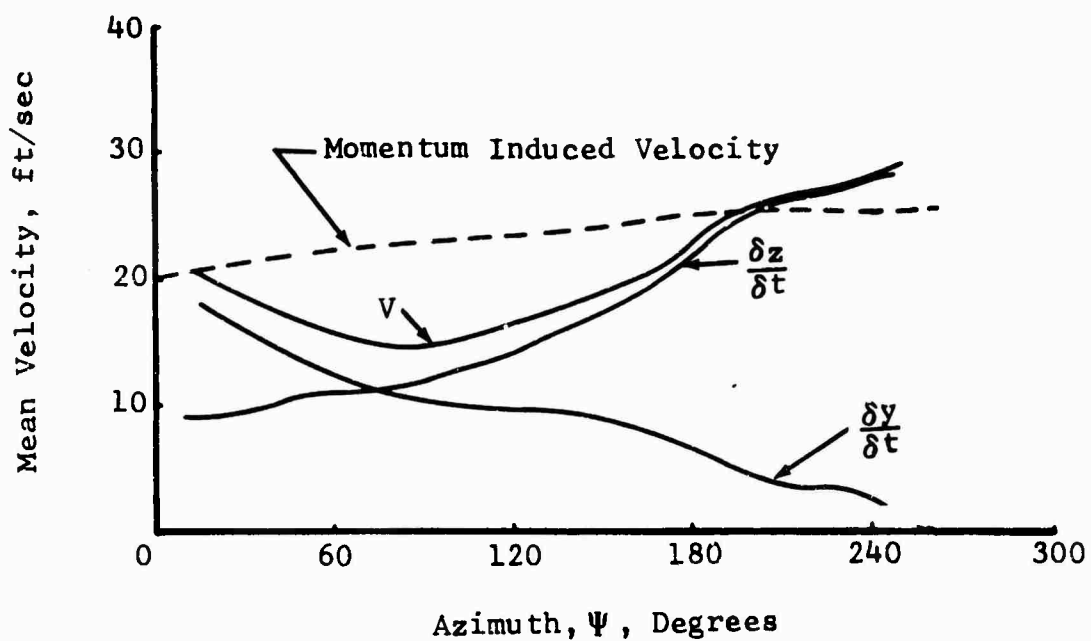
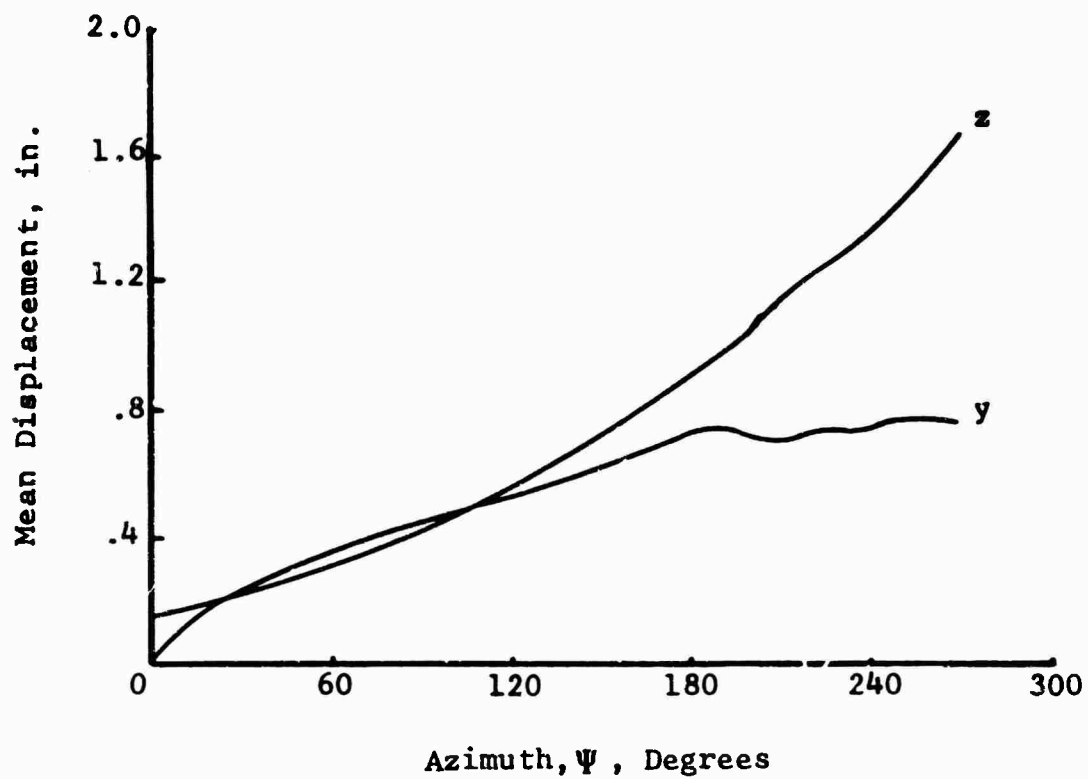


FIGURE 9. VORTEX CORE DISPLACEMENTS AND VELOCITIES, TWO-BLADES, 4000 RPM.

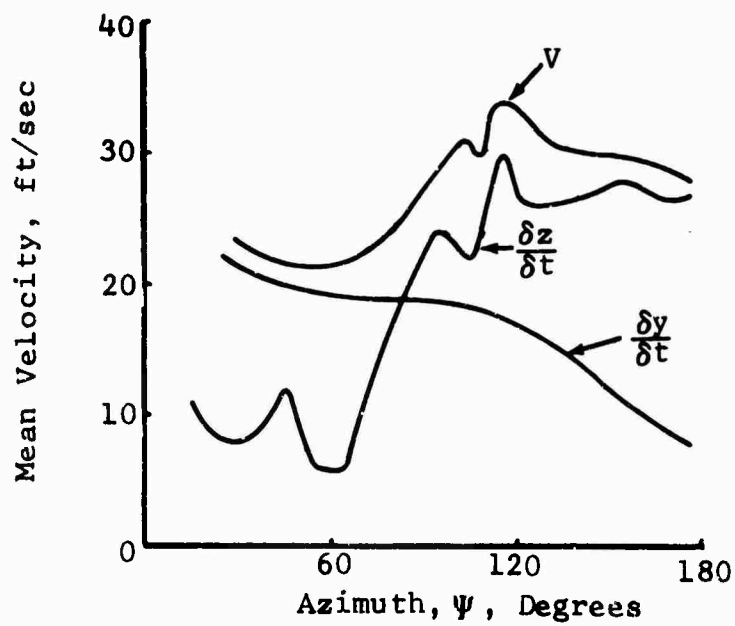
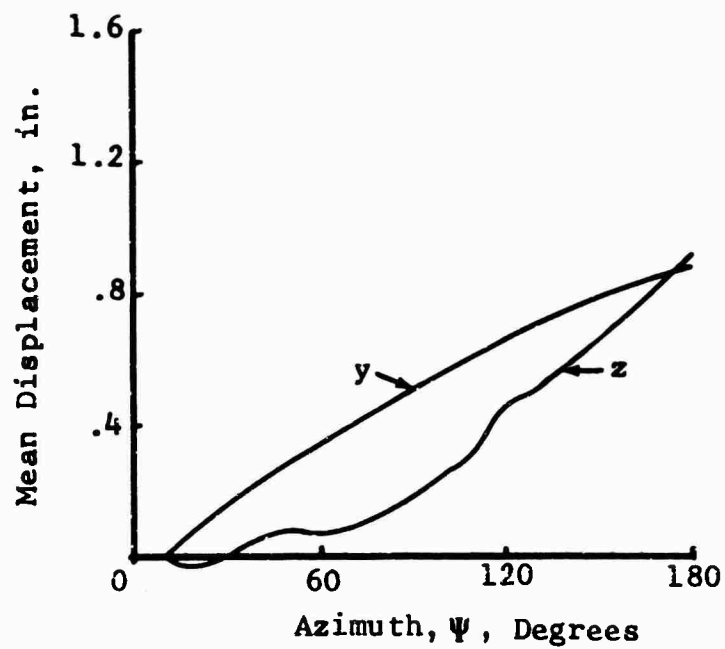


FIGURE 10. VORTEX CORE DISPLACEMENT AND VELOCITIES, FOUR-BLADES, 6500 RPM.

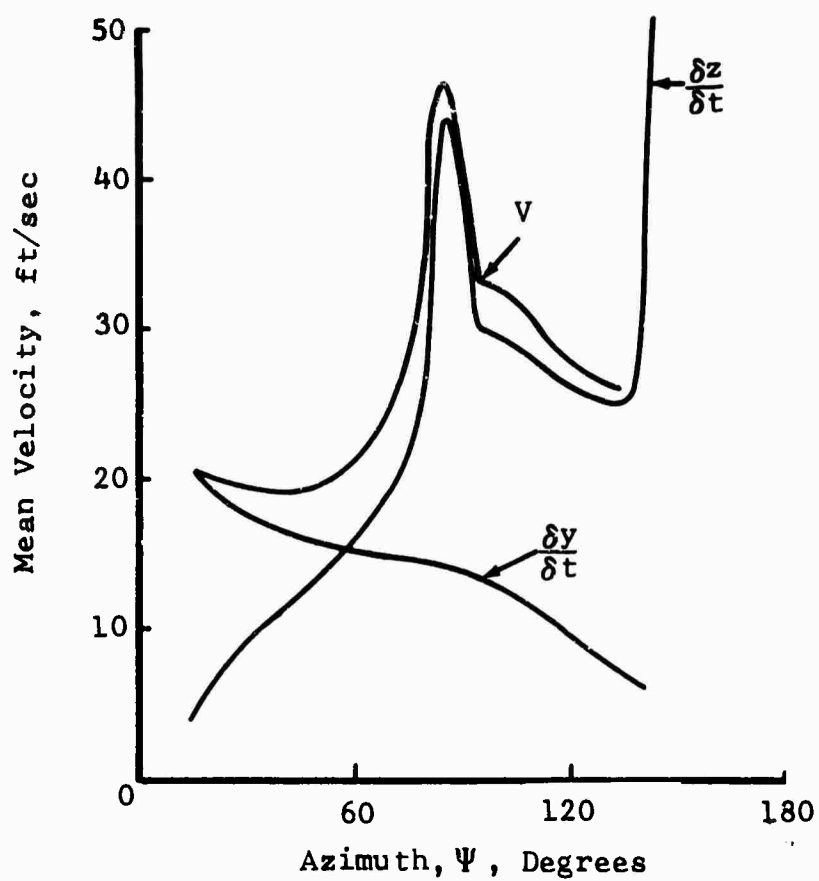
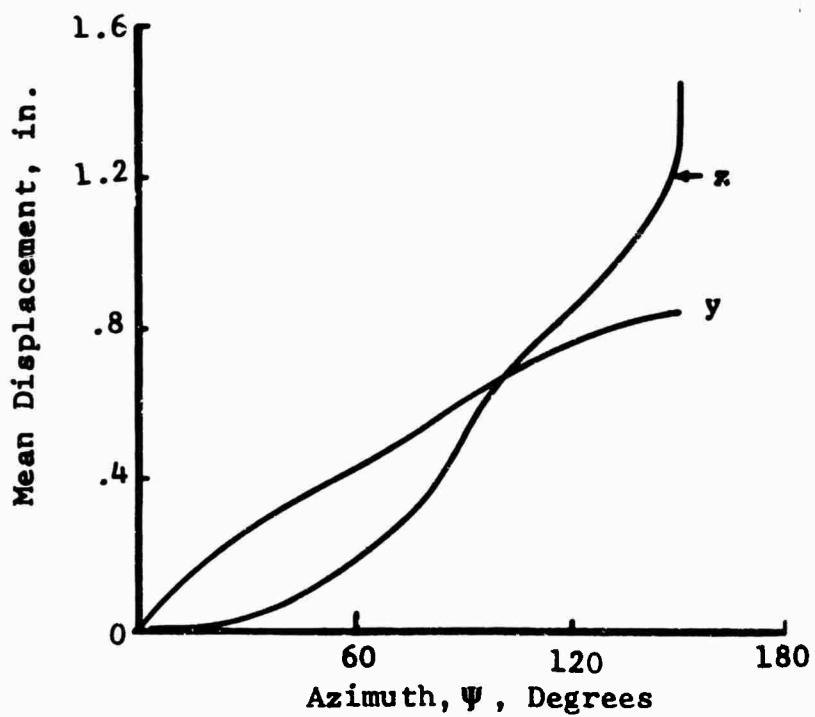


FIGURE 11. VORTEX CORE DISPLACEMENTS AND VELOCITIES, SIX-BLADES, 5000 RPM.

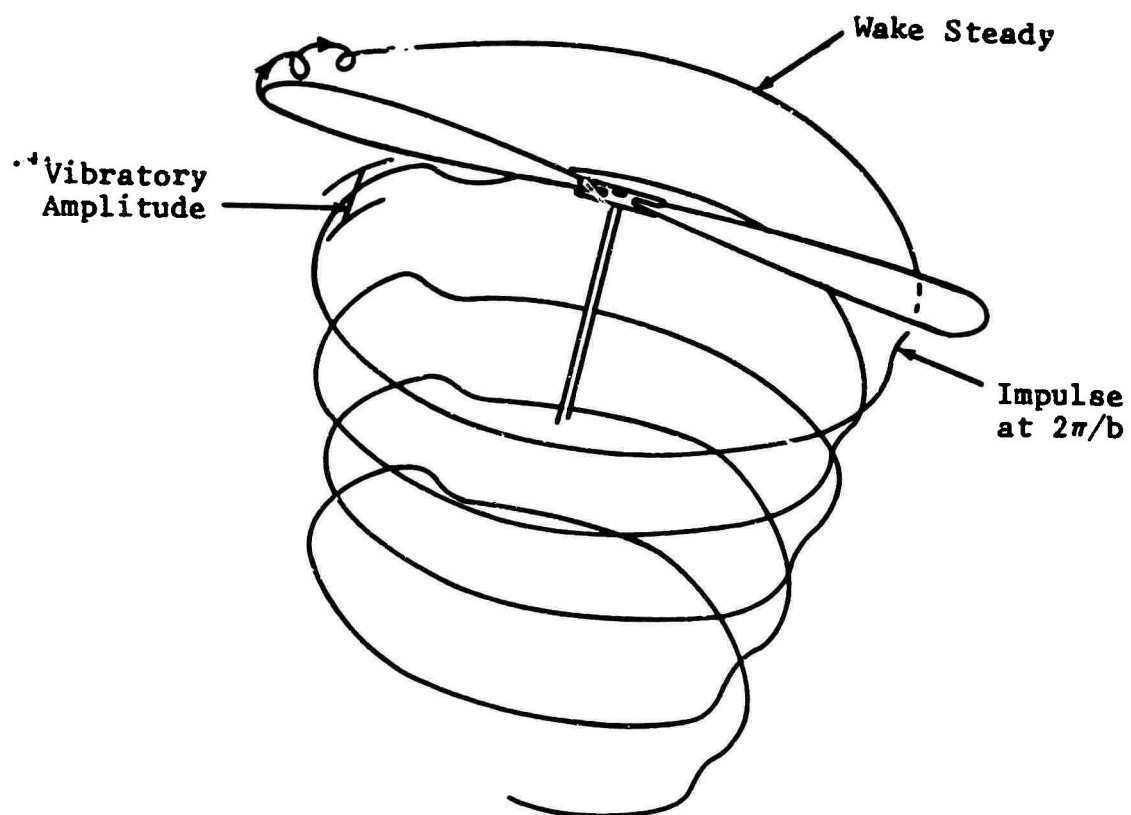


FIGURE 12. SKETCH OF WAKE SHOWING IMPULSE AND VIBRATORY AMPLITUDE.



NOTE: Rotation is out of the paper on a through e.

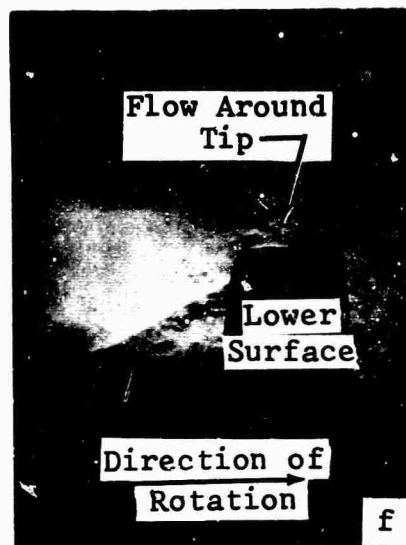
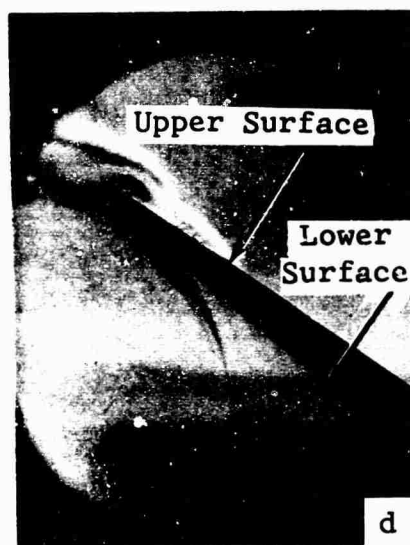


FIGURE 13. PHOTOGRAPHS OF THE FLOW AROUND THE TIP OF A TWO BLADED PROPELLER.

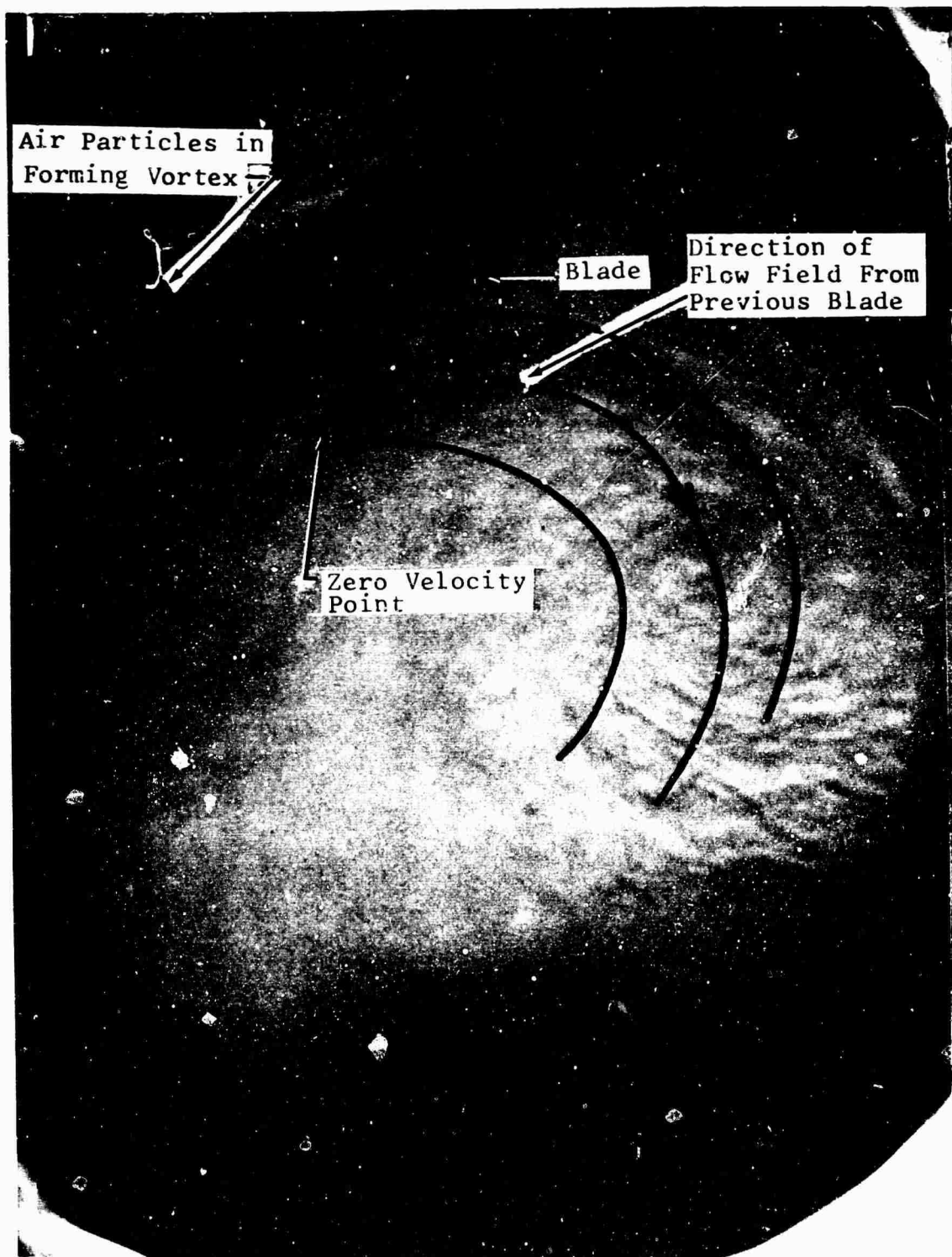


FIGURE 14. VORTEX WHICH IS 180° OLD, WITH THE HYPHOTHESIZED FLOW SUPERIMPOSED.

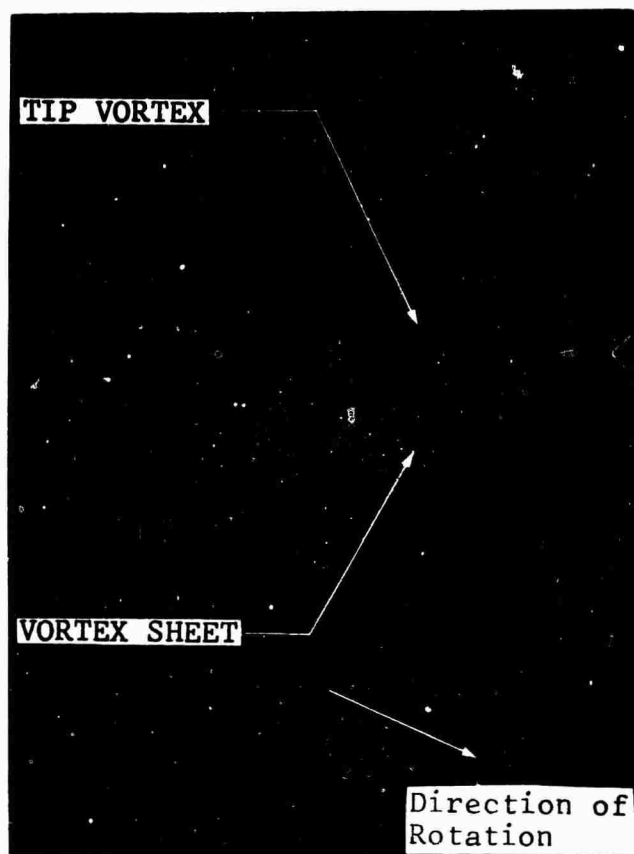


FIGURE 15. PHOTOGRAPH OF BLADE SHOWING
VORTEX SHEET AND TIP VORTEX.

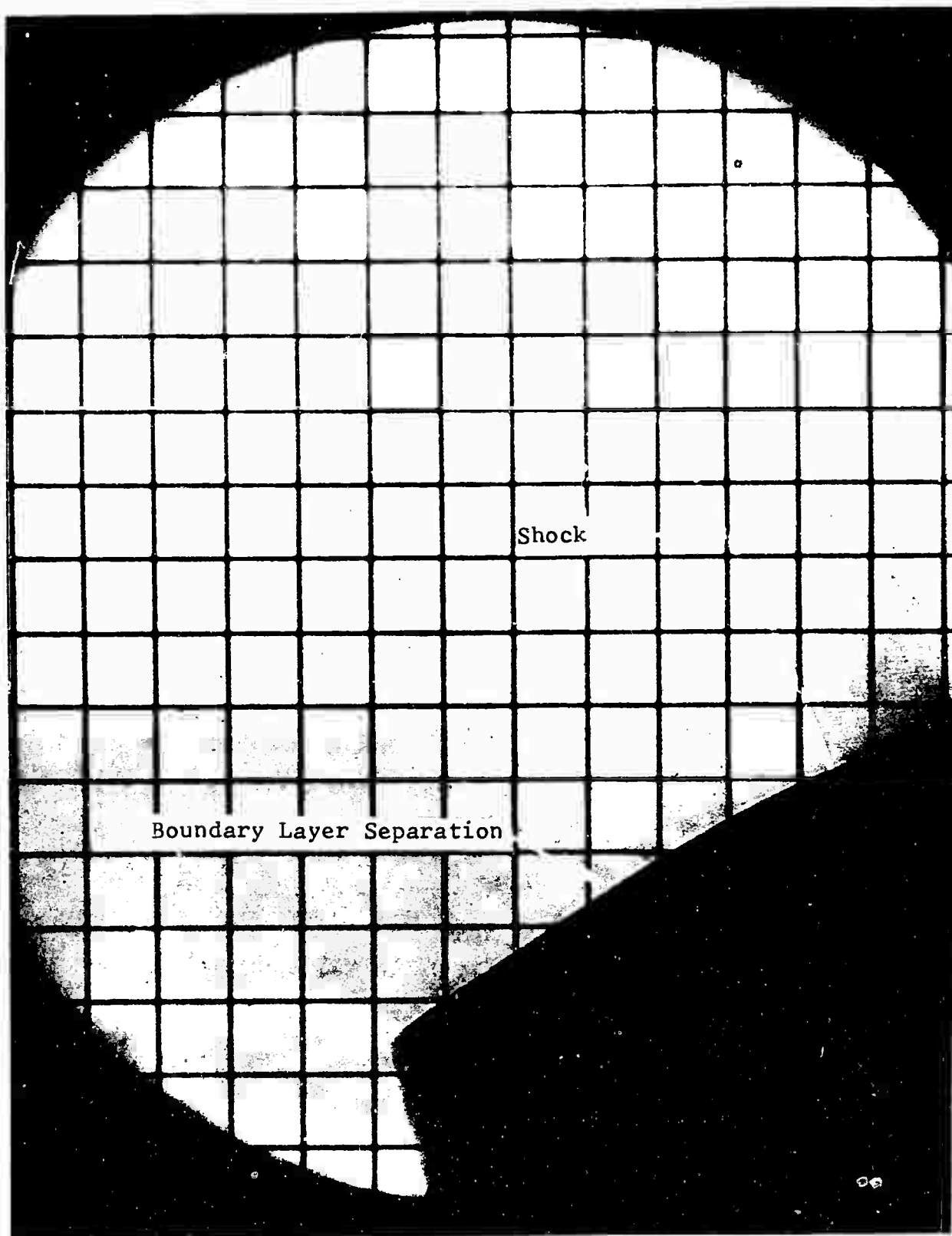


FIGURE 16. PHOTOGRAPH SHOWING A SHOCK AT THE BLADE TIP
WITH BOUNDARY LAYER SEPARATION BEHIND THE SHOCK.

**AN EXPERIMENTAL INVESTIGATION OF AN OSCILLATING
TWO-DIMENSIONAL AIRFOIL IN REVERSE FLOW**

by

RICHARD F. CHILD

Supervisor, Aerodynamics Research Unit
Vertol Division
The Boeing Company

ABSTRACT

The airloads on a helicopter rotor blade vary with the blade's azimuth position and are highest when the blade is on the retreating side of the rotor. The aerodynamic environment and the resulting airloads on the blade in such a position fall into three distinct categories: The outer portion of the blade is subjected to normal oscillatory loads in the sense that the flow approaches the blunt or normal leading edge of the blade. An intermediate segment of the blade approaches stall with the flow also in the classical sense; i. e., wind over the leading edge. The inner segment of the blade is also subjected to oscillatory airloads but they are created by flow over the "trailing" or sharp edge of the airfoil (reverse flow). The extent of these load categories over the blade is a function of tip speed and flight speed. Due to present limits on tip speed, because of Mach number effects, extensive reverse flow conditions exist over the blade span on the retreating side of the rotor at high flight speeds.

Airloads imposed on the retreating blade must be accurately defined because of the resulting high pitch link loads. Analytical definition of the loads is more difficult at high flight speeds, where the loads are highest, and the contribution from the reverse flow region most significant. Considerable data exists on aerodynamics of oscillating airfoils in forward flight including stall. However, no data on airfoils oscillating in reverse flow was known to exist.

Because of the importance of these loads, an experimental study was conducted to define the aerodynamic behavior of an airfoil oscillating in reverse flow. This paper reports the results of the study.

A Vertol 23010-1.58 airfoil equipped with a trailing edge tab was tested over a Mach number range from 0.1 to 0.4 at typical flight Reynolds numbers. Pitching oscillation frequencies typical of rotor first bending mode and first torsional mode conditions and static runs were included. The airfoil was tested at angles of attack up to 20 degrees with oscillatory amplitudes between 5 and 10 degrees. The trailing edge tab was placed in an up, down and neutral position. Chordwise pressure distributions were measured on the airfoil as a function of time and integrated to provide C_L , $C_{M_{1/4}}$ and aerodynamic damping data on the airfoil. Comparisons are made with the static data to show the effects of pitching oscillation rate on airfoils in reverse flow.

This work was performed under USAAVLABS Contract DAAJ02-68-C-0064.

INTRODUCTION

Rotor RPM of a helicopter at high flight speeds is limited by the onset of severe compressibility effects on the advancing blades because of both power requirements to overcome the rapidly increasing blade drag and by the need to limit the noise level due to "Mach bang." Limiting the rpm has not, however, limited the desire to develop high flight speed helicopters and, consequently, methods of flying faster are under investigation.

As has been pointed out in previous papers (1), the high speed requirements have led to conflicting airfoil requirements on the advancing and retreating blades of a rotor; thin airfoil sections for the advancing blades to accommodate high Mach number conditions and thick airfoils for the retreating blade to accommodate high C_L requirements. Recognition of the problem led to development of airfoils providing a reasonable compromise of these requirements. Furthermore, the dynamic effects on the aerodynamic properties of these and other airfoils have been extensively investigated and documented (1-4). Until recently, the studies have emphasized the aerodynamic properties of airfoils in forward flight (i.e. with the blunt edge forward). High speed rotors for which rpm limits are maintained to produce $M_{TIP} = 0.92$, however, have large segments of the retreating blades subjected to a reverse flow condition as is shown in Figure 1. $M_{TIP} = 0.92$ at $\psi = 90^\circ$ appears to be the maximum possible for practical rotors without encountering "Mach bang" (see section on Utilization of New Airfoils). The dynamic pressures acting on those portions of the blade subject to reverse flow are as much as 315% of the dynamic pressure at the blade tip at a ψ of 270° for the flight conditions shown in Figure 1. Consequently, the reverse flow airloads are an important consideration in predicting blade motions and pitch link loads.

The Boeing Company, working under contract to USAAVLABS, has conducted an experimental program to define the aerodynamic properties of an airfoil performing pitching oscillations in reverse flow so that information is available to define the effects of reverse flow airloads on blade motion. The study was based on the Vertol 23010-1.58 airfoil in order to provide a complete set of oscillating data (i. e. for both forward and reverse flow). A full report on the dynamic tests of the Vertol 23010-1.58 airfoil is available in Reference 2. A description of the test mechanism and data gathering and reduction system for both the forward and reverse flow tests is also available in Reference 2. The data from the reverse flow tests will be available later this year.

This paper presents and compares the significant data for the forward and reverse flow tests.

EXPERIMENTAL RESULTS

A diagram of the coordinate systems used in forward and reverse flow data analysis is shown in Figure 2 along with a sketch of the airfoil. The systems were chosen to show positive loads for the most probable direction of loading on a helicopter rotor airfoil.

Static Data

The airfoil was tested under steady α conditions over the entire range of Mach numbers and angles of attack for which dynamic data were taken. The normal force coefficient (C_N) and pitching moment coefficient (C_M) characteristics of the airfoil in forward and reverse flow are shown in Figures 3 and 4 for Mach numbers of 0.2 and 0.4. At $M = 0.2$, the C_{N_α} of the airfoil for both flow conditions is nearly identical. However, the reverse flow condition produces an earlier stall with a

substantial loss in C_{NMAX} . Furthermore, the stall in reverse flow has the character of a trailing edge stall rather than the leading edge stall behavior demonstrated by the airfoil in forward flight. The C_M behavior of the airfoil in reverse flow resembles the C_N behavior when referenced to the 1/4-chord of the airfoil in forward flight. This is due to the large contribution of C_N . However, when C_M for reverse flow is referenced to the airfoil 3/4-chord, the C_M level for reverse flow compares well with that for forward flight showing only an earlier and more gentle "moment stall" than is shown for forward flight. At $M = 0.4$, the airfoil in forward flight has the expected C_N behavior showing a higher $C_{N\alpha}$, a lower C_{NMAX} and still retains the leading edge stall characteristic of a large, abrupt drop in C_N . The C_N trace for the airfoil in reverse flow, however, has the character of a high Mach number stall (i. e., a brief region where $C_N \approx 0$ followed by a region of increasing C_N with α but with a lower slope). The $C_{M_{1/4}}$ for the airfoil in reverse flow again follows the C_N behavior while the reverse flow $C_{M_{3/4}}$ still follows the trend of the $C_{M_{1/4}}$ of the airfoil in forward flight.

It should be pointed out that the $C_{M_{1/4}}$ is the level of interest as most rotor blades rotate about a point near the 1/4-chord. Consequently, the large positive C_M 's will produce large pitch link load changes if any significant segment of the blade encounters reverse flow.

Note that the region of linear behavior of C_N for the airfoil in reverse flow is restricted to $\alpha < 4^\circ$ for both Mach numbers shown.

Figure 5 compared airfoil pressure loading along the airfoils (i. e. $\Delta C_p = C_{p(upper)} - C_{p(lower)}$) for conditions below stall ($C_N = 0.468$), near stall ($C_N = .805$), and above stall ($C_N = .899$). The general shapes of the pressure distributions

are retained for both forward and reverse flow conditions but the implications change. The strong pressure gradient over the first 1% of the chord in reverse flow implies flow separation and explains the trailing edge stall behavior as the point of separation appears to move forward with increasing α .

Trailing Edge Tab Effects

The effect of changing the trailing edge tab setting on the static aerodynamic behavior of the airfoil in reverse flow is shown in Figure 6 for Mach numbers of 0.2 and 0.4. Three tab settings were tested ($\delta_{TAB} = 0^\circ, \pm 3^\circ$). The general effect is to produce some small change in C_N and C_M near stall. However, the same trends are evident for all values of δ_{TAB} . Further discussion of the tab effect is, therefore, not considered necessary since the objective of this paper is to show general comparisons between forward and reverse flow airfoil aerodynamic behavior.

Typical Dynamic Data

Reference 1 plotted typical C_N and C_M response loops for the V23010-1.58 airfoil and compared them with the static data. This comparison is reproduced here as Figure 7 for reference. The loops show behavior below stall ($\alpha_0 = 7.33^\circ$), near stall ($\alpha_0 = 14.92^\circ$) and above stall ($\alpha_0 = 24.57^\circ$). Typical dynamic response plots for the airfoil in reverse flow are shown and compared with the static data in Figure 8 again for conditions below stall ($\alpha_0 = 5.0^\circ$), near stall ($\alpha_0 = 12.5^\circ$) and above stall ($\alpha_0 = 20.0^\circ$).

The model was forced in pitch oscillation about the 1/4-chord position (measured from the leading edge) at a frequency of 16 Hertz. This frequency is the scaled 1/rev. frequency of the full-scale rotor blade based on the reduced frequency

parameter, $k = \frac{f c}{v}$. The Mach number for both the forward and reverse flow tests was 0.4. The C_N and C_M traces for both forward and reverse flow show the characteristic elliptical shape predicted by oscillating airfoil theory (5) for α 's below stall.

The area inside the C_M trace indicates the work per cycle and a "cycle damping" can be defined as:

$$\text{Damping} = \oint C_M d\alpha$$

This integral is positive for a counter clockwise circuit of the area. If the damping is negative, the airfoil extracts energy from the air which can lead to a flutter condition. Note that for α 's near stall, the airfoil in reverse flow shows considerably more negative damping than when in forward flight and that for α 's well above stall, the airfoil in reverse flow still shows negative damping while in the forward flight case the damping has become positive.

Pitch Frequency Effects

The effect of increasing the pitching frequency on maximum C_N and C_M in reverse flow is shown and compared with the forward flight data on Figures 9 and 10. Comparison of high frequency effects cannot be made at the same frequency for both forward and reverse flow due to the limited data available. However, the results plotted show: At low frequency, the airfoil stalls during the pitch cycle in both forward and reverse flow. At high frequency it does not suddenly stall as indicated by the C_M loops. This suggests that there is an upper limit to the time rate of change of circulation about the airfoil.

Summary of Dynamic Data

The characteristics of the dynamic data can best be summarized in terms of the parameters $C_{N\text{MAX}}$ and cycle damping. The cycle damping is divided by the theoretical damping based on Reference (5), i.e.

$$\text{Damping Ratio} = \frac{\int (C_M)_{\text{TEST}} d\alpha}{\int (C_M)_{\text{THEORY}} d\alpha}$$

Maximum Dynamic Normal Force

The maximum C_N attained during a cycle both in forward and reverse flow is presented in Figure 11 as a function of frequency and at specific Mach numbers. Strong frequency and Mach number effects are evident in the reverse flow condition while the forward flight data shows strong effects of these parameters on C_N only at low frequencies. Replotting the same data against reduced frequency, k , Figure 12, shows the reverse flow $C_{N\text{MAX}}$ to be insensitive to Mach number while the forward flight data still shows a Mach number effect at low values of k . Note that at high frequencies or values of k , the dynamic $C_{N\text{MAX}}$ for reverse flow is equal to or greater than the forward flight values.

Cycle Damping

Cycle damping of the airfoil in forward and reverse flow is compared at $M = 0.2$ in Figure 13 at a frequency of 16 Hertz and at $M = 0.4$ in Figure 14 for frequencies of 16 and 80 Hertz. The airfoil in reverse flow encounters negative damping at a lower angle of attack than for forward flow for all conditions shown.

Furthermore, the airfoil in reverse flow remains negatively damped as α increases above the point for zero damping while in forward flight a return to positive damping is achieved at very high angles of attack.

Cycle to Cycle and Moment Variations

The damping and dynamic C_N characteristics presented in this paper were obtained by averaging the data from groups of five or more consecutive cycles of oscillation. Recognizing that the dynamic response of a rotor blade will depend on the loads acting over individual cycles, the question of variation from cycle to cycle is of importance.

Figure 15 compares normal force and moment traces for the V23010-1.58 airfoil in reverse flow under conditions where stall is present. Five successive cycles are given for each parameter. The traces match well on the increasing α part of the cycle including stall. However, they divide into several patterns during stall recovery. Because of this behavior, it is concluded that the cause for the scatter is due to turbulence in the stalled flow and is not due to wind tunnel flow. The same conclusion was reached for the airfoil in forward flight in Reference 1. Insufficient data on the scatter patterns are available to define a meaningful statistical description.

UTILIZATION OF NEW AIRFOILS

Present high speed helicopter rotors are designed to operate efficiently in hover as well as in forward flight and this consideration dictates the tip airfoil not be less than 6% thick. This thickness restriction is what limits the $M_{\psi=90}$ to about 0.92 if "Mach bang" is to be avoided. Design of airfoils with improved Mach number capability has been part of fixed wing aircraft research for some years.

The empirical approach of Pearcy (6) and theoretical approach of Nieuwland (7) may prove of benefit to the helicopter industry eventually. To the author's knowledge, however, no direct effort to design an airfoil for a helicopter rotor (i.e. with wide ranges of usable C_L over wide M ranges) has been attempted using these techniques. Evaluation of the design of such airfoils is required if the $M_{\psi} = 90$ limit is to be raised.

CONCLUSIONS

1. The V23010-1.58 airfoil in reverse flow exhibits dynamic properties qualitatively similar to those reported for the airfoil in forward flight.
2. The airfoil in reverse flow encounters negative damping at lower angles of attack than would occur in forward flight.
3. Consideration of reverse flow dynamics airfoil data should be incorporated into all high speed rotor analysis.
4. Development of new higher speed airfoils may relieve the extent of reverse flow but this will require additional research.

ACKNOWLEDGMENTS

The substantial contributions made to the Reverse Flow Oscillating Airfoil Program by individuals in the Vertol and Airplane Divisions of The Boeing Company are acknowledged. Particular thanks are given to L. Dadone, I. Walton, P. Davis, H. Dittmer, H. Louth, and D. Seleyo. Acknowledgment of the contributions of J. Yeates and P. Cancro of USAAVLABS is also made.

REFERENCES

1. Liiva, J. and Davenport, F.J., DYNAMIC STALL OF AIRFOIL SECTIONS FOR HIGH-SPEED ROTORS, American Helicopter Society, Inc., 24th Annual

National Forum, Washington, D.C., May 1968.

2. Liiva, J., Davenport, F., Gray, L., and Walton, I., TWO-DIMENSIONAL TESTS OF AIRFOILS OSCILLATING NEAR STALL, VOLUME I, SUMMARY AND EVALUATION OF RESULTS, Boeing Document D8-0678-1, October 1967.

3. Liiva, J., UNSTEADY AERODYNAMIC AND STALL EFFECTS ON HELICOPTER ROTOR BLADE AIRFOIL SECTIONS, Paper No. 68-58 presented at the 6th Aerospace Sciences Meeting of the American Institute of Aeronautics and Astronautics, January 1968.

4. Liiva, J., Gray, L., and Davenport, F.J., INVESTIGATION OF THIN AIRFOILS OSCILLATING NEAR STALL, Boeing Document D8-0925, to be released January 1969.

5. Bisplinghoff, Raymond L., Ashley, Holt, and Halfman, Robert L., AEROELASTICITY, Addison-Wesley Publishing Company, Inc., Reading, Massachusetts, 1955.

6. Percy, H.H., THE AERODYNAMIC DESIGN OF SECTION SHAPES FOR SWEPT WINGS, ADVANCES IN AERONAUTICAL SCIENCES, VOL. 3, LONDON, 1962.

7. Nieuwland, G.Y., TRANSONIC POTENTIAL FLOW AROUND A FAMILY OF QUASI-ELLIPTICAL AEROFOIL SECTIONS, National Aerospace Laboratory, Technical Report 172, Amsterdam 1967.

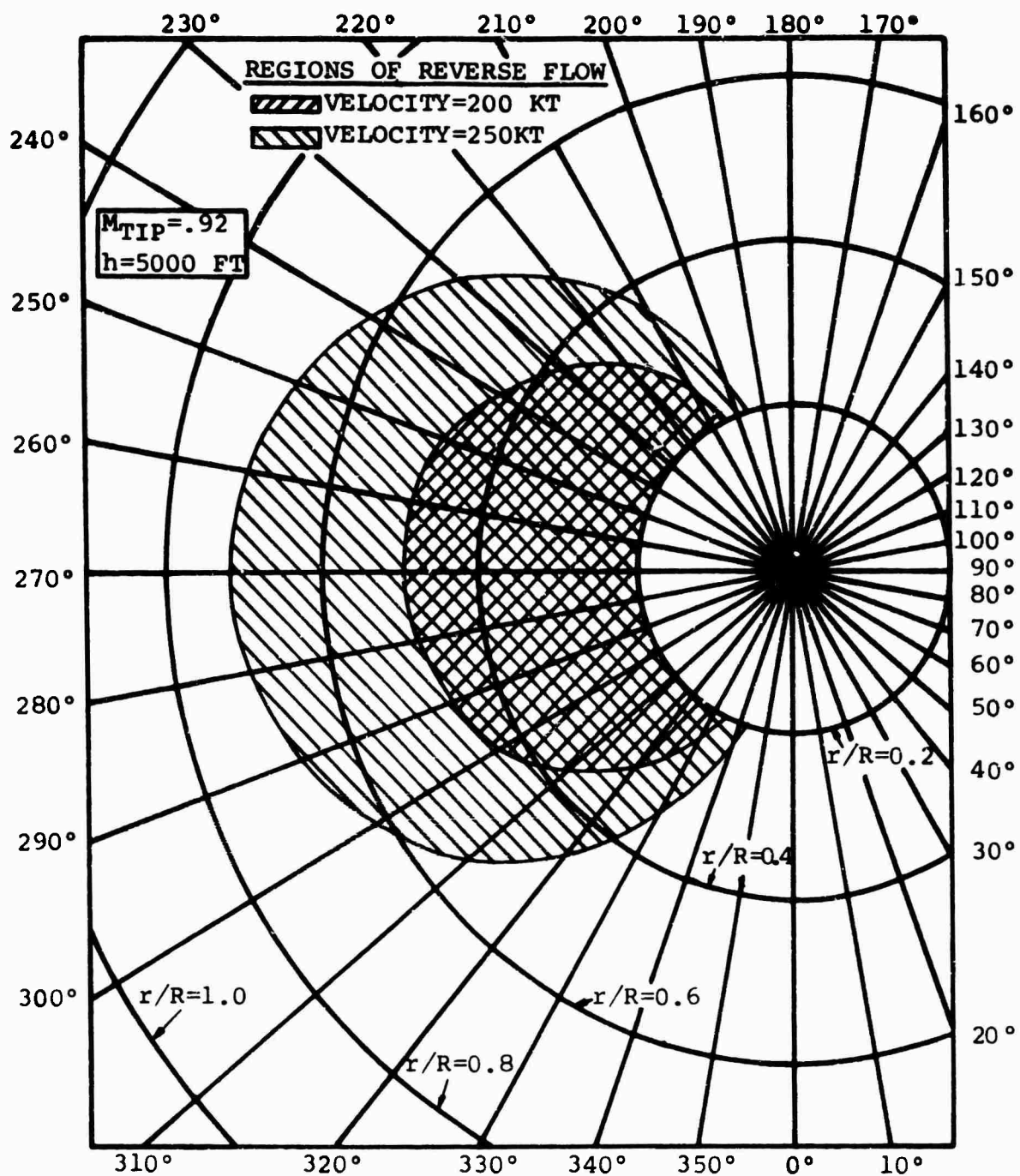
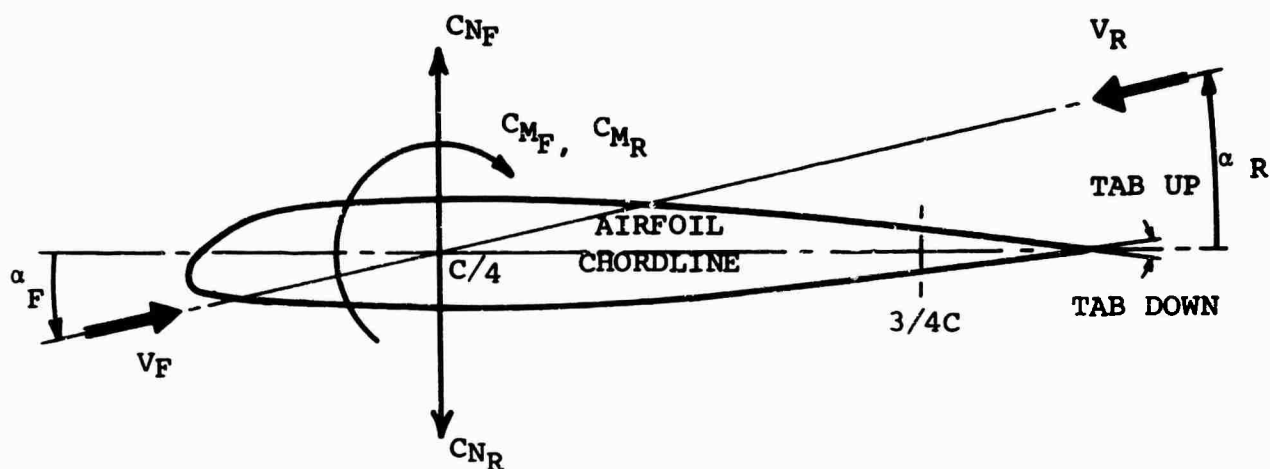


FIGURE 1. REGIONS OF REVERSE FLOW FOR ROTOR BLADE AT HIGH SPEED



NOTATION:

C_N NORMAL FORCE COEFFICIENT
 C_M PITCHING MOMENT COEFFICIENT
 α ANGLE OF ATTACK
 V TUNNEL VELOCITY

SUFFIXES:

F DENOTES FORWARD FLOW CONDITION
 R DENOTES REVERSE FLOW CONDITION

FIGURE 2. CO-ORDINATE REFERENCE SYSTEM FOR VERTOL 23010-1.58 IN FORWARD AND REVERSE FLOW

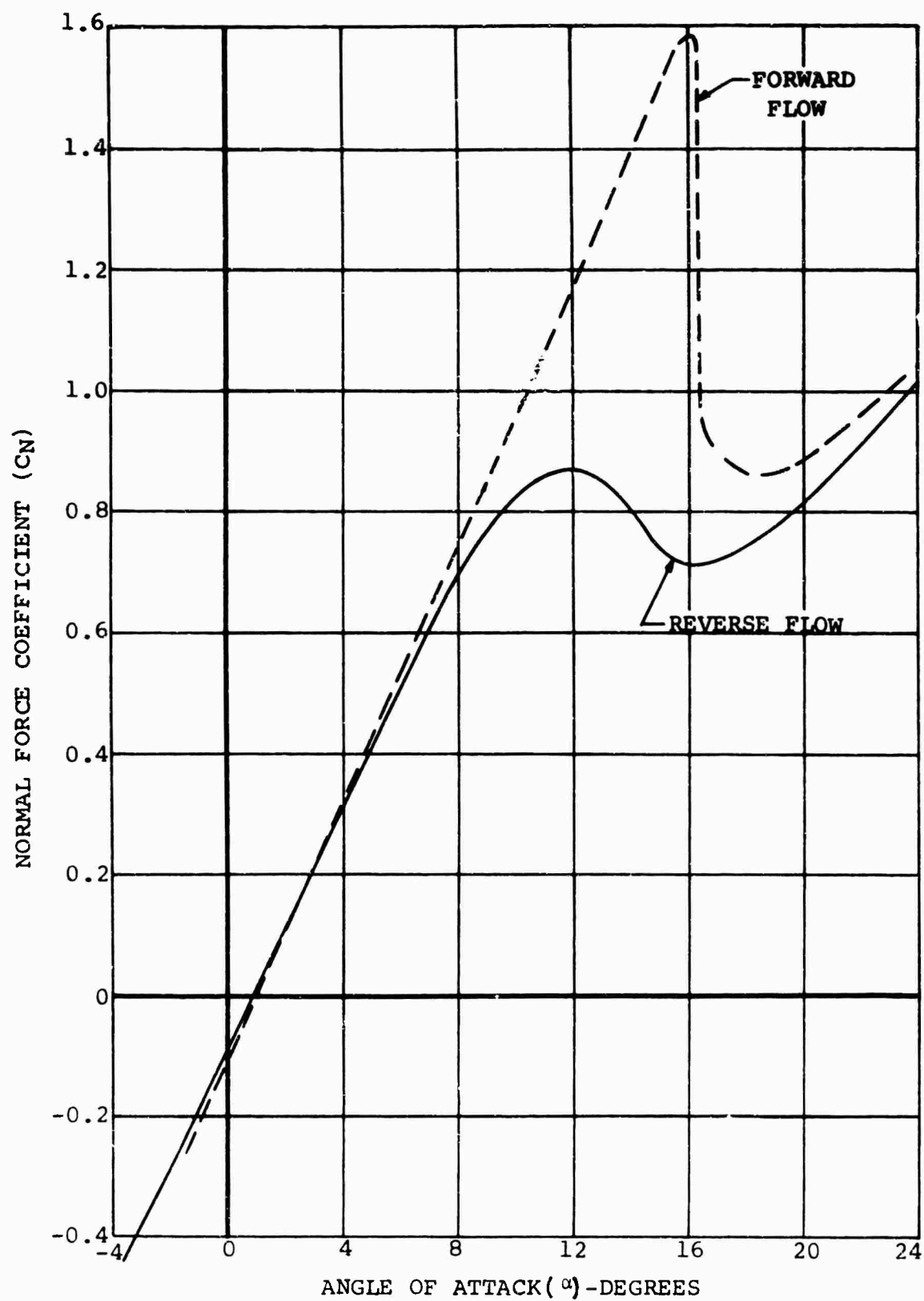


FIGURE 3a. STATIC AERODYNAMIC COEFFICIENTS OF VERTOL 23010-1.58 AIRFOIL, $M=0.2$

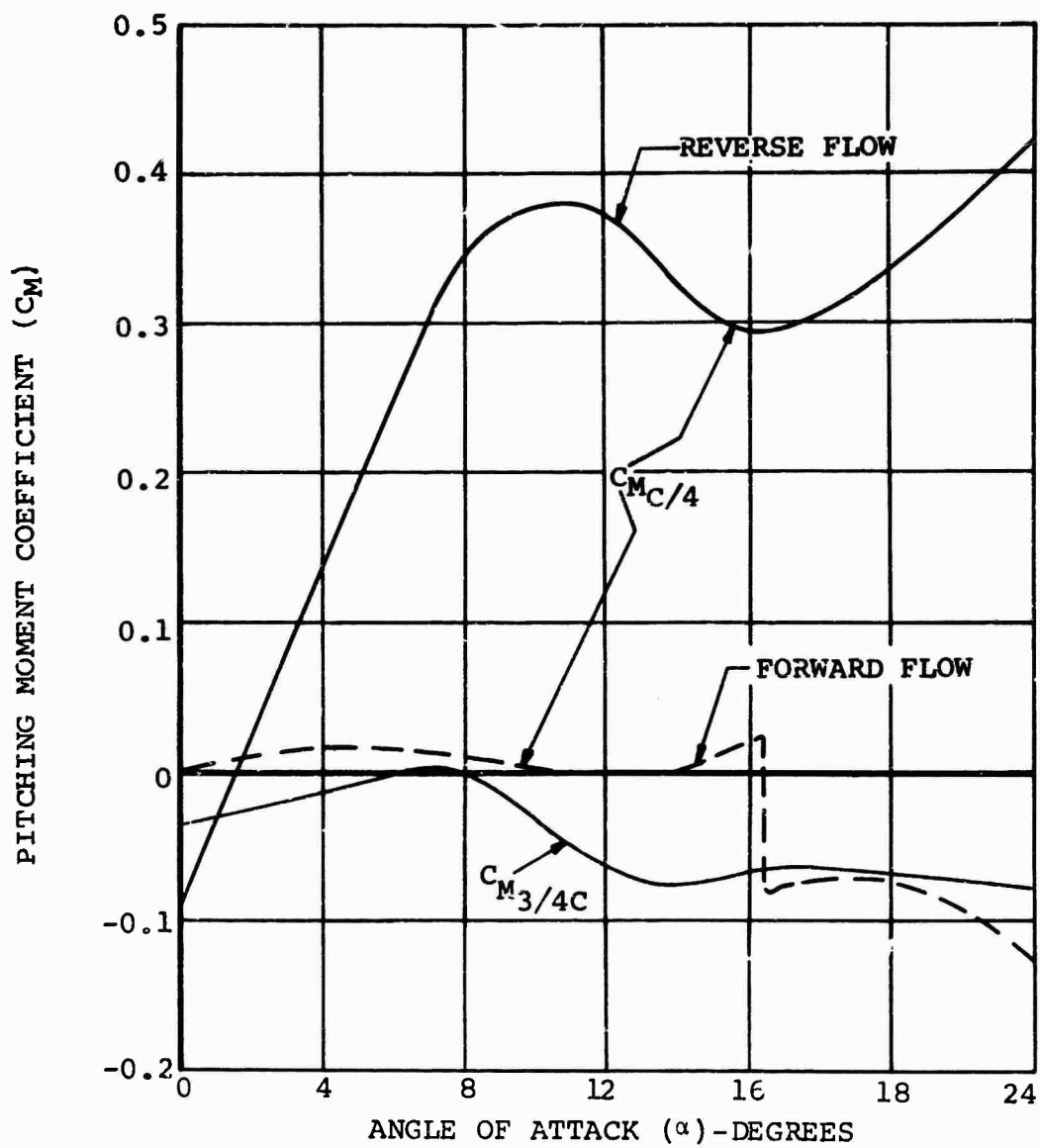


FIGURE 3b. STATIC AERODYNAMIC COEFFICIENTS OF VERTOL 23010-1.58 AIRFOIL, $M=0.2$

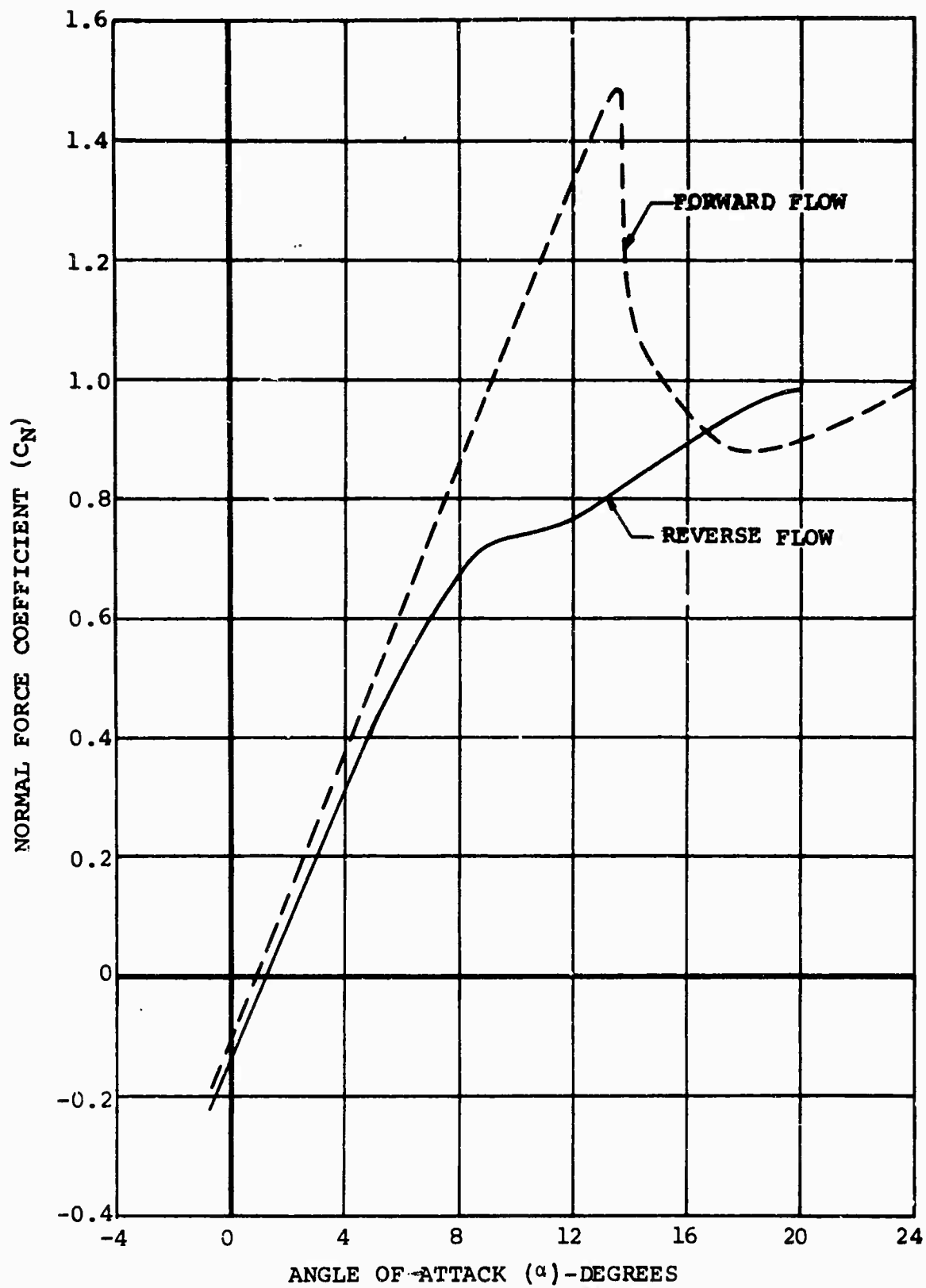


FIGURE 4a. STATIC AERODYNAMIC COEFFICIENTS OF VERTOL
23010-1.58 AIRFOIL, $M=0.4$

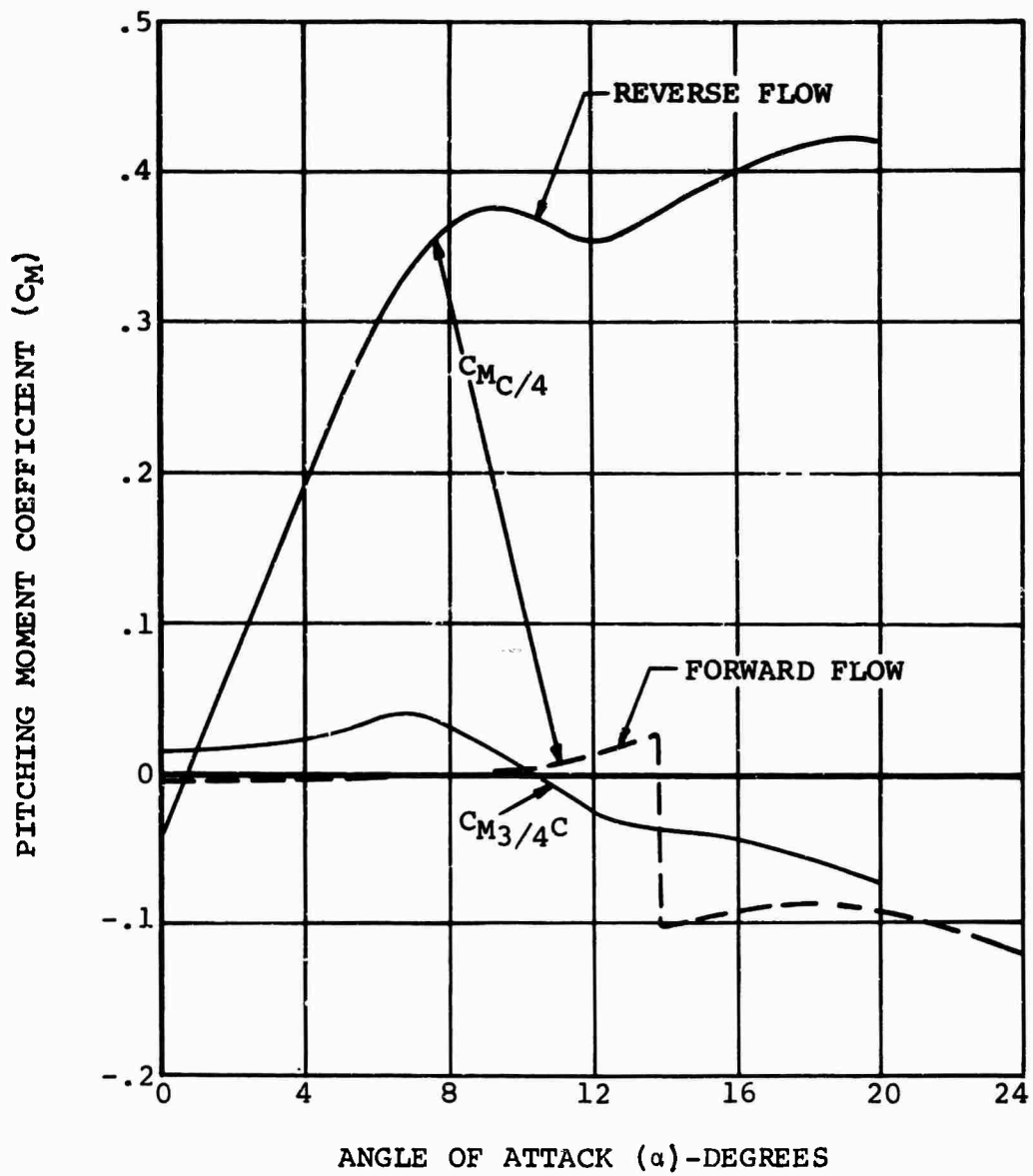


FIGURE 4b. STATIC AERODYNAMIC COEFFICIENTS OF VERTOL 23010-1.58 AIRFOIL, $M=0.4$

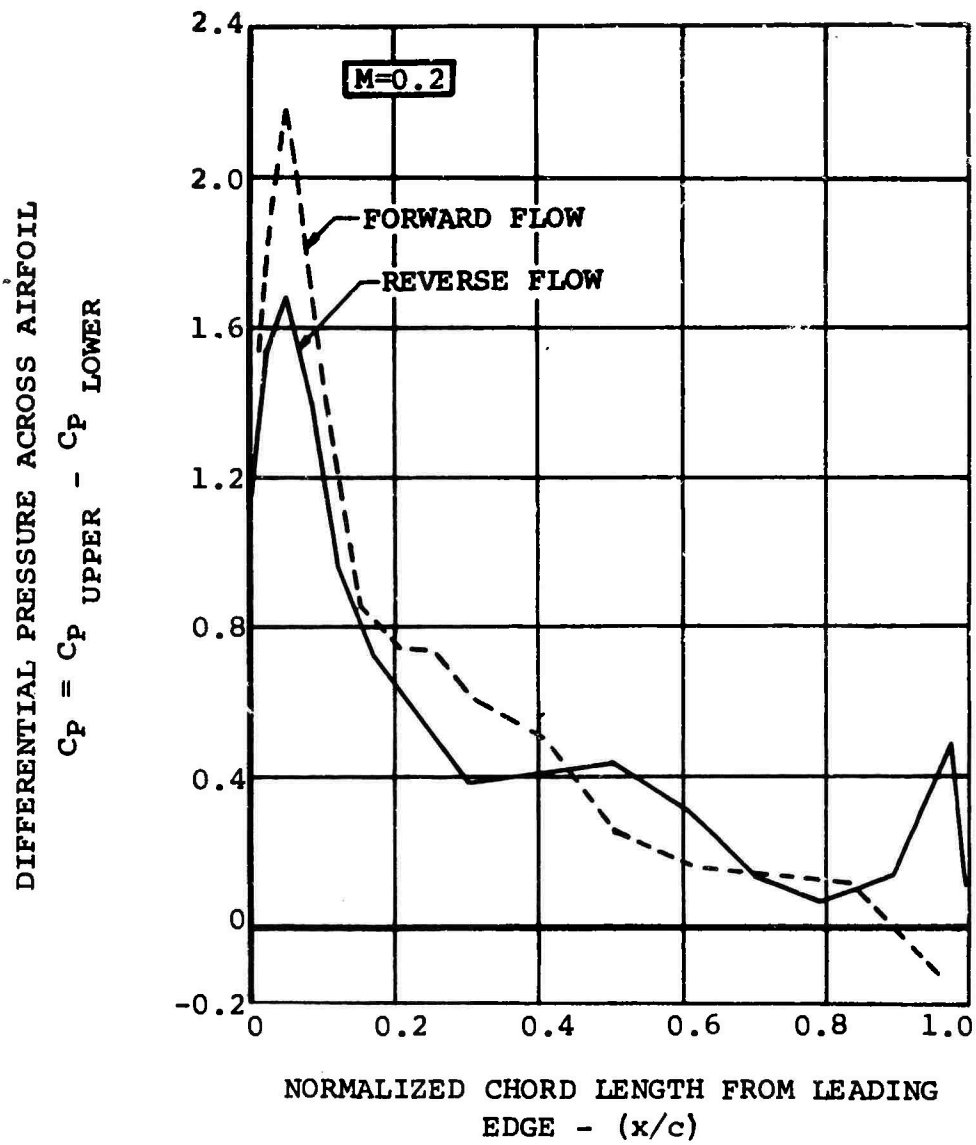


FIGURE 5a. BLADE LOADING OF V23010-1.58 AIRFOIL
IN FORWARD AND REVERSE FLOW, $C_N = 0.468$

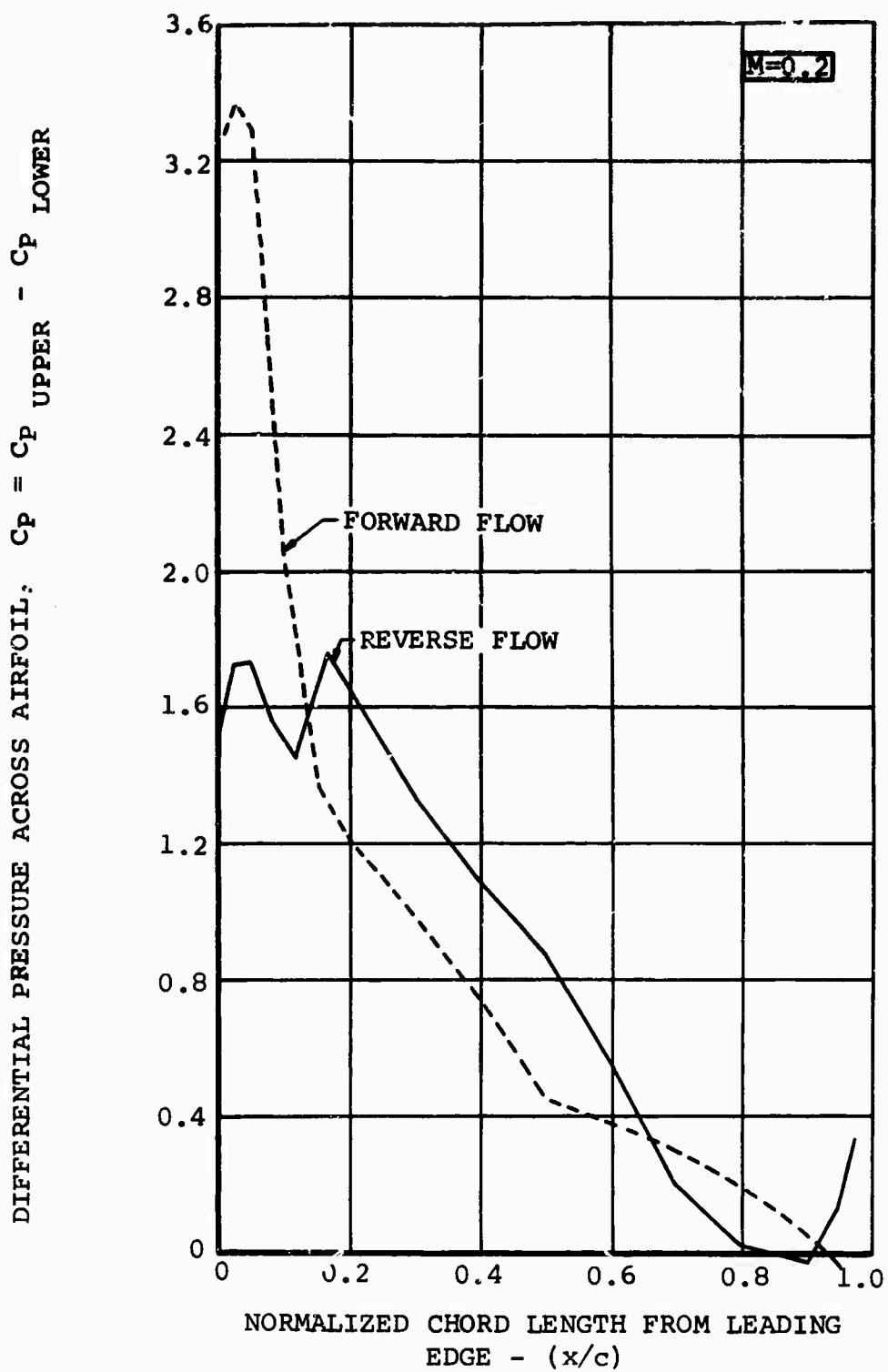


FIGURE 5b. BLADE LOADING OF V23010-1.58 AIRFOIL IN FORWARD AND REVERSE FLOW, $C_N = 0.805$

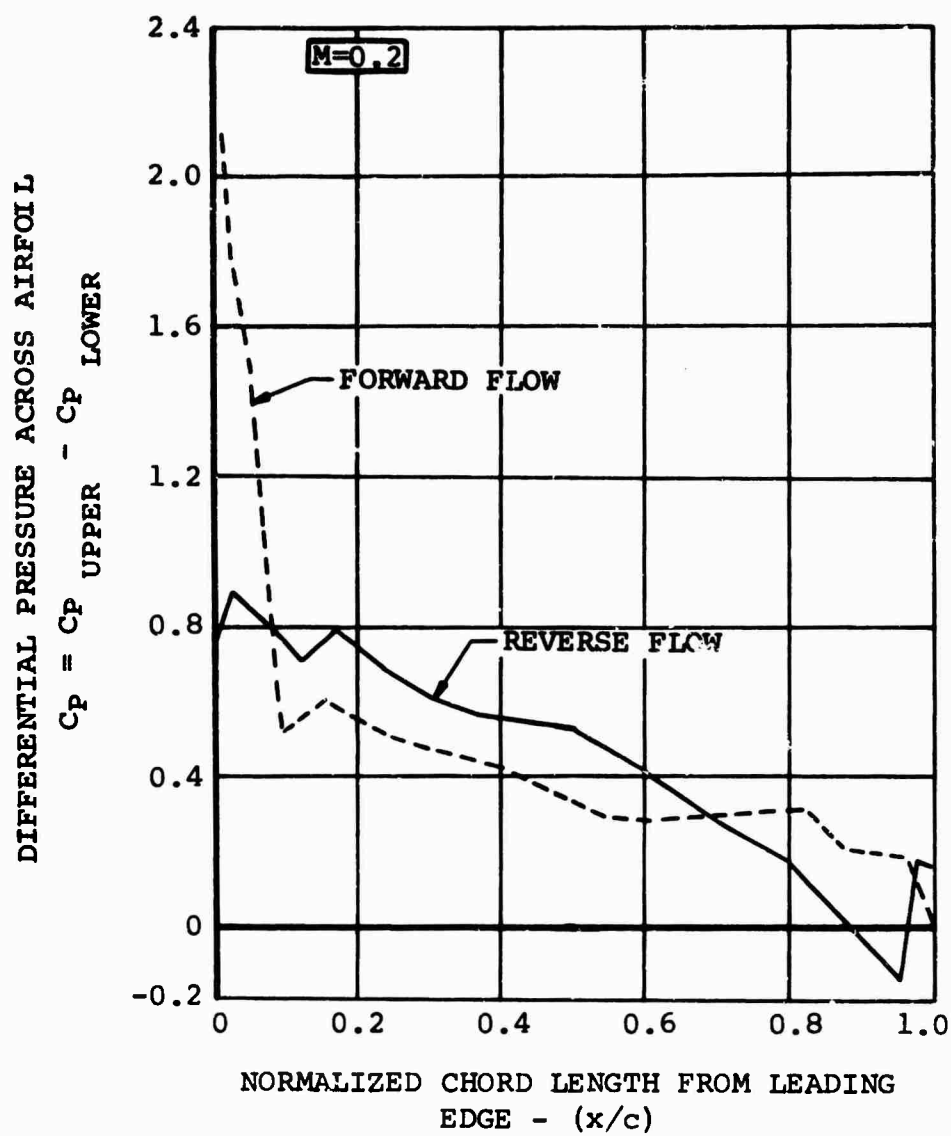


FIGURE 5c. BLADE LOADING OF V23010-1.58 AIRFOIL
IN FORWARD AND REVERSE FLOW, $C_N = 0.899$

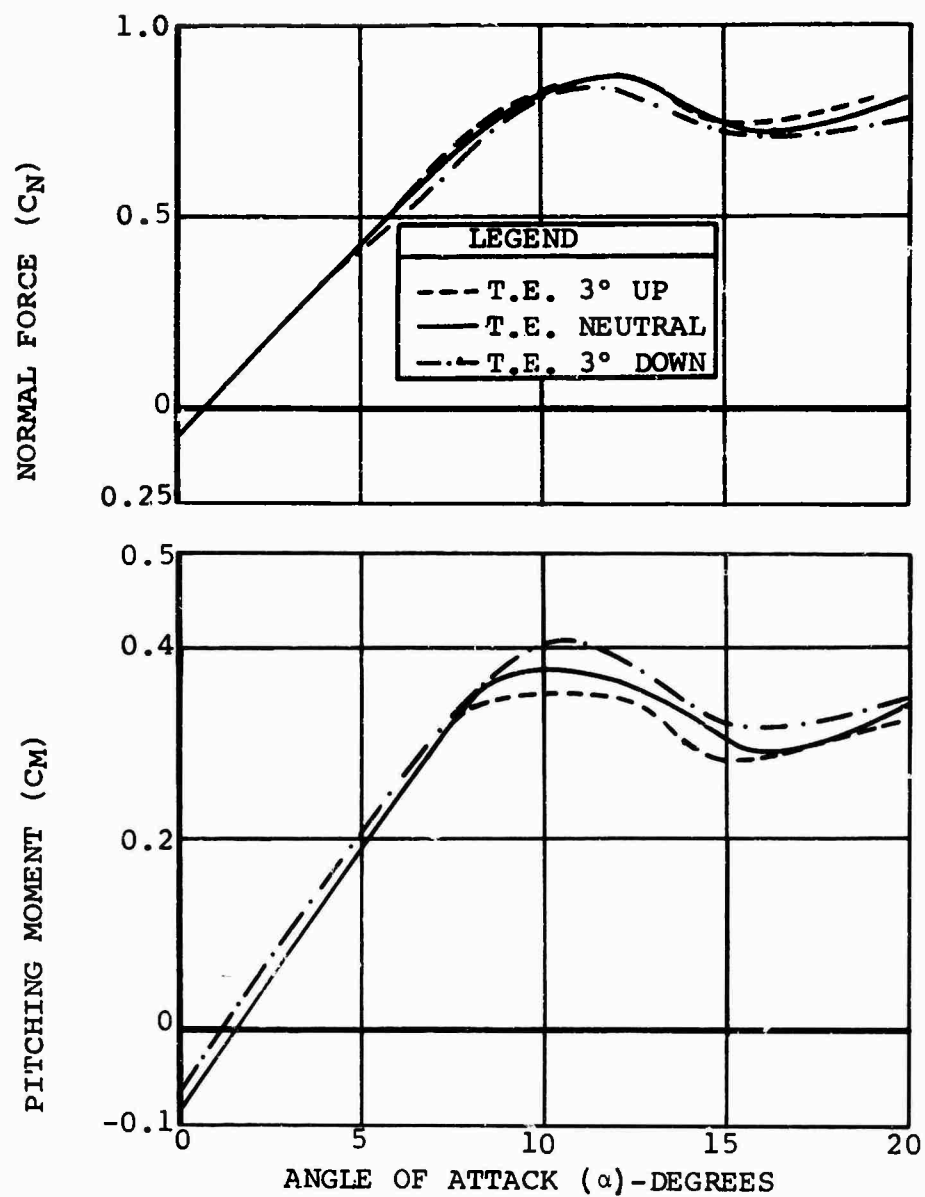


FIGURE 6a. EFFECT OF TRAILING EDGE TAB ON STATIC AERODYNAMIC COEFFICIENTS OF THE V23010-1.58 AIRFOIL IN REVERSE FLOW, $M=0.2$

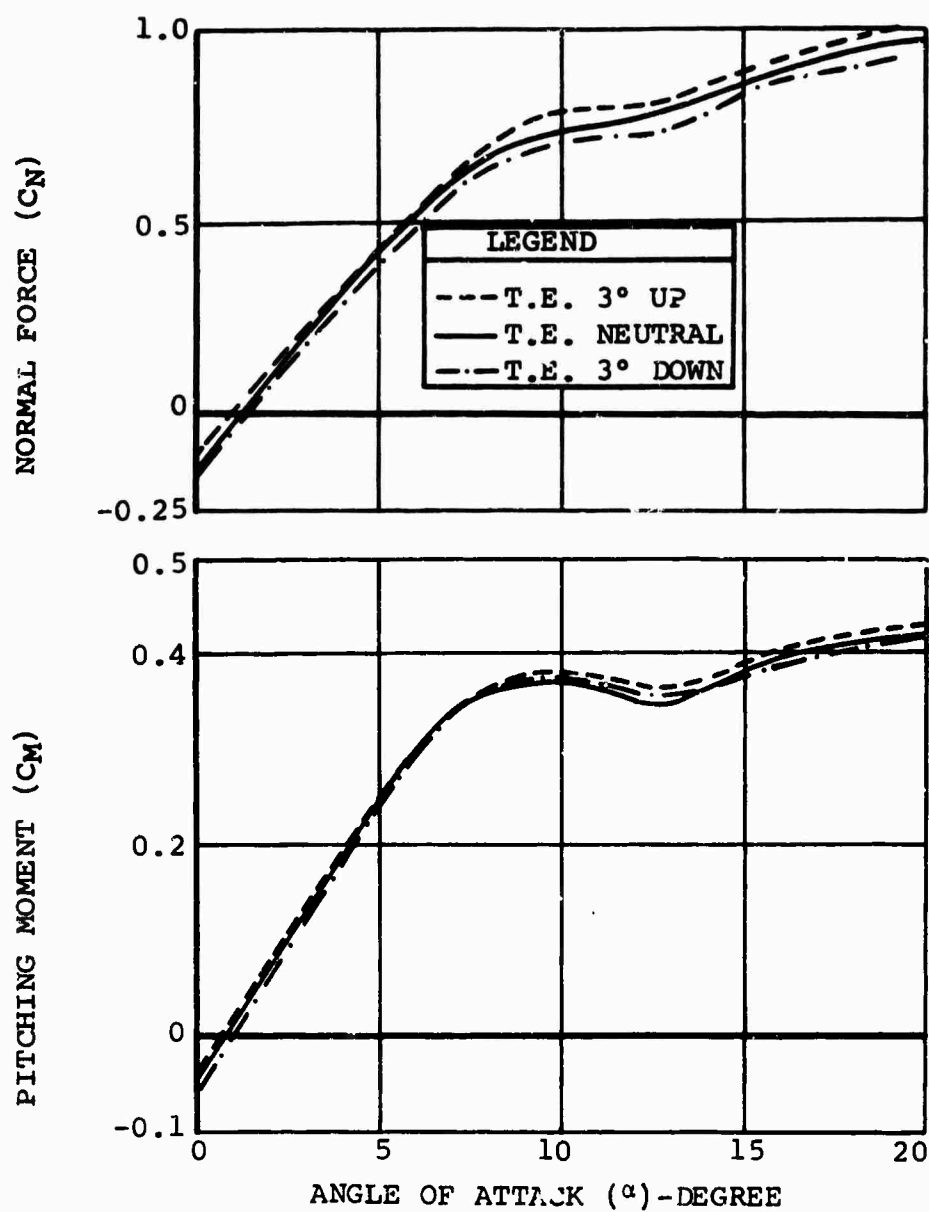


FIGURE 6b. EFFECT OF TRAILING EDGE TAB ON STATIC AERODYNAMIC COEFFICIENTS OF THE V23010-1.58 AIRFOIL IN REVERSE FLOW, $M=0.4$

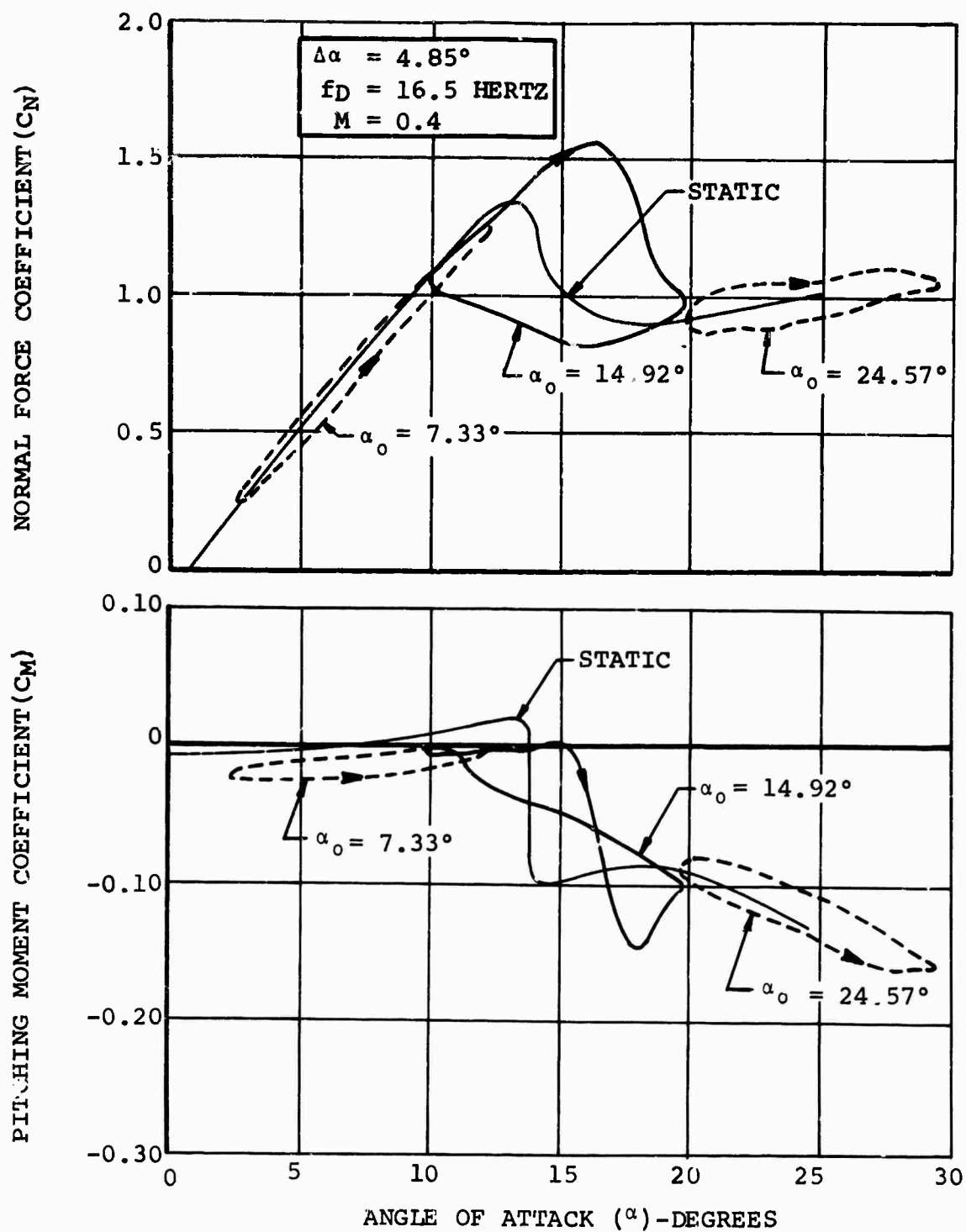


FIGURE 7. TYPICAL PITCH OSCILLATION DATA FOR THE V23010-1.58 AIRFOIL IN FORWARD FLOW

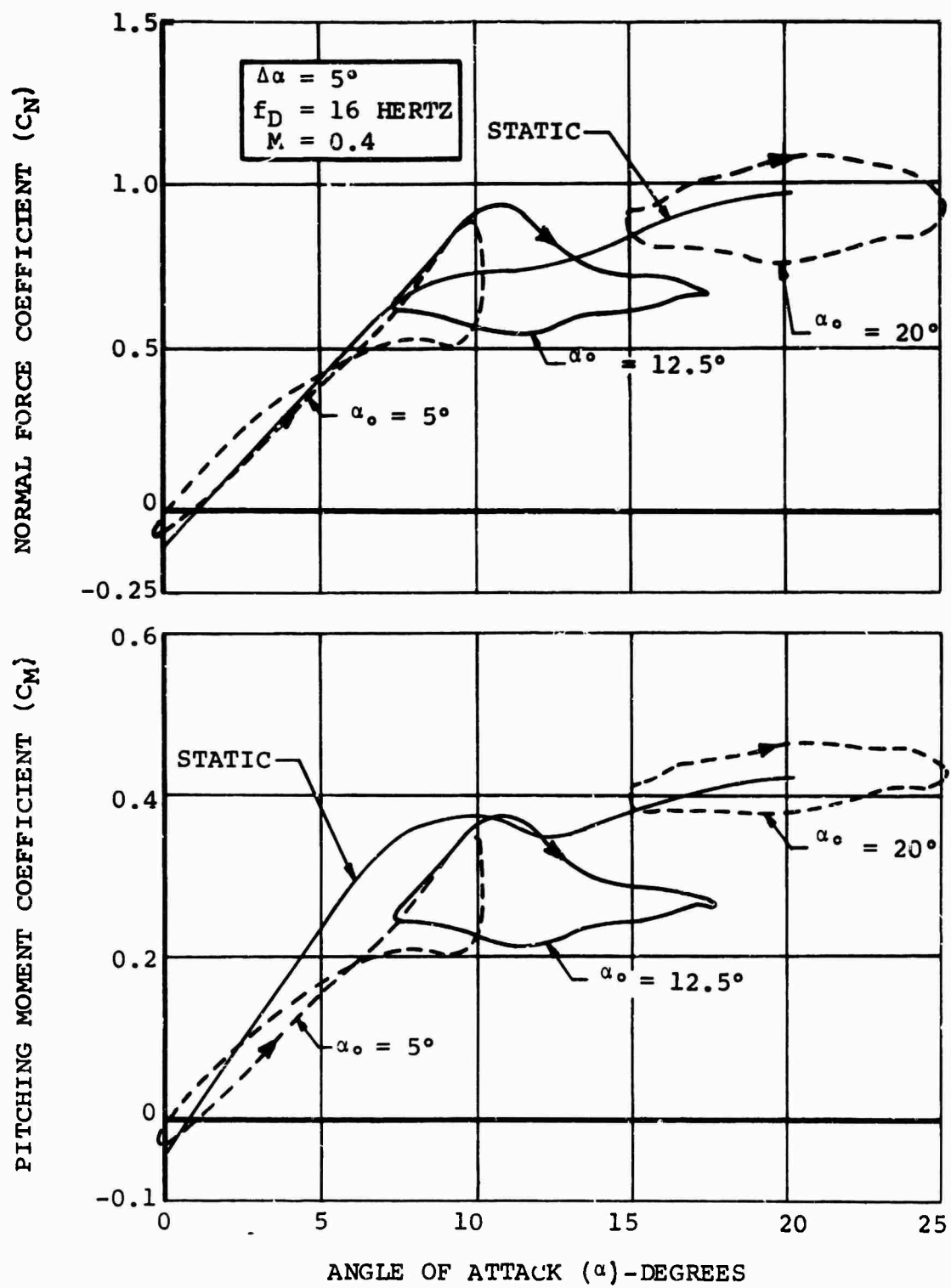


FIGURE 8. TYPICAL PITCH OSCILLATION DATA FOR THE V23010-1.58 AIRFOIL IN REVERSE FLOW

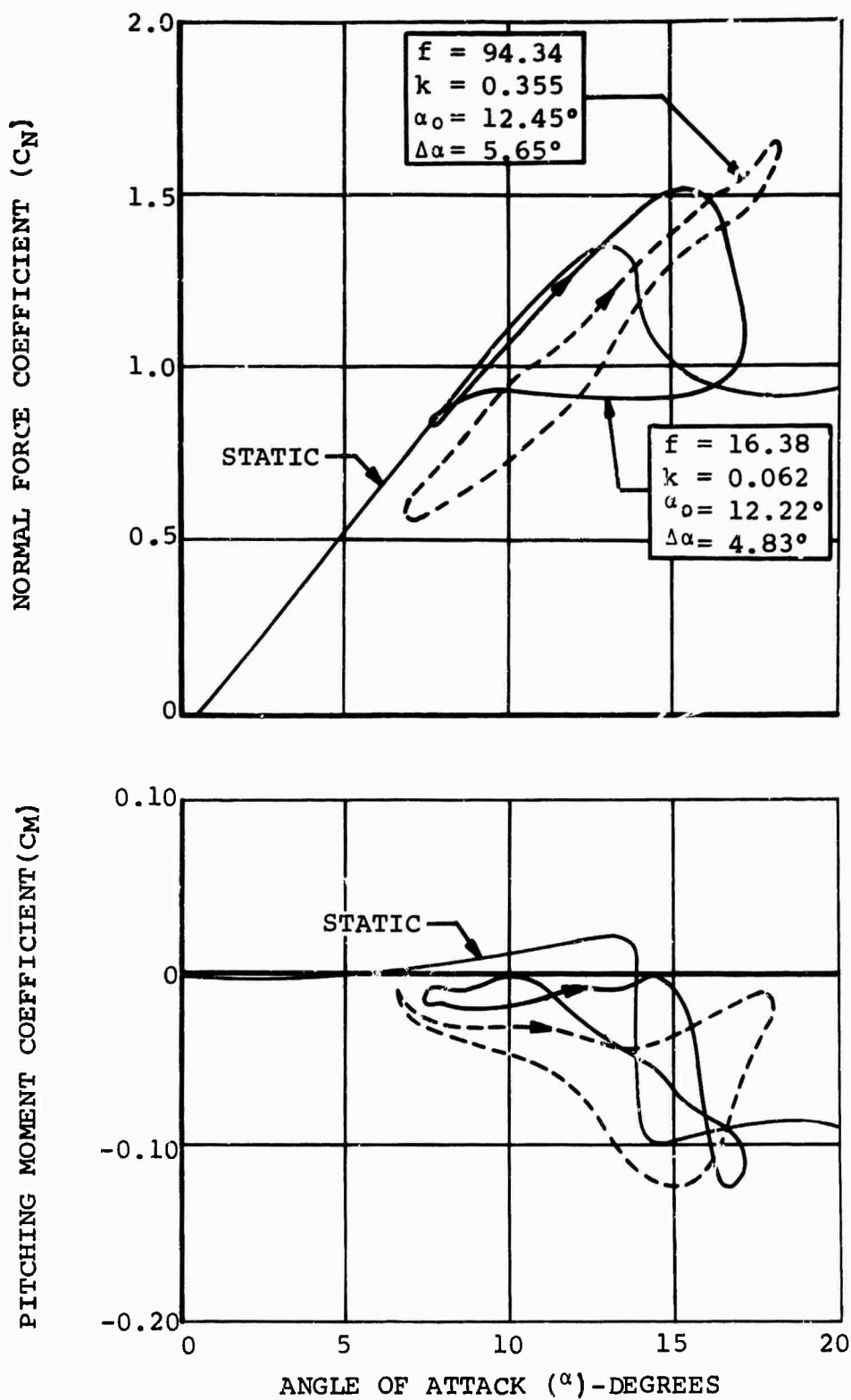


FIGURE 9. EFFECT OF FREQUENCY ON DYNAMIC C_N , C_M , AT $M=0.4$ FOR THE V23010-1.58 AIRFOIL IN FORWARD FLOW

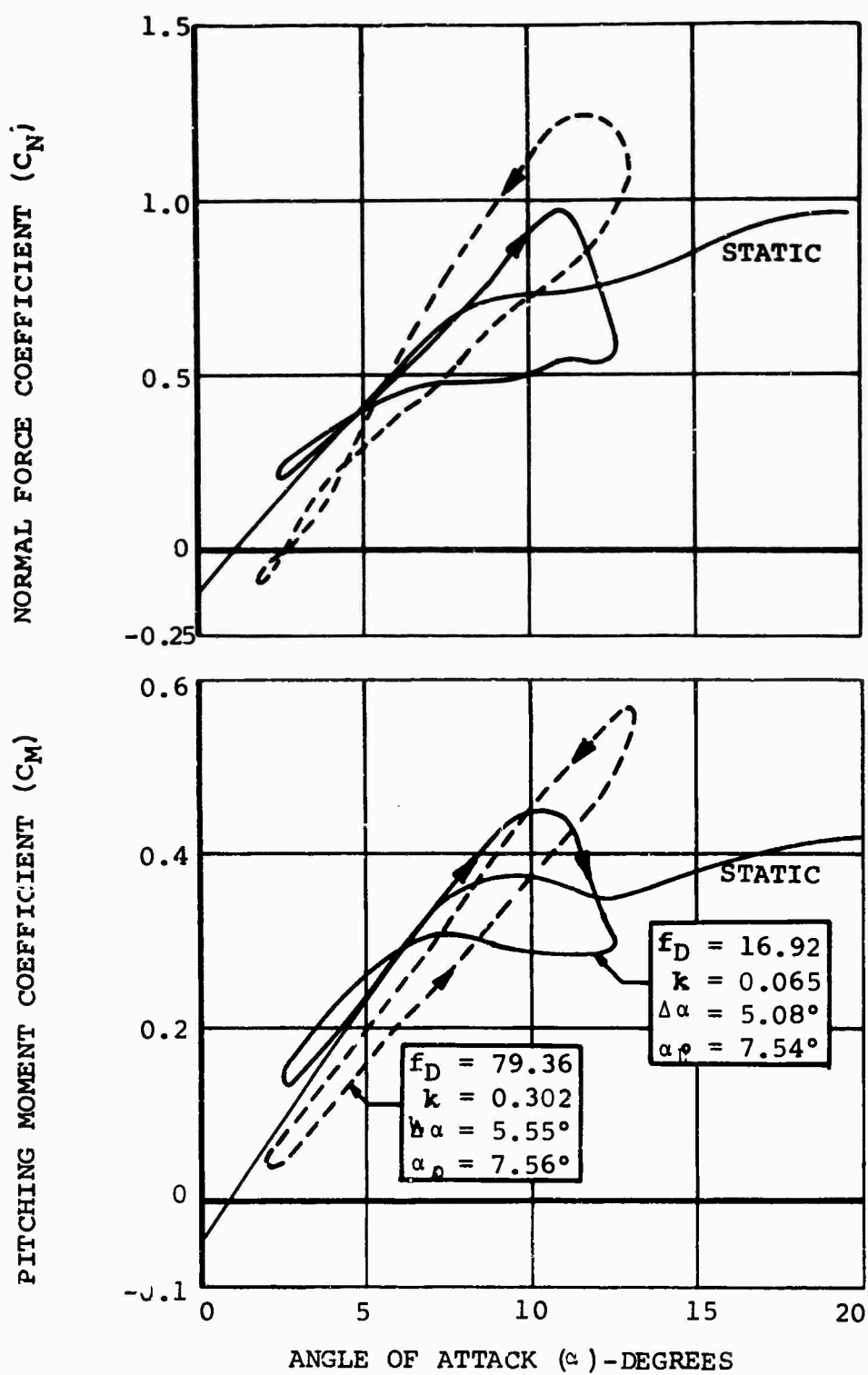


FIGURE 10. EFFECT OF FREQUENCY ON DYNAMIC C_N , C_M , AT $M=0.4$ FOR THE V23010-1.58 AIRFOIL IN REVERSE FLOW

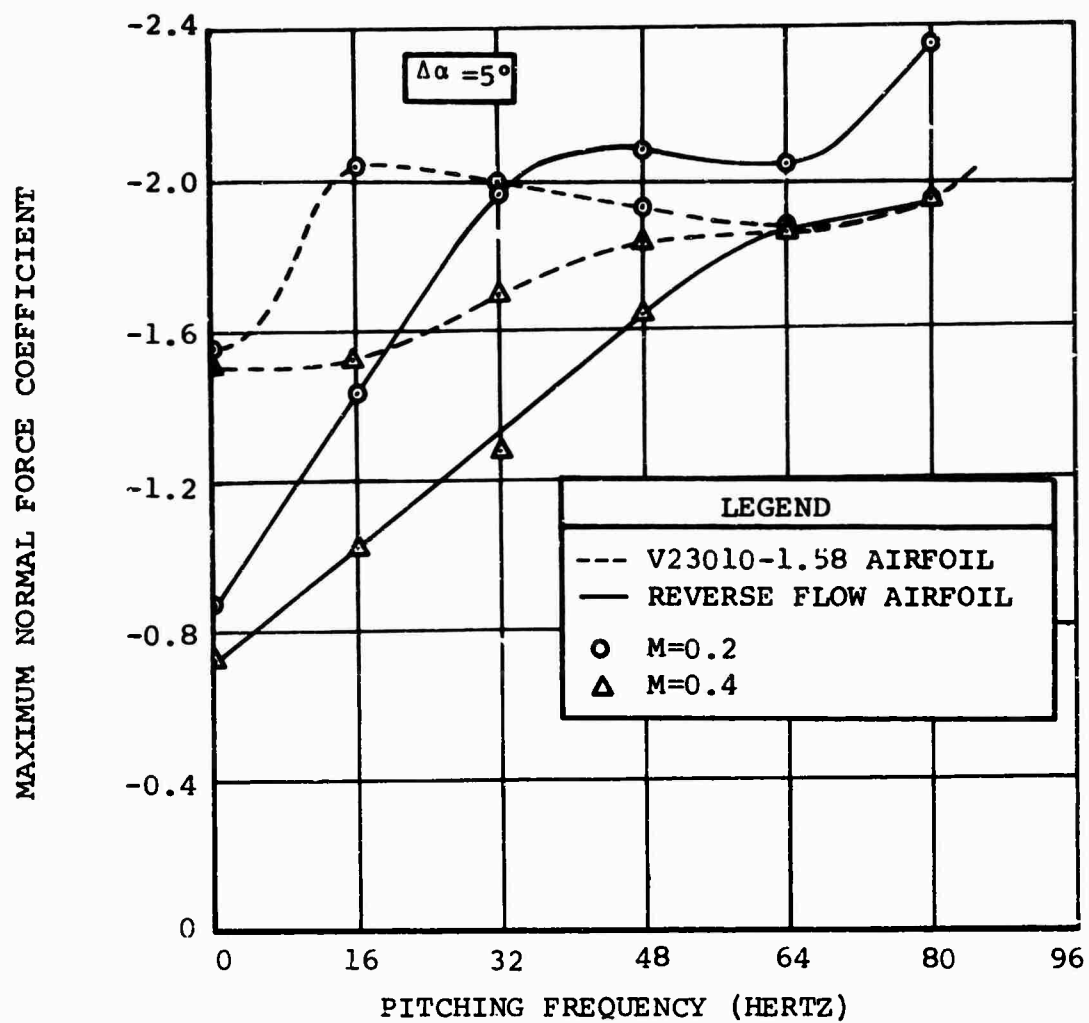


FIGURE 11. EFFECT OF PITCHING FREQUENCY ON NORMAL FORCE, V23010-1.58 AIRFOIL

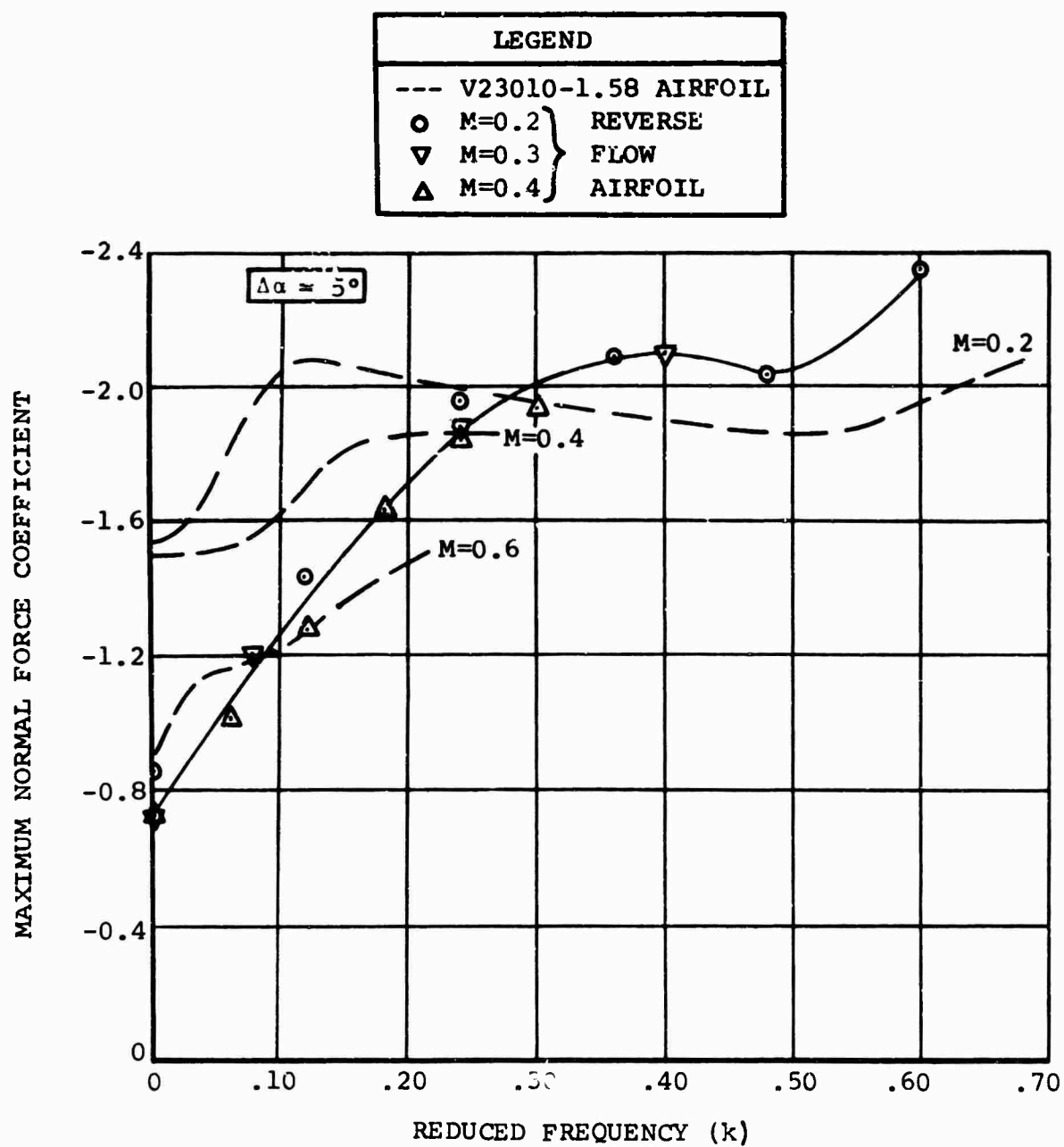


FIGURE 12. EFFECT OF REDUCED FREQUENCY ON NORMAL FORCE, V23010-1.58 AIRFOIL

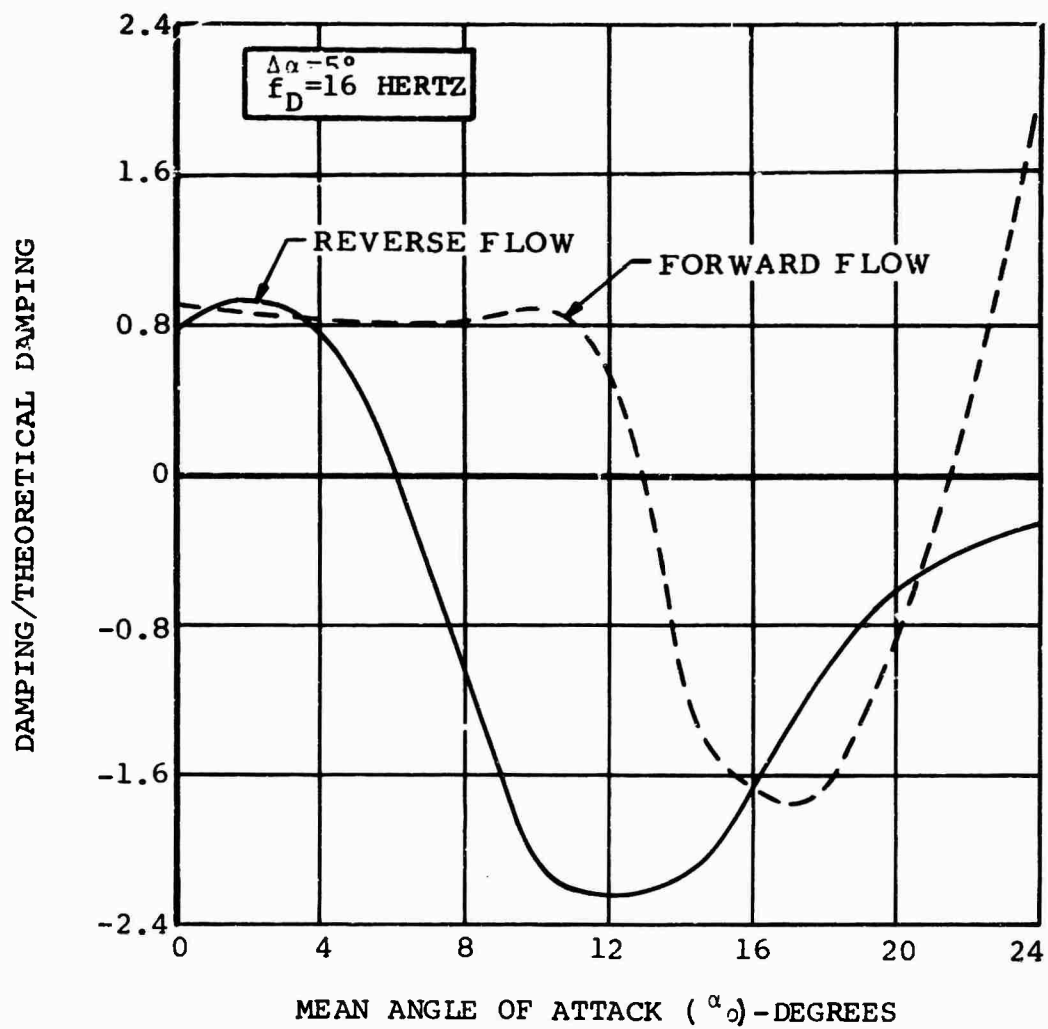


FIGURE 13. COMPARISON OF AERODYNAMIC DAMPING FOR THE VERTOL 23010-1.58 AIRFOIL IN FORWARD AND REVERSE FLOW, $M=0.2$

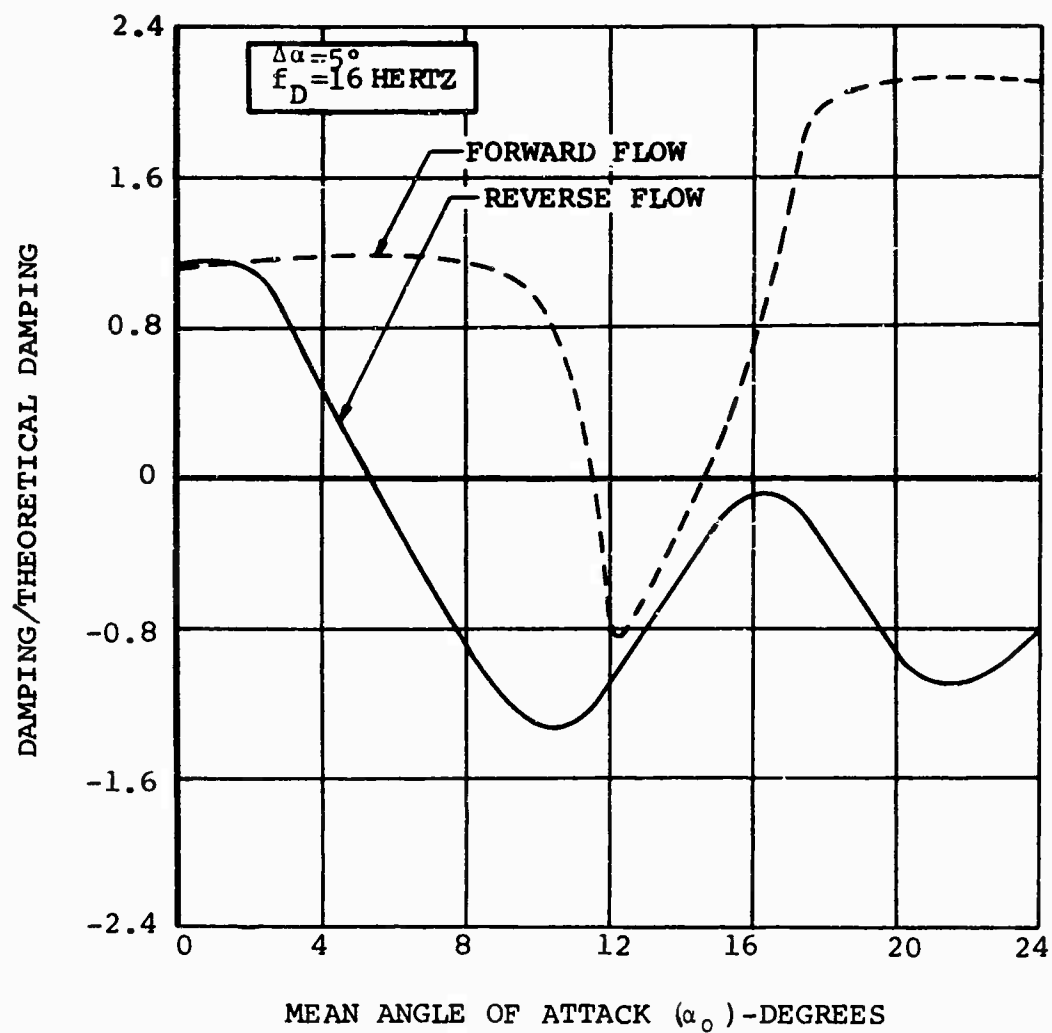


FIGURE 14a. COMPARISON OF AERODYNAMIC DAMPING
FOR THE VERTOL 23010-1.58 AIRFOIL IN
FORWARD AND REVERSE FLOW, $M=0.4$

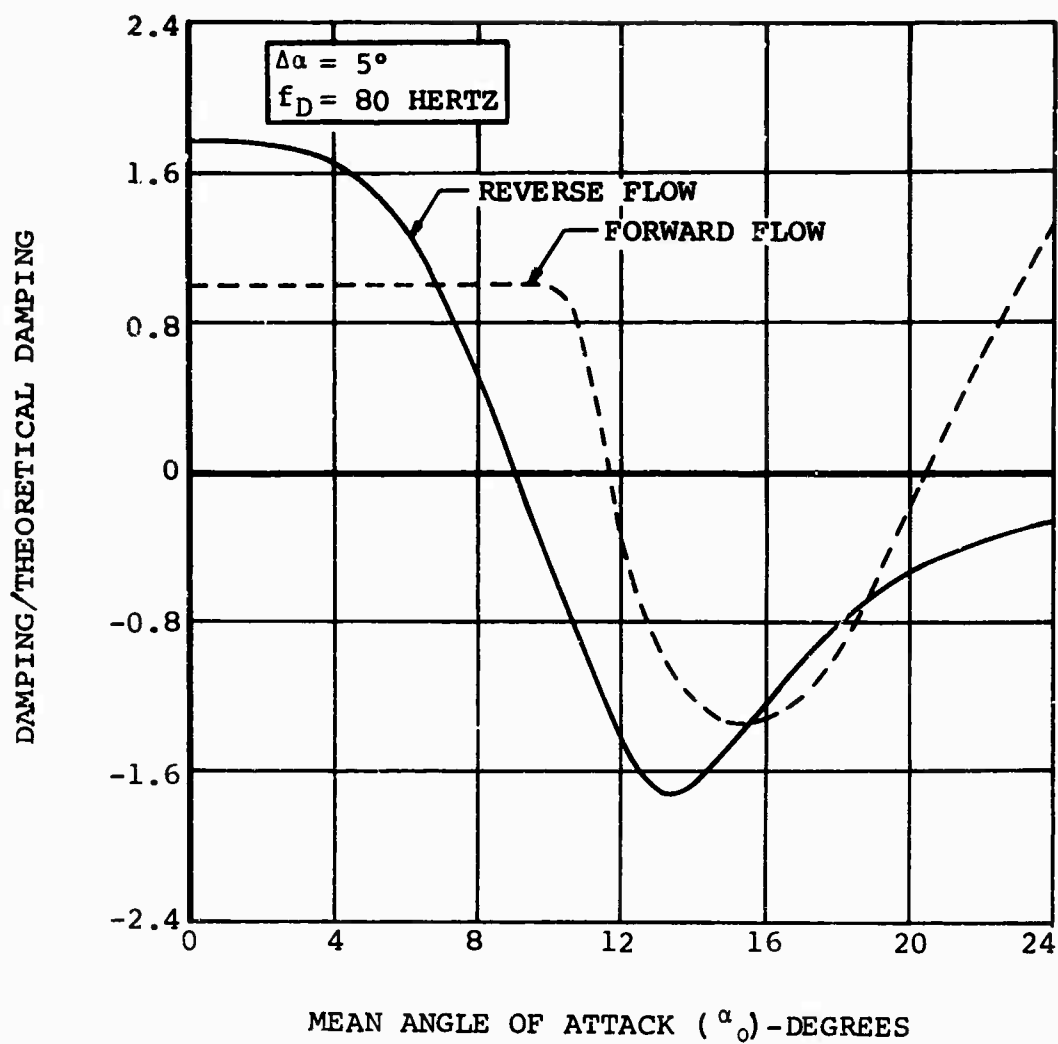


FIGURE 14b. COMPARISON OF AERODYNAMIC DAMPING FOR THE VERTOL 23010-1.58 AIRFOIL IN FORWARD AND REVERSE FLOW, $M=0.4$

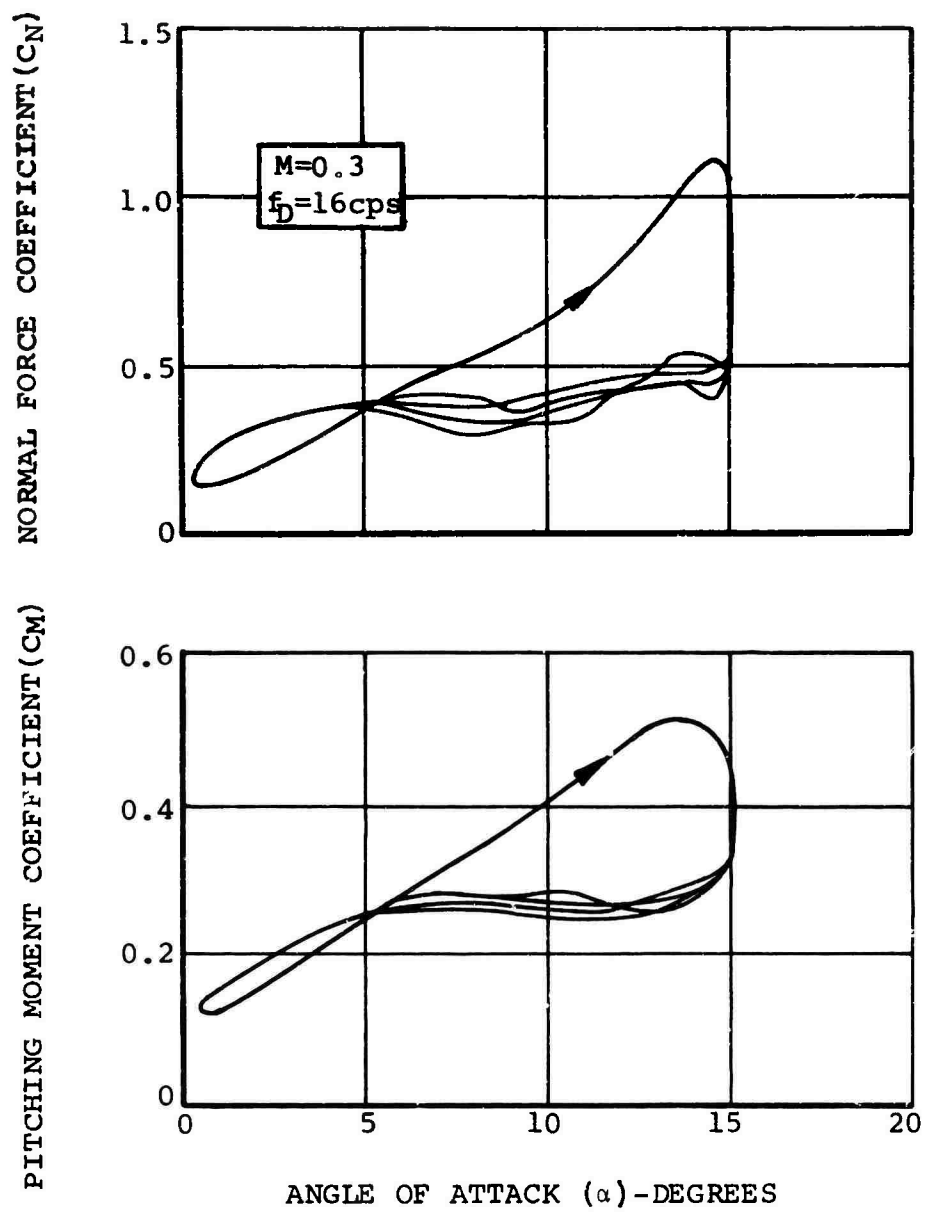


FIGURE 15. STALL RECOVERY VARIATION

DESIGN OF AIRFOILS FOR ROTORS

by

Dr. F. X. Wortmann, Professor, University of Stuttgart,
Germany and Consultant to Bell Helicopter Company and
Jan M. Drees, Chief, Flight Technology Section,
Bell Helicopter Company

ABSTRACT

Airfoil design methods have recently become available which permit the analytical optimization of performance at selected operating conditions with one airfoil. Given this capability, the helicopter designer can specify airfoil requirements in relation to the aircraft's performance and operation. In the first part of the paper, a paradox concerning the relation of hovering Figure of Merit to the blade-profile characteristics is presented and the importance of the maneuver and high-speed requirements in terms of airfoil design is analyzed.

In the second part, analytical design techniques for rotor airfoils are discussed in light of the requirements discussed in the first part. Methods for minimizing profile drag in hover and when the advancing tip operates at high Mach numbers are evaluated. Recent insights into the factors that determine the maximum lift coefficient when the Mach number of the retreating blade is moderate should also make it possible to increase the g-capabilities of rotors. Although the complexity of this task now precludes considering nonsteady, yawed, and three-dimensional effects, we believe that these new design approaches make possible some important advances in the state of the art.

Paper presented at the CAL/AVLABS 1969 Symposium on Aerodynamics of Rotary Wing and VTOL aircraft.

I. INTRODUCTION

It was with good foresight that the NACA 0012 profile was selected early in the development of the helicopter. As an all-around airfoil, it has served well. Aerodynamically, it is "forgiving." Structurally, it permits easy-to-manufacture designs with acceptable beam properties. It has proved to be a hard airfoil to dethrone.

NASA made a first valiant attempt to find an airfoil for helicopters that would show an improvement over the 0012 about 20 years ago by applying the then newly found principles of laminar flow to the design of a rotor blade. A specially designed full-scale rotor was built and tested on the Langley rotor tower. This development, reported in detail in NASA publications^{(1), (2)} did not mature into a flight-test program, although the test results were quite encouraging. Figure 1 indicates that the hovering profile power required was reduced by 15 to 20%. This reduction could be used to increase the payload, typically, by a similar percentage. It is believed that the difficulty of fabricating blades with the required close contours was one factor in discontinuing the project.

Recent years have brought renewed attempts to improve rotor-blade profiles. Leading-edge camber, or "droopsnoot," has been successfully introduced. This development proved to be a solid improvement over the 0012 airfoils. Its main feature is that $C_{L_{max}}$ is increased without adversely affecting any of the other characteristics. Figure 2 clearly shows its effect on the maximum g-capability of two Bell rotors as measured by flight tests.

Another recent and important development is the introduction of spanwise profile variation and its combination with plan-form variation. Thin-tipped blades and blade-tip sweep have markedly improved performance, as shown by Spivey⁽³⁾, mainly because the formation of shockwaves on the advancing-blade tip is delayed.

THRUST COEFFICIENT

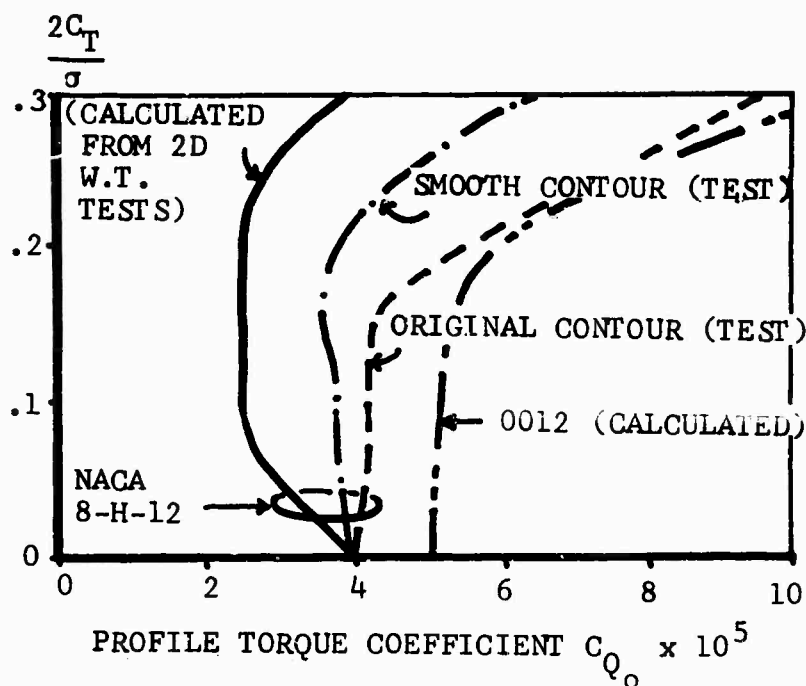


Figure 1. Results of Laminar Flow Rotor Test by NACA in 1954

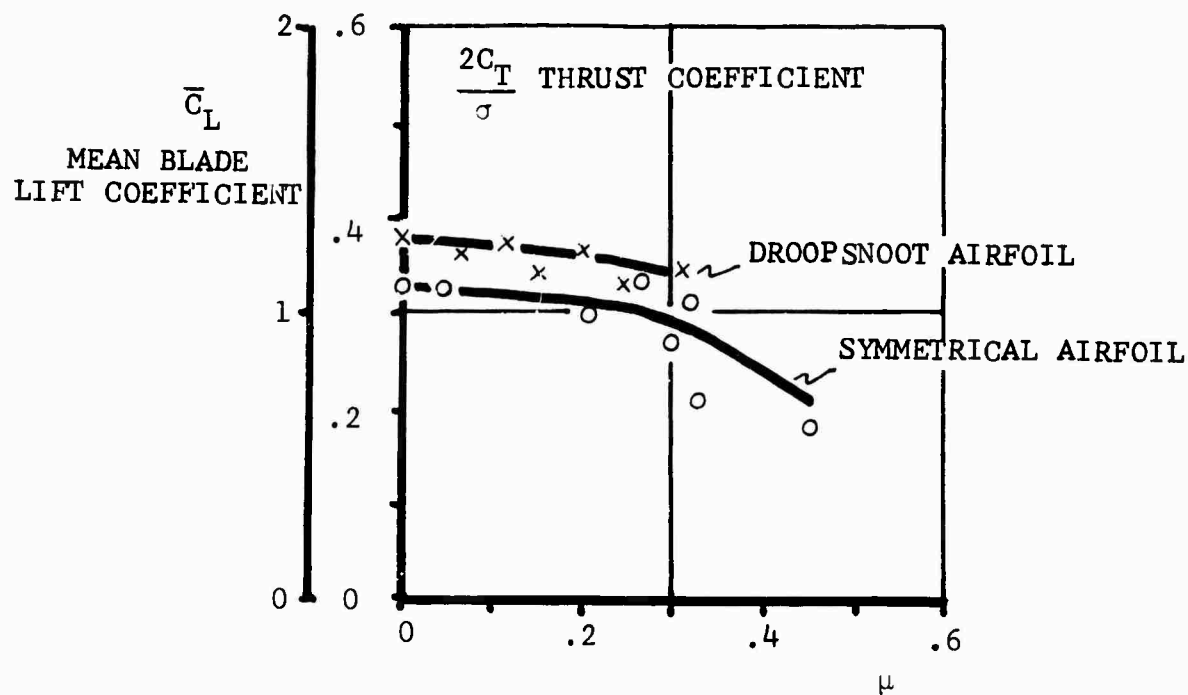


Figure 2. An Increase of 15 Percent in Maximum Rotor Thrust Capability is Realized by Application of a Droop-Snoot Profile

Rotor noise is simultaneously reduced, as discussed by Cox.⁽⁴⁾ The following table gives some test results that illustrate the order-of magnitude improvement.

9500 Lb SL Standard Day 815 Ft/Sec Tipspeed	Power Required	Flyover Noise Level at 200 Ft
UH-1D Standard-tip at 120 kt 0012	1020 hp	103 db
UH-1D Thin-tip 0006 at 120 kt with droopsnoot	940 hp	98 db
Difference	80 hp	5 db

These examples show that each airfoil development brought about improvements in one of three areas:

1. Low-drag profiles improve hover performance.
2. Droopsnoot profiles improve maneuvering capability.
3. Thin profiles improve high-speed performance.

Figure 3 shows these areas plotted for the combination of C_L and Mach number that are critical for the three corresponding flight conditions.

In contrast to the results of the previous approaches, it appears that we may improve rotor airfoils in all three areas simultaneously. We now have a better understanding of the requirements for advanced rotors, and more sophisticated analyses have been developed. The objective of this paper is to discuss these new techniques for designing profiles, after first evaluating the profile-design requirements as they relate to the three operating areas of Figure 3.

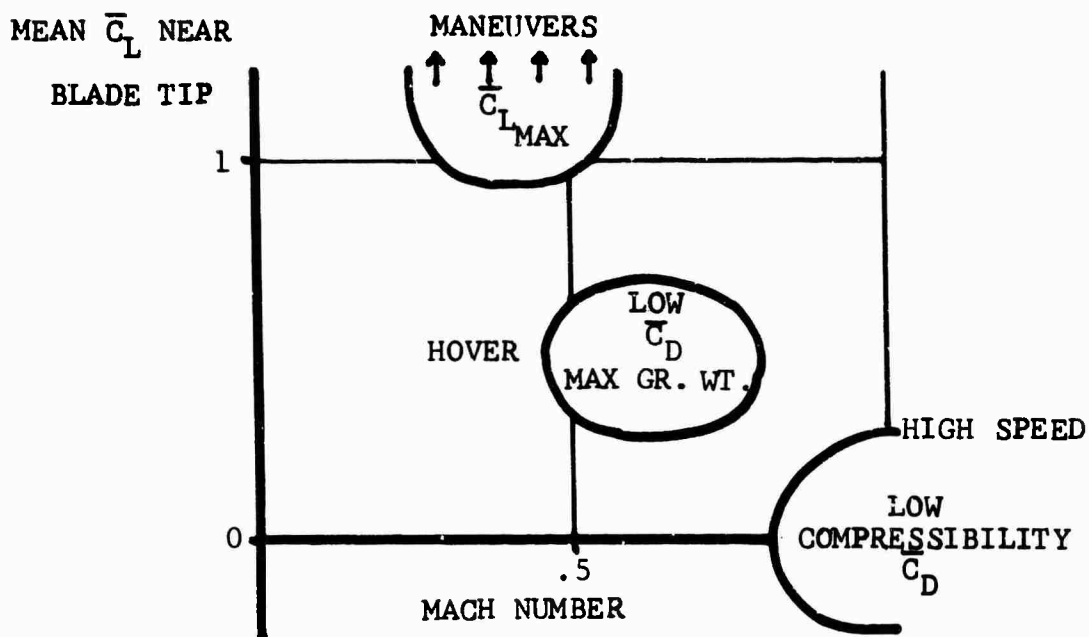


Figure 3. The Regions Critical for Helicopter Operations

Our approach is simplified despite the complexity of the task. The state of the art has not yet progressed sufficiently that nonsteady, yawed, and three-dimensional effects can be included in the profile-design analysis. Much of the necessary information is being developed in tests such as those of Tanner and Yaggy,⁽⁵⁾ Velkoff, Blaser, Jones,⁽⁶⁾ and others. Nevertheless, it is believed that the technique presented here will help to improve the efficiency of future rotary-wing aircraft.

II. AIRFOIL REQUIREMENTS

Before the airfoil designer can go to work he needs to know to what requirements he should design his new airfoil, and he has to know what features are most desired in case he cannot achieve all the goals simultaneously. This puts the burden on the rotor aerodynamicist, who is soon embarrassed by these questions. This

section of the paper attempts to define some of the desired features and to establish an order of importance, so that a set of requirements can be formulated.

a. Hovering Performance and the Figure of Merit Paradox

In most VTOL designs the operational efficiency of the aircraft is largely determined by the maximum weight that can be lifted off the ground with a given powerplant at the critical altitude and temperature. For that condition the rotor should operate as efficiently as possible: at its optimum Figure of Merit (M).

The Figure of Merit was defined a long time ago by C. Renard for the static thrust of propellers and is still in wide spread use for helicopter rotor analyses. Glauert⁽⁷⁾ and later Gessow and Meyers⁽⁸⁾ give a good discussion of its use. Yet anyone who has worked with it must have noticed that M depends on many factors, which may easily confuse the user. For example, M will usually be higher for high discloading rotors than for low discloading rotors, yet the high discloading rotor will lift less per horsepower. Much insight can be gained by expanding the well known expression for M by including the average blade profile coefficients \bar{C}_L and \bar{C}_D . Following the equations and notations of Reference (8):

$$\bar{C}_L = 6 \frac{C_T}{\sigma}$$

and, with a factor 1.15 to account for nonuniform inflow and swirl, we find

$$\bar{C}_D = \delta = \frac{8}{\sigma} \left[C_P - 1.15 \frac{(C_T)^{3/2}}{\sqrt{2}} \right]$$

The Figure of Merit can now be expressed two ways:

$$M = \frac{1}{\sqrt{2}} \frac{(C_T)^{3/2}}{C_P} = \frac{1}{1.15 + \frac{2.6}{\frac{(\bar{C}_L)^{3/2}}{\bar{C}_D} \sqrt{\sigma}}} \quad (1)$$

or

$$M = \frac{1}{1.15 + \frac{2.6}{\frac{\bar{C}_L}{\bar{C}_D} \sqrt{6C_T}}} \quad (2)$$

This leads to a paradox that the Figure of Merit is optimum at two different points of the $\bar{C}_L - \bar{C}_D$ blade polar:

- 1) With the solidity constant, M is optimum when $\frac{(\bar{C}_L)^{3/2}}{\bar{C}_D}$ is maximum.
- 2) With constant C_T , M is optimum, when $\frac{\bar{C}_L}{\bar{C}_D}$ is maximum.

Figure 4 shows these points for a typical rotor, based on flight test data.

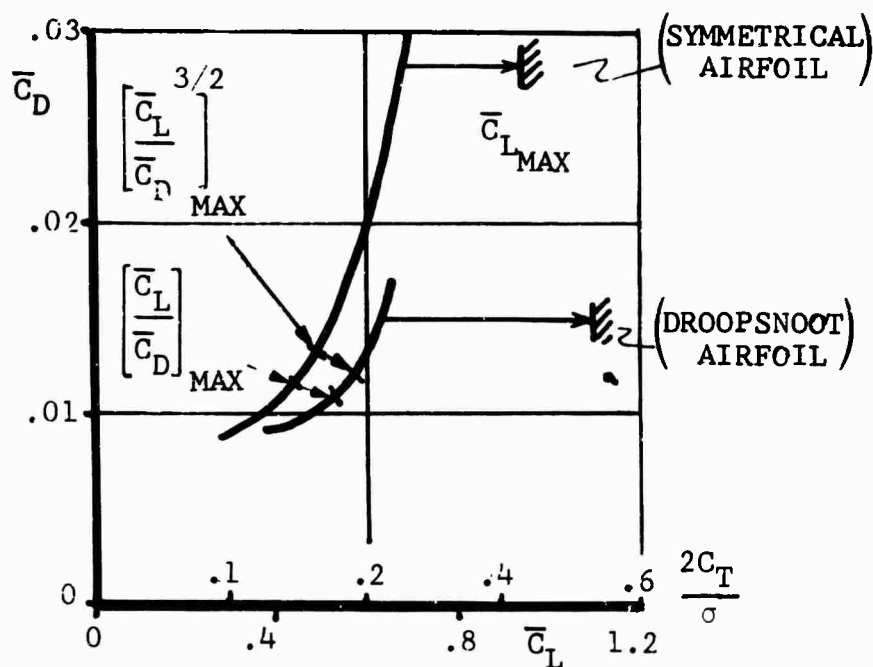


Figure 4. Average $\bar{C}_L - \bar{C}_D$ Rotor Blade Coefficients Determined by Hovering Flight Tests

The implication of the above finding is, that for a given rotor (σ constant) the lowest power to sustain a given weight will be found when rpm is reduced until the average blade \bar{C}_L is reached so that $\bar{C}_L^{3/2} / \bar{C}_D$ is maximum. However, if one is free to change the solidity, but not the rpm (C_T constant), then chord should be added until \bar{C}_L is lowered to the point where \bar{C}_L / \bar{C}_D is maximum. These two steps, an rpm change followed by a chord change, can be repeated until the rpm, from considerations such as transmission limits, etc., cannot be further reduced. The last step then will be to increase chord. This, of course is a very important conclusion for designing a blade profile, because now we know that we not only must operate at the \bar{C}_L for $[\bar{C}_L / \bar{C}_D]_{\max}$, but, with equation (2), the value of this ratio must be increased as much as possible. The optimum situation for a given C_L distribution along the span is, of course, obtained if $[\bar{C}_L / \bar{C}_D]_{\max}$ is reached simultaneously all along the blade span.

b. Maximum g-Capability Related to $C_{L_{\max}}$ - Mach Number Relationship

The maximum g capability of a rotor is most conveniently expressed by the $\frac{2C_T}{\sigma}$ vs μ relationship as shown in Figure 2. Since $\frac{\bar{C}_T}{\sigma} = \frac{1}{6} \bar{C}_L$, as was mentioned earlier, the connection between the maximum rotor thrust and the average blade $\bar{C}_{L_{\max}}$ is evident. Other factors which should not be overlooked, such as stall flutter and severe vibrations or rotor loads, ⁽⁹⁾ may tend to lower the g-capability at high advance ratios. By and large, however, these phenomena are also interrelated with the maximum blade lift coefficient and its dependence on the local Mach number.

A simple calculation may reveal an important characteristic of the $\frac{2C_T}{\sigma} - \mu$ relationship. By averaging the maximum attainable

blade lift at azimuth positions 0, 90, 180 and 270 degrees in a 3/4R blade analysis, and keeping the rolling moment zero by reducing the lift on the advancing blade to that of the retreating blade, one finds (valid only for $\mu < .75$):

$$\bar{C}_{L_{\max}} = .89 \left[\left(\frac{3}{4}\right)^2 C_{L_{\max}}_{\psi=0^\circ} + \left(\frac{3}{4} - \mu\right)^2 C_{L_{\max}}_{\psi=270^\circ} \right] \quad (3)$$

This expression is interesting since it takes into account the change of $C_{L_{\max}}$ with Mach number, ($C_{L_{\max}}$ is the local blade maximum lift coefficient; $\bar{C}_{L_{\max}}$ is the maximum average blade lift coefficient).

Figure 5 shows the results for three cases using a rotating tip Mach number of .7 and three different airfoils with different $C_{L_{\max}} - M$ characteristics. One airfoil (a) follows

closely the familiar 0012 pattern, the second airfoil (b) represents an airfoil designed for high Mach number operation typical for fixed wing use, and the third airfoil (c) illustrates what may be a more optimum airfoil for helicopter rotors.

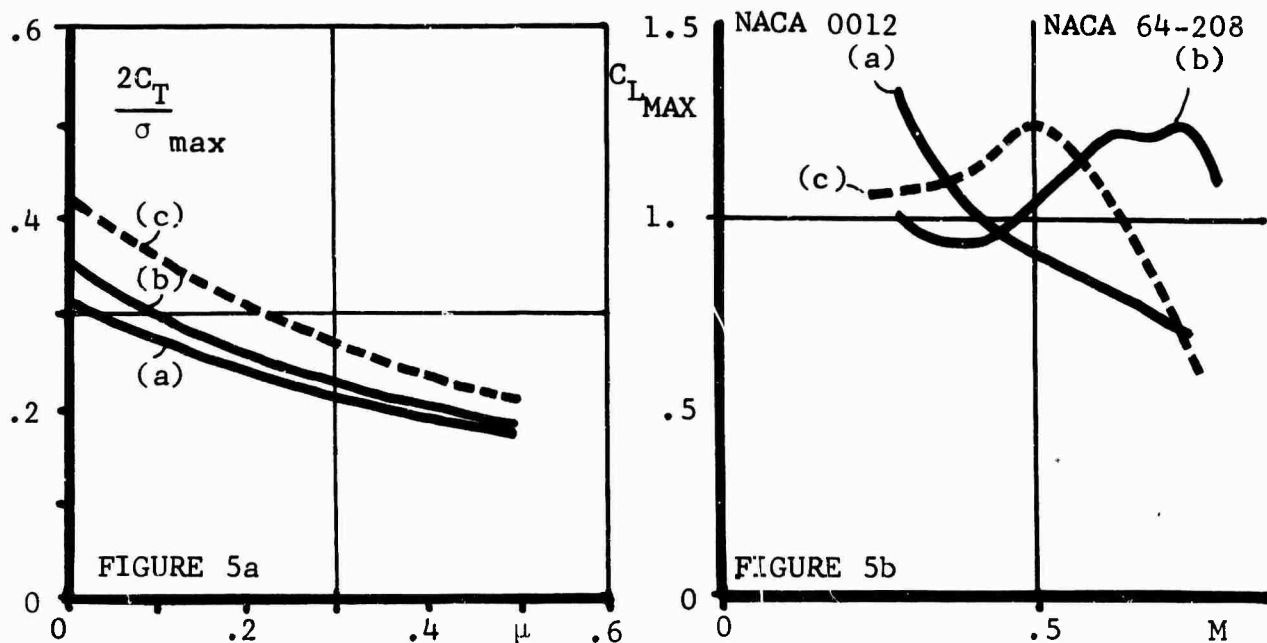


Figure 5.—The Effect of Airfoil $C_{L_{\max}} - M$ Relationship on the Maximum Thrust Coefficient $2C_T/\sigma - \mu$ Relation

It is concluded from Figure 5 that it is advantageous to increase $C_{L_{\max}}$ in the Mach number range of .4 to .6. It is also interesting to note that it follows from equation (3) that at high advance ratios the $C_{L_{\max \psi=0^\circ}}$ is the most important factor: the Mach numbers in that position are equal to those of the hovering blade. The retreating blade $C_{L_{\max \psi=270^\circ}}$ is probably most important in the medium speed range where the dynamic pressure on that side is still high enough to cause blade buffeting. Below a Mach number of .4 $C_{L_{\max}}$ becomes decreasingly important. The use of wings, naturally, will alleviate the high advance ratio maneuver burden for the rotor, but is ineffective at advance ratios below approximately .25. The best airfoil selection for a rotor is one that just reaches $\bar{C}_{L_{\max}}$ at the maximum flight load factor at the required altitude, temperature and gross weight and operates at a \bar{C}_L for maximum \bar{C}_L / \bar{C}_D in hover under the most critical condition.

c. High Forward Speed Advancing Tip Drag

With the hovering optimization and g-capability taken care of, the high-speed environment of the advancing side becomes the next most important criterion for the design of the rotor airfoil. Of course, this is only of consequence for the tip of the rotor blade.

Tip aerodynamics was discussed in detail by Spivey.⁽³⁾ It is known that the tip angle of attack on the advancing side on high speed helicopters is near zero and may even become negative. Figure 6 shows the typical behavior of a cambered airfoil at varying Mach numbers. The important point is the shift of C_L for $C_{D_{\min}}$ to lower and even negative values with increasing Mach numbers. This suggests the possibility of combining in one cambered airfoil good transonic characteristics with low drag at hover angles of attack and high $C_{L_{\max}}$ values for maneuvers.

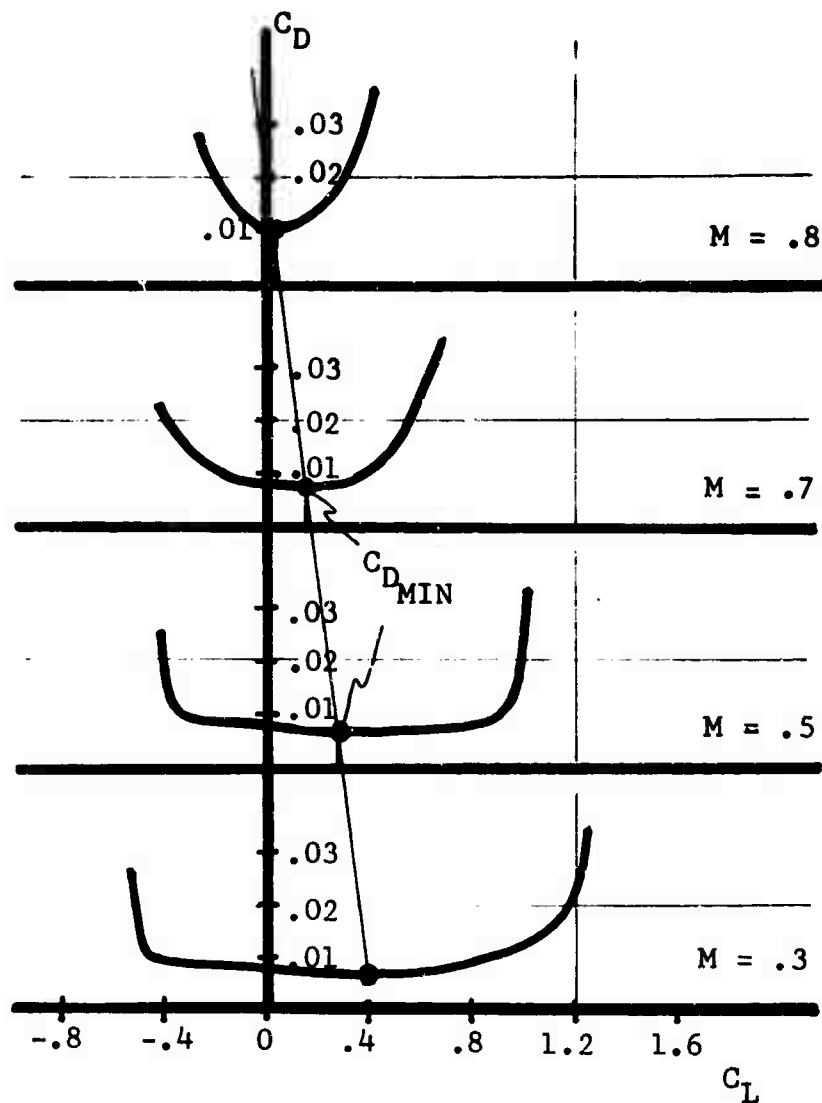


Figure 6. $C_L - C_D$ Relations at Various Mach Numbers Show Shift of C_L for $C_{D_{min}}$

d. Airfoil Design Goals

Based on the foregoing study typical design goals are outlined for the outboard sections of an advanced rotor in the next table.

Hover	$\left[\frac{C_L}{C_D} \right]_{\max}$	≈ 100	at $M \approx .6$ and $C_L \approx .65$
Maneuver	$C_{L_{\max}}$	≈ 1.25	$M \approx .5$
Advancing	C_D	≈ 0.02	at $M \approx .8$ and $C_L \approx 0$

For the inboard sections the most important condition is to keep hover $\left[\frac{C_L}{C_D} \right]_{\max}$ at $C_L \approx .65$ as high as possible at the local Mach number. The pitching moments should be kept small.

III. AIRFOIL DESIGN METHODS

a. Historical Review of Available Analytical Tools

In the preceding part of the paper, the most desirable qualities of rotor airfoils are specified. Before we discuss how to meet these conditions, we should have a short look at the methods which enable us to design airfoils for specific requirements. For lower Mach numbers we can use the powerful methods of potential theory or the singularity methods to calculate the airfoil form for a prescribed pressure distribution or vice versa. If we combine this ability with a boundary layer calculation we get a theoretical drag polar. A more important possibility is to feed back boundary layer results into the design procedure and to optimize the pressure distributions in accordance with the design goals.⁽¹⁰⁾ In the past some improved laminar airfoils which are now widely used for most modern sailplanes, were developed in this way.⁽¹¹⁾ These airfoils operate in a Reynolds number range of $0.5 \cdot 10^6 < Re < 3 \cdot 10^6$. Design capabilities can now be expanded to optimize the pressure distribution for airfoils with prescribed flap deflections.⁽¹²⁾ The progress which has been made in the last decade with respect to the calculation of turbulent boundary layers⁽¹³⁾ gives, together with sensible criteria for transition, reasonable accuracy in the prediction of airfoil drag at lower Mach numbers.⁽¹⁴⁾

The next step was a simulation of the wake by an equivalent lift-free body⁽¹⁵⁾ which forms, together with the boundary layer displacement, a "fluid" airfoil and yields a lift value including viscosity effects. If the turbulent boundary layer separates, the flow field between separation and trailing edge can be replaced by a kind of split flap with a flap angle which yields a nearly constant pressure along the separated region.⁽¹⁶⁾ These steps are illustrated in Figure 7. Calculations of the so-called "trailing edge" and "leading edge" stall should be possible, if the behavior of the laminar separation bubble could be described reliably.

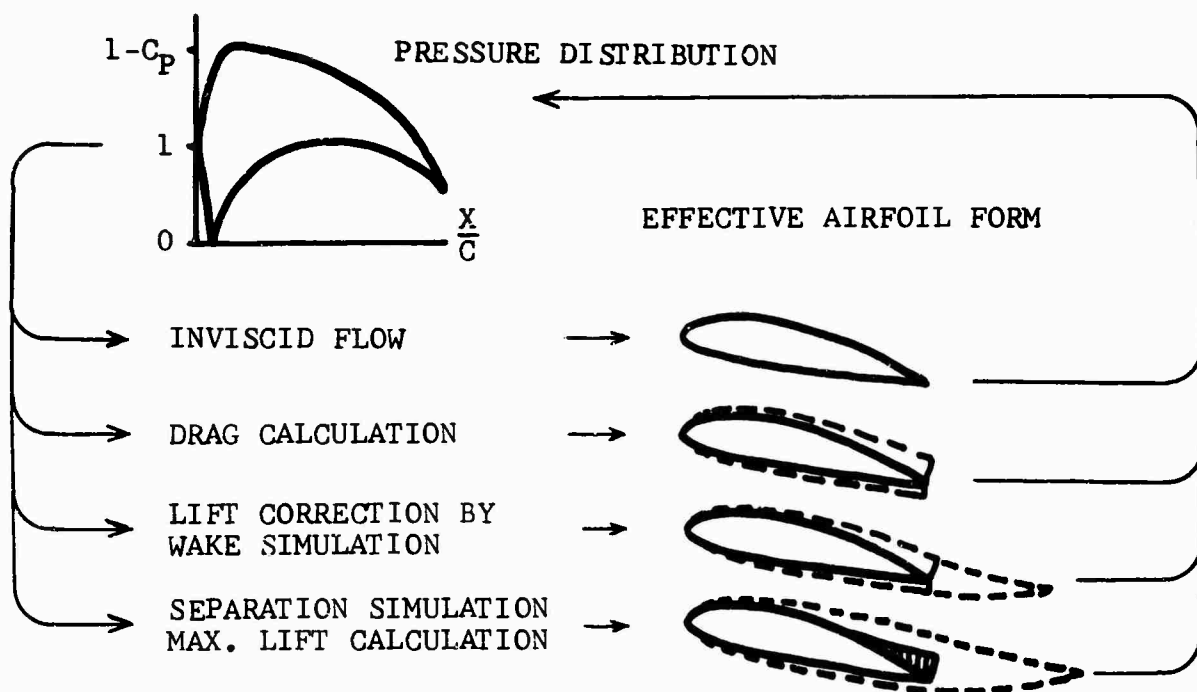


Figure 7.—Iterations to Obtain Desired Pressure Distribution and Airfoil Forms

For higher Mach numbers the main problem is the calculation of pressure distributions. Very recent progress makes it possible to improve the similarity rules and to transform the

incompressible solution into the compressible one with local Mach numbers of nearly 1.0.^{(17),(18)} From this might follow a procedure for optimizing a "subcritical" pressure distribution. If the Mach number is high enough to develop a local supersonic field the empirical method given by Sinnot⁽¹⁹⁾ often allows the calculation of pressure distribution, including shocks. Besides the Mach divergence number, one gets information about lift and pitching moments, and the buffeting boundary in this range. However, the method cannot be applied to higher angles of attack or to the so-called "peaky" distribution.

The quality "peaky" means a favorable reflection pattern of expansion and compression waves in the supersonic field, which leads to some extent to an isentropic recompression. The recompression in front of the shock allows, for a given shock strength, higher local Mach numbers and lower pressures in the supersonic field.⁽²⁰⁾ Both the formation of expansion waves and their reflection as compression waves at the sonic line depend on the combined effect of airfoil form and pressure distribution. Experimental evidence tells us that the quality "peaky" can be characterized by a special plot of the pressure distribution which includes some influence of the airfoil form.⁽²¹⁾ Figure 8 shows an inclined airfoil and the incompressible pressure distribution projected in the free-stream direction. The left part of the pressure loop is the suction loop and it is this part which is most influenced by the supersonic field. If the suction loop between the minimum pressure and the crest is "concave" as in the sketch, it is called "peaky."

b. Design Goals and Concepts

As explained in the first part of the paper, the airfoil for the conventional helicopter should have a high drag divergence and buffeting Mach number at about zero lift on the advancing blade and a high $C_{L_{max}}$ at a Mach number of about 0.5 on the retreating

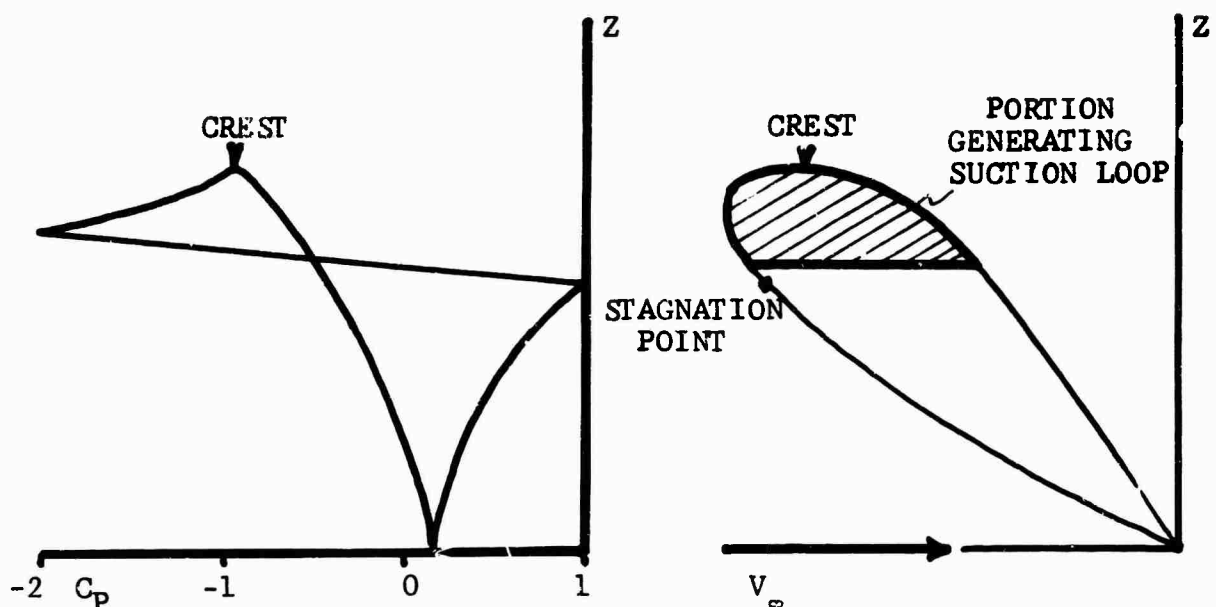


Figure 8. Drag and Suction Loop. Z = Airfoil Ordinates Projected in Free Stream Direction.

blade. For the hover mode a high glide ratio, i.e., low drag is needed at lift coefficients and Mach numbers of up to about 0.65. Finally all this has to be accomplished with a low pitching moment. Obviously these requirements are not entirely compatible. In order to find the best compromise, some of the basic requirements for meeting the design goals may be considered.

1. High drag divergence Mach number at low C_L (high forward velocity) - Usually a symmetrical airfoil has a higher drag divergence Mach number than its cambered counterpart at low C_L , but because of the high lift requirement we would like to use some sort of camber. The negative angle of incidence necessary for $C_L \approx 0$ could reduce the upper side velocities to values as low as for the symmetrical airfoil, but inevitably produces pronounced velocity peaks on the lower side of the nose of the cambered airfoil. Here the only way out is the

peaky effect. Figure 9 illustrates the advantage of this effect. In the left part the pressure loops of the symmetrical NACA 64A010 and the cambered 64A410, which has an "ideal" lift coefficient of 0.4, are given, and in the right part, the drag polars at $M_\infty = 0.87$, taken from Reference 20.

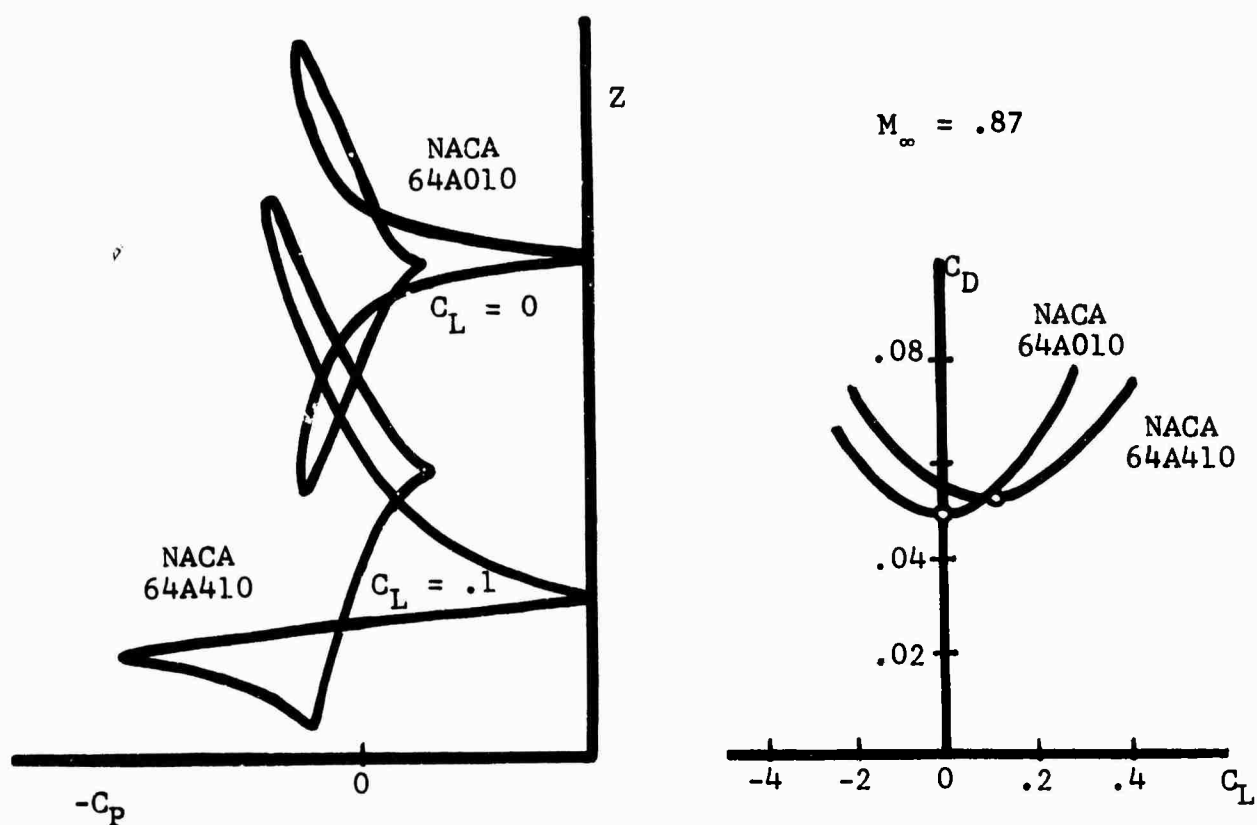


Figure 9. Example of a Peaky Suction Loop on a Cambered Airfoil at Low Lift Coefficient

The suction loop of the lower side of the cambered airfoil is obviously "peaky" and despite the high velocities associated with low C_p values, its drag at high Mach numbers and $C_L = 0.1$ is for

all practical purposes, as low as on the symmetrical airfoil. Therefore, a careful design of the lower side with respect to a peaky distribution opens the door to introduce camber without adversely affecting the transonic drag at low lift coefficient values.

2. Low drag at C_L and $M_\infty < 0.6$ (hover) - With some sort of camber this case is usually completely subsonic and the problem of drag reduction reduces to the well known principle of delaying the transition and controlling the turbulent boundary layer in a favorable way,⁽¹⁰⁾ as long as this is compatible with other requirements. It is worthwhile to mention that the concept of laminar flow on a helicopter blade is very feasible because the Reynolds numbers are low enough to maintain laminar flow even for skewed blades (values between $2 \cdot 10^6 < Re < 10 \cdot 10^6$) and as shown by Tanner⁽⁵⁾ the roughness by erosion does not easily destroy the laminar boundary layer. However, surface irregularities must be avoided in the production process.

3. High $C_{L_{max}}$ at $M_\infty \approx 0.5$ (maneuvers) - It is not really the $C_{L_{max}}$ which counts but the highest lift combined with the requirements for a low pitching moment. In some respects the high C_L may prove the key problem, and here we encounter the complete spectrum of complications: laminar separation bubbles, local supersonic fields, strong adverse pressure gradients, shock-induced separation and finally the interaction of each of these effects. In the following, this complicated subject is discussed in detail.

c. Factors Determining $C_{L_{max}}$

From test experience we learn that the $C_{L_{max}}$ is a strong function of the Mach number and the type of airfoil. As shown in

Figure 5b, we can roughly distinguish two classes of airfoils. For the first type (a) Mach number has mostly a detrimental influence, but the second type (b) demonstrates in a certain Mach number range a very beneficial effect from compressibility. At $M_\infty \approx 0.5$, i.e., within the most interesting Mach number range for helicopters, there exists a pronounced separation between the $C_{L_{\max}}$ peaks of

both classes. The first class has usually excellent high lift values at very low Mach numbers but with the $C_{L_{\max}}$ decreasing continuously above $M_\infty \approx 0.2$. These airfoils develop high suction peaks at the nose and the local supersonic field starts at very low Mach numbers. Now several facts come together to restrict the lift production. These airfoils are "non-peaky" types, which means there is practically no compression in front of the shock. With increasing Mach numbers the supersonic field cannot expand because the large subsonic pressure gradients behind the shock would require shock strength far beyond the boundary layer capabilities. Therefore, the shock fixed to the neighborhood of the subsonic pressure peak soon induces some type of boundary layer separation. Under high lift conditions this danger is further enhanced by the large pressure differences between shock and trailing edge, which exhaust the boundary layer even more. Finally to make the picture worse, due to the decreasing pressure before the shock, there is some probability that the shock interacts with a laminar boundary layer.

Therefore, it is understandable that the $C_{L_{\max}}(M_\infty)$ curve follows closely the curve of a constant local Mach number $M_L(M_\infty)$ $1.0 \div 1.1$. We can try to improve this type of airfoil by shifting the $M_L(M_\infty)$ constant lines to higher Mach numbers. In terms of airfoil design this means a reduced pressure peak for a certain lift coefficient and it is this principle which underlies the success

of the so-called "droop nose" airfoils in comparison with symmetrical airfoils.⁽²²⁾ However, further improvements in this way seem somewhat restricted, due to the high speed requirements especially for the thinner airfoil types now in use on advanced rotor designs.

In contrast to the aforementioned behavior, the second class of airfoils can show at $M_\infty > 0$, a very beneficial effect of the compressibility on maximum lift. An analysis of these airfoils, which usually have small nose radii and are often of the NACA 6-series, reveals that they all possess to some extent the peaky quality. Due to the now favorable reflection pattern inside the supersonic field the pressure behind the minimum pressure peak rises, which in turn reduces the shock strength and allows a rearward movement of the shock wave. This is shown in Figure 10. For three different Mach numbers at a constant angle of attack, the subsonic suction loops are indicated by the dotted line while the solid lines indicate the modification caused by the supersonic field. The lowest Mach number in (a) yields a shock position before the crest, in (b) at the crest, and in (c) behind the crest.

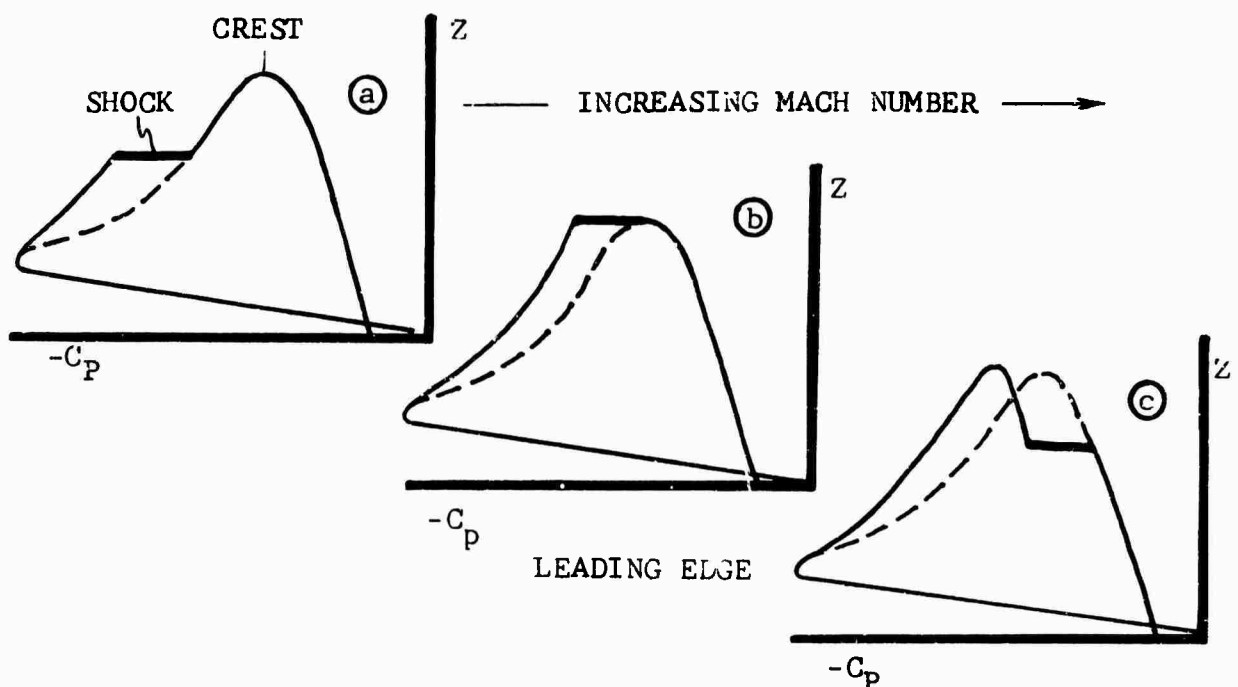


Figure 10. Development of Subsonic Peaky Suction Loop with Increasing Mach Numbers - (a) Shock in Front of the Crest. (b) Shock at the Crest. (c) Shock Behind the Crest.

This expansion of the local supersonic field with its low pressure is the main reason for the compressibility gain in $C_{L_{max}}$, which may increase as long as the shock boundary layer interaction is weak. The pressure recovery in front of the shock eliminates any laminar boundary layer. When the maximum local Mach number values are above $1.5 \div 1.6$, the shock induced separation begins and reduces the lift for higher Mach numbers in a similar way as with the first class of airfoils.

d. Placing of $C_{L_{max}}$ at $M \approx .5$

With respect to helicopter airfoil design, we need an answer for the most important question: how can we fill the valley between the two classes of airfoils and place $C_{L_{max}}$ at $M_{\infty} \approx 0.5$? In other words, can we shift the favorable lift increase to lower Mach numbers? In the absence of a theoretical method for calculating the pressure distribution of peaky airfoils at high angles of attack, we have to develop a tentative concept which should be backed by experimental data if possible. We can start with the variation of the suction loop for different angles of attack. The value of $C_{p_{min}}$, necessary to release the supersonic field for a given M_{∞} , is extremely sensitive to changes of angle of attack, whereas the pressure at crest changes only slowly. Therefore there exists only one angle of attack which yields an optimum reflection pattern and allows, for the optimum Mach number the largest expansion of the supersonic field without serious boundary layer interaction. Evaluation of pressure distributions, for example for the NACA 64A410,⁽²¹⁾ reveals that the optimum shock position for the optimum $C_{L_{max}}$ is slightly behind the crest. If we accept this concept, the position of the crest on the C_p axis of the suction loop becomes the deciding point. At a low absolute value of $C_{p_{(crest)}}$ only a relatively low angle of attack

yields the optimum peaky distribution. A higher Mach number is needed to exploit this case. On the other hand a high absolute value of $C_{p_{(crest)}}$ yields an optimum peaky distribution at higher angles of attack, but in this case the necessary Mach numbers for the supersonic field are lower.

Figure 11a shows this development for three different airfoils very clearly: when the absolute value of $C_{p_{(crest)}}$ increases (at a constant C_L), the maximum in the $C_{L_{max}}(M_\infty)$ curve also shifts to the left in the same way. These airfoils are droop-nosed modifications of the NACA 0008 airfoil and have been tested by Bell Helicopter Company. The 0008 Mod 15 airfoil shows only a halt in the decreasing $C_{L_{max}}(M_\infty)$ curve which may be interpreted as a slightly beneficial effect of compressibility. Figure 11b shows the same fact perhaps more strikingly because the $C_{L_{max}}(M_\infty)$ curve for the airfoil FX 66-H-080 has a sharp pronounced maximum just at the right Mach number for helicopter rotors. It seems to be the only airfoil with this quality.

These results give evidence that, with the assumption of a peaky suction loop, the C_p value of the crest has a strong influence on the position of the maximum of $C_{L_{max}}$ as a function of M_∞ . This may prove to be a new design concept which should allow filling the void in the $C_{L_{max}}$ envelope near $M_\infty = 0.5$, which is especially important for the helicopter.

e. Compatibility

The design of a practical airfoil for the prescribed conditions is always a compromise between somewhat incompatible qualities, but this makes the problem challenging. Older airfoils like

Figure 11a

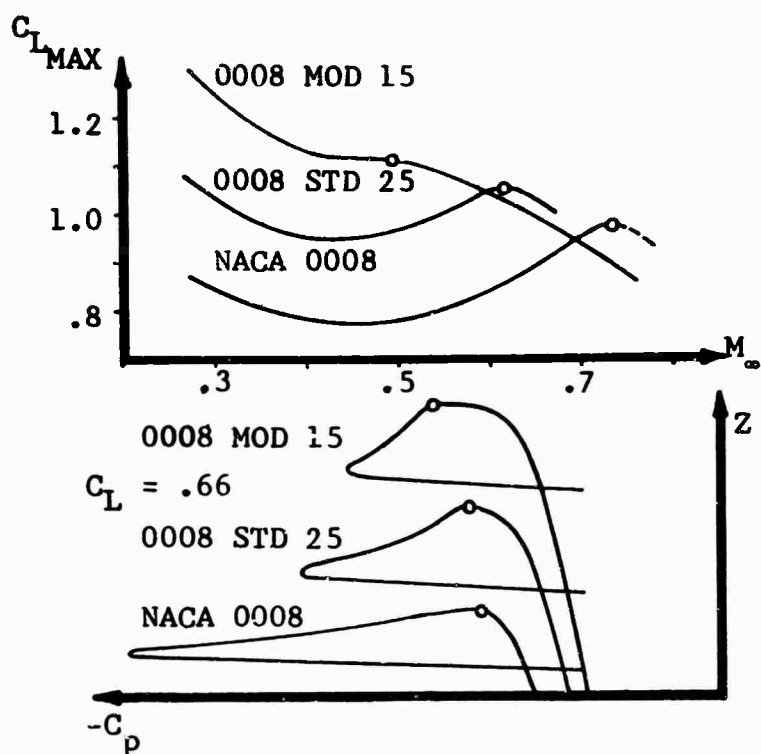


Figure 11b

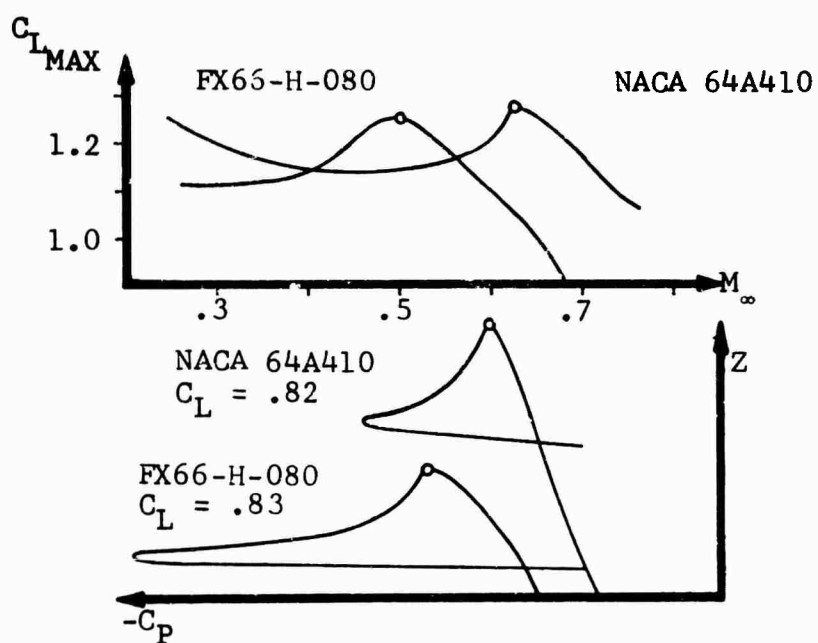


Figure 11a and 11b. Examples Showing Correlation Between The Pressures at the Crest and the Mach Number of the Peak of $C_{L\text{max}}$

the droop nose variety combine to some extent good high-speed characteristics with fair $C_{L_{\max}}$ values, but the glide ratio for

the hover mode could be higher. On the other hand a laminar airfoil with reflexed camber line, like the FX66-H-080, can combine high lift and very low drag for the hover mode, but has poor high-speed qualities.

With the help of the concepts developed above, present studies indicate that it is possible to design advanced rotor airfoils. These airfoils promise lower drag in hover and higher $C_{L_{\max}}$ at the right Mach numbers with practically no drag penalty in high speed flight. Test work is presently under way and carefully aimed wind-tunnel tests are planned.

IV. CONCLUSIONS

1. The airfoil requirements are analysed in terms of aircraft performance and operation. A paradox was found in determining the optimum hover figure of merit, which optimizes at either

$\left[\bar{C}_L^{3/2} / \bar{C}_D \right]_{\max}$ or $\left[\bar{C}_L / \bar{C}_D \right]_{\max}$ depending on whether solidity or

C_T is held constant. For practical rotor design, operating at $\left[\bar{C}_L / \bar{C}_D \right]_{\max}$ appears to be preferable. The airfoil design methods

for achieving this goal seem to be well in hand.

2. The maneuver requirements are shown to depend on the $C_{L_{\max}} - M$ relationship. The best results are obtained with airfoils for which $C_{L_{\max}}$ near the blade tip peaks out in the Mach number range from

.4 to .6. The analytical airfoil design methods for satisfying this condition are not available but new insight into this problem is advanced in this paper. Test results on existing airfoils relative

to the $C_{L_{max}}$ - M behavior could be explained. This opens the door for optimization of airfoils for rotors.

3. The high speed analyses indicate that low transonic drag coefficients are required at low values of C_L on the advancing side.

This offers the possibility of using cambered airfoils which have a "peaky" pressure distribution on the lower side.

4. Present studies indicate the possibility to combine into one airfoil design features that optimize the conditions in hover, maneuver, and high speed.

REFERENCES

1. Shaeffer, R. F. and Smith, H. A., Aerodynamic Characteristics of the NACA 8-H-12 Aerofoil Section at Six Reynolds Numbers 1.8×10^6 to 11.0×10^6 , NACA Technical Note 1998, 1949.
2. Powell, R. D., Jr., Hovering Performance of a Helicopter Rotor Using NACA 8-H-12 Airfoil Sections, Technical Note 3237, August 1954.
3. Spivey, R. F., Blade Tip Aerodynamics - Profile and Planform Effects, 24th National Forum of the American Helicopter Society, May 1968.
4. Cox, C. R., Rotor Noise Measurements in Wind Tunnels, Bell Helicopter Company, Paper to be presented at Third CAL/AVLABS Symposium, Aerodynamics of Rotary Wing and V/STOL Aircraft, June 1969.
5. Tanner, W. H., Yaggy, P. F., Experimental Boundary Layer Study on Hovering Rotors, 22nd National Forum of the American Helicopter Society, May 1966.
6. Velkoff, H. R., Blaser, D. A., Jones, K. M., Boundary Layer Discontinuity on a Helicopter Rotor in Hovering, AIAA - AHS - VTOL - Research, Design and Operations Meeting, February 1969.
7. Glauert, H., Aerodynamic Theory, Vol. IV, Airplane Propellers, Durand, Dover Publications.
8. Gessow and Meyers, Aerodynamics of the Helicopter, The Macmillan Company, New York, C.1952.
9. Drees, J. M., Aeroelastic Rotor Phenomena and Non-Steady Rotor Aerodynamics, International Congress on Subsonic Aeronautics, Annals of the New York Academy of Sciences, Vol. 154, Art. 2, p. 481.

10. Wortmann, F. X., Progress in the Design of Low Drag Aerofoils, Boundary Layer and Flow Control, G. V. Lachmann, London 1961.
11. Wortmann, F. X., Einige neue Laminarprofile für Segelflugzeuge, Swiss Aero Revue, November 1963, or OSTIV Publication No. VII.
12. Wortmann, F. X., Optimierung von Klappenprofilen, Swiss Aero Revue, February 1969 or OSTIV Publication No. X.
13. Walz, A., New General Law for the Turbulent Dissipation Integral Physics of Fluids, Supplement 1967, p. S161.
14. Cebeci, T., Smith, A.M.O., Calculation of Profile Drag of Airfoils at Low Mach Numbers, Journal Aircraft (5(1968) p. 535.
15. Walz, A., Berechnung der Druckverteilung von Klappenprofilen mit Totwasser, Jahrbuch der Deutschen Luftfahrt I, 1940, p. 265.
16. Jungclaus, G., Druckverteilungen angestellter ebener Platten mit angenähertem Totwassereinfluss, Zeitschr. f. Flugwissenschaften 5 (1957) p. 172.
17. Lock, R. C., Powell, B. J., Sells, C. C. L., Wilby, P. G., The Prediction of Aerofoil Pressure Distribution for Subcritical Viscous Flows, AGARD Conference Proceeding No. 35 (1968) Paris.
18. Labrujere, T. E., Loeve, W., Slooff, J. W., An Approximate Method for the Determination of the Pressure Distribution on Wings in the Lower Critical Speed Range, AGARD Conference Proceeding No. 35 (1968) Paris.
19. Sinnott, C. S., On the Prediction of Mixed Subsonic/Supersonic Pressure Distributions, Journal of Aero-Space Science, 27, (1960) p. 767.
20. Pearcy, H. H., The Aerodynamic Design of Section Shapes for Swept Wings, Advanced in Aeronautical Sciences (Vols. 3-4) Pergamon London 1962.

21. Stivers, Jr., L. S., Effects of Subsonic Mach Number on the Forces and Pressure Distributions on Four NACA 64A-Series Airfoil Sections at Angles of Attack as High as 25°, NACA T. N. 3162.
22. Davenport, F. J., and Front, J. V., Airfoil Sections for Rotor Blades - A Reconsideration, American Helicopter Society, Inc., 22nd Annual National Forum Proceedings, 12 May 1966.

ADDENDUM

To the paper DESIGN OF AIRFOILS FOR ROTORS by
Dr. F. X. Wortmann and J. M. Drees.

After completing the paper we received a number of publications concerning the Dutch development of shock free transonic airfoil sections. The work of Nieuwland²³ provides for the first time exact solutions for subcritical transonic flows for what are called quasi-elliptical airfoils. There is little doubt that application of this new insight will greatly improve our ability to design airfoils, specifically for rotary wing aircraft.

23. Nieuwland G. Y., Theoretical Design of Shock-free Transonic Flow Around Airfoil Sections, I.C.A.S. Congress, London, September 12-16, 1966. McMillan, 1966.

THE PRESCRIBED WAKE-MOMENTUM ANALYSIS

A Hover Performance Analysis Combining the Strip-Momentum and Prescribed Wake Theories.

by

JAMES B. RORKE AND CLIFFORD D. WELLS

© Sikorsky Aircraft, Division of United Aircraft Corporation,
USA 1969. All Rights reserved.

ABSTRACT

As helicopter blade loadings and numbers of blades have increased, the accuracy of classical hover performance calculation methods has decreased. The errors arise mainly from the increasing influence of the "near wake" vortex system.

The Sikorsky Prescribed Wake Momentum Analysis was developed as a practical, rapid method of rotor static performance calculation which includes the effects of the near wake's interference on the rotor inflow distribution. The method involves a simple extension of conventional strip-momentum theory to include the effects of the near wake vortex system.

The wake structure prescribed in the analysis was determined empirically from detailed analysis of model rotor smoke studies and full scale vapor trails, and analytically from the Sikorsky Free Wake Analysis. The wake structure is a function only of rotor geometry.

Excellent correlation with full scale test data has been achieved for a wide variety of rotors which fall within the following limits:

Number of blades	3 to 6
Solidity	.057 to .115
Twist	-5° linear to -14° non-linear
C_T/σ	.05 to .095

NOTATION

A_{DISK}	Rotor disk area
A_{∞}	Cross sectional area of contracted wake
B	Number of blade wakes considered
C_Q	Rotor torque coefficient - $HP \times 550 / \pi R^2 \rho (\Omega R)^3$
C_T	Rotor thrust coefficient - $T / \pi R^2 \rho (\Omega R)^2$
HP	Horsepower
L	Lift (element)
M	Mach Number
N	Total number of blade segments
R	Rotor radius
T	Thrust
V_{nib}	Total velocity induced in the r-z plane at blade segment n from trailing vortex filament ib.
Y_{nib}	Component of V_{nib} normal to blade radius
α_o	Coning angle
b	Number of blades
c	Blade chord
C_d	2-dimensional drag coefficient
C_l	2-dimensional lift coefficient
d_{nib}	Distance to blade segment n from vortex filament ib
k	Viscous damping factor
\dot{m}	Mass flow rate
q	Dynamic pressure

r	Radial distance (dimensional)
t	Time elapsed from generation of vortex
x	r/R
z	Axial distance measured from blade
Γ_B	Bound vortex strength
Γ_T	Trailing vortex strength
Γ_{ib}	Circulation strength of vortex trailing from <u>ith</u> segment of <u>bth</u> previous blade
Ω	Rotor rotational speed
α	Aerodynamic angle of attack
β	Inflow angle induced at blade segment by interference velocities from wake
ϵ_{nib}	Angle between V_{nib} and Y_{nib}
θ	Geometric angle of attack
θ_1	Total blade twist
ν	Axial velocity proportional to bound vorticity of blade (calculated by momentum theory)
ρ	Atmospheric density
σ	Rotor Solidity ($bc/\pi R$)
ϕ	$\arctan \nu/\Omega r$
ψ_b	Angular rotation of blade b from point where it deposited a vortex filament in the wake

INTRODUCTION

The accurate prediction of payload capability requires improvement in the accuracy of methods used to calculate rotor hovering performance. A 5% error in predicted rotor thrust is reflected as approximately a 20% payload uncertainty when an out of ground effect hover requirement establishes the mission take off weight. Errors of this magnitude clearly impose unacceptable restraints on helicopter designers.

The design of helicopters to operate efficiently at high gross weights has led to an increase in rotor disk loadings to minimize size and weight. The trend toward higher cruise speed requirements has led to increased rotor solidity to avoid retreating blade stall by reducing blade loadings. The influence of the near wake on the hovering efficiency of these high disk loading, high solidity rotors has increased accordingly. Classical methods of calculation have failed to accurately predict the hovering performance of these "heavy lift" rotor systems because they neglect the effect of the near wake on the rotor inflow distribution. Figure (1) illustrates the impact of blade loading on the performance predicted by two classical methods, strip-momentum theory and the more sophisticated Goldstein-Lock Analysis. The figure indicates that as blade loading increases, the classical methods predict increasingly optimistic performance.

Neglecting the effect of the contraction of the near wake in

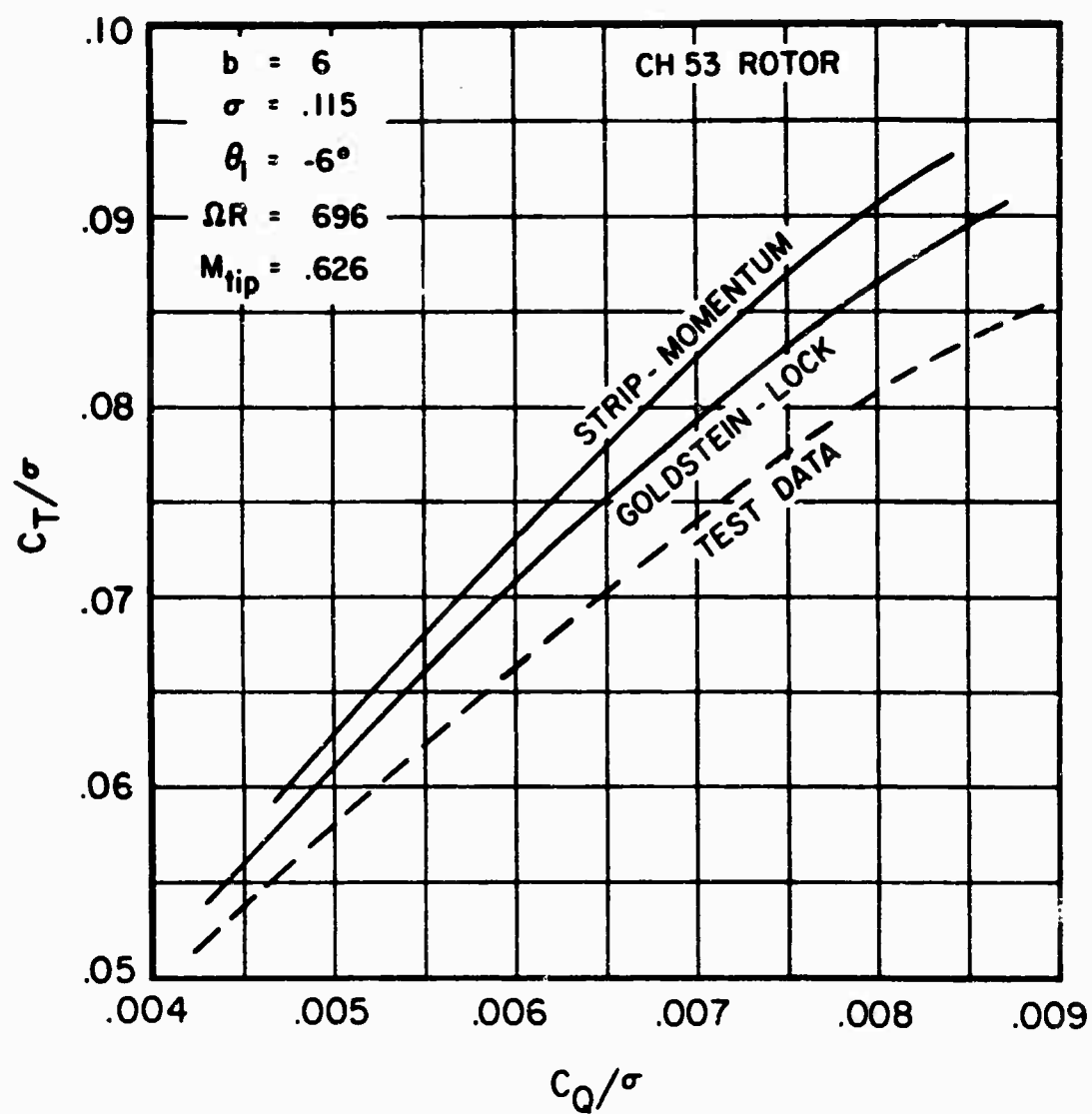


FIGURE 1. EFFECT OF LOADING ON HOVER PERFORMANCE PREDICTED BY CLASSICAL HOVER THEORY.

the Goldstein-Lock and momentum theories leads to the prediction of optimistic performance for highly loaded rotors because these theories do not correctly depict the inflow conditions near the blade tip. Figure (2) compares the angle of attack distributions for a highly loaded 6 bladed rotor as derived from a typical far wake analysis, and from a method which includes blade interference effects. The severe angle of attack distortion in the tip region calculated using the near wake analysis produces high profile drag losses not predicted by the classical methods. This angle of attack distortion is caused by the passage, close beneath the blade under consideration, of a strong tip vortex produced by the preceding blade. Omitting the influence of this trailing tip vortex results in highly optimistic performance calculations as illustrated in Figure (1) and treated in detail in Reference (1).

Generally, there is wide agreement that the inclusion of near wake effects is essential to obtaining a realistic representation of the rotor blade's spanwise load distribution. Many investigators have developed methods which consider wake contraction and blade interference effects for analysis of both the forward flight and hover modes (References (1) through (8)). Included in these studies are two basic approaches to the "near wake" problem: (1) methods which calculate the trajectory of each trailing vortex filament; and (2) methods which prescribe the trajectories of the vortex system. To calculate the inflow resulting from the lift distribution on the blade, all of these

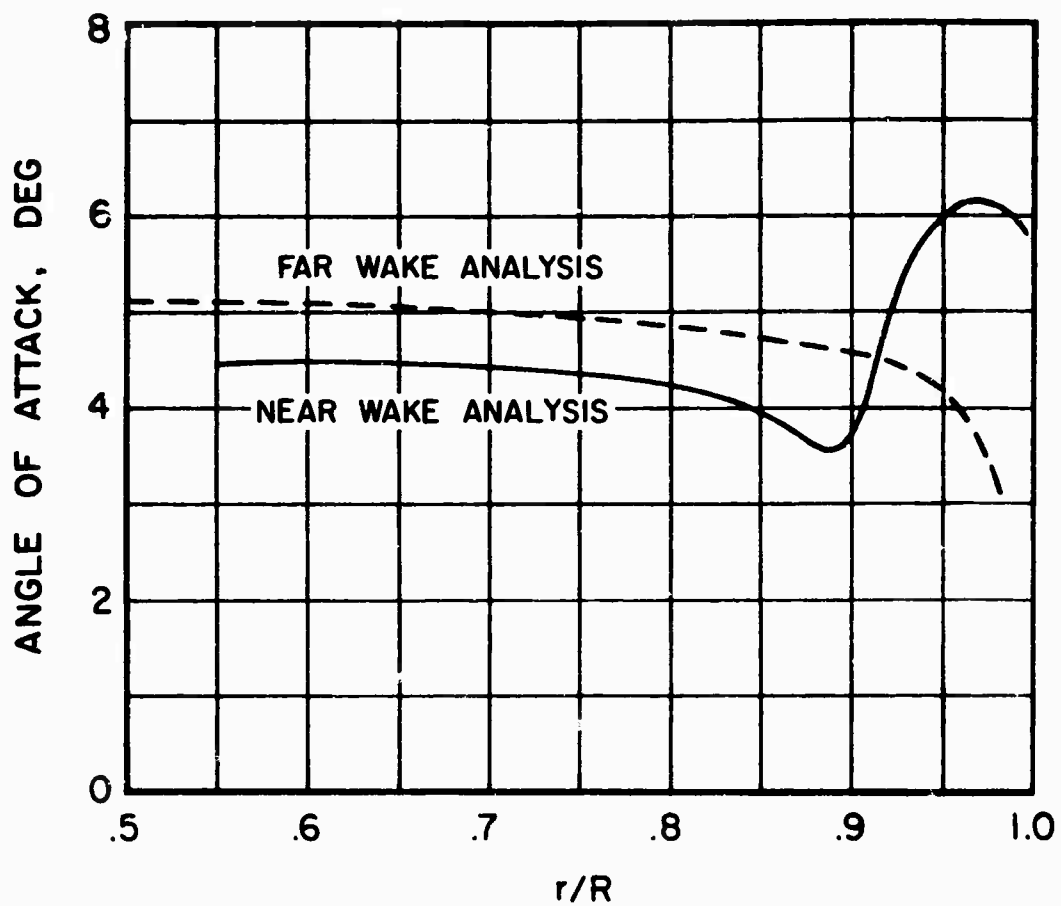


FIGURE 2. COMPARISON OF ANGLE OF ATTACK DISTRIBUTIONS WITH AND WITHOUT NEAR WAKE INTERFERENCE.

methods use a form of lifting line theory.

In developing the method presented in the following pages, two requirements were adhered to: (1) the analysis must be consistently accurate, correlating with all available test data within the accuracy of that data for a broad range of blade loadings, number of blades, twist distributions, etc., and (2) the computation time on a high speed digital computer should be short enough to allow use of the method in day to day performance work. The second requirement immediately precluded the use of a calculated wake analysis, and dictated the use of the more economic prescribed wake approach. While the calculated wake approach is analytically more rigorous and independent of smoke studies and other means required to compile a family of wake geometries, the computer time required for such an analysis is still excessive for use in day to day performance calculations where a reasonable budget must be adhered to.

The analysis utilizes the basic strip-momentum theory modified to include the effects of the near wake by adding a wake-induced "interference" velocity to the strip-momentum calculated inflow. The addition of this interference velocity, however, necessitates some modification to the basic momentum equations.

This paper discusses in detail the modifications to strip-momentum theory which resulted in the formulation of the Sikorsky Prescribed Wake-Momentum Analysis. The correlation of this method with

test data for a broad range of blade loadings, disk loadings, numbers of blades and blade twists is illustrated.

DESCRIPTION OF WAKE STRUCTURE

An accurate model of the structure of the near wake is fundamental to the development of a useful prescribed wake hover analysis. Because the spanwise load distribution is very sensitive to the wake structure, the wake geometry must be as accurate as possible for all rotor geometries and thrust levels to be analyzed. In order to maintain the versatility and simplicity desired in a standard calculation procedure, a generalized wake structure has been developed which varies only as a function of those rotor parameters to which the wake is particularly sensitive. Studies conducted to date strongly indicate that, over the range of normal helicopter blade loadings, this generalized wake geometry varies only as a function of the number of blades in the rotor system, blade planform and twist distribution.

Basis of Wake Structure

The wake structure used in this analysis has been compiled from three independent sources, all of which are in basic agreement.

1. Wake structures calculated by the Sikorsky Free Wake Analysis (Reference (3));
2. Model rotor smoke study photographs;
3. Photographs of vapor trails in the wake of full scale rotors.

The theoretical base of the wake structure presented in this paper is the Sikorsky Free Wake Analysis developed by Clark and Leiper (Reference (3)). The Free Wake Analysis starts with an assumed wake structure and computes the velocity field about this structure. The assumed wake structure is then allowed to propagate as dictated by the original velocity field. A new velocity field is then computed, and the iteration repeated until equilibrium exists between the wake structure and the velocity field, producing the structure of both the inboard sheet (simulated by a finite number of discrete vortex filaments) and the tip vortex.

In order to verify these calculated wake geometries, Sikorsky Aircraft and the United Aircraft Research Laboratories are jointly conducting extensive flow visualization tests in hover with small scale model rotors. Rotors of the following characteristics have been tested to C_T/σ values as high as .09:

Radius	26.75 inches
Chord	1.47 inches
Tip Speed	350 to 700 fps
Tip Mach Number	to .62
Number of Blades	3 to 8
Linear Twist	-8 degrees
Airfoil	NACA 0012

The early phases of this test program were reported in Reference (1) and except for improvements in equipment and an increase in the rotor tip speed, the basic technique remains essentially unchanged. Excellent wake geometry photographs have been obtained at tip speeds of 700 feet per

second (3000 rpm) as illustrated in Figure (3).

When the ambient temperature and dew point are within a few degrees of each other, the trajectory of the tip vortex of a full scale rotor can be observed directly through the condensation of water vapor in the core of the tip vortex. This vapor is often visible for at least one rotor revolution. When this occurs on the Sikorsky main rotor test stand, high speed motion pictures are taken from a distance with a telescopic lens in the plane of the disk. The acquisition and analysis of this data is discussed in detail in Reference (1). Figure (4) illustrates the extent of the vapor trails and clarity of the photographs.

Wake geometries derived analytically are in good agreement with those derived through photography of both full scale tip vortex vapor trails and model rotor smoke studies. Tip vortex trajectories for a six bladed rotor as derived from the three separate sources are plotted for comparison in Figure (5).

Effect of Rotor Geometry

If a Prescribed Wake method is to be of practical use, small changes in blade geometry must not significantly affect the wake structure. For example, all rotor systems which have blades of rectangular planform and moderate linear twist should have essentially the same wake structure when operating in the same range of blade loading. However, a rotor system with tapering planform tip caps and a high non-linear twist would

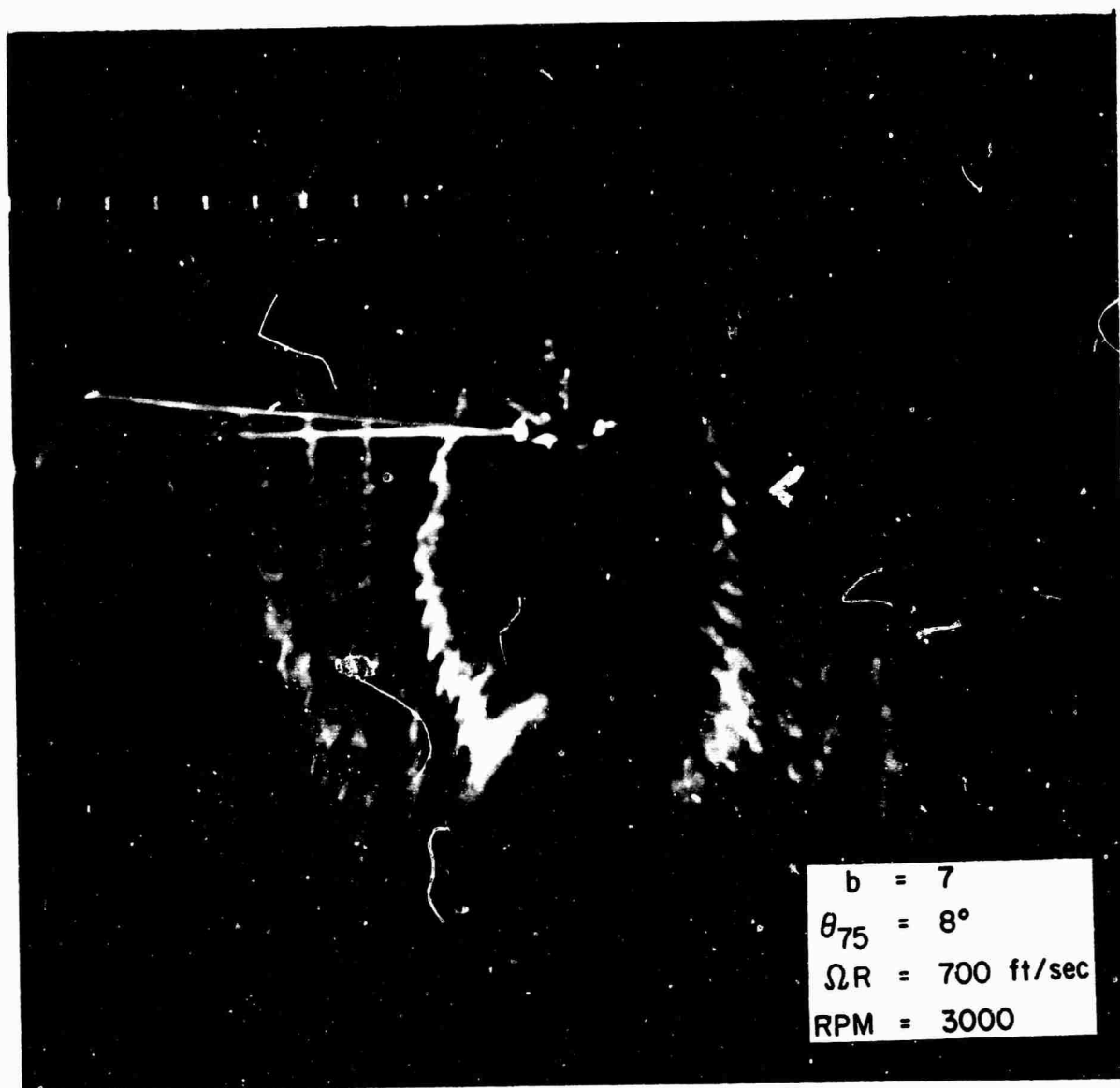


FIGURE 3. MODEL ROTOR WAKE GEOMETRY PHOTOGRAPH.

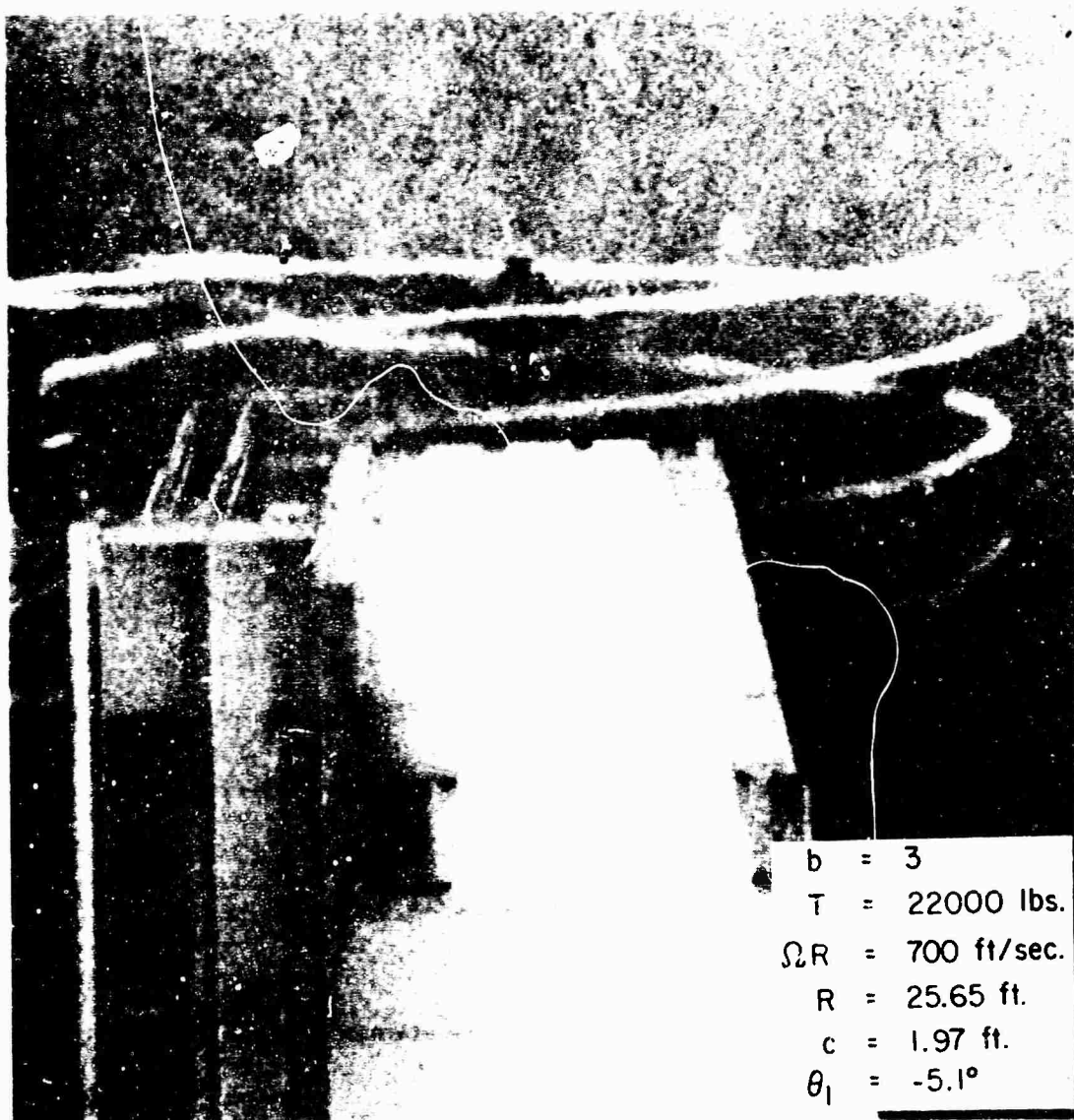


FIGURE 4. EXAMPLE OF FULL SCALE VAPOR TRAILS.

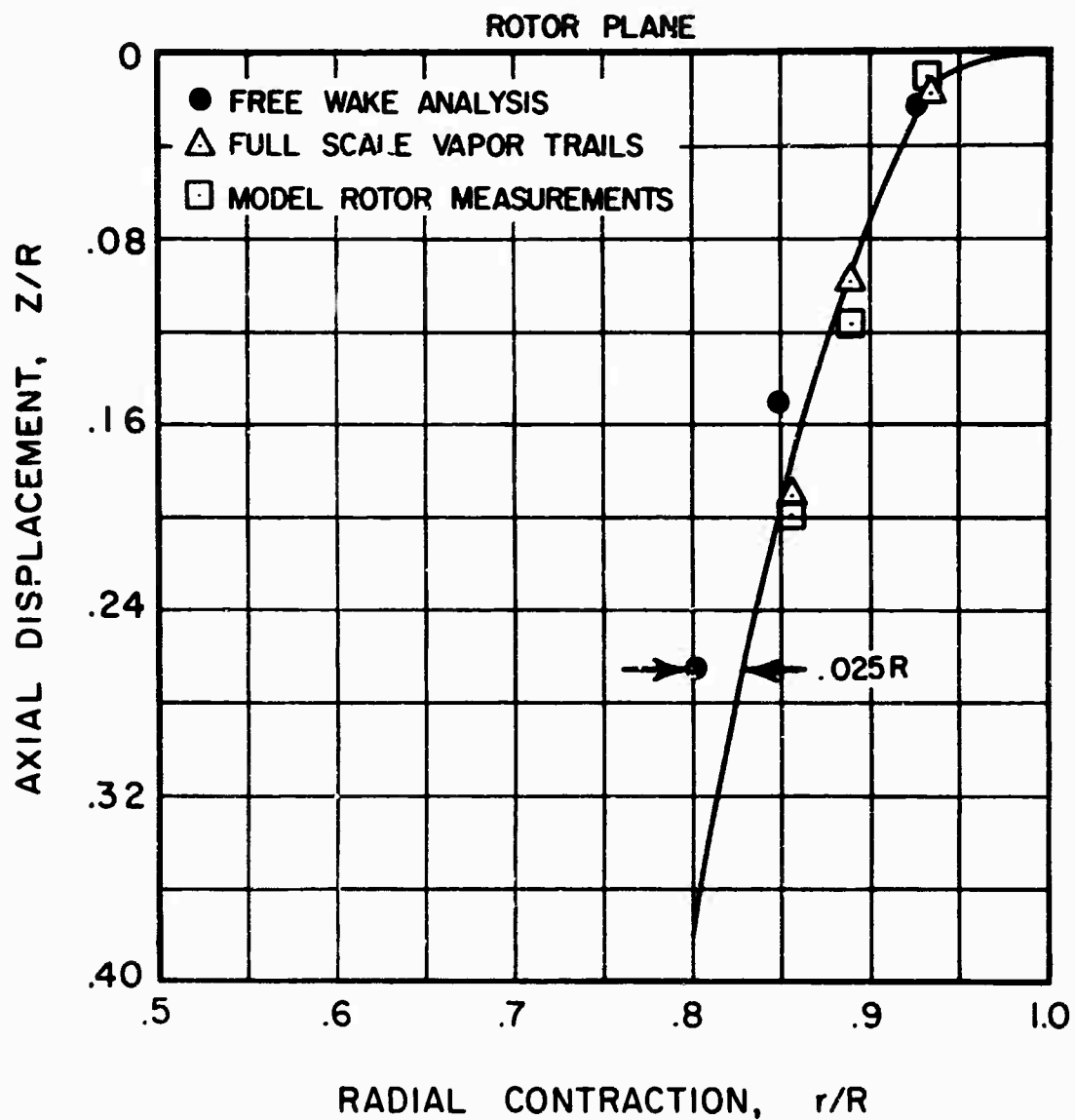


FIGURE 5. COMPARISON OF EXPERIMENTAL AND THEORETICAL TIP VORTEX TRAJECTORIES.

be expected to have a different wake structure because of the impact of the planform and twist changes on the spanwise loading. Analytical (Reference (3)) and experimental studies have shown these hypotheses to be true as illustrated by Figure (6).

Once the wake structure for a given rotor has been established by inspecting its general geometric characteristics, the wake structure is of such a general nature that changes in chord and airfoil, and moderate changes in twist are allowable without requiring a new wake geometry.

Effect of Loading

The variation of wake geometry with disk loading, within the normal operating range of current heavy lift helicopters, has been shown by both analytic and experimental studies to be negligible for the purpose of rotor performance calculation. At low disk loadings, although the wake geometry may change significantly, the strength of the wake is so low that its effect on the blade load distribution becomes insignificant. At higher disk loadings, within the normal operating range of current helicopters, variations in wake geometry have proved to be small enough to allow the use of a single wake structure which is independent of loading. Therefore, when using the Prescribed Wake-Momentum Analysis, a wake geometry derived for a C_T/σ of .065 is generally applicable in the C_T/σ range from 0. to 0.10. If performance is to be calculated for disk loadings beyond this range, the wake geometry will require some modification to ensure precise results. Further investigation is required to extend

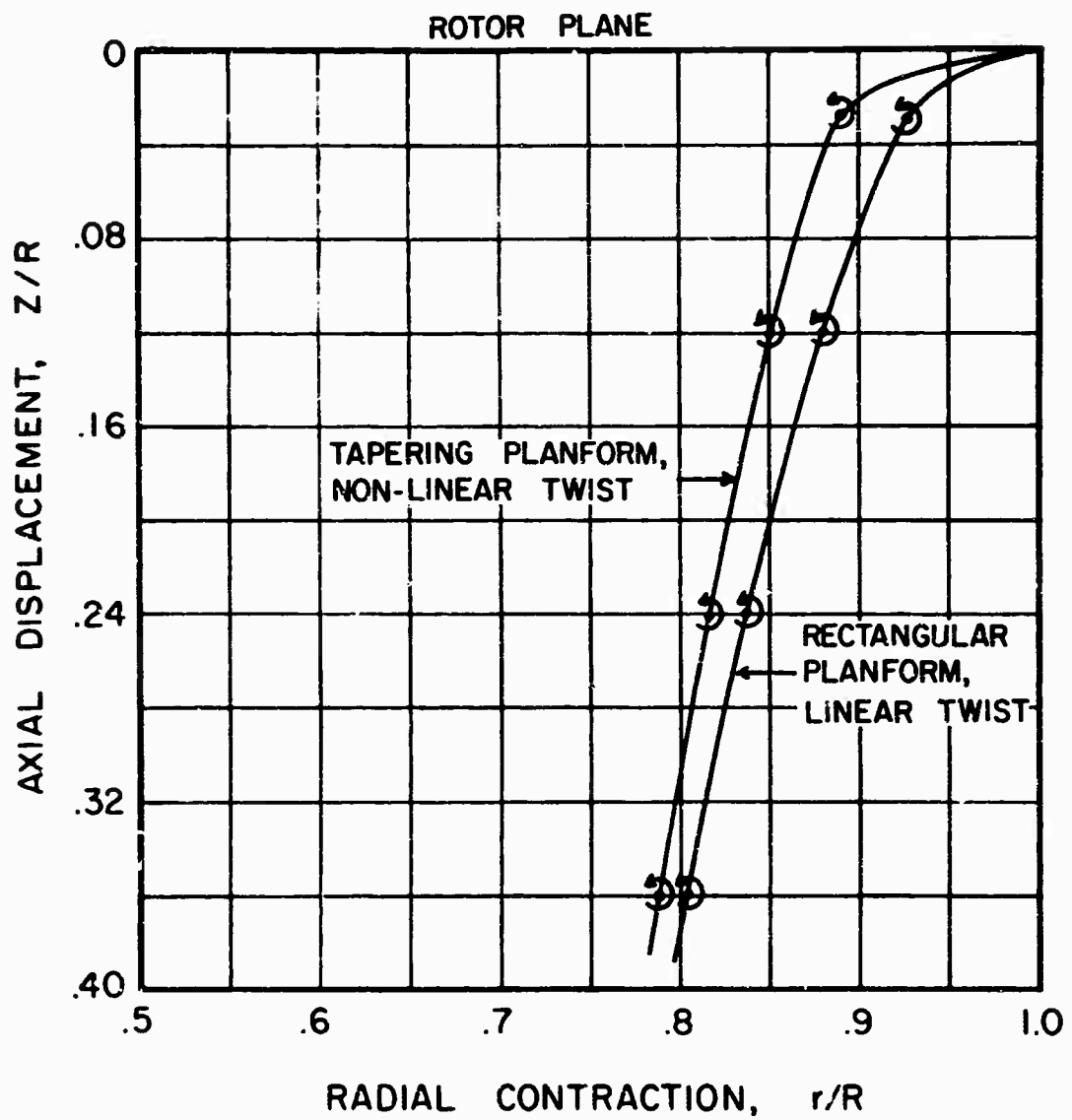


FIGURE 6. EFFECT OF BLADE GEOMETRY
ON TIP VORTEX TRAJECTORY.

the generalized wake geometries presently available in order to obtain general trends with increasing disk loading.

Effect of Number of Blades

The number of blades in the rotor system influences the wake structure more than any other variable. When the tip vortex is shed from a blade, its rate of axial displacement is very slow until it passes beneath the following blade. The downwash from that blade then accelerates the vortex in the axial direction.

The important characteristic of the axial displacement of the tip vortex is that the rates of descent before and after interaction with the following blade are independent of the number of blades. This characteristic is illustrated by Figure (7) which gives the non-dimensional axial displacement, z/R , as a function ψ , the azimuth angle through which the blade shedding the vortex has passed, for a rotor with blades of rectangular planform and moderate linear twist. The figure indicates that although the point at which the downward acceleration is induced varies predictably with number of blades, the rate of descent is constant.

The radial position of the vortex as a function of azimuth has been found to be insensitive to the number of blades in the rotor system.

Typical Wake Structure

The wake structure utilized in the Sikorsky Prescribed Wake-

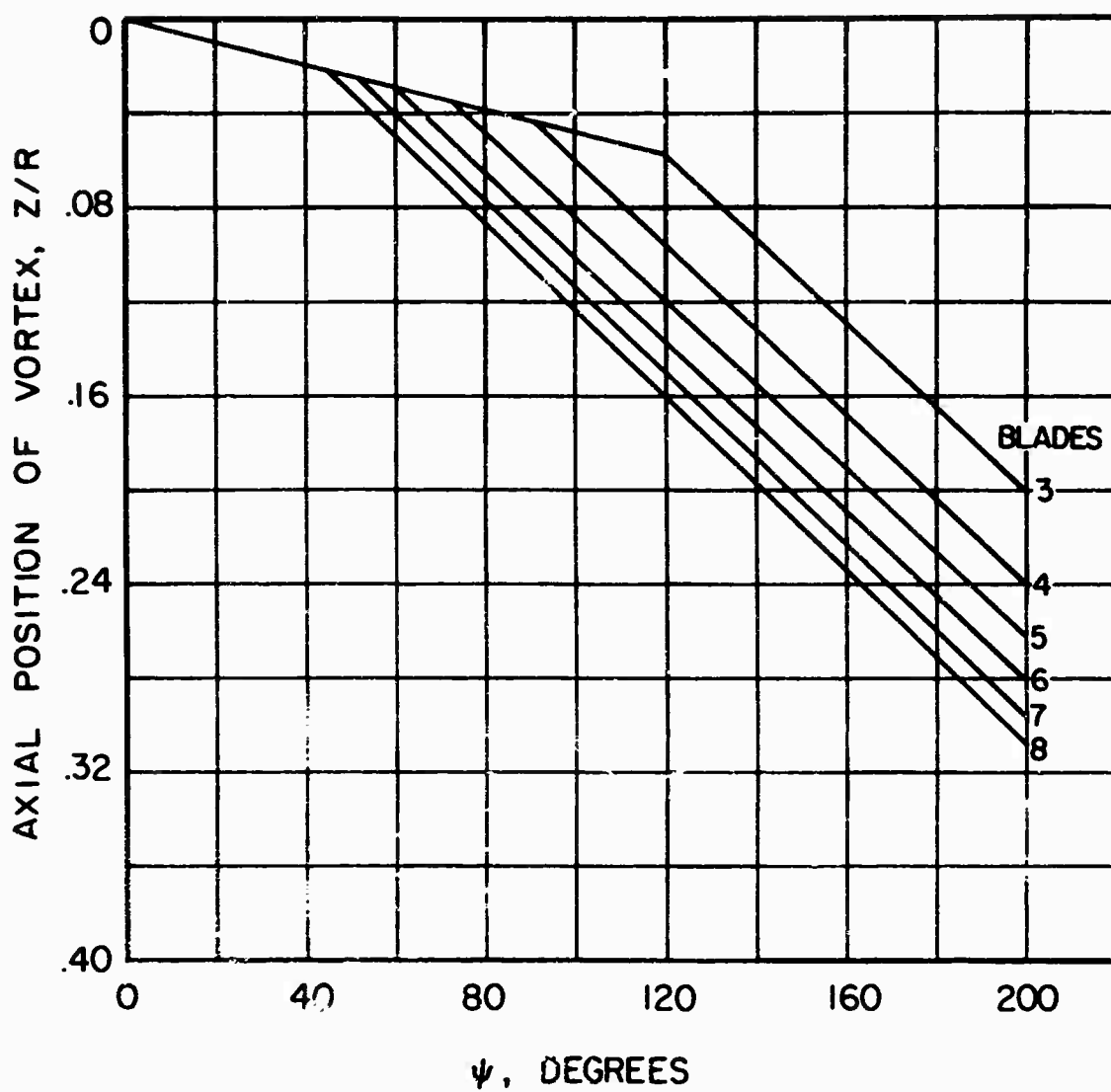


FIGURE 7. EFFECT OF NUMBER OF BLADES ON AXIAL DISPLACEMENT OF TIP VORTEX.

Momentum Analysis for 6 bladed rotors with rectangular planform and linear twist is illustrated in Figures (7) and (8). The unique aspects of this wake geometry are the inboard boundary and the non-linearity in the spanwise direction. Similar wake geometries have been developed for rotors with 3, 4, 5, 7 and 8 blades (Figure (7)) and for blades with non-linear twist rates and "elliptic" planform tip caps.

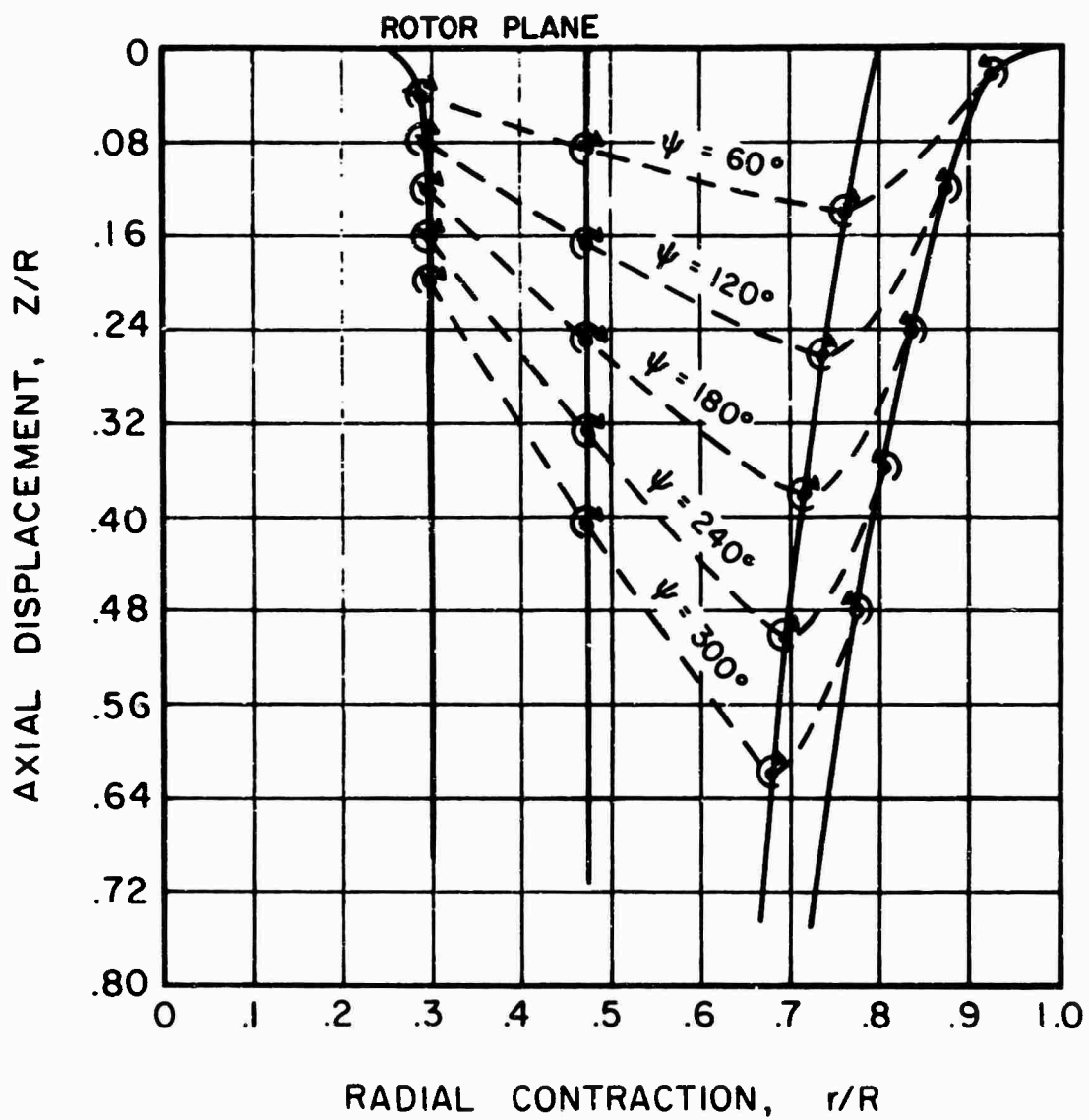
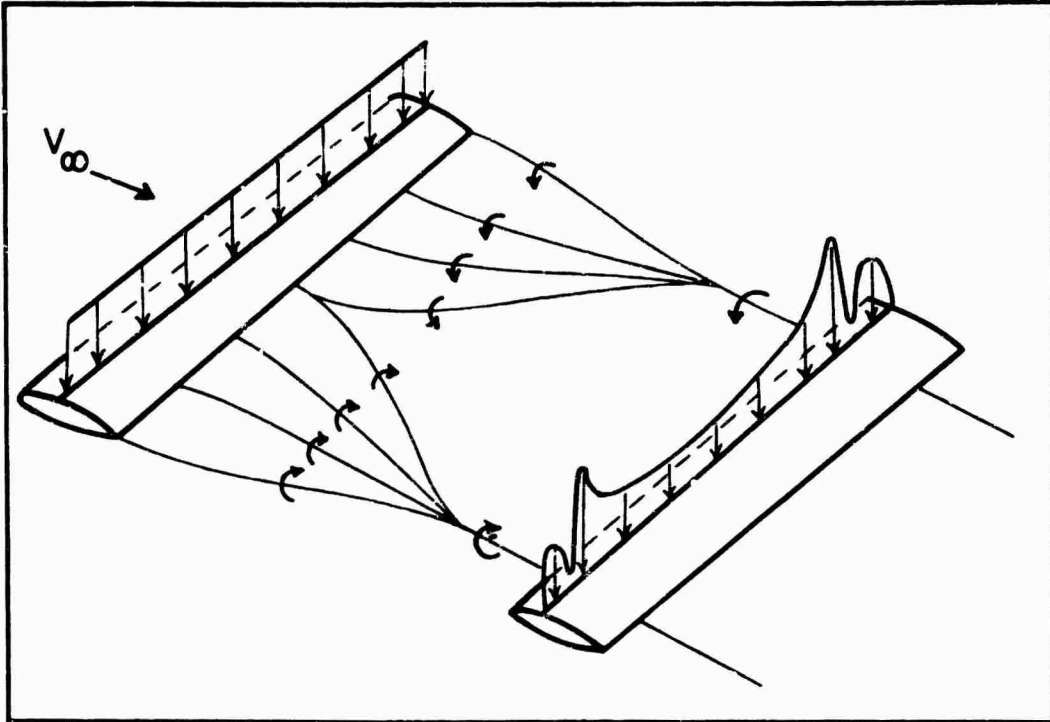


FIGURE 8. TYPICAL WAKE STRUCTURE FOR SIX BLADED ROTOR.

CONCEPT OF INTERFERENCE VELOCITY AND MOMENTUM VELOCITY

The Sikorsky Prescribed Wake-Momentum Analysis differs from other "near wake" methods in that strip-momentum theory rather than lifting line theory is used to calculate the component of inflow velocity at the disk produced by the lift distribution of the rotor blade. The method retains the general features of strip-momentum theory (adequately described in Reference (9)), but extends it to include the localized interference effects of the near wake vortex system.

As an introduction to the analysis, consider the case of two fixed wing aircraft flying in the same horizontal plane, with one a short distance ahead of the other. The lead aircraft generates a system of trailing vortices which passes closely beneath the following aircraft and exerts considerable influence on its angle of attack distribution. The span loading of the lead aircraft can be calculated by momentum theory considering that the wing influences the mass of air which passes through a cylinder of diameter equal to the wing span. This case has been treated in Reference (10). The sketch below depicts how the downwash distributions of the two wings might differ. The interference velocities from the lead aircraft influence both the mass flow rate and angle of attack of the second aircraft's wing. However, because the interference velocities are present both in front of and behind the second aircraft, they do not directly contribute to the net change of velocity through the control volume used to compute the lift of the second wing.



The rotary wing analogy to the fixed wing discussion is clear. Each blade in a rotor system is always under the influence of a system of trailing vortices from the previous blades and from the blade under consideration from its previous revolutions. These vortex filaments pass closely beneath the blade and induce an interference velocity which influences both the local mass flow and local angle of attack as was the case for the tandem fixed wing example.

Neglecting the interference velocities, and considering one segment of the blade span, Δr , the following relationships for the elemental thrust on the segment can be derived from strip-momentum and

blade element theory:

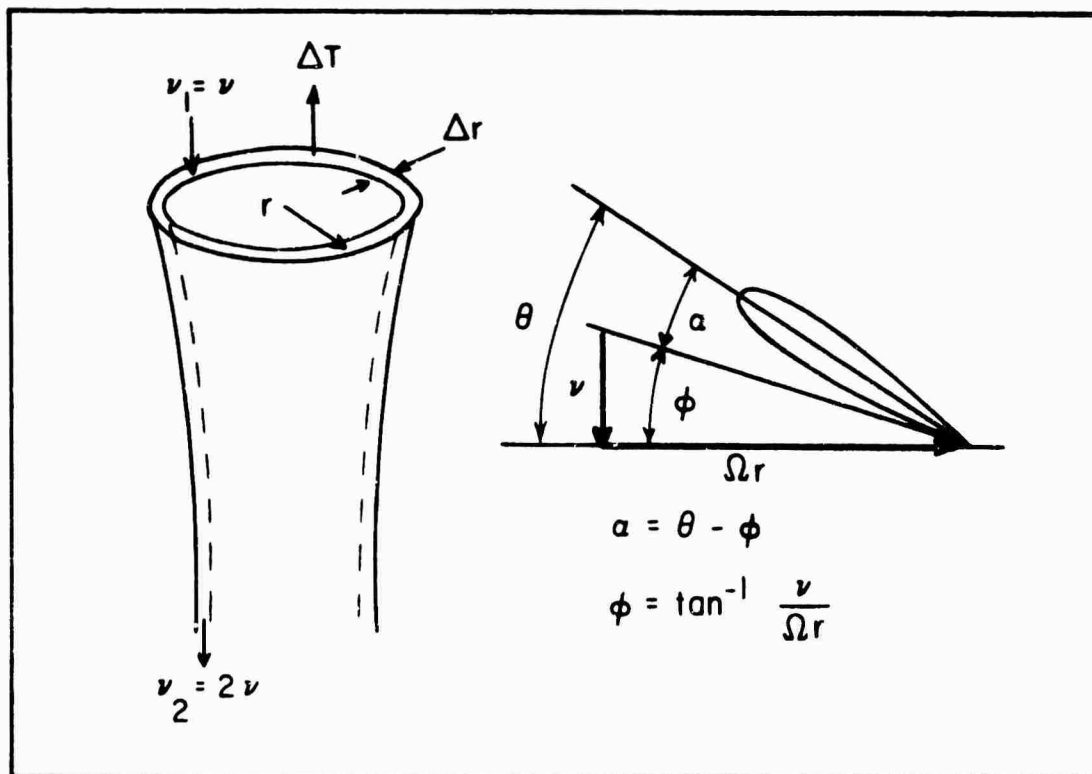
momentum thrust

$$\begin{aligned}\Delta T &= \dot{m} \Delta v \\ \dot{m} &= \rho (2\pi r \Delta r) v \quad \Delta v = 2v \\ \Delta T &= \rho (2\pi r \Delta r) v (2v)\end{aligned}\tag{1}$$

blade element thrust

$$\begin{aligned}\Delta T &= \frac{1}{2} \rho [(\Omega r)^2 + v^2] bc \Delta r [c_l \cos \phi - c_d \sin \phi] \\ c_l \text{ and } c_d &= f(\alpha, M) \quad \phi = \tan^{-1} \frac{v}{\Omega r}\end{aligned}\tag{2}$$

where the terms of the relations are defined by the sketch below.



A numerical solution is found by equating relations (1) and (2) and iteratively solving for ϕ .

When considering interference velocities, it is assumed that only the local mass flow and the angle of attack are different from the non-interference case. With respect to the momentum control volume, this assumption implies the following:

1. The interference velocities are zero at the control volume entrance far above the disk and at the control volume exit far below the disk;
2. The interference velocities have a finite value, Y , at the disk;
3. The area contraction ratio of the slipstream is not necessarily 1:2, but is a function of the blade loading and blade loading distribution.

The expression for the slipstream contraction ratio is given by:

$$\frac{A_{\infty}}{A_{\text{disk}}} = \frac{Y + \nu}{2\nu}$$

which gives a ratio of 1:2 only when Y is equal to zero, the non-interference case. The contraction ratio is a function of both disk loading and spanwise loading distribution, since Y and ν are functions of these parameters. This characteristic is consistent with a recent theoretical development by Dr. T. Theodorsen (Reference (11)) which derives the

contraction ratio of an ideal rotor as a function of disk loading and number of blades. Some general conclusions of Dr. Theodorsen's work are:

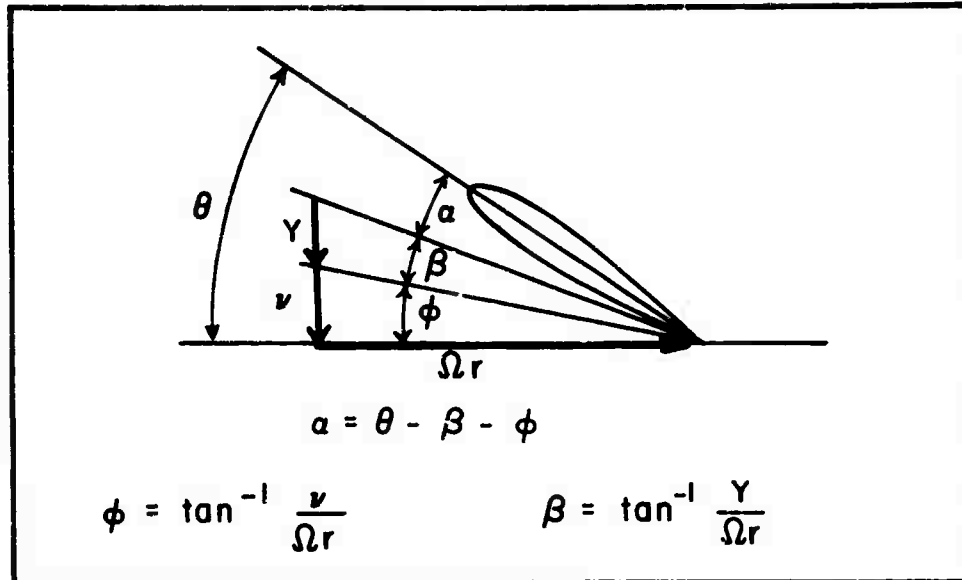
1. The contraction ratio increases with increasing disk loading;
2. The contraction ratio decreases with increasing number of blades (constant disk loading);
3. The contraction ratio is generally less than 2.

The trends of contraction ratio predicted by the Prescribed Wake-Momentum Analysis are not always consistent with the values derived by Dr. Theodorsen, because the Prescribed Wake-Momentum Analysis deals with a realistically loaded rotor influenced by the near wake rather than an ideally loaded rotor.

With the interference velocity at the disk defined as Y , equation (1) is modified as follows:

$$\begin{aligned}\dot{m} &= \rho (2 \pi r \Delta r) (Y + v) \\ \Delta T &= \rho (2 \pi r \Delta r) (Y + v) 2 v\end{aligned}\tag{3}$$

The equation for angle of attack is modified as depicted in the following sketch.



Equation (2) therefore takes the form:

$$\Delta T = \frac{1}{2} \rho \left[(\Omega r)^2 + (Y + v)^2 \right] bc \Delta r \left[c_l \cos(\beta + \phi) - c_d \sin(\beta + \phi) \right] \quad (4)$$

Equating relations (3) and (4) gives an equation which is called the Error Function. An error of zero denotes exact agreement between momentum theory and blade element calculated thrust.

$$ERR = \left[\frac{8 \pi r}{bc} \frac{(\beta + \phi) \phi}{\left[c_l \cos(\beta + \phi) - c_d \sin(\beta + \phi) \right]} - 1 \right] \quad (5)$$

For a given value of β , there is a unique value of ϕ which will satisfy equation (5). The use of the error equation to iteratively predict the spanwise inflow distribution and thereby determine the hover performance

is discussed below.

APPLICATION OF ANALYSIS

Figure (9) presents a simplified flow diagram which outlines the major iterative scheme used in the computer program. For the sake of clarity, several internal loops, designed to reduce the computer time required for convergence at all blade stations, have been omitted. These loops have no bearing on the general analysis.

The inputs required for the program are:

1. rotor geometry (chord and twist distribution, radius, number of blades),
2. operating conditions (collective pitch, rotor speed, atmospheric conditions),
3. airfoil data,
4. wake geometry (previously described).

The allowable rotor geometry is unrestricted except for limits imposed by the availability of an appropriate wake geometry. The program will accept spanwise variations in chord and airfoil section, and a non-linear or even discontinuous twist distribution.

The first step in the computative scheme is the assignment of an initial β distribution (Block 2) to enable the program to compute starting values of ϕ and C_1 (Block 3). The relationship between β , ϕ , and C_1 is given by equation (5), where C_1 is a function of the aerodynamic angle of

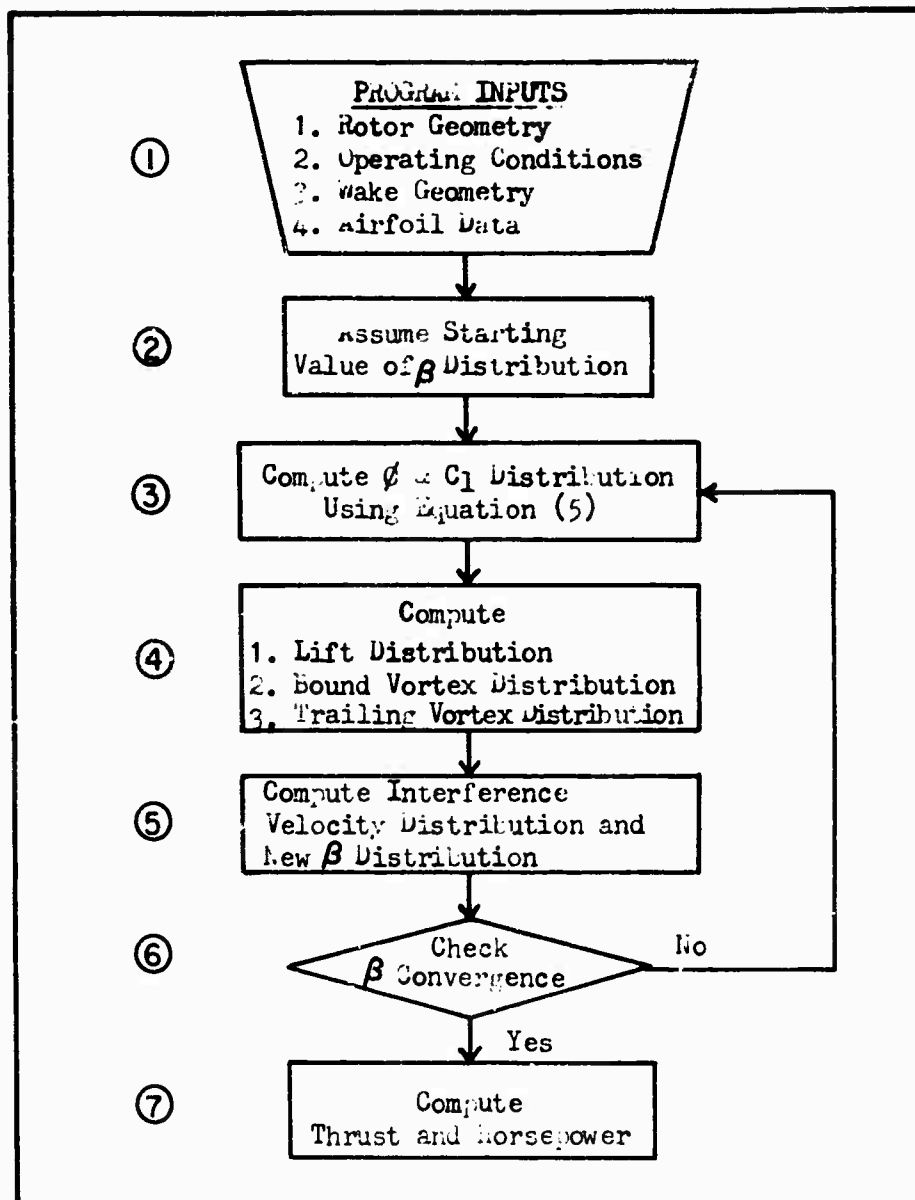
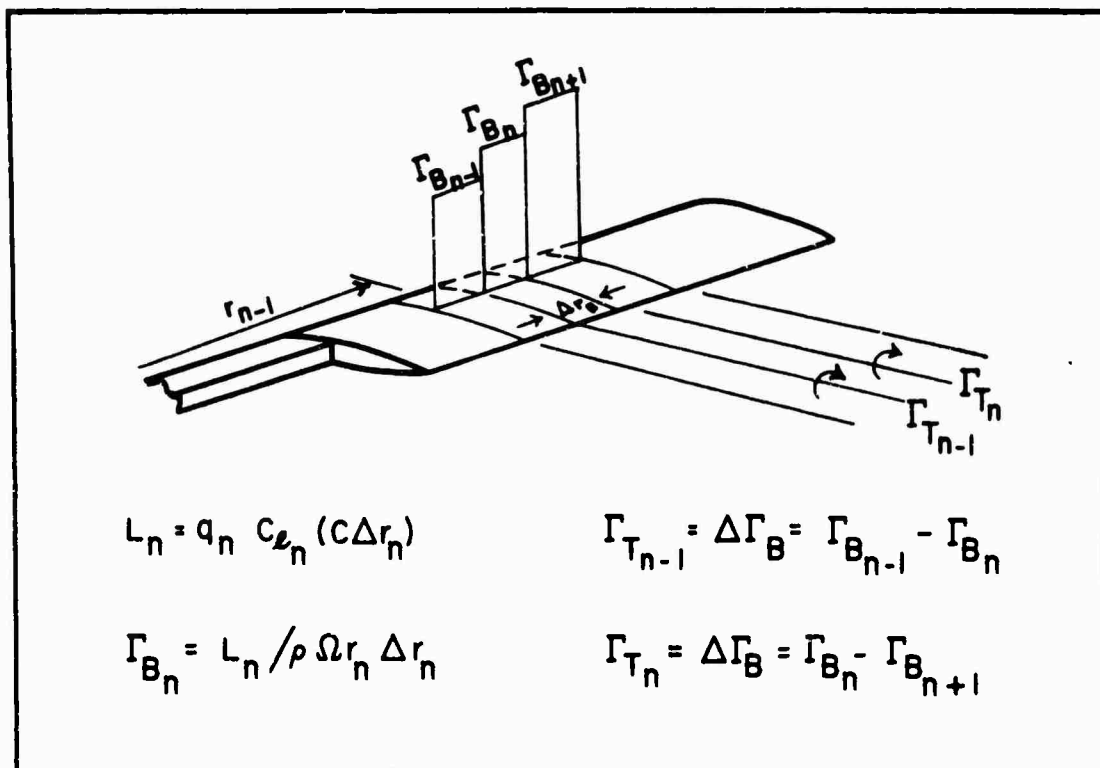


FIGURE 9. FLOW DIAGRAM OF COMPUTER PROGRAM BASED ON PRESCRIBED WAKE - MOMENTUM ANALYSIS.

attack, α (given by $\alpha = \theta - \beta - \phi$), and Mach Number. For a given β (assumed at this point), there is a single combination of ϕ and C_L at each spanwise station which will satisfy equation (5) within the specified tolerance or allowable error.

With initial values of inflow ($\beta + \phi$) and lift coefficient defined at each spanwise segment of the blade, the lift distribution (L), the bound vortex distribution (Γ_B), and then the strength of the trailing vortex system (Γ_T) can be computed (Block 4) as depicted in the following sketch.

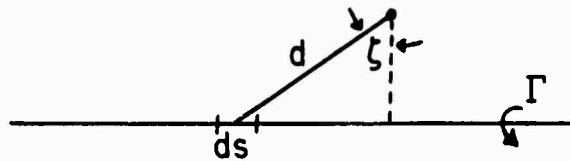


After determining the strength of each trailing vortex filament, the vortex system is positioned beneath the blade as prescribed by the input wake geometry, and a new distribution of interference velocities is computed (Block 5). The assumptions used in computing these velocities are:

1. The vortex filaments are straight lines which extend a distance $r\psi$ in front of the blade and to $-\infty$ behind the blade (Figure (10));
2. the vortices have a finite core radius;
3. viscous time damping factors are included;
4. the spanwise component of the interference velocity is neglected.

Figure (11) defines the geometric relationship between the vortex shed from the i^{th} segment of the b^{th} previous blade to the n^{th} segment of the blade considered. Beginning with the Biot-Savart Law,

$$dV = \frac{\Gamma}{4\pi} \frac{\cos \zeta}{d^2} ds \quad (6)$$



and referring to Figures (10) and (11), applying the first of the assumptions results in the following equation for the velocity induced at the

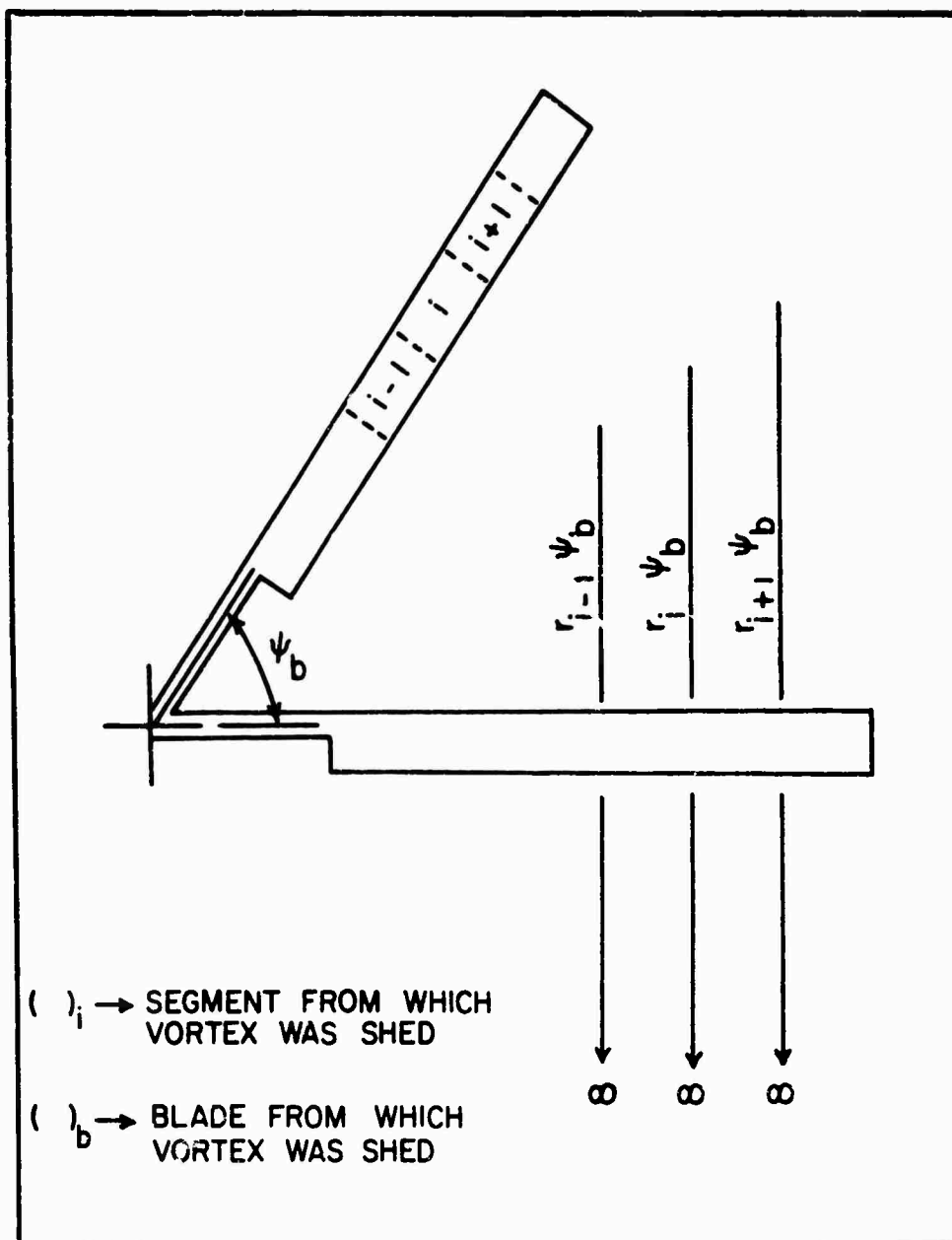


FIGURE 10. DEFINITION OF VORTEX
FILAMENT LENGTH.

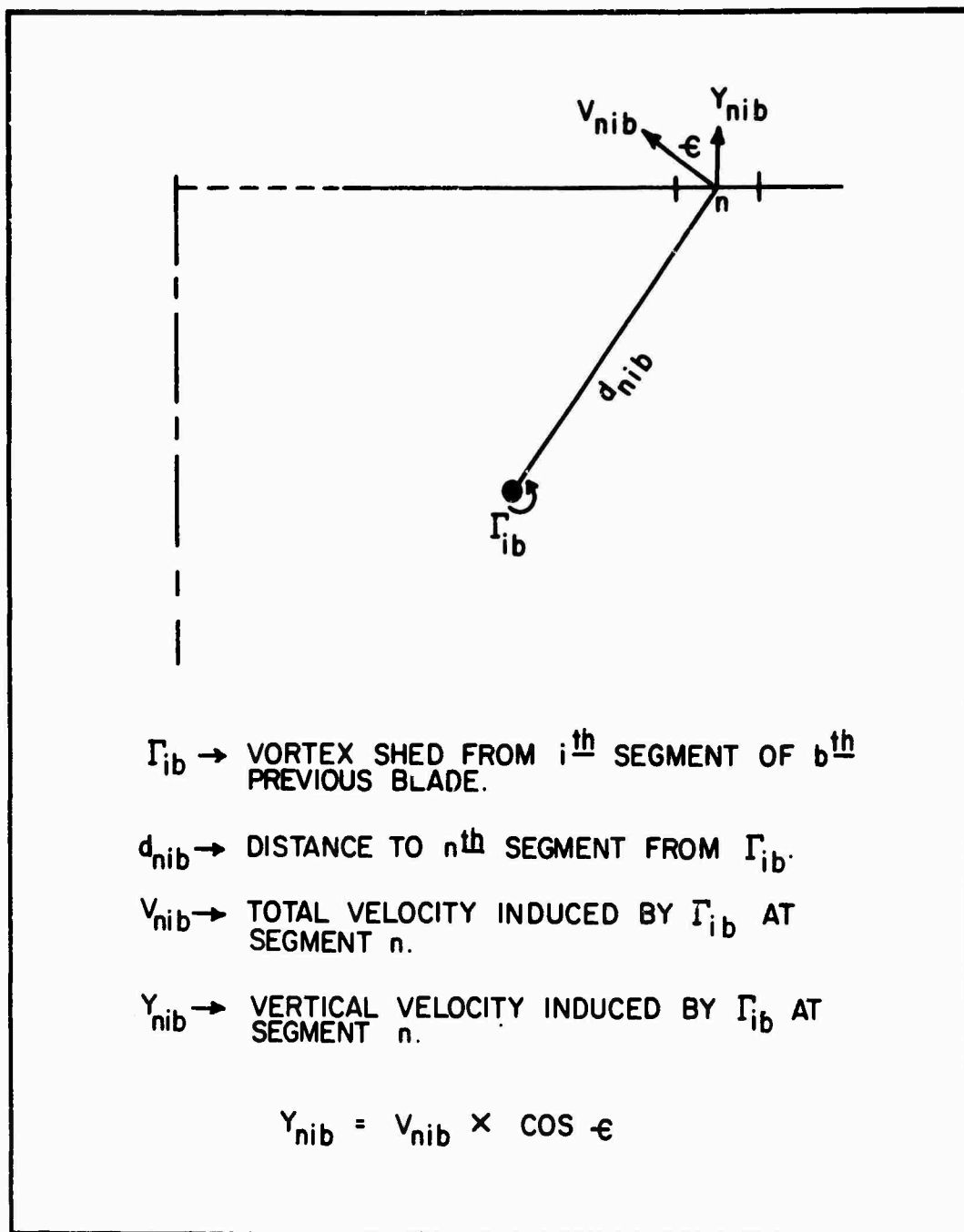


FIGURE II. GEOMETRIC DEFINITIONS.

blade element under consideration:

$$v_{nib} = \frac{\Gamma_{ib}}{4\pi d_{nib}} \left\{ 1 + \sin \left[\tan^{-1} \left(\frac{r_i \psi_b}{d_{nib}} \right) \right] \right\} \quad (7)$$

Applying Lamb's solution to include a finite core radius and viscous damping, equation (7) becomes:

$$v_{nib} = \frac{\Gamma_{ib}}{4\pi d_{nib}} \left\{ 1 + \sin \left[\tan^{-1} \left(\frac{r_i \psi_b}{d_{nib}} \right) \right] \right\} \left[1 - e^{\left(\frac{-d_{nib}^2}{kt} \right)} \right] \quad (8)$$

where the term "kt" determines the core radius and is a function of the eddy viscosity in the vortex core. In the present analysis, k is chosen such that the vortex core radius is 3 inches at the time when $\psi_b = \psi_i$. The value of k chosen is not generally critical, because under normal conditions the vortices are far enough below the rotor so that the core radius does not effect the velocity induced. Core radius has been shown to be a function of vortex strength and Reynolds Number and should vary as a function of these parameters, but much more work is required to properly define vortex eddy viscosity and core radius. Considering only the component of velocity normal to the blade results in the velocity relationship given by:

$$v_{nib} = \frac{\Gamma_{ib}}{4\pi d_{nib}} \left\{ 1 + \sin \left[\tan^{-1} \left(\frac{r_i \psi_b}{d_{nib}} \right) \right] \right\} \left[1 - e^{\left(\frac{-d_{nib}^2}{kt} \right)} \right] \cos \epsilon_{nib} \quad (9)$$

Equation (9) gives the vertical velocity induced at blade segment n by the vortex shed from the i^{th} segment of the b^{th} previous blade. If considering B previous blades, and the blade is divided into N segments, the total velocity at the n^{th} segment of the blade considered is given by:

$$Y_n = \sum_{b=1}^B \sum_{i=1}^N Y_{nib} \quad (10)$$

After computing the interference velocity, Y_n , at each blade segment, a new β distribution can be computed and compared with the initial assumed β values (Block 6, Figure 9). If $\Delta\beta$ ($\Delta\beta =$ calculated $\beta -$ assumed β) is less than the required tolerance at each blade segment, the case is converged. If the $\Delta\beta$ for each blade element is not within the tolerance, then the calculated β distribution is used to compute a new ϕ and C_l distribution in Block (2), and the iteration is repeated until convergence is accomplished, at which time the thrust and horsepower are computed (Block 7).

The calculation of rotor thrust and power is accomplished by resolving the rotor lift and drag forces and numerically integrating in the spanwise direction. The following equations result:

$$T = \sum_1^N \frac{1}{2} b \rho (\Omega r)^2 \cos^3 \alpha_0 c \Delta r [1 + (\beta + \phi)^2] [C_l \cos(\beta + \phi) - C_d \sin(\beta + \phi)] \quad (11)$$

$$HP = \sum_1^N \frac{b \Omega}{550} \frac{1}{2} \rho (\Omega r)^2 \cos^3 \alpha_0 r c \Delta r [1 + (\beta + \phi)^2] [C_d \cos(\beta + \phi) + C_l \sin(\beta + \phi)] \quad (12)$$

where a_0 = blade coning angle.

CORRELATION

The Sikorsky Prescribed Wake-Momentum Analysis has demonstrated an ability to predict hover performance accurately for a wide variety of rotor systems which fall within these limits:

Number of Blades	3 to 6
Solidity	.057 to .115
Twist	-5° Linear to -14° non-linear

Figure (12) compares the hover performance of the Sikorsky CH-53A main rotor as calculated by the Prescribed Wake-Momentum Analysis with test data from the Sikorsky 8000 Horsepower Main Rotor Test Stand. In a comparative test, this facility is capable of thrust measurements with a precision of $\pm 0.5\%$ and absolute accuracy for thrust measurements is $\pm 2.0\%$. The test data plotted in Figure (12) have been corrected for ground effect by the Cheeseman method (Reference (12)) and for the interference effects of the test tower as determined by model tests. The small differences between the calculated and measured performance are well within the accuracy of the test data. Figure (13) illustrates the corresponding agreement between theory and experiment on a thrust versus collective pitch basis

Similar correlation has been demonstrated for the following rotors, all of which have moderate, linear twist and rectangular planform blades:

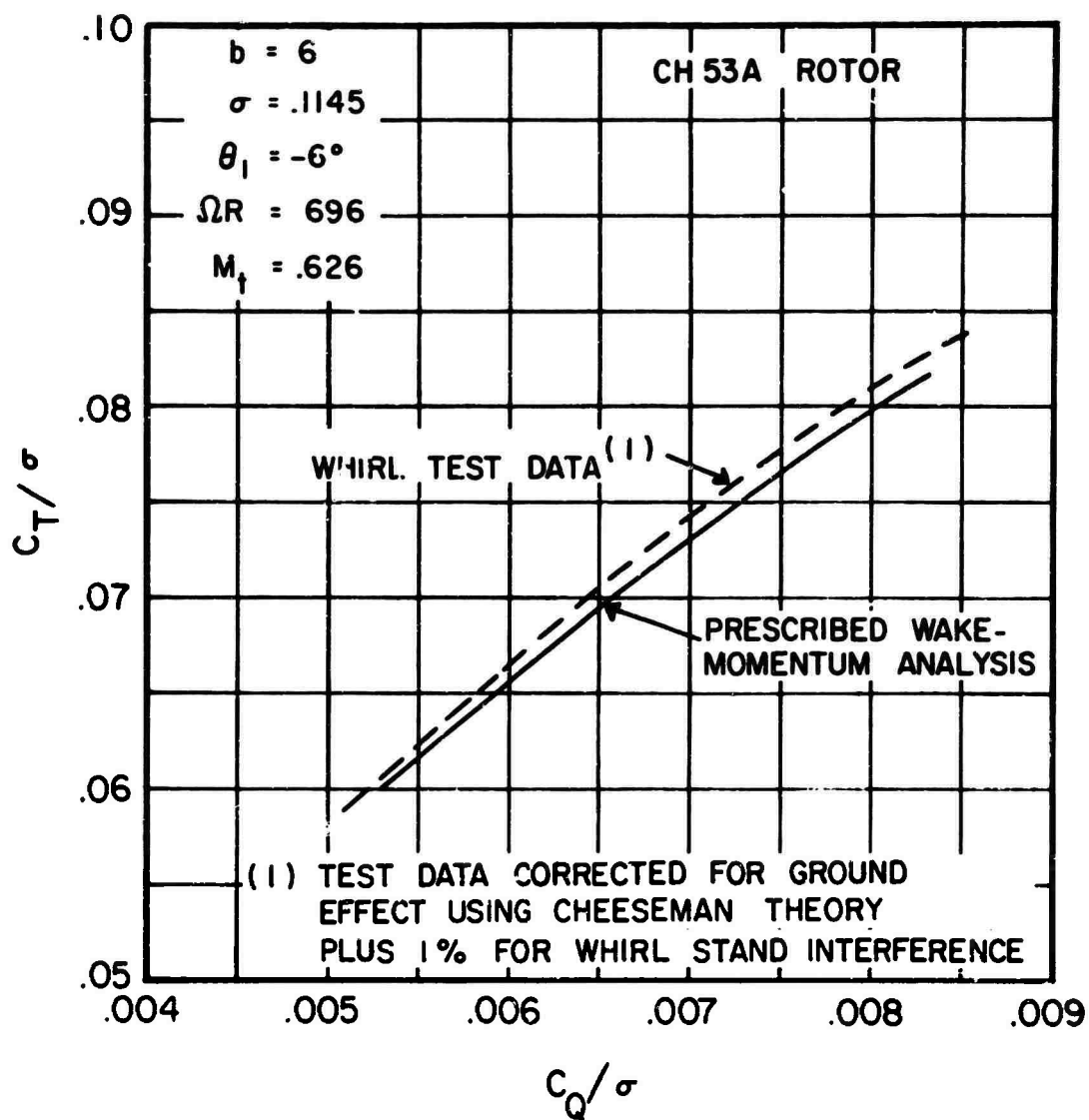


FIGURE 12. COMPARISON OF MEASURED AND PREDICTED HOVER PERFORMANCE.

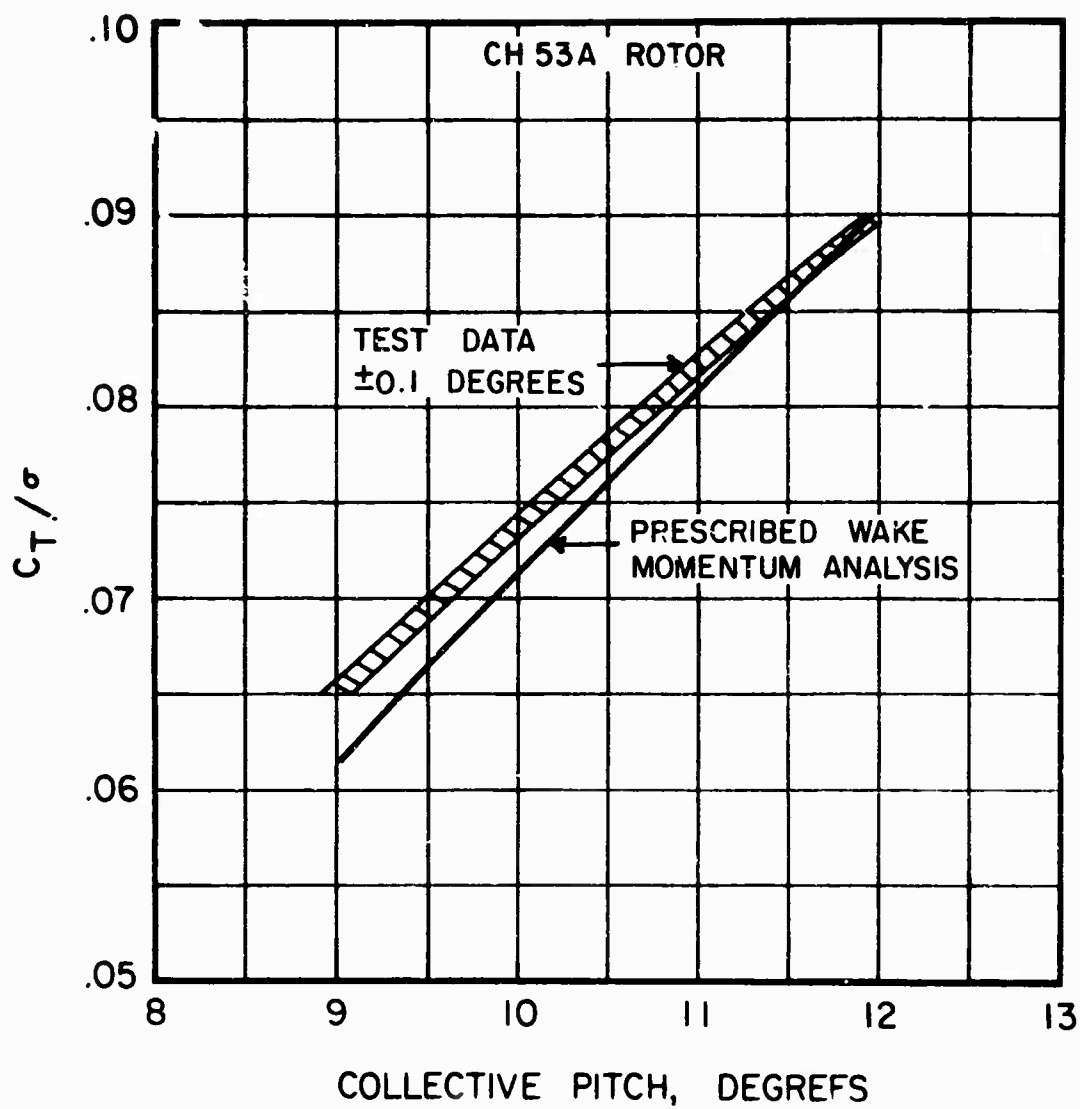


FIGURE 13. CORRELATION WITH COLLECTIVE PITCH.

Rotor System	b	σ	θ_1	Radius
CH-53A (Figure 1)	6	.1146	-6°	36'
CH-53A -79'	6	.1046	-6.6°	39.5'
CH-54A	6	.1046	-8°	36'
S55	6	.0894	-9.25°	26.5'
S61R	5	.0775	-8°	31'
S58	4	.0621	-8°	28.0'
CH-53A 3 Blades	3	.0574	-6°	36'
CH37 Shortened	3	.0734	-5.1°	26.5'

A single wake structure, which varies only as a function of the number of blades in the rotor system, was used in the calculation of the hovering performance of these rotors.

The Prescribed Wake-Momentum Analysis has also accurately calculated the hover performance of the Sikorsky CH-54B main rotor which incorporates a tapering planform near the blade tip and a high, nonlinear twist rate. The effect of the planform and twist changes on the wake geometry of this rotor, required utilization of a new wake structure (Figure 6) derived from the Sikorsky Free Wake Analysis.

CONCLUSIONS

The Sikorsky Prescribed Wake-Momentum Analysis offers the rotor designer a unique approach to the solution of hover performance problems. The analysis includes the first order effects of rapid initial contraction and the resulting near wake interference, and satisfies the momentum requirements dictated by the final contraction ratio. The wake geometry used is simply defined in terms of basic rotor parameters and has been

independently substantiated by analytical and experimental studies.

In addition, the analysis satisfies the following criteria making it useful as a standard analytic procedure:

1. The analysis, when compared with test data, has accurately predicted the hover performance of every existing Sikorsky main rotor system.
2. the computer program requires only 15 seconds per case.

REFERENCES

1. Jenney, D. S., Olson, J. R., Landgrebe, A. J., A Reassessment of Rotor Hovering Performance Prediction Methods, AHS 23rd Annual National Forum, May 1967.
2. Landgrebe, A. J., An Analytical Method For Predicting Rotor Wake Geometry, AIAA Paper No. 69-196, February 1969.
3. Clark, D. R., and Leiper, A. C., The Free Wake Analysis, AHS 25th Annual National Forum, May, 1969.
4. Piziali, R. A., and DuWaldt, F. A., A Method of Computing Rotary Wind Airload Distribution in Forward Flight, C.A.L. Report BB-1495-S-1, TCRRC Technical Report 62-11, November, 1962.
5. Brady, W. G., and Crimi, P., Representation of Propeller wakes by Systems of Finite Core Vortices, C.A.L. Report BB-1665-S-2, February, 1965.
6. Miller, R. H., On the Computation of Airloads Acting on Rotor Blades in Forward Flight, AHS Journal, Vol. 7, No. 2, April 1962.
7. Erickson, J. C., and Ordway, D. E., A Theory for Static Propeller Performance, CAL/AAVLABS Symposium Proceedings, Vol. 1, June 1966.
8. Willmer, M. A. P., The Loading of Helicopter Rotor Blades in Forward Flight, RAE Report Naval 2-H-76935 No. 8, April 1959.
9. Gessow, A., and Myers, G. C., Aerodynamics of the Helicopter, Ungar Publishing Co., New York, 1952.
10. Donnasch, D. O., Sherby, S. S. and Connolly, T. F., Airplane Aerodynamics, Pitman Publishing Corporation, New York, 1951.
11. Theodorsen, T., Theory of Static Propellers and Helicopter Rotors, AHS 25th Annual National Forum, May 1969.
12. Cheeseman, I.C., Bennett, J.E., The Effect of the Ground on a Helicopter Rotor in Forward Flight, AAEE/RES/288, 1955.

SESSION III

Rotor Noise

*Chairman: Robert G. Loewy
University of Rochester
Rochester, New York*

**THURSDAY MORNING
19 JUNE 1969**

HELICOPTER ROTOR NOISE GENERATION

by

S.E. WRIGHT and J.W. LEVERTON*

Institute of Sound and Vibration Research
University of Southampton
Southampton, Hampshire, England.

SUMMARY

This paper outlines the recent advances made in the understanding of helicopter rotor noise generation. The theoretical work has been carried out at Southampton University and sponsored by the Ministry of Technology and the National Aeronautics and Space Administration. Full details concerning the investigation are reported in I.S.V.R. Technical Reports No.5, 13, 14, 15.

The paper briefly discusses rotor noise sources and then sites a distributive loading rotational theory as being the dominant rotor noise mechanism. The distinction is made between steady and fluctuating force radiation and the importance of their properties listed. The extent of the near field is given and the properties of impulsive blade loading (blade slap) considered. Priorities for noise prediction techniques and further research directives are then discussed.

Experimental results are included to indicate the relative importance of rotational and broadband noise for a number of rotor configurations. A generalised fall-off envelope for main rotor rotational noise is given, together with directivity patterns on a model rig.

*Now at Westland Helicopters Ltd., YEOVIL, England.

ROTOR NOISE SOURCES

Pure jet engines which produce high fluid velocities make very good noise generators. The vorticity associated with these high induced velocities, radiates broadband sound energy according to the eighth power (law) of the mean convected air velocity. So by distributing the load over a wider area as in the case of a helicopter, not only is the efficiency increased but also the induced velocity is lowered and the first step in noise reduction is achieved. We can see this tendency in the present generation of gas turbines in the form of the by-pass engine.

Vorticity noise on helicopters is therefore no problem, but the noise levels are still high. It is the blade noise that is the dominant noise source here. The work described in this study has therefore concentrated on blade noise and in particular rotational noise. Rotational noise becomes particularly evident when the source motion becomes supersonic, and the rotational waves collect in front of the source producing a shock wave. The most prominent examples are the sonic boom and the ship's bow wave. In each case moving forces are involved, sending out rotational waves, like a line of dipoles in the path of the force being triggered successively. For subsonic sources the waves are less obvious as the wave front becomes less impulsive.

A second kind of blade noise is vortex-shedding force noise. This noise is generated by the shedding of vortices which produce a fluctuating bound circulation or lift force on the obstruction in the flow. The shedding can either be periodic for low Reynolds numbers (low velocity, small obstacle dimension, low density), as in the case of the whistling sound arising from

wind through telegraph wires or around sharp corners on buildings.

Alternatively the shedding can be random as in the case of the swishing sound of rotating rods.

The vortex shedding noise on aerofoils is detectable particularly in the absence of other blade noises. On high solidity devices such as fans, in the absence of rotor stator interaction the rotational noise is weak. (due to the strong source cancellation mechanism) and the vortex noise is heard as a (broadband) rushing sound. On a helicopter under zero lift conditions, the vortex noise can be heard near to a rotor amid weak rotational noise, as an amplitude modulated swishing sound. The modulation arises from the fact that the source (blade) comes near to and then goes far away from the observer (inverse square law effect). In the far field, this noise level is of relatively low level and unmodulated.

Subjectively then vortex noise is less important than the impulsive thumping or shopping sound of the rotational noise. When the helicopter pilot puts pitch on the blades to lift off, the sharp impulsive rotational waves dominate all the other noise sources. The contrast is much more pronounced in the absence of the continual drone of the rotational noise from the tail rotor. Under positive lift conditions, narrow band analysis shows that discrete rotational noise can be resolved high into the helicopter spectrum (500 Hz). It was therefore concluded that for a helicopter working under normal conditions, the vortex shedding noise generating mechanism could be ignored at the frequencies of interest. This does not, however, imply that broadband noise is always insignificant.

Typical rotor spectra show acoustic radiation falling off smoothly

with frequency. However in particular cases (or instances) the spectra can show large discrete radiation at particular frequencies or bands of frequencies. In fans, if the support vanes or stators are too close to the rotor blades, then large fluctuating forces are experienced by the blades resulting in large discrete radiations, usually referred to as gas turbine compression whine in the aircraft industry. On single rotor helicopters in certain flight regimes or on tandem helicopters, the rotor blades cut or pass very close to the shed tip vortices. Again, the blades experience severe or partial force fluctuations, radiating an impulsive sound commonly known as blade slap. A third source of impulsive blade loading of current interest is noise produced by locally supersonic rotors. When the blades are running near to supersonic or local supersonic flow conditions, momentary local shock waves are formed on the blades. It is not so much that local shock waves are formed (they do not radiate), it is the change in aerodynamic lift, blade stall, etc. that is the potential radiator.

Generally if a rotor takes in rough flow of any kind (cross wind, atmospheric turbulence, regurgitation of its slip stream, upstream wakes from support vanes) the rotor blades experience fluctuating forces and the rotor noise increases.

ROTATIONAL NOISE PROPERTIES

Rotational noise under normal operating conditions is therefore considered as the dominant rotor noise mechanism. The properties of rotational noise are considered in detail in the References listed (1), (3) (4). However the basic parameters will now be briefly discussed.

Steady Lift (S = 0)

$$SP_{mB} = K \cdot \gamma_{mB} \cdot \chi_{chord}$$

(a) The steady lift radiation is very important on low solidity rotors. Here the source cancellation mechanism is weak due to the absence of a large number of blades.

(b) On both high and low solidity rotors, the steady lift radiation can be important in the near field where the cancellation mechanism breaks down.

(c) The steady lift radiation dominates in all rotor spectra at supersonic speeds; here the cancellation is inoperative.

(d) The radiated spectrum is the upper 'cut off tail' of the $S = 0$ radiation passband.

(e) For a given thrust, the steady lift radiation is very sensitive to tip speed and number of blades (low noise for low tip speeds and large number of blades).

(f) Distributive loading at subsonic speeds has little effect, as the radiated spectrum is of low frequency. At high tip speeds, chord distributive loading suppresses the higher frequencies.

(g) The polar elevation diagram is Gutin shaped i.e. it has zero radiation along the axis of rotation, considerable torque force radiation in the plane of rotation, and a maximum radiation at about 30° below the rotor disc.

(h) The near field can extend to considerable distances from the rotor, particularly for low tip speeds, given by $NF = \frac{r_e}{M_e}$. Within the near field, the sound pressure is very much higher than the far field radiation equation predicts.

Fluctuating Lift ($S \neq 0$)

$$SP_{mB} = \frac{\alpha_{ST}}{2} \cdot K \cdot \gamma_q \cdot x_{chord} \cdot x_{span}$$

(a) Fluctuating lift can produce radiation in any part of the acoustic spectrum depending on the frequency of the fluctuation. For each blade loading harmonic S , there is a radiation passband given by $mB = \frac{S}{1 + M_e}$.

(b) For a given blade loading coefficient and thrust, the radiation level is basically independent of tip speed, and blade number; it is however dependent on rotor frequency.

(c) The polar elevation diagram is a distributive dipole with its axis along the rotor axis for $mB = S$, and Guttin shaped for all other radiations in the passband.

(d) Distributive loading, both chord and span, reduces the radiation at high frequencies; the larger the rotor geometry the more the radiation reduction.

Composite Blade Loading Radiation (All Values of S except $S = 0$)

$$SP_{mB} = \alpha_{ST} \cdot K_T \cdot mB \cdot \chi_{chord} \cdot \chi_{span}$$

(a) For a given rotor geometry and operating conditions, the radiation spectrum is proportional to the blade loading spectrum.

(b) Weak high frequency blade loading harmonics radiate appreciably. For example, the acoustic spectrum from a flat blade loading spectrum for non distributive loading, increases at 6 dB per octave in S or mB .

(c) The radiation level for a particular thrust is independent of tip speed providing that α_{ST} is independent of M_e . In this situation the sound pressure is proportional to the rotor frequency only. If α_{ST} is constant, and the thrust is proportional to M_e^2 , then the sound pressure level, for a given rotor radius, increases according to the sixth power of the blade speed. For any other function α_{ST} with M_e the sound pressure will

increase accordingly. The idea that blade force noise must be V^6 is nonsense; the acoustics say that the radiation increases at the rate of V^2 , the total power law then depends on the aerodynamics.

(d) The radiation is thrust dominated (dipole) with maximum radiation along the axis of rotation and residual torque force radiation in the plane of rotation.

(e) Distributive loading suppresses the high frequency radiation.

Impulsive Blade Loading Radiation

$$SP_{mB} = \frac{\Delta L}{L} \cdot E \cdot \rho \cdot K_T \cdot mB \cdot \chi_{chord} \cdot \chi_{span} \cdot \chi_S$$

(a) The radiation is proportional to the size and duration and number of impulses per blade revolution.

(b) The radiated spectrum shape depends on the blade loading spectrum content, which in turn depends on the profile and duration of the blade loading function excursion, the duration being the most significant parameter.

(c) For a truly impulsive blade loading function, the spectrum envelope increases at 6 dB per octave, distributive loading attenuating the higher frequencies.

(d) For a single excursion the radiation is purely thrust derived (dipole shaped) and the extent of the near field is very small.

(e) A zero-lift spectrum function, either $\chi_{chord}\chi_{span}$ or χ_S gives zero radiation only at zero frequency.

ROTOR NOISE PREDICTIONS

For heavily loaded low solidity rotors, the steady lift radiation will dominate the low frequency rotor spectrum. For a given number of rotor

blades, total thrust developed and operating speed, this form of radiation can be predicted reasonably well.

Before anything precise can be said about predicting the higher frequency noise, harmonic fall off, etc., or the complete spectrum on high solidity rotors, it is imperative to have a knowledge of the typical blade loading spectrum for the rotor. The relevant information in order of importance for noise predictions is

(a) The blade loading spectrum or trends in α_{ST} as a function of rotor geometry and tip speed: not at present available.

(b) Geometry of rotor, i.e. chord and span dimensions: modifies the blade loading spectrum radiation at the higher frequencies.

(c) Blade loading profile details: providing the loading is correlated both in chord and span, the profile details are only of secondary importance. (It is the total arithmetic loading that matters). If the loading wavelength is less than the chord or span length, then to a first approximation the respective loading wavelength replaces the blade dimensions in the χ_{chord} and χ_{span} functions, giving less radiation attenuation at the higher frequencies.

(d) Random element: two of the above parameters (a) and (c) will have a random element. In the first instance, the blade loading functions, under zero lift conditions, might be a purely random function arising from turbulence or random vortex shedding (unlikely under any circumstances with twisted blades). Under normal operating conditions, the blade loading function and hence the blade loading spectrum will vary slightly in amplitude and frequency content with each blade revolution; also the blade loading between blades could vary. Therefore the resultant spectrum will show band

spreading of the discretely giving rise to broadband radiation. However the blade loading spectrum function on average will basically determine the radiation spectrum envelope.

Secondly the effective chord and span loading regions, or the loading profiles might vary as the blade rotates. Providing on average the total arithmetic blade loading does not change, then the above effects will fluctuate the typical χ_{chord} and χ_{span} about an effective value.

RESEARCH RECOMMENDATIONS

Although the basic acoustic properties of rotor noise are now understood, the aerodynamic information vital to this work is unavailable. In order to develop reliable noise prediction techniques and reduce rotor noise generally, the following areas for further work are recommended.

(a) Blade loading harmonic spectra or blade loading coefficient α_{ST} should be measured simultaneously with acoustic radiation measurements. This is necessary to prove or disprove the theoretical relationship between α_{ST} and acoustic radiation. The relationship holds for low order blade loading data; the loading needs to be measured up to, say, 1000 Hz, which corresponds to about $S = 300$ for a helicopter rotor ($f = S.N$). Need to measure the total arithmetic blade loading and establish the general chord and span profile details. Also measurements of the effect of tip speed and rotor geometry (number of blades, pitch angle, etc.) on α_{ST} are required, and to establish if there is such a thing as a typical α_{ST} for a rotor. If it is found that there is good agreement in the relation between α_{ST} and the acoustic spectrum, then this relationship might be a useful concept in obtaining aerodynamic data.

(b) Study tip vortex properties. According to available acoustic

measurements and blade loading data, it appears there is not much difference in rotor noise levels between different flight regimes including hover, providing blade slap is not present. It is therefore thought that there is an intrinsic fluctuating force mechanism inherent in all free field rotors irrespective of external conditions. Such a possible source is the induced loading caused by either the production, shedding or paths of the tip vortices. If it can be established that tip vortices do affect rotor noise generation, then perhaps by adjusting the rotor geometry rotor noise can be reduced.

(c) Removal of fluctuating forces. There is little that can be done with existing rotor geometry to reduce helicopter rotor noise, unless the geometry affects α_{ST} . The fluctuating lift radiation level is effectively independent of tip speed and blade number, although perhaps the tail rotor solidity could be increased to reduce the audible tail rotor steady lift radiation. Therefore methods of reducing the fluctuating lift at the blade should now be studied. For example reactive, resistive and balanced lift aerofoils should be seriously considered to reduce the force fluctuations.

(d) Measure and compare rotor spectrums from a variety of clean flow rotors, to see if there are any trends in radiation patterns and therefore α_{ST} (to support item (b)). We require typical blade loading fluctuations, therefore measurements need to be made in the 'open air'. (The best anechoic facilities produce a degree of recirculation and therefore excessive blade loading variations).

(e) Study high forward speed effects. Measure blade aerodynamics in high speed forward flight and theoretically assess radiation (important for future generation helicopters).

(f) Long term study. Consider possibilities of new approach in thrust production. Conventional devices are noisy, crude but effective. They lose energy in drag and rotation, and accelerate the air impulsively. The possibilities of a linear device should be considered.

EXPERIMENTAL RESULTS

In the light of the discussion of the formal properties of rotor noise presented in the preceding sections, we now consider some relevant experimental results.

It is already a well established fact that rotational noise harmonics (discrete frequencies) occur in the broadband (vortex) noise region. For this reason it would appear that some authors have considered discrete frequency noise to be the most important from the point of view of the 'overall noise' level in all cases. It is clear, however, from experimental results that broadband noise of very significant levels are produced by some rotor configurations. In this section of the paper an attempt is made to illustrate the relative importance of these two main types of rotor noise.

It was known from tests on the I.S.V.R. single rotor rig that broadband noise, free from discrete components, could be obtained provided the turbulence and/or the re-circulation around the rotor was small. Unfortunately this could only be obtained in the laboratory with low lift conditions. Since it was desirable to know if these 'peaks' also occurred in the broadband - vortex region when the lift on the blade was high, a carefully controlled test was carried out using a Wessex helicopter. Recordings of the Wessex, hovering at an altitude of 40 ft. and 200 ft. from the microphone, were made in normal wind conditions (wind speed about 8 knots) and again with a very low wind speed environment (less than 2 knots). The narrow band

analysis results are shown in Figure 1; trace (a) shows a typical 1.5% narrow band analysis while (b) and (c) are $\frac{1}{2}$ Hz bandwidth analyses of the 'less than 2 knot' and '8 knot' wind conditions respectively. It will be noted there are many discrete components in the light wing case, trace c, and that the 'broadband' noise is practically the same level for both conditions. Further test results have shown that 'wind' is not the controlling parameter, and that the use of different helicopters and/or pilots produce the same order of differences in the spectrum. The two results reproduced do however tend to show the minimum and maximum discrete frequency noise content in the broadband region for this particular helicopter under normal operating conditions.

This clearly illustrates the effect of small scale turbulence and the occurrence of discrete frequencies in the broadband region. This does not imply that the rotational noise components are more important to the overall noise level for condition shown in trace (c), since if the energy is computed for a wide frequency range it will be greater from the 'broadband' than the discrete components.

It is worth noting that a 1.5% or 10 Hz analysis of the two conditions gives practically identical spectra shape with the '8 knot case' having slightly higher levels. Thus if a semi-narrow band analyser is used to measure broadband noise the maximum level detected could be due to the discrete components. This could explain the apparent anomalies in the 'broadband velocity laws' which have been found on certain helicopters.

On other rotor configurations rotational noise will dominate the overall level and the narrow band spectrum. A number of examples are illustrated in the narrow band analysis results reproduced in Figure 2.

Trace (a) is for a hovercraft propeller operating at moderate thrust, trace (b) shows the results from a Bell Helicopter in flight, and trace (c) is an analysis of one of the I.S.V.R. test rigs. All the recordings were taken at angles in the range $105/120^{\circ}$ from the direction of thrust and it is clear that in each case the 'overall levels' are dependent on the rotational noise components. It is also of interest to observe the large number of rotational components that can be detected on the latter two traces. From the results on Figures 1 and 2 it is obvious that either rotational (discrete frequency) or broadband noise can dominate the overall noise level, and in many cases the two types of noise can be equally important.

In the preceeding discussion on rotational and broadband noise, it should be remembered that the results do not imply that the two categories of noise are produced by separate mechanisms. Experimentally, however, it is necessary at the present time to consider the two types separately since they appear to follow different trends and theories are not sufficiently developed to allow the 'total noise' concept to be used.

An extensive study has been made of experimental data available to determine if the rotational noise spectra follows any general pattern. According to theoretical considerations the results should be studied as a function of 'mB' and not in terms of blade passing harmonics m. To date, however, the majority of results available are for 3 and 4 bladed rotors and it has only been possible to correlate the results relative to the fundamental frequency (first blade passing harmonic).

The envelope of the results is presented in Figure 3, together with the mean fall-off curve used for estimation purposes. Although the envelope applies in general to multibladed rotors operating at moderate tip speeds,

some results for a full size single bladed rotor show a similar pattern. A comparison has also been made between the Gutin 1st harmonic value, at an angle of $110/120^\circ$ from the direction of thrust, and measured levels of the fundamental. Good agreement was found to occur provided the thrust was large compared to the torque force, as in normal operating conditions.

As explained in earlier sections the directivity pattern associated with rotational noise, according to the fluctuating lift theory, is very different from that indicated by the 'Gutin' relationship. To date there has not been, to the authors knowledge, any full scale directivity tests although a programme of such work is due to commence at Westland Helicopters Ltd. in the near future. A series of model tests have been carried out at the I.S.V.R. using a small single rotor model in the anechoic room (5). A typical set of results is reproduced in Figure 4, where the patterns shown represent the average level for any angle. A narrow band analysis, at 110° to the direction of thrust, for this condition is shown in Figure 2(c).

The fundamental (1B) tends to be circular in shape, with the higher harmonics following a "figure 8" form (see figure). Theoretical estimates (3,4) and directivity plots obtained for the S58 (6) show similar characteristics. There is also close agreement between the experimental results and 'Gutin' predictions at an angle of 115° (position of maximum thrust effect) and good correlation between the 'Gutin solution' and measurements in the 'torque dominated region' in the rotor disc plane ($75^\circ - 105^\circ$).

It is obvious from a study of available data that further detailed experimental results are urgently required. It is thought, however, that in addition to the 'clean' type of investigation quoted in Section 4, ad hoc and flight tests will be required before the subject of rotor noise is fully understood.

REFERENCES

1. S.E. WRIGHT 1968 I.S.V.R. Technical Report No.5. Sound Radiation from a Lifting Rotor Generated by Asymmetric Disc Loading. (Also J.Sound Vib.)
2. H.K. TANNA 1968 I.S.V.R. Technical Report No.13. Computer Programme for the Prediction of Rotational Noise due to Fluctuating Loading on Rotor Blades.
3. S.E. WRIGHT 1969 I.S.V.R. Technical Report No.14. Theoretical Study of Rotational Noise.
4. S.E. WRIGHT and H.K. TANNA 1969 I.S.V.R. Technical Report No.15. Computational Study of Rotational Noise.
5. N.J. STAINER 1969 M.Sc. Thesis I.S.V.R., University of Southampton. (Unpublished).
6. J.W. LEVERTON and W.F. GRIMINSTER 1969 Westland Helicopters Ltd. (Unpublished). Rotational Noise Study.

SYMBOLS

B	blade number
F_T	total torque force on rotor ($F_T = L_T \sin \beta$)
$J_n(Z)$	Bessel function of first kind order n, argument Z
K	total operating constant ($K = K_T - K_q$)
K_q	torque force operating constant ($K_q = \frac{N}{Ra_o} \frac{F_T}{M_e}$)
K_T	thrust operating constant ($K_T = \frac{N}{Ra_o} T_T \sin \sigma$)
L_{OT}	total arithmetic steady lift on rotor
L_{ST}	total arithmetic fluctuating lift of order S
L_T	total lift on rotor
m	harmonic number
M_e	effective radial Mach number
N	ratio frequency Hz
R	observer dist. from rotor centre
r_e	effective rotor radius
S	blade loading harmonic number
SP	peak sound pressure
T	thrust per blade
T_T	total thrust on rotor ($T_T = L_T \sin \beta$)
W	width of load excursion
α_o	speed of sound
α_{ST}	total arithmetic B.L. coefficient ($\alpha_{ST} = \frac{L_{ST}}{L_{OT}}$)
β	force (or effective blade lift) angle
γ_{mB}	directivity function $\gamma = mB J_{mB} (mBM_e \cos \sigma)$
γ_q	directivity function $\gamma_q = mB J_q (mBM_e \cos \sigma)$

ΔL	load change per blade
$\frac{\Delta L}{L}$	fractional steady load change per blade
ρ	load solidity $\rho = \frac{W}{2\pi r_e}$
σ	observer elevation angle to rotor disc
x_{chord}	chord spectrum function
x_{span}	span spectrum function
x_s	blade loading spectrum function

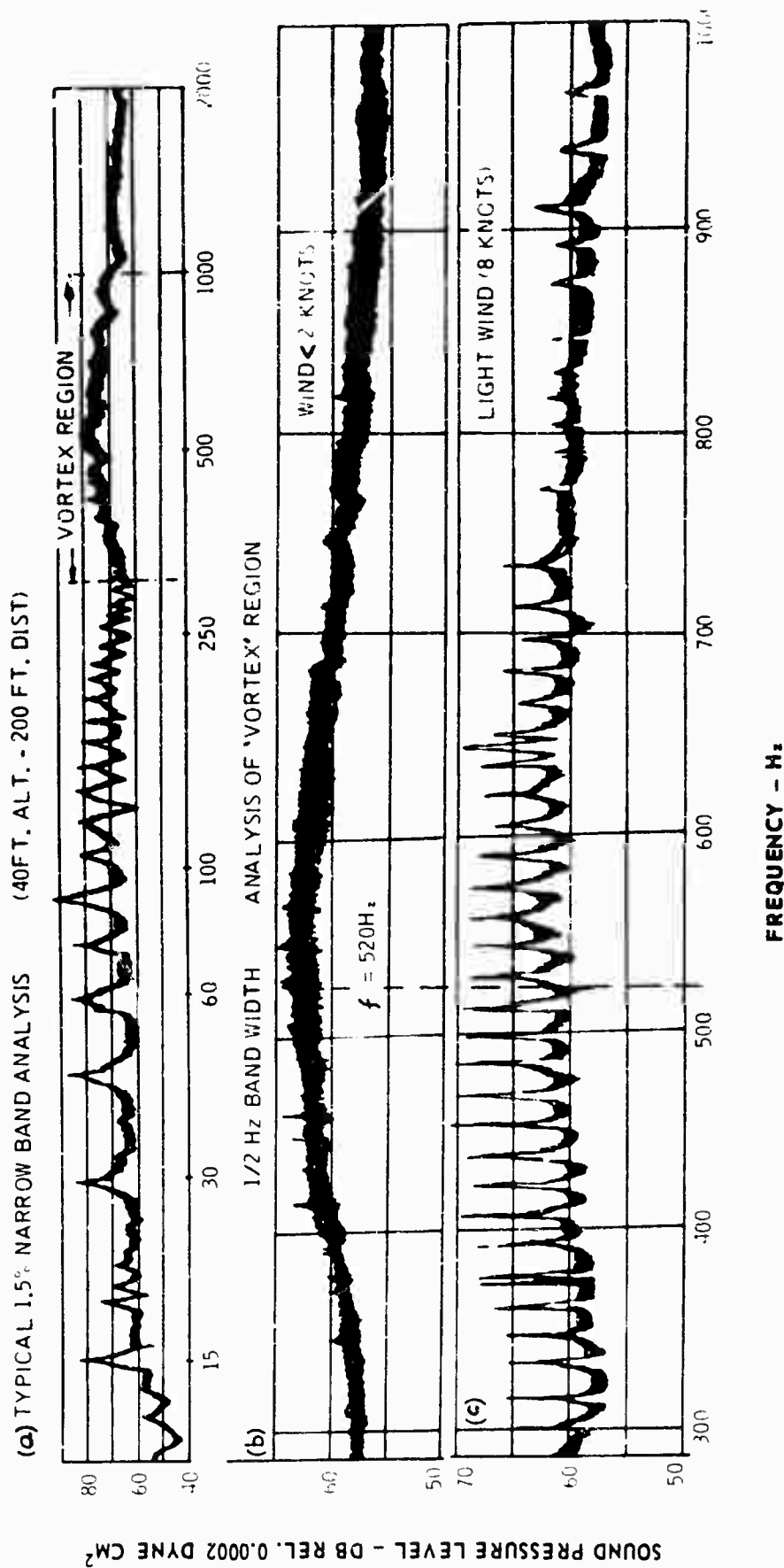


FIG. 1. NARROWBAND ANALYSIS OF HELICOPTER NOISE — HOVERING WESSEX.

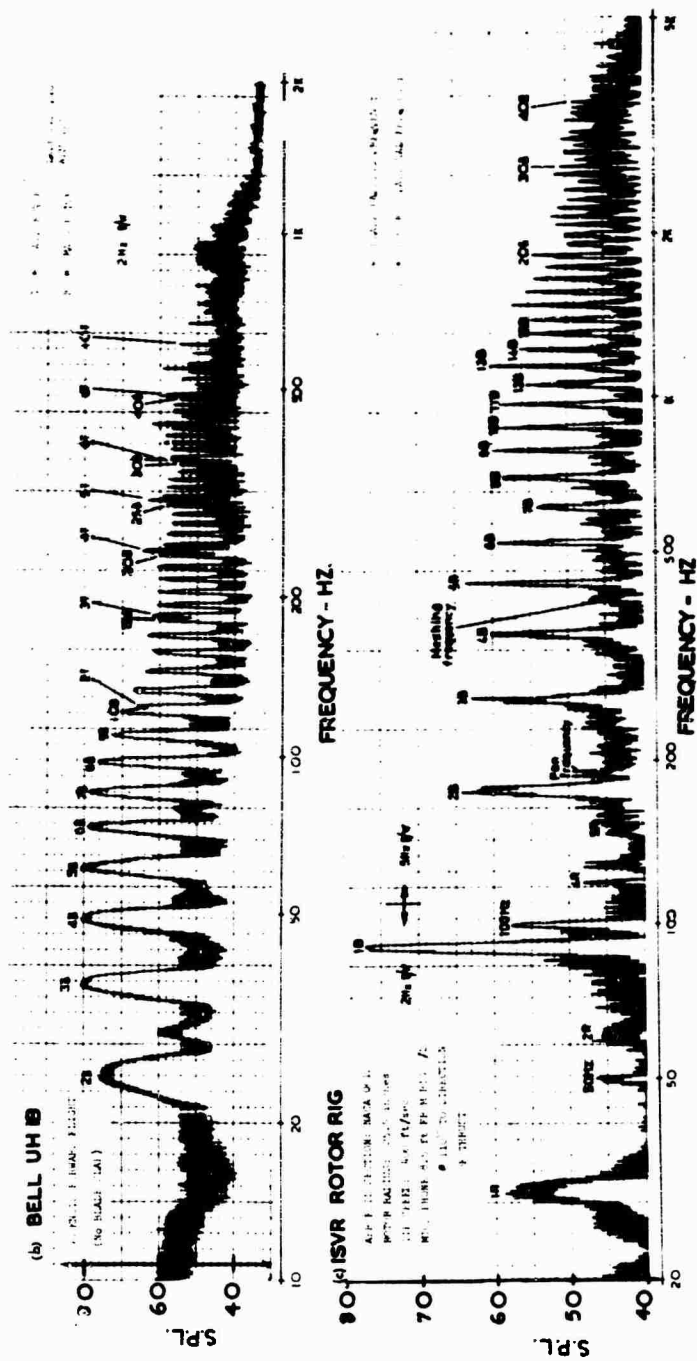


FIG. 2. NARROWBAND ANALYSIS OF ROTOR NOISE

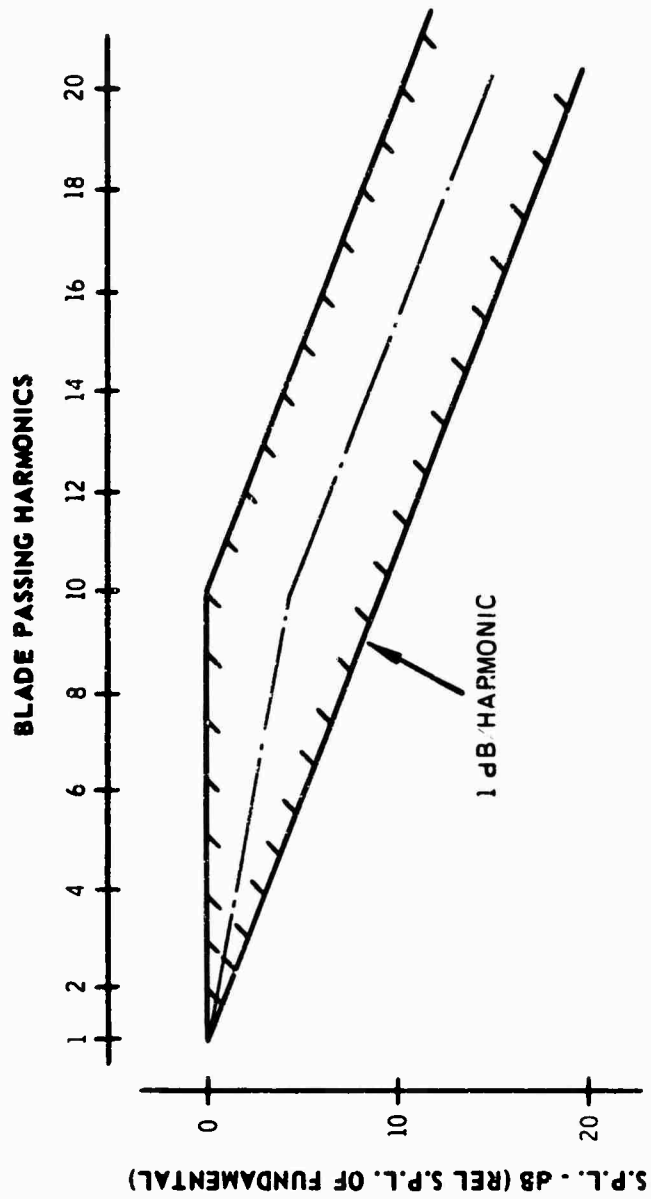


FIG. 3. MAIN ROTOR ROTATIONAL NOISE - HARMONIC 'FALL OFF'

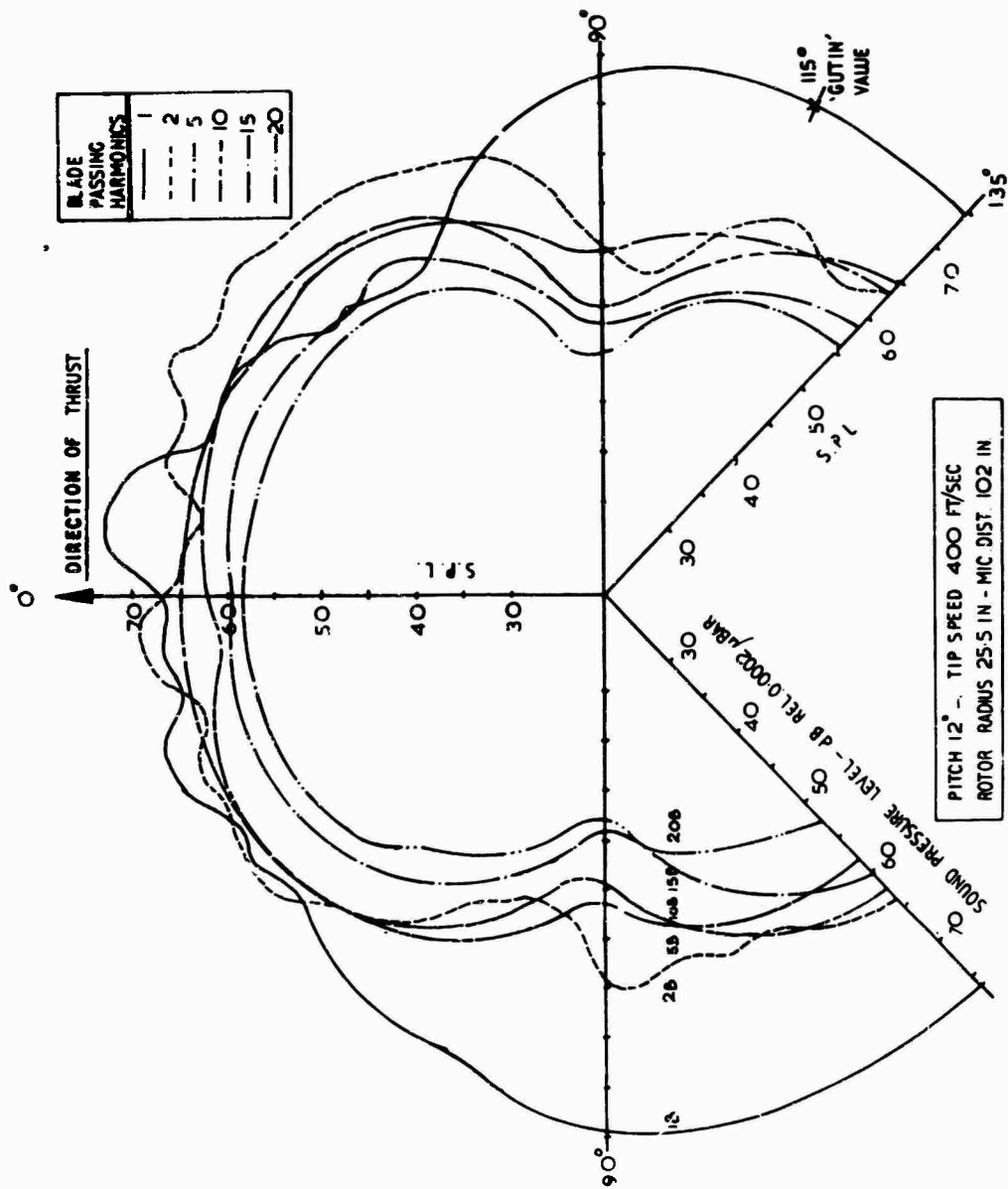


Fig. 4. POLAR PLOT OF ROTATIONAL NOISE

THE IMPORTANCE OF VORTEX SHEDDING EFFECTS ON
HELICOPTER ROTOR NOISE WITH AND WITHOUT
BLADE SLAP*

By

S. G. Sadler
Rochester Applied Science Associates, Inc.

R. G. Loewy
University of Rochester
Rochester, New York
U.S.A.

SUMMARY

Vortex noise is an important noise source for helicopters in some flight conditions, and contains frequencies in the range of high sensitivity of the human ear. There are indications that vortex noise may be an important source of noise in blade slap, which is one of the most objectionable helicopter noises. This paper reports results of a theoretical investigation directed toward prediction of helicopter rotor noise, including both rotational and vortex noise.

The prediction method developed for this investigation allows either near or far field noise to be calculated, including all effects other than blade thickness and random turbulence in the boundary layer or the wake. The effects of both impulsive changes in load around the azimuth and that of vortex noise were investigated for various flight conditions for the H-34 helicopter and for the HU-1A helicopter in hover. The predicted noise is presented both as plots of sound pressure level versus harmonic number and by plots of pressure time history. Comparisons of predicted results with appropriate measurements obtained for the HU-1A and

*Based on work supported by NASA under Contract No. NAS1-7618.

H-34 were made for selected cases.

The main results of the investigation were that the inclusion of vortex shedding effects in addition to the rotational effects significantly improved the prediction of the measured noise levels as compared to that obtained by considering only rotational effects, and that "blade slap" characteristics are most readily observed and thus investigated through the use of pressure time history plots. These theoretical results, together with previously obtained experimental results, indicate that discrete vortex shedding from a rotor blade may be a predominant source of noise during normal operation and when blade slap occurs. Further investigations are necessary to determine the characteristics of such vortex shedding from helicopter blades.

INTRODUCTION

The use of turbine power plants in rotary wing and V/STOL aircraft leaves the rotor-propeller as an important source of low-frequency noise. Military applications of helicopters in tactical situations (ref. 1), as well as increased commercial use in heavily populated areas, have made understanding the lifting rotor-propeller as a noise source an important technical objective. Discomfort, proficiency impairment, and the danger of permanent hearing loss due to high intensity noise inside the aircraft are important additional motivations for developing better understanding of rotor noise. This is especially true since it is generally accepted (see ref. 2, for example) that reductions of low frequency noise inside the aircraft must be achieved at the source. In particular, the weight penalty for significant attenuation inside the aircraft is usually prohibitive for frequencies below about 200 cps.

In addition to the reasons outlined above for studying the origin of the noise generated by a rotor, it is believed

vitally important to investigate the characteristics of vortex noise since the pulsatile nature of helicopter noise may be due in part to modulated high frequency noise such as vortex noise. In particular, it is generally agreed that this pulsatile characteristic is important in detection of helicopters in tactical situations. It is known that vortex noise is an important noise source for helicopters in some flight conditions, and it is expected that it may become a relatively more important noise source for all flight conditions as engine noise, tail and main rotor rotational noise, and other noise sources are understood and more effectively controlled. Vortex noise is reported in some cases (ref. 3) to be the dominant noise source in a frequency range which is that of maximum human ear sensitivity. Thus, the subjective loudness of vortex noise in such cases may be greater than the loudness of low frequency rotor rotational noise of higher absolute magnitude.

When blade slap occurs in high speed forward flight or in maneuvers, it is the dominant noise source, and is one of the most objectionable helicopter noises. There are indications that vortex street noise may be an important source of noise in blade slap. For example, some of the characteristics of the noise signature associated with blade slap, such as its high frequency content, can be explained by the vortex street phenomenon (ref. 3). That is, aerodynamic separation on the airfoil can result in the generation of high amplitude high frequency vortex noise. Such separation could be due to a number of effects, such as stall, blade interaction with the trailed vortex of another blade, and formation of a shock, which would result in separated flow over a portion of the azimuth. Sadler and Loewy, (4), have shown that predicted pressure time histories with rotational but not vortex shedding forces as a noise source do not show the typical blade slap characteristic of high amplitude high frequency noise over

a limited portion of the period. The inclusion of vortex shedding forces in addition to rotational forces, however, did result in a pressure time history with this blade slap characteristic.

While vortex noise has long been considered an important source of noise of rotating lifting surfaces, relatively little has been done to determine its basic functional characteristics and effects. Vortex shedding noise from rotating cylindrical bodies was first measured by Stowell and Deming, (5). Later Yudin, (6), and Blokhintsev, (7) developed theories predicting such noise. Hubbard (8), has reported overall noise levels due to all sources on propeller blades, and has given an estimate of the noise due to vortex shedding. Schlegel, et al., (9), have made further refinements in Hubbard's vortex noise magnitude formula. However, neither the frequency nor magnitude of the oscillatory lift and drag forces due to vortex shedding have been measured on airfoils in the range of flow conditions of normal helicopter rotor blades. Krzywoblocki, (10), has measured the vortex shedding frequency for airfoils at low Reynolds numbers; however, the data for angles of attack below stall has wide scatter. Roshko, (11), has measured the frequency of shedding from circular cylinders in high Reynolds number flow, but not for airfoil type sections. Until such time as the necessary experimental measurements are made, approximate methods for estimating the necessary characteristics must be used in predicting helicopter noise due to vortex shedding.

Although there are fundamental gaps in the knowledge of vortex shedding characteristics from helicopter rotors, reasonable assumptions can be made, which result in approximate blade loads due to vortex shedding. This together with measured or theoretical aerodynamic blade loads provides the basic information needed for sound pressure calculations. A considerable foundation of experience

that can be applied to the problem of predicting helicopter rotor noise exists by virtue of propeller noise research performed in the past (ref. 12, 13 and 14). In addition, several programs directed at increasing the understanding of rotor noise have been carried out recently (ref. 3, 9, and 15 through 17). Nevertheless, successful prediction of the sound pressure level versus frequency has not been realized to date. It is believed that previous attempts have not been successful because both the rotational and the vortex shedding effects have not been considered simultaneously in the development of these methods. Acceptable prediction of the sound pressure level versus frequency is important to provide the understanding that is required before any investigation to reduce the noise level can be successfully accomplished. The purpose of the present study, therefore, was to develop a method by which both the rotational and vortex shedding effects are properly accounted for in the prediction of the noise generated by a lifting rotor.

Garrick and Watkins' work (ref. 14) and extensions of it have dealt with rotational noise generated by propellers. In reference 16 the theory of Garrick & Watkins was extended to allow prediction of the rotational noise generated by lifting rotors in forward flight. This theory for predicting helicopter rotor noise has been extended here to include the effects of the rotor being acted upon by lift and drag forces associated with vortex street type of shed vorticity as described by Yudin (ref. 6).

The authors wish to acknowledge the assistance of Mr. Harry Sternfeld and Mr. Robert Spencer of The Vertol Division of The Boeing Company, who provided narrow band sound spectrum analyses and pressure time histories for use in the comparison of theoretical and measured data.

SYMBOLS

a_{m_i}, b_{m_i}	Fourier coefficients of pressure time history, psi
ASL	aerodynamic section loading, i.e., force normal to the blade chord per unit span, pounds/inch
B	number of rotor blades
C_i	blade chord at i^{th} radial station, feet
C_{Lv}, C_{Dv}	coefficients of oscillatory lift and drag, dimensionless
d	projected body dimension in a direction perpendicular to the local resultant velocity, feet
e	flapping hinge offset, feet
f	frequency of vortex street shedding, cycles per second
$F_{m_{x_{ij}}}, F_{m_{y_{ij}}}, F_{m_{z_{ij}}}$	complex amplitude of force acting on the fluid in the x, y, z directions, respectively, at the frequency of the m^{th} harmonic, at the source point ij
h	vertical distance between rows of vortices in the vortex street, feet
$i = \sqrt{-1}$	imaginary unit
$k_m = \frac{mB\Omega}{C}$	inverse of wavelength of m^{th} harmonic, 1/feet
L_v, D_v	oscillatory lift and drag acting on incremental span length, pound/foot
m	harmonic number

$M_N = V/C$	Mach number
P	sinusoidally varying pressure, dynes/cm ²
P_ω, P_m	complex amplitude of pressure sinusoidally varying at frequency ω or harmonic m
r_i	blade radius at station i , measured from shaft axis along unflapped blade, feet
R	total rotor radius, feet
$S_t = \frac{fU}{d}$	Strouhal number
$SPL = 20 \log_{10} \frac{P_{rms}}{P_{ref}}$	sound pressure level, decibels
t	time, sec, measured from $\psi = 0$
$T = \frac{2\pi}{B\Omega}$	fundamental period, second
U	resultant air velocity perpendicular to a blade leading edge, feet/ second
U_p	component of U perpendicular to plane perpendicular to shaft axis swept surface, positive up, feet/ second
U_T	component of U tangent to a plane perpendicular to the shaft axis, feet/second
V	aircraft forward velocity, feet/ second
V_D	aircraft descent velocity, feet/ second

γ_s	tilt of rotor shaft relative to vertical, positive aft, radians
β_0	coning angle, measured positive up from a plane perpendicular to the shaft arm, radians
β_1	coefficient of longitudinal flapping, positive so as to make rotor shaft tilt aft, radians
β_2	coefficient of lateral flapping positive so as to make rotor shaft tilt to port, radians

$$\gamma = \sqrt{1 - M_N^2}$$

ρ	air mass density, slugs/feet ³
ψ	azimuth angle, zero in the trailed position, degrees or radians
ω	frequency of oscillatory pressure, radians/second
Ω	rotor angular velocity, radians/second

Subscripts

i	radial station
j	azimuthal station
m	harmonic number
o	field point, or steady component
x, y, z	direction of force, along positive Cartesian axes
ω	frequency component

ANALYSIS

The formulation of the technique discussed herein follows the general procedure developed in reference 16. That is, pressures applied to the air by the rotor blades are assumed to be known, based on available theory or experimental measurements. The pressures at a point on the rotor disc are of a pulsatile nature, and are assumed to be periodic with blade passage frequency. This periodic pressure pulse is then approximated by a finite Fourier series, and the resulting sound field at an observer location is found by summing the effects of all the harmonic oscillators over the entire rotor disc. The magnitude and phase of each harmonic of rotor blade passage frequency is then known at the observer, so that pressure time histories, SPL versus frequency plots or other desired information may be obtained. Theoretically, any source of pressure on the blades can be represented by this approach. The effects of the approximately "white" noise which exists in the turbulent boundary layer sheathing the blades, which is modulated for the observer at the blade passage frequency (ref. 3) was ignored in this study. Also, as discussed in references 18 and 19, pressure fluctuations due to the passage of the complex wake of trailed vorticity as experienced by an observer translating with the rotor were not considered. The effects of the trailed vorticity were accounted for indirectly through their effect on the azimuthal and radial distribution of the blade loads. Effects specifically accounted for in the analysis procedure developed herein include:

1. Azimuthal and radial variations of the velocity normal to the leading edge, the angle of attack, the lift and drag forces, and the vortex street shedding frequency and strength;

2. non-linear and compressible airfoil section characteristics;
3. numerical integration over the rotor, eliminating near and far-field approximations;
4. reversed flow; and
5. blade coning, collective pitch, and first harmonic flapping and cyclic pitch.

The effects of radial and azimuthal inflow nonuniformities at the rotor whether due to the fundamental aerodynamic characteristics of rotors in forward flight or due to blade-fuselage and/or rotor-rotor interference were, of course, included in that the method uses measured blade air loads.

A numerical approach to the prediction of the rotational noise has been shown to be useful (ref. 16) in that the previously discussed effects can be included to any desired degree of refinement. For this reason, the same approach has been used in the development of the method reported herein, which includes both rotational and shed vortex effects. Since the method formulated herein makes use of Garrick & Watkins' basic theory (ref. 14) the distortion of dipole radiation pattern and Doppler effects (which can cause significant frequency shifts for an observer in the non-rotating system) are an inherent part of the analysis procedure.

Derivation of Acoustic and Geometric Relationships

Three coordinate systems were used in the analysis technique that is developed herein. A polar coordinate system was used to describe the azimuthal and radial variation of blade forces in the rotor disc, a Cartesian coordinate system was used to describe the location of a source point on the disc with respect to an observer, and a polar coordinate system was used to describe the

location of an observer. All of the coordinate systems have their origin at the center of the rotor hub (see figure 1), so that they translate with the flight velocity, V . The Cartesian coordinate system is oriented such that (1) the z -axis is vertical, and (2) the positive x -direction points in the direction of flight. The polar coordinate system which describes the location of an observer measures the azimuth angle, ψ_0 , in the x - y plane and is zero on the negative x -axis. The polar coordinate system which describes the location of quantities in the rotor disc is oriented such that the azimuth angle, ψ , is defined in a plane perpendicular to the shaft and is taken to be zero on the negative x -axis, as is shown in figure 2. Points on the surface area swept out by the rotor blades at which the instantaneous blade forces are assumed to act are called "source points" and are located by x, y, z coordinates. A general point outside the swept area but translating with the rotor is called a "field point" and is located by x_0, y_0, z_0 in the Cartesian coordinate system and by R_0, ψ_0, Z_0 in a polar coordinate system. Since integration is performed over the swept area, the "source points" are specified using a double subscript notation i, j . Here i identifies the radial position and j the azimuthal position.

Equations for determining x, y, z coordinates of the source points are derived geometrically by examining the position of a particular blade of the rotor at any time, t . It was assumed that the blade is inflexible but has a "flapping hinge," offset a distance, e , from the center of rotation. This allows a blade to rotate out of the plane of rotation through an angle β_j , which is assumed to be small. A point on the blade is defined as being a distance r from the center of rotation when $\beta = 0$. No other motion of the blades with respect to the hub, other than pitch changes, were taken into account. The rotor shaft is allowed to be tilted through an angle α_s in the longitudinal plane. Blade

point coordinates are then given (see, for example, ref. 20), when small angle assumptions are made for $\sin \beta$ and $\cos \beta$, by

$$x_{ij} = - r_i \cos \psi_j \cos \alpha_s - \beta_j (r_i - e) \sin \alpha_s \quad (1a)$$

$$y_{ij} = - r_i \sin \psi_j \quad (1b)$$

$$z_{ij} = - r_i \cos \psi_j \sin \alpha_s + \beta_j (r_i - e) \cos \alpha_s \quad (1c)$$

As in reference 14, the sinusoidally varying pressure at a field point (x_0, y_0, z_0) with the frequency $\omega = mB\Omega$ is defined as

$$P(x_0, y_0, z_0, t) = \text{Re} \left[P_\omega(x_0, y_0, z_0) e^{i\omega t} \right] = \text{Re} \left[P_m(x_0, y_0, z_0) e^{imB\Omega t} \right].$$

Here Ω is the rotating frequency of the rotor, and Re , of course, signifies taking the real part of a complex number. Periodic conditions are assumed; i.e., what happens in one revolution happens in every other, and in fact, what happens to one blade at a particular azimuth is repeated on every other blade when it is at that azimuth. It follows, therefore, that the fundamental period is $T = \frac{2\pi}{\Omega B}$; and m is the harmonic number. By determining the harmonic components of the forces acting on the fluid at a source point in the directions of the coordinate axes, namely $F_{m x_{ij}}$, $F_{m y_{ij}}$, and

$F_{m z_{ij}}$, then the sound pressure at a field point can be calculated

from the expression

$$\begin{aligned}
& \text{Re} \left[P_m(x_0, y_0, z_0) e^{imB\Omega t} \right] \\
&= \text{Re} \left[\frac{1}{4\pi} \left(F_{m_x} \frac{\partial}{\partial x_0} + F_{m_y} \frac{\partial}{\partial y_0} + F_{m_z} \frac{\partial}{\partial z_0} \right) \frac{e^{-ik\sigma}}{S} e^{imB\Omega t} \right] \quad (2)
\end{aligned}$$

which was given, in slightly different form, as eq.(6) in reference 14. Here,

$$k = \frac{mB\Omega}{C}$$

$$S = \sqrt{(x_0 - x)^2 + \gamma[(y_0 - y)^2 + (z_0 - z)^2]}$$

$$\sigma = \frac{M_N(x_0 - x) + S}{\gamma^2}$$

$$M_N = \frac{V}{C}$$

C = velocity of sound

$$\gamma = \sqrt{1 - M_N^2}$$

As may be seen from equation (2), Fourier components of force vectors are needed for computation of sound pressures. In order to compute these forces, however, the blade normal and tangential velocity components and the angle of attack must be determined.

The normal velocity component designated by U_p is parallel to the shaft axis and is positive up, and the tangential velocity component U_T , is perpendicular to the shaft axis and is positive when directed toward the airfoil leading edge. Accounting for

components of forward speed, rotational speed, descent speed, an average induced velocity component v , (assumed positive down) and an effective component normal to the chord as a result of flapping velocity $\dot{\beta}$, yields the following expressions for the two velocity components.

$$U_R = V \cos \alpha_s \sin \psi + \Omega r - V_D \sin \alpha_s \sin \psi,$$

$$U_P = V (\sin \alpha_s - \beta \cos \alpha_s \cos \psi) - v - \dot{\beta}(r - e) + V_D \cos \alpha_s. \quad (3)$$

These expressions for the velocity components were derived neglecting the radial component of velocity, applying the small angle approximation to the flapping motion, and assuming that the usual two-dimensional strip theory approach is applicable. The actual induced velocity is a quantity, which, in general, varies both over the blade radius and azimuth, and its calculation has been the subject of extensive research. Its effect on angle of attack may be quite significant, especially where U_P might otherwise be small. It is usually assumed, however, that induced velocities in the plane of the rotor are small compared to U_T , except where that velocity is small, in which case the resulting forces are unimportant. For this reason, the resulting velocity U_{ij} is calculated using an induced velocity v assumed to be uniform over the disc, and calculated for hover and forward flight from the momentum theory expression (ref. 21),

$$v = \frac{\text{thrust}}{2\pi R^2 \rho [(v \sin \alpha_s - v)^2 + (V \cos \alpha_s)^2]^{1/2}}.$$

For the case of a helicopter in vertical descent the induced velocity was determined approximately from figure 6-9 of reference 20.

As shown in figure 3, the blade angle of attack, α_{ij} is a function of the velocity components U_p and U_T and the local geometric blade pitch angle, θ_{ij} . As in reference 16, these velocity components are used in conjunction with experimentally determined airfoil section coefficients and measured aerodynamic normal forces to determine the radial and azimuthal variations of the section angle of attack and the lift and drag forces. The manner in which this is accomplished is presented in detail in reference 16 and is outlined briefly below. The resultant velocity for each element of swept area corresponding to a source point is calculated from

$$\begin{aligned}
 U_{ij} &= \sqrt{U_p^2 + U_T^2} \\
 &= [(V \cos \alpha_s \sin \psi + \Omega r - V_D \sin \alpha_s \sin \psi)^2 \\
 &\quad + (V \sin \alpha_s - V\beta \cos \alpha_s \cos \psi - v - \dot{\beta}(r - e) + V_D \cos \alpha_s)^2]^{1/2}
 \end{aligned}
 \tag{4}$$

the Mach number from

$$M_{N_{ij}} = U_{ij}/C$$

and the normal force coefficient, $C_{N_{ij}}$, from

$$C_{N_{ij}} = \frac{(ASL)_{ij}}{1/2 \rho (U_{ij})^2 C_i} \tag{5}$$

These values for $M_{N_{ij}}$ and $C_{N_{ij}}$ were used to determine aerodynamic angle of attack, coefficients of lift, incompressible drag, and

compressible drag from measured data by a table look-up procedure. Aerodynamic forces acting on the blade as vectors parallel to and perpendicular to the instantaneous resultant velocity were then computed. The ASL, or aerodynamic section loading, data is taken from references 22 and 23 for the H-34 and HU-1A, respectively, and are given there at various azimuthal and radial stations, as loading in lb/in.

Representation of Vortex Street Characteristics

The vortex street phenomenon exists only when a separated wake exists, and viscous effects as seen in the boundary layer are the source of the wake. One of the objects of airfoil design is, of course, to minimize separation. It cannot be completely prevented, but in the normal operating range of angles of attack of smooth airfoils it occurs near the trailing edge. There is a dearth of references in the literature concerning vortex streets associated with airfoil shapes at angles of attack below stall. Some evidence that it does exist, as has been implicitly assumed by Yudin (6), Hubbard and Regier (24), and Schlegel, et al. (9), can be found. For example, Stowell and Deming (5) could not find a discrete vortex noise frequency during experiments in which all sections but one of a rotating rod were streamlined cross sections. This suggests strongly that the streamlined sections shed vortices as well as the non-streamlined section. As another instance, measurements of axial-flow fan noise showed a velocity dependency proportional to the sixth power of the tip speed (ref. 25). This result correlates well with the tip speed power dependence predicted by Yudin's theory, which is based on the vortex street mechanism. Also, Blokhintsev (ref. 7) reports that the vortex noise of propellers has a spectrum in which a narrow range of frequencies stands out relatively strongly, which is understandable if the intensity of the vortex noise is proportional to the sixth power of the velocity. These cases support the intuition of the

earlier investigators (refs. 9, 19, and 24); namely, that the wake formed from a separated boundary layer might be influenced by its width at the separation point and the flow conditions there, but not by the detailed shape of the generating body.

Roshko (ref. 26) has shown from theory and experiment that the distance between the separation points on a bluff cylinder and the value of the pressure coefficient there determines the frequency of the vortex street. Roshko, therefore, defined a new "universal Strouhal number" which is not a function of Reynolds number. Such an approach is useful for the prediction of vortex shedding effects from airfoils, but existing data is insufficient for evaluating some of the parameters in Roshko's expressions or for determining their applicability to streamlined bodies such as airfoils at low angles of attack. Therefore, the standard definition of Strouhal number was used in all calculations, that is

$$S_t = fh/U \quad (6)$$

where S_t = Strouhal number (about .17),

f = vortex street shedding frequency, cps,

h = (constant) $\times d$,

d = projected dimension of the body perpendicular to the resultant velocity, ft, and

U = resultant velocity, ft/sec.

For thin airfoils at small angles of attack, α , the projected dimension is approximately

$$d = c \sin \alpha + t_{\max} \cos \alpha.$$

Values of h/d between 1 and 1.54 have been used or suggested in the literature, and no experimental measurements on airfoils at

low angles of attack exist from which these relationships might be more accurately determined.

In order to determine vortex street noise there are other characteristics which also must be defined. These characteristics include the frequency of the oscillatory drag associated with the vortex street, as compared to the frequency of the oscillatory lift; and the magnitude of the oscillatory vortex street lift and drag forces. The oscillatory drag force associated with the vortex street has twice the frequency of the oscillatory lift force when the body is symmetrical with respect to the free stream, as is the case for a circular cylinder or a symmetrical airfoil at zero lift. That is, the effect of the vortex arrangement at an instant in time on the pressure distribution about the body gives the same drag effect as a vortex arrangement one half cycle later. In figure 4, the two vortex street arrangements which are 180° out of phase are indicated by solid and dashed lines, respectively. When the body is not symmetrical with respect to the free stream, vortices one-half cycle apart do not necessarily give the same drag effect. Therefore, as angle of attack increases there is an increasingly important component of the oscillatory drag which has the same frequency as the oscillatory vortex lift. In addition, it is expected that the airfoils will operate most of the time at non-zero angles of attack. Therefore, only the component of oscillatory drag which has the same frequency as the oscillatory lift is considered in the present analysis.

Yudin (ref. 6) has made a dimensional analysis of the magnitude of the oscillatory lift force with the conclusion that this lift force magnitude has the form

$$L_v = C_{Lv} (1/2 \rho U^2 c) \quad (7)$$

where

$$C_{Lv} = 2k_L (c/h) (CD_v)^2$$

k_L = constant of proportionality for lift

CD_v = steady drag coefficient

The oscillatory drag force magnitude may be assumed to have a similar form, that is

$$D_v = C_{Dv} (1/2 \rho U^2 c) \quad (8)$$

where

$$C_{Dv} = 2k_D (c/h) (CD_v)^2$$

k_D = constant of proportionality for drag.

The functional dependence of k_L and k_D on CD_v and h/c , and an estimate of the magnitude of k_L may be obtained from theoretical expressions due to Lamb (ref. 27) and Blokhintsev (ref. 7). It is found that for circular cylinders with vortex shedding that

$$k_L = K_L (h/c) / CD_v . \quad (9)$$

It can be determined that $K_L \approx 0.09$, as an estimate of magnitude. For this form for k_L , and assuming the same form for k_D , the vortex street lift and drag force magnitudes for airfoils are assumed to be

$$L = K_L \rho U^2 c \Delta r CD_v \quad (10)$$

and

$$D = K_D \rho U^2 c \Delta r CD_v \quad (11)$$

where K_L and K_D are vortex street constants for lift and drag and are to be determined.

Lighthill (ref. 28) points out that sound intensity is not always proportional to $(\Delta r)^2$ as was assumed by Lamb and Blokhintsev, but that it is proportional to $(\Delta r) (\ell_c)$, where ℓ_c varies with Reynolds number, and is called a correlation length. This length is that within which lift fluctuations are well correlated. The correlation length generally decreases with increasing Reynolds number from Δr to the order of magnitude of the projected body dimension, d . The effect of using $(\Delta r) (\ell_c)$ instead of Δr^2 on eqs. (10) and (11) is that Δr would be replaced by $(\Delta r \ell_c)^{1/2}$. It was assumed that $\ell_c = \Delta r$ for all the results reported herein. Cancellation of noise between various radial and azimuthal stations is allowed.

It is noted, however, that the work of Etkin, et al., (ref. 29) indicates that $K_L = 0.09$ as determined by the preceding theoretical approach for circular cylinders is approximately one-fifth the magnitude of that found by experimental methods. They also observed that the drag force had an order of magnitude of about one-tenth the oscillatory lift force magnitude, and oscillated at twice the lift force frequency. Work reported by Foughner and Duncan (ref. 30) indicated that for large circular cylindrical bodies the magnitude of the oscillatory drag was about one-half of the oscillatory lift force magnitude. Based on the above noted experimental work, $K_L = 0.1$ to 1.0 and $K_D = 0.05$ to 0.5 might be expected.

No measurements of the magnitude of the vortex street lift and drag forces are known to exist for airfoils. The method by which estimated values of K_L , K_D for airfoils were determined for use in predicting the noise characteristics of helicopters was to assume nonzero values for K_L and K_D , and to adjust these values

as guided by the method of least squares fit. It was assumed that the proper values for the vortex street constants are those which make the theoretical noise levels approximate the measured noise level at off-harmonic frequencies.

Once the magnitude and time dependence of all forces on the rotor blades are known, the sound pressure at a point may be determined from Eq.(2) by the appropriate summation, and has the form

$$P(t) = a_0/2 + \sum_{m=1}^N (a_m \cos mB\Omega t + b_m \sin mB\Omega t). \quad (12)$$

In theory $N \rightarrow \infty$, but in practice N is finite, and in this program $N=20$ was used. The a_m and b_m are summations of Fourier coefficients from all the rotor disc sources, and have units of psi. The SPL in dB (referred to 0.0002 dynes/cm²) is given for the m^{th} harmonic frequency as

$$\text{SPL} = 10 \log_{10} \left\{ \frac{1}{2} \left[\frac{478.8}{0.0002} \right]^2 [a_m^2 + b_m^2] \right\} . \quad (13)$$

RESULTS AND DISCUSSION

This section of the paper will first present and discuss an evaluation of the pertinent characteristics of the experimental measurements with which the predicted noise will be compared. The manner in which the controlling shed vortex parameters were determined will then be presented. A comparison of measured and predicted SPL's for two different helicopters in hover flight will be made, predicted SPL's for various flight conditions for one of the helicopters will be presented and discussed, and predicted and measured pressure time histories will be presented. The need for further investigation of vortex shedding characteristics will then be discussed.

Analysis of Experimental Measurements

Noise characteristics of helicopters are usually described on the basis of plots of sound pressure level versus frequency, or pressure time histories. Correct understanding and interpretation of such experimental data is vital to the use of such data for comparison with theoretical data or to give proper direction to the development of analysis techniques.

The following discussion presents experimental data which will later be used for comparison with predicted results. It is necessary to understand the pertinent characteristics of the experimental data in order to make a meaningful comparison between theory and measurement. Data for the HU-1A and the H-34 are used in this report as a basis for such comparisons.

Figure 5 shows a measured sound pressure level versus frequency curve for an HU-1A. Main rotor harmonic number locations are indicated. Instrumentation calibration characteristics, together with the SPL versus frequency plot give harmonic spacing within 2% of the spacing predicted for the normal rotor speed of 314 RPM. This error is well within that expected for rotor speed measurement. High amplitude off-harmonic peaks are not expected and do not occur for frequencies up to the fifth blade passage harmonic since the dominant source of noise in this frequency range is rotational noise from the main rotor which generates sound only at harmonics of the blade passage frequency. (The first main rotor harmonic is not recorded due to low frequency cut-off of the instrumentation).

Tail rotor noise is significant, as is seen from figure 5. Gear ratios and effectively inflexible shafting result in tail rotor harmonic spacing approximately 5.14 times the main rotor harmonic spacing. The first five main rotor harmonic peaks and

and the first three or four tail rotor harmonic peaks are dominant in their respective frequency ranges, and come very near the expected frequencies. However, above the sixth main rotor harmonic (about 60 cps) there are off-harmonic peaks of the same order of magnitude as the main rotor peaks. Since the HU-1A has a turbine engine, the engine noise should be small at these relatively low frequencies. As may be seen from figure 5, the tail rotor harmonic spacing is uniform, which strongly suggests that the instrumentation is not causing frequency shifting of the peaks of the SPL versus frequency plot. However, peaks on the order of magnitude of main rotor noise peaks do occur at frequencies not identified as main rotor or tail rotor frequencies (and with spacing which is not main rotor harmonic spacing). Since the frequency scale appears to be reliable, and since peaks were measured at frequencies and with spacings which cannot be due to main or tail rotor peaks, these off-harmonic peaks must be due to another source which is not periodic with respect to main rotor or tail rotor blade passage. A nonuniform rotor speed could result in blade loadings which differ from blade to blade at the same azimuth point, and thus produce off-harmonic noise. This however is not believed to be the case. Vortex shedding of the vortex street type is a noise source which is not periodic with respect to blade passage and which may account for some of the off-harmonic noise peaks that are observed.

Figure 6 shows a plot of SPL versus frequency for an H-34 helicopter with which theoretical predictions will be compared. The largest peaks that are observed do not generally occur near main rotor harmonic frequencies and have been identified as engine noise. The engine firing frequency is about 20.5 cps, and this is the spacing of SPL peaks marked by the letter E. The main rotor harmonic spacing is about 14.7 cps, and these harmonic positions

have been indicated by M. (As with the HU-1A data, the first main rotor harmonic is not recorded due to low frequency cut-off of the instrumentation). Tail rotor harmonic positions are six times the main rotor harmonic spacing, and are marked T. It is noted that some of the larger peaks are due to a combination of engine-main rotor, or engine-tail rotor noise. (It is noted that the peaks due to engine noise were not identified as such until after the publication of reference 16.) Figure 6 data is for the exhaust side of the H-34, so the dominance of engine exhaust noise is not unexpected. Plots of SPL versus frequency for several other field points were studied however and engine noise still dominates although not always by the extent indicated in figure 6. As noted previously for the HU-1A, there are off-harmonic peaks for the H-34 of the same magnitude as the main rotor harmonic peaks above the 6th main rotor harmonic. Both the HU-1A and the H-34 have approximately the same SPL values for main rotor harmonic positions, where the tail or engine noise effects are not dominant.

Comparison of the data presented in figures 5 and 6 show some important characteristics. First, the SPL of the main rotor harmonics do not drop off as rapidly as predicted by theories including only rotational noise. Rather, there is a very gradual decrease for the HU-1A and an increase followed by a decrease for the H-34. Second, the main rotor is not the dominant noise source over the entire frequency range. Engine noise is dominant for the H-34 and tail rotor noise is dominant for the HU-1A, for the particular field points of these measurements. Elimination of H-34 engine noise would leave main rotor, tail rotor and (especially above 100 cps) off-harmonic noise as the dominant noise sources. Elimination of HU-1A tail rotor noise leaves main rotor and off-harmonic noise as the dominant noise sources. Third,

the off-harmonic peaks above approximately 100 cps are of the same order of magnitude as the main rotor noise peaks. Plots of SPL versus frequency for these two helicopters at other field points show essentially the same characteristics. The tail rotor noise for the HU-1A and the engine noise for the H-34 appear to be the dominant noise sources over most of the field. Most published plots of SPL versus frequency which are made with narrow bandwidth filters of 6 cps bandwidth or less show significant off-harmonic noise over portions of the frequency spectrum.

Theoretical Results and Comparison With Experiment

Vortex street type vortex shedding can contribute noise over a wide range of frequencies and are believed to be the main source of the observed off-harmonic peaks. The magnitude of the vortex street constants K_L and K_D of equations (10) and (11) respectively, were determined on the basis that the vortex street noise should be on the order of the off-harmonic noise level. The theoretical method assumes that identical events take place at the same azimuthal positions regardless of particular blade or its passage. It, therefore, computes noise only at main rotor harmonic frequencies. Although disordered vortex shedding may invalidate this assumption, nevertheless, the vortex street noise levels were assumed to occur at the main rotor harmonics and were used to evaluate the vortex street constants. The vortex shedding frequency is an important factor in the computation of the magnitude of the Fourier coefficients of the vortex street noise and is inversely proportional to the distance between the rows of vortices shed from a particular blade at any time. While this distance is known for cylinders, no such measurements are known to exist for airfoils at low angles of attack, and, therefore, values of h/d of 1.0 and 1.54 as suggested in references 9 and 10 respectively, were used in computing the vortex street constants, K_L and K_D .

The values of K_L and K_D as computed by the method of least squares fit varied for different field points and h/d ratio. Generally $0.5 \leq K_L \leq 1.0$ and $0.1 \leq K_D \leq 0.5$ resulted. Because of cancellation effects these values of K_L and K_D are order of magnitude estimates. While various K_L and K_D values were used to study the effect of these parameters, $K_L = 1.0$ and $K_D = 0.5$ seemed to give good correlation for several field points, so they were used for most of the computations. These values of K_L and K_D give vortex street lift and drag force magnitudes of the order of the steady drag force for an airfoil, and therefore seem reasonable.

Figure 7 shows a comparison between the measured SPL's and the computed SPL's at main rotor harmonics for an HU-1A helicopter for an h/d of 1.54 and for different values of K_L and K_D . (Note that SPL values are computed at main rotor harmonic frequencies only. The lines joining the data points are for ease of identification, and do not represent a continuous SPL versus spectrum). The rotational only ($K_L = 0$, $K_D = 0$) noise shown in figure 7 is the same as computed in reference 16. In general, for $K_L, K_D > 0$, there is a significant increase of predicted noise above the seventh harmonic. The larger values of K_L and K_D give larger SPL values, except where there is almost complete cancellation between the various sources, such as at the eighteenth harmonic, and to a limited degree for the twelfth harmonic. All of the predicted SPL values are very close to the rotational values for the low harmonics, so the SPL's for the nonrotational noise sources are shown only as they become distinct from the rotational noise SPL's on this and subsequent plots of SPL versus harmonic number. There is substantial improvement between the predicted and measured SPL with the inclusion of vortex street noise in addition to rotational noise. The largest peaks of the measured SPL values are near the tail rotor harmonics. There is no representation of the tail rotor in the predicted SPL, so no comparison

should be made at these points. The predicted SPL values fall below the harmonic peaks at all harmonics. However, the predicted values do come closer to the level of the off-harmonic noise.

Figure 8 shows the measured and computed SPL values with two different h/d values for the vortex noise computation. The value of h/d of 1.54 gives generally better agreement with the measured SPL values than does the value of h/d of 1. Both the SPL values individually, and the trend with increasing harmonic number appear to be better for an h/d of 1.54. Except for the results for h/d of 1.0 for harmonic numbers 10 and 11, which are probably due to cancellation effects, comparison of the results presented in figures 10 and 11 indicate that the parameters K_L and K_D are more significant than h/d . Because of the results shown in figures 7 and 8, and because of additional results that have not been presented, the values of h/d of 1.54, K_L of 1.0, and K_D of 0.5 were used in computing SPL values and pressure time histories for the HU-1A and the H-34 in hover, and for the H-34 in various flight conditions.

As may be seen from figures 7 and 8, there is considerable improvement between predicted and measured SPL values with the inclusion of vortex street effects. However, there remains a rather serious lack of agreement at the harmonic peaks. As previously mentioned, only sources which are periodic should be expected to result in such peaks. There are several possible reasons why the present predicted rotational noise is below the measured noise, particularly in the higher harmonics. One is that possible noise sources (such as blade thickness effects) have been neglected in this analysis. The high peaks near the 5th, 10th, 15th, and 20th harmonics for the HU-1A are most likely due to tail rotor noise, which has not been included. Perhaps more

important is the lack of sufficient data to accurately determine the high frequency content of the measured airloads. Airload measurements made and recorded with high frequency response instrumentation would provide a significantly improved foundation for noise prediction methods based on measured airloads (which are the basis of all current rotational noise prediction methods).

The vortex street constants as determined for the HU-1A in hover were used to compute the sound pressure levels for the H-34 in hover, and in forward and steep descent flight conditions. The results of these computations are shown plotted in figures 9 and 10.

As may be seen from figure 9, the inclusion of vortex noise has similar results for the H-34 as for the HU-1A in hover. There is significant improvement in the agreement between the measured and predicted noise with the use of the same values of h/d , K_L and K_D as were used for the HU-1A. Measured off-harmonic peaks exist above the sixth harmonic, and the predicted noise is of approximately the same level as this off-harmonic noise.

Figure 10 shows the plot of SPL versus harmonic number for a steep descent flight condition. This case was chosen because it was indicated in reference 22 that blade slap may have been present, i.e., remarks made included the comments "rough; blades flapping erratically; unsteady flight." Some characteristics of the SPL versus harmonic plot for this steep descent flight case are different than for either the hover or the forward flight cases. While the maximum SPL value is about the same as for the hover case, and also occurs at the first main rotor harmonic, the second and higher harmonics have SPL values about 10dB higher on the average. The inclusion of vortex street noise increased the SPL values above the fourth harmonic. This increase is on the order of twenty to thirty dB, which is the same order of magnitude increase as was observed for the hover case. An unusual feature

of this SPL versus harmonic number curve is the relatively uniform level of noise for the vortex street plus rotational noise above the eighth harmonic. This may be an indication of strong vortex shedding over a wide portion of the blades, with a resulting uniform SPL over a wide frequency range.

Calculations were also made for the H-34 helicopter at $V = 115$ knots. The rotational noise alone is significantly higher than for hover flight condition, and the addition of vortex noise does not give as large an increase in noise level as it did in hover. The inclusion of vortex noise has the greatest effect above the eighth main rotor harmonic, and as in the hover case, inclusion of vortex street noise in addition to rotational noise generally increases the SPL values in the higher harmonics, and leaves the lower harmonics unaffected. Both the higher level for the rotational noise only, and the increased values of SPL in the higher harmonics are expected results for high forward speed flight conditions as compared to hover flight conditions.

To investigate the effect on the noise characteristics of a blade experiencing impulsive loading, as occurs when a blade passes through or near a trailed vortex, the azimuthal variation of aerodynamic section loading was modified by the type of modification suggested in reference 18, i.e., an impulsive loading change over a small section of the azimuth. Such loading is thought to be an important factor in noise characteristics called "slap" or "bang." The SPL versus harmonic number plots for rotational noise only differ slightly for the modified and unmodified ASL, for $V = 115$ knots, and slap or bang noise characteristics are not obvious from this form of noise data presentation.

It is noted that noise characteristics generally associated with impulsive blade loading have been identified from experimental pressure time histories rather than plots of SPL versus

frequency. Predicted pressure time histories were computed, therefore, for several flight conditions to determine if the distinctive characteristics related to impulsive blade loading could be predicted. Pressure time histories were computed for the H-34 in high speed forward flight with and without modified airload data, for the H-34 in steep descent, and for the HU-1A and H-34 in hover. The high speed forward flight case was done to see if any significant differences in the pressure time histories would be obtained when the measured azimuthal variation of the airloads was modified. The steep descent case was done to see if any indication of blade slap could be observed from the predicted pressure time history. Since measured time histories were available for the H-34 and HU-1A in hover, predicted time histories for these ships in the same flight condition were obtained. The measured time histories for the HU-1A is shown in figure 11, and predicted time histories for the HU-1A without and with vortex noise effects included are shown in figure 12 and 13, respectively. There are limitations on both the measured and the predicted pressure time histories which seriously restrict any attempt for comparison between them. Some of the limitations are as follows.

1. As previously noted, the instrumentation has a low frequency cut-off which affects frequencies in the range of the first or second harmonic of blade passage. The predicted noise for both the HU-1A and H-34 has its largest component in the first harmonic. Because of the low frequency cut-off, noise at these frequencies does not appear in the measured pressure time histories.
2. The measured noise has significant frequency content above the twentieth harmonic of blade passage frequency, which is the present upper limit on harmonic number for the computer program.

3. The measured noise for the HU-1A contains a large amount of tail rotor noise and the engine exhaust noise is predominant in the H-34 data. The predicted noise, however, contains only main rotor noise.
4. There is no correlation between rotor position and noise measurement at the field point, so the time axis origin cannot be established for comparative purposes.
5. The measured airloads used to compute the time histories were obtained during a different set of flights than those during which the noise measurements were made.

Because of these severe limitations, a comparison of predicted and measured pressure time histories for the helicopters in hover is difficult to accomplish, and has not been attempted.

On the basis of just theoretical results, however, interesting effects may be observed from the predicted pressure time histories. There is a definite similarity in the shapes of the pressure time histories for the HU-1A at a field point at eleven o'clock ($\psi_0 = 210^\circ$) as shown in figure 13 and in other plots, not shown in this paper, in that one large pressure pulse occurs in each period, and that this pulse occurs at different times at different locations. Inspection of the measured airload data indicates that there is not a distinctive airload variation near azimuthal locations at which such a sound pressure peak might be related to an airload variation. Differences in times of arrival of a pressure time history pattern at different field points could occur for a uniformly loaded rotor. The time shift of the pattern would be proportional to the difference in azimuthal location of the field point, and depends solely on the distance

from the blades to the field point. That is, a sound pattern may be thought of as rotating with the helicopter rotor. The predicted pressure time histories do not show agreement with either of the simple models used to explain the possible shift of time of the sound pattern. In reality, both effects will be in operation, and a combination of them will control the pressure time histories over the entire field. (It is worth noting that it may be possible to determine the location in the rotor disc of a distinct variation in the airload from the pressure time histories at more than one field point.)

Figures 14 and 15 show the pressure time histories as computed for the H-34 in high speed flight including the combined rotational and vortex street airloads. Figure 14 presents the predicted time histories for the unmodified airloads and figure 15 presents the results using the modified airloads. It is interesting to note that the combined vortex and rotational noise seemed to concentrate the high frequency oscillations due to vortex shedding over a narrow azimuth range when the modified airloads were used. The high frequency content, however, is present over a majority of the time periods for the unmodified airload case. High frequency variation of sound pressure over a narrow azimuth band has been associated with blade slap (ref. 3) as caused by blade-vortex interaction.

The pressure time history for the steep descent case, presented in figure 16, also has large magnitude high frequency variations over a limited portion of the period. The large magnitude high frequency noise comes from vortex shedding which is the dominant noise source in the high harmonics. As previously noted, the combination of large magnitude high frequency noise over a limited ψ range has been identified as blade slap. It is noted, however, in reference 3 the frequency content is significantly higher than

that shown in figure 16. This difference is believed to be caused by the fact that the upper limit on frequency of the present computer program is the twentieth harmonic of blade passage. The nondimensional time period over which the observer receives this high frequency noise corresponds to a blade-vortex interaction occurring near the 90° azimuthal location of the rotor disc, which is not an unusual location for this phenomenon to occur.

An important conclusion that can be drawn from the results obtained during the analysis of the high speed forward flight and steep descent cases is that important noise characteristics, such as blade slap, are shown from plots of pressure time history but are not recognizable from the usual plots of SPL versus harmonic number.

CONCLUDING REMARKS

The theory for calculating helicopter rotor noise has been extended to include vortex street shedding noise as a noise source in addition to rotational noise. A numerical integration was used to evaluate the sound pressure levels and pressure time histories for up to 20 harmonics of the main rotor blade at a general field point translating with the hub.

Vortex street force magnitude constants were determined by a least squares fit approach using the difference between the total measured noise and the predicted rotational noise for the HU-1A helicopter in hover. While it was hoped that these might be "universal constants," the approximations involved in predicting the magnitude of the rotational noise, and limitations in the measured data results in these values for the vortex street constants being order of magnitude estimates only.

These vortex street constants were, however, used to predict sound pressure levels and pressure time histories for the HU-1A helicopter in hover and for the H-34 helicopter in various

flight conditions. Results showed that (for hover, high forward speed, and steep descent) the first four or five harmonics are the largest and are unaffected by the vortex noise. Higher harmonic levels do appear to have significant vortex noise, so that application of this new theory resulted in an appreciable improvement between predicted and measured sound pressure levels. It is noted, however, that with the addition of the vortex shedding effects, the increase in the noise levels at the higher harmonics for the hover and the steep descent flight conditions was approximately twice that determined for the high forward speed case.

While a significant improvement in predicted noise was achieved, noise levels at harmonics of the blade passage frequency still were not accurately predicted. This may be due to deficiencies in the theory, or it may be due to deficiencies in the experimental airload data required for the calculation of the higher harmonics of the rotational noise. Since the vortex noise occurs over a wide range of frequencies rather than only at the discrete frequencies of rotational noise, the level of the vortex noise is that of the off-harmonic noise, and significant changes in the isolated harmonic peaks should not be expected from the vortex noise. While the forces associated with thickness effects and vortex shedding are relatively small, it is noted that high frequency forces of relatively small magnitude can make a significant contribution to the rotor noise in the higher frequency range, regardless of their origin.

Predicted sound pressure time histories were presented for various flight conditions. Results of these theoretical calculations indicate that blade slap characteristics may be observed from predicted pressure time histories for both high forward speed and steep descent flight conditions, but will probably not be

recognizable from the corresponding plots of sound pressure levels versus harmonic number.

Based on the research effort reported herein the following specific comments are presented.

1. The experimentally determined sound pressure level data for hover flight condition which was used for correlation shows that the off-harmonic peaks are the same order of magnitude as the harmonic peaks, in the higher harmonics.
2. Vortex noise is a significant noise source in all flight conditions but is more pronounced in hover and steep descent flight conditions.
3. Use of the same nondimensional constants describing the frequency and force characteristics of vortex shedding for two different helicopter rotor systems produced comparable improvement in the prediction of the rotor noise in the high frequency range.
4. Rotational noise alone, even that associated with a rapid change in airloading, does not yield a pressure time history similar to that measured for blade slap (high frequency high amplitude noise over a limited portion of a blade passage time period).
5. The inclusion of both vortex and rotational noise effects yields a pressure time history similar to that associated with blade slap for high forward speed and steep descent flight conditions.
6. Published measured airload data is currently inadequate for use in predicting the higher harmonics of rotational noise.

7. It is considered unlikely that theoretical methods can be developed to accurately predict the required harmonic airloads in the harmonic range of 10 through 100.
8. Measurements of the basic characteristics of vortex shedding from airfoils should be made in order to develop an understanding of their effects on rotor noise. Successful measurements could lead to a direct means of vortex noise reduction.
9. A different prediction technique, capable of predicting pressure time histories due to non-periodic loads would be useful in obtaining more realistic predicted pressure time histories.

REFERENCES

1. Loewy, Robert G., Aural Detection of Helicopters in Tactical Situations, J. Am. Helicopter Soc., Vol. 8, No. 4, Oct. 1963, pp. 36-53.
2. Sternfeld, Harry, Jr., and Forehand, J. Everette, Helicopter Noise, Its Evaluation and Treatment. Proceedings of the American Helicopter Society Seventeenth Annual Forum, Washington, D.C., May 3-5, 1961.
3. Cox, C.R., and Lynn, R.R., A Study of the Origin and Means of Reducing Helicopter Noise, TCREC Tech. Report 62-73, Nov. 1962.
4. Sadler, S.G., and Loewy, R.G., A Theory for Predicting the Rotational and Vortex Noise of Lifting Rotors in Hover and Forward Flight, Rochester Applied Science Associates, Inc. Report 68-11, (NASA number to be assigned), Dec. 1968.
5. Stowell, E.Z., and Deming, A.F., Vortex Noise from Rotating Cylindrical Rods, NACA TN 519, 1935.
6. Yudin, E.Y., On the Vortex Sound from Rotating Rods, NACA TM 1136, 1947.

7. Blokhintsev, D., Acoustics of a Nonhomogeneous Moving Medium, NACA TM 1399, 1959.
8. Hubbard, H.H., Propeller-Noise Charts for Transport Airplanes, NACA TN 2968, 1953.
9. Schlegel, Robert; King, Robert; and Mull, Harold; Helicopter Rotor Noise Generation and Propagation, USAAVLABS Tech. Rpt. 66-4, Oct. 1966.
10. Krzywoblocki, M.Z., Investigation of the Wing-Wake Frequency with Application of the Strouhal Number, J. Aeron. Sci., Vol. 12, No. 1, Jan. 1945, pp. 51-62.
11. Roshko, A., Experiments on the Flow Past a Circular Cylinder at Very High Reynolds Number, J. Fluid Mechanics, Vol. 10, Part 3, May 1961.
12. Gutin, L., On the Sound Field of a Rotating Propeller, NACA TM 1195, 1948.
13. Deming, Arthur F., Propeller Rotation Noise Due to Torque and Thrust, NACA TN 747, 1940.
14. Garrick, I.E., and Watkins, C.E., A Theoretical Study of the Effect of Forward Speed on the Free-Space Sound-Pressure Field Around Propellers, NACA TN 3018, 1953.
15. Spencer, R.H.; Sternfeld, H. Jr.; and McCormick, B.W.; Tip Vortex Core Thickening for Application to Helicopter Rotor Noise Reductions, USAAVLABS Tech. Report 66-1, Sept. 1966.
16. Loewy, R.G. and Sutton, L.R., A Theory for Predicting the Rotational Noise of Lifting Rotors in Forward Flight, Including a Comparison With Experiment, USAAVLABS Tech. Report 65-82, Jan. 1966.
17. Lowson, M.V., Basic Mechanisms of Noise Generation by Helicopters, V/STOL Aircraft, and Ground Effect Machines, Wyle Labs., Report No. WR65-9, May 1965.
18. Miller, R.H., On the Computation of Airloads Acting on Rotor Blades in Forward Flight, J. Am. Helicopter Soc., Vol. 7, No. 2, Apr. 1962, pp. 56-66.
19. Piziali, R.A., and DuWaldt, F.A., A Method for Computing Rotary Wind Airload Distributions in Forward Flight, TCRC TR 62-44, Nov. 1962.

20. Gessow, A., and Myers, G.C., Aerodynamics of the Helicopter, MacMillan Company, 1952.
21. Nikolsky, A.A., Helicopter Analysis, John Wiley and Sons, Inc., 1951.
22. Scheiman, James, A Tabulation of Helicopter Rotor-Blade Differential Pressures, Stresses, and Motions as Measured in Flight, NASA TM X-952, 1964.
23. Anon; Measurement of Dynamic Air Loads on a Full-Scale Semi-rigid Rotor, TCREC Tech. Report 62-42, Dec. 1962.
24. Hubbard, H.H., and Regier, A.A., Propeller-Loudness Charts for Light Airplanes, NACA TN 1358, 1947.
25. Sharland, I.J., Sources of Noise in Axial Flow Fans, Journal of Sound and Vibration, Vol. 1, No. 3, 1964, pp. 302-332.
26. Roshko, A., On the Drag and Shedding Frequencies of Two-dimensional Bluff Bodies, NACA TN 3169, 1954.
27. Lamb, H., The Dynamical Theory of Sound, Second ed., Dover, 1960.
28. Lighthill, M.J., The Bakerian Lecture, 1961, Sound Generated Aerodynamically, Royal Aircraft Establishment Technical Memorandum No. Dir. 8, Nov. 1961.
29. Etkin, B.; Korbacher, G.K.; and Keefe, R.T.; Acoustic Radiation from a Stationary Cylinder in a Fluid Stream (Aeolian Tones), J. Acoust. Soc. Am., Vol. 29, No. 1, Jan. 1957, pp. 30-36. (See also Vol. 34, No. 11, Nov. 1962, pp. 1711-1714).
30. Foughner, J.T., Jr., and Duncan, R.L., A Full-Scale Ground Wind Load Program, Paper presented at the Meeting on Ground Wind Load Problems in Relation to Launch Vehicles, NASA TM X-57779, 1966, pp. 4.1 - 4.19.

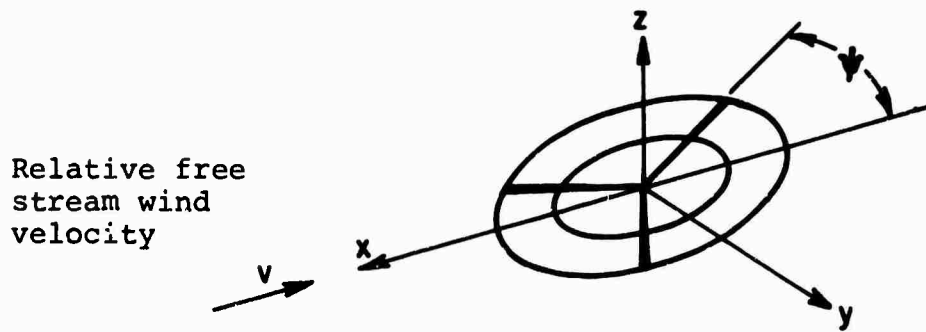


Figure 1. Coordinate system, isometric view.

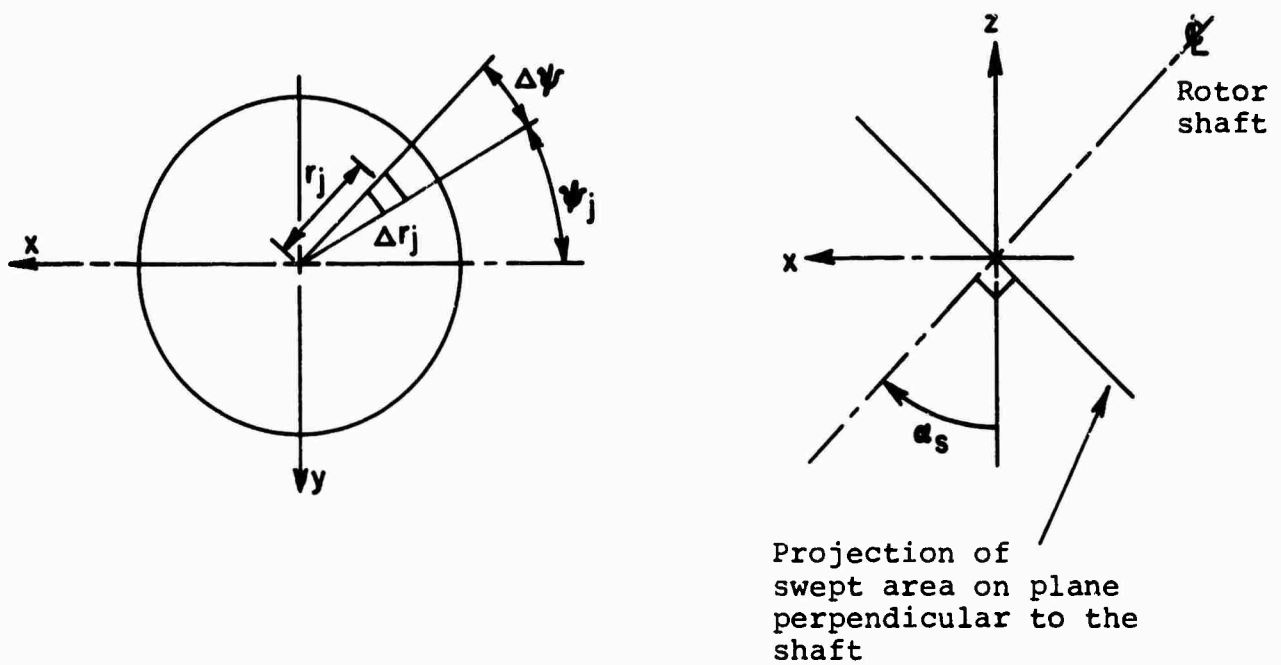


Figure 2. Coordinate system.

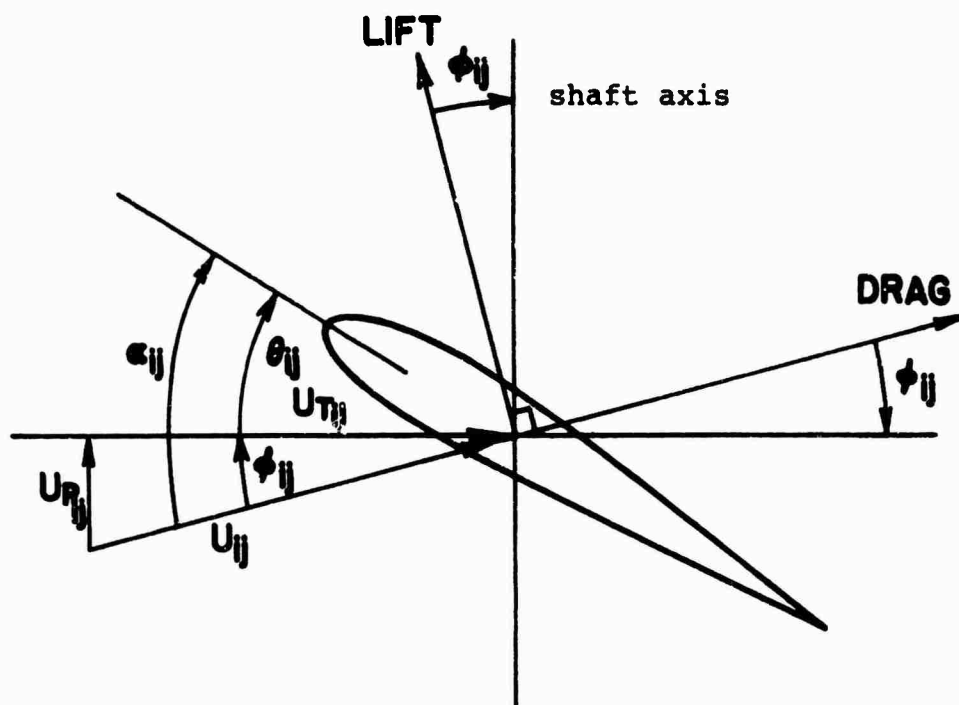
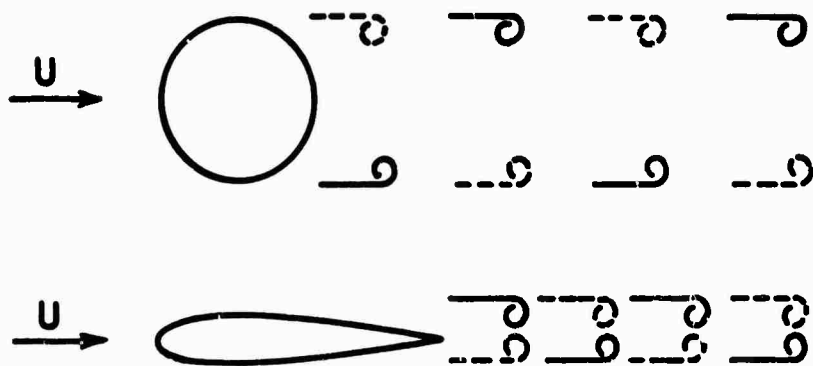


Figure 3. Blade section quantities.



Symmetrical bodies, vortex drag frequency is twice the shedding frequency.



Nonsymmetrical bodies includes vortex drag frequency the same as vortex shedding frequency.

Figure 4. Effect of body symmetry on vortex street drag frequency.

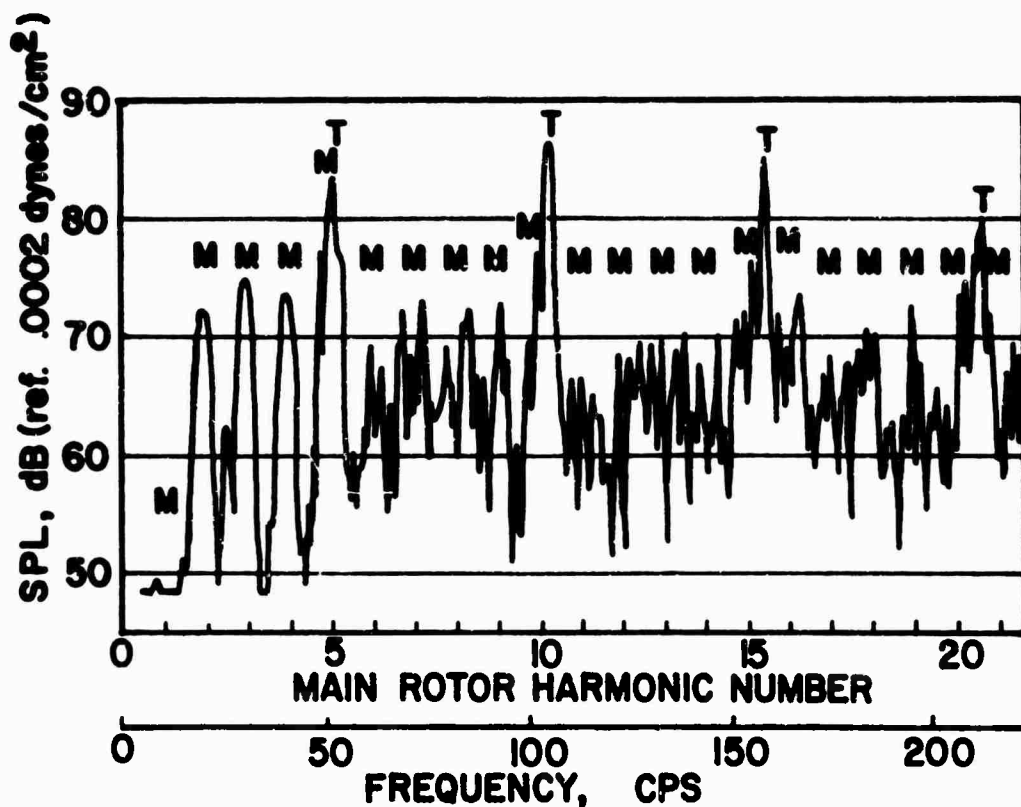


Figure 5. SPL vs. frequency for HU-1A helicopter in hover. (Main rotor and tail rotor harmonics are indicated by the letters M and T, respectively.) $R_0=200$ ft., $\psi_0=330^\circ$, $Z_0=-11.4$ ft., 3 cps bandwidth filter.

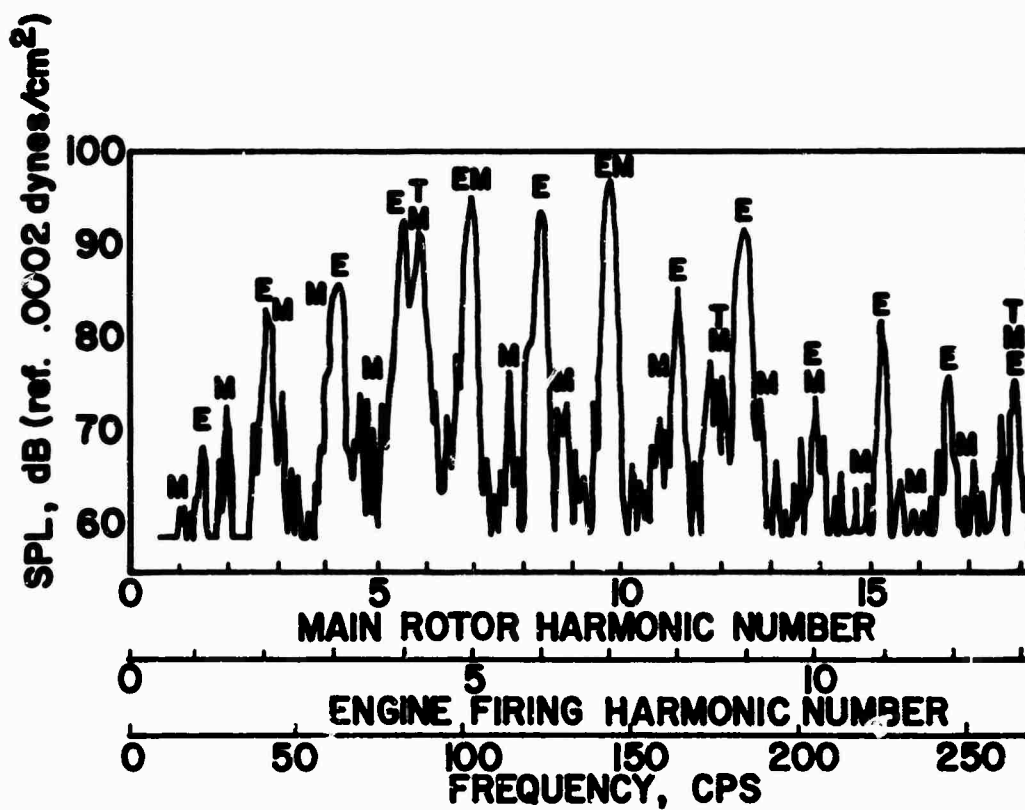


Figure 6. SPL vs. frequency for H-34 helicopter in hover. (Engine, main rotor, and tail rotor harmonics are indicated by the letters E, M, and T, respectively.) $R_0=200$ ft., $\psi_0=330^\circ$, $Z_0=-16$ ft., 3 cps bandwidth filter.

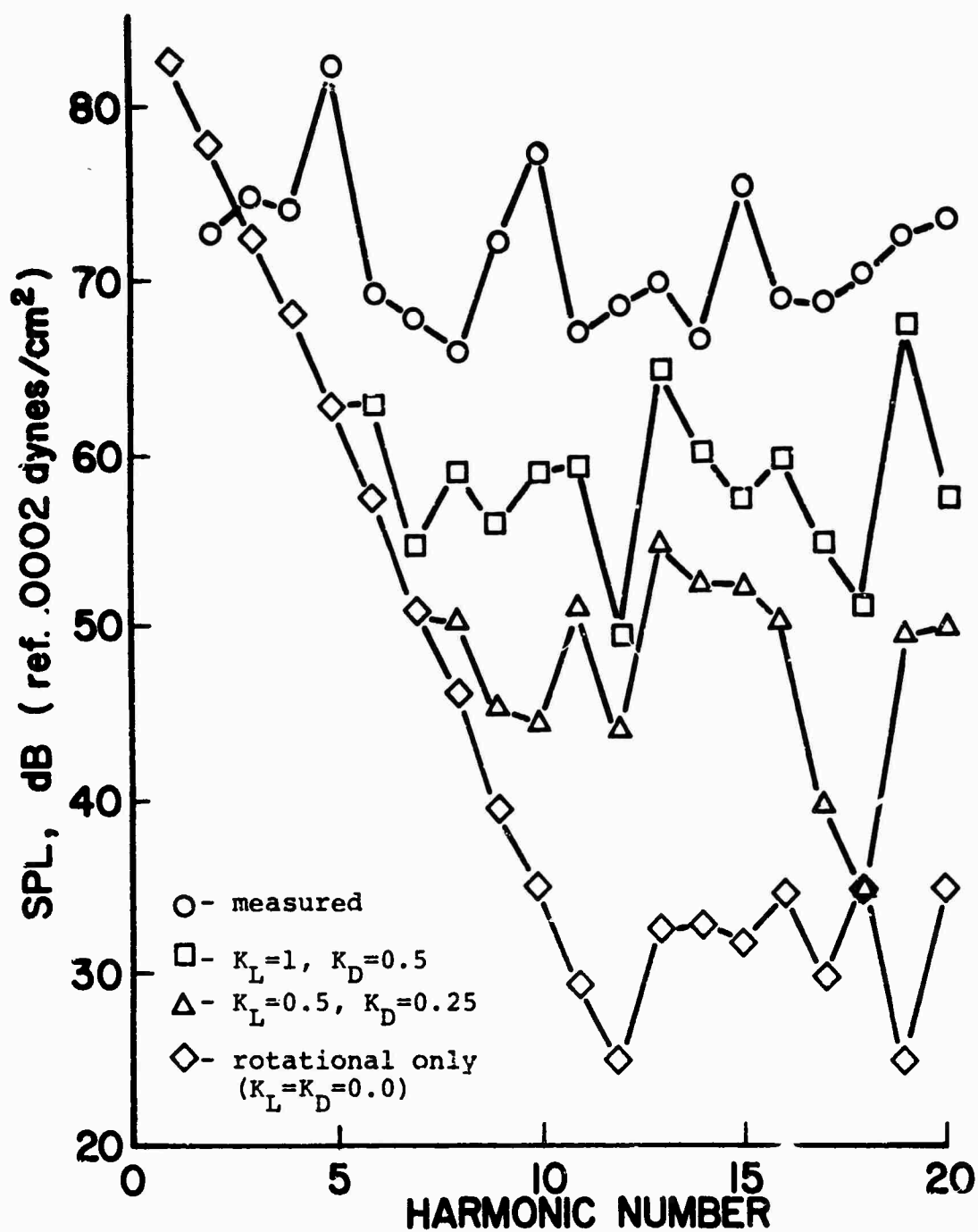


Figure 7. Comparison of computed SPL's vs. harmonic number for various K_L and K_D , with measured SPL's. HU-1A helicopter in hover, $h/d=1.54$, $R_0=200$ ft., $\psi_0=330^\circ$, $Z_0=-11.4$ ft.

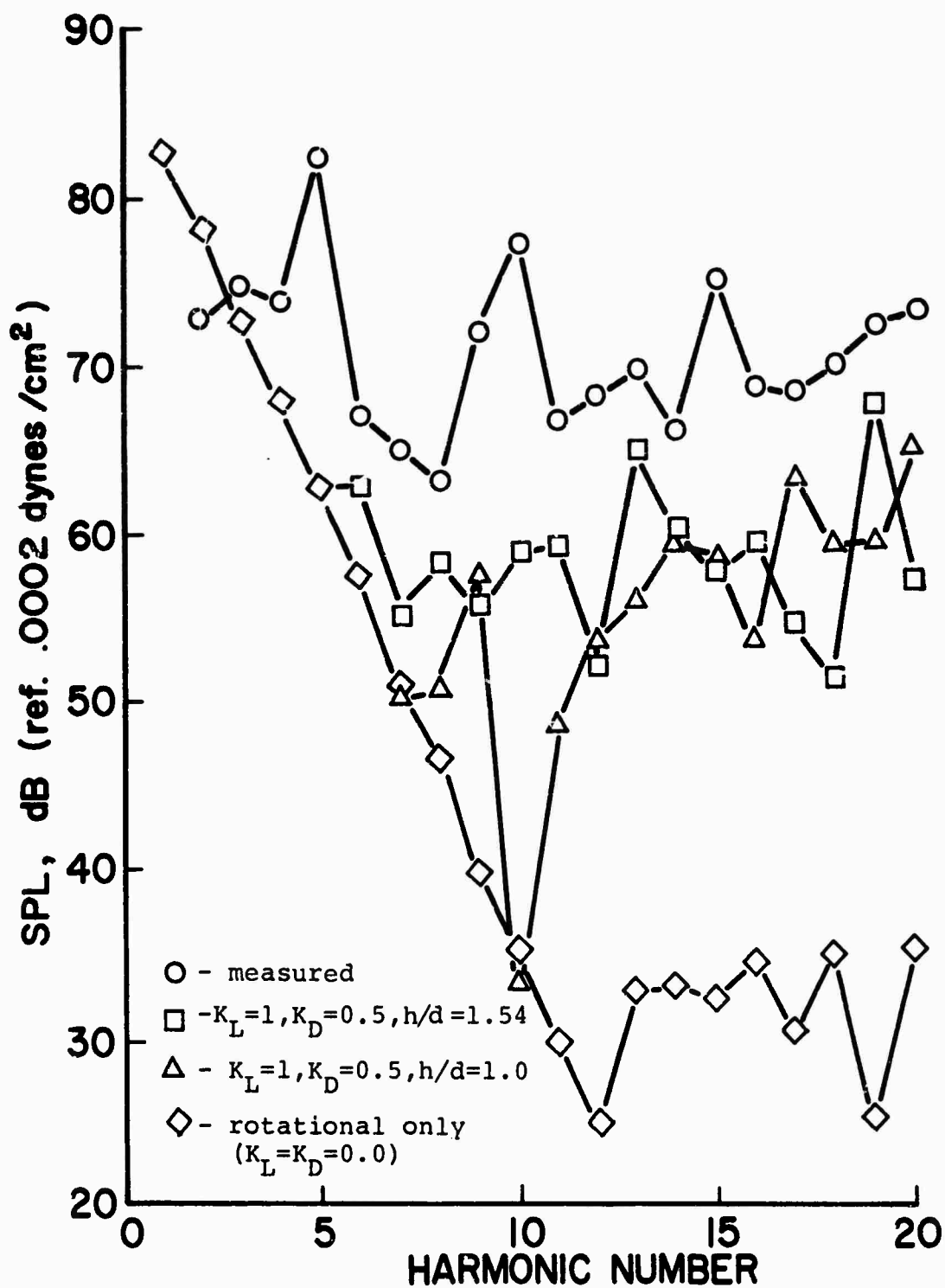


Figure 8. Comparison of computed SPL's vs. harmonic number for h/d of 1.0 and 1.54. HU-1A helicopter in hover, $R_0=200$ ft., $\psi_0=330^\circ$, $Z_0=-11.4$ ft.

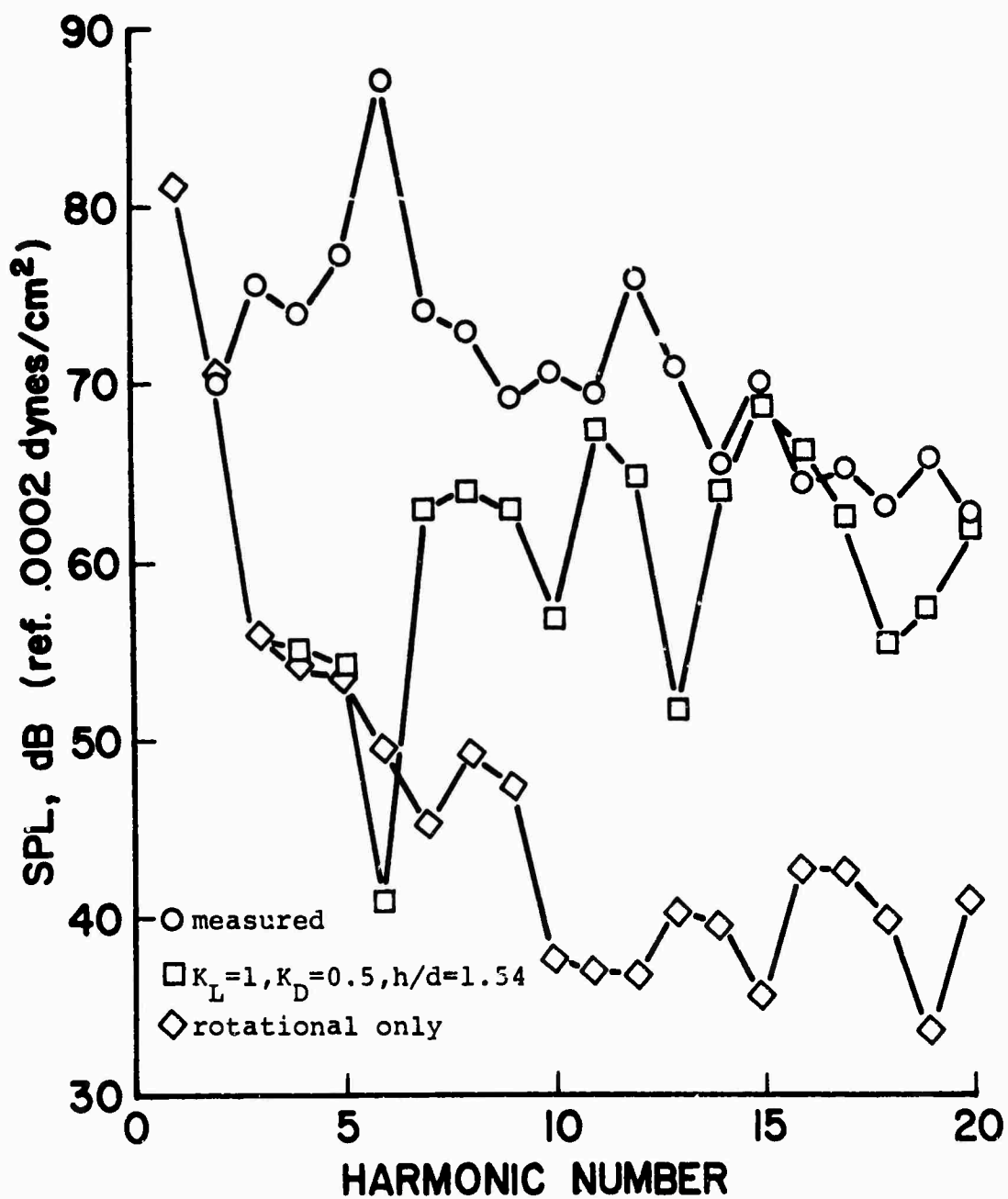


Figure 9. Comparison of computed SPL's vs. harmonic number with measured SPL's. H-34 helicopter in hover, $R_0=200$ ft., $\psi_0=120^\circ$, $Z_0=-16$ ft.

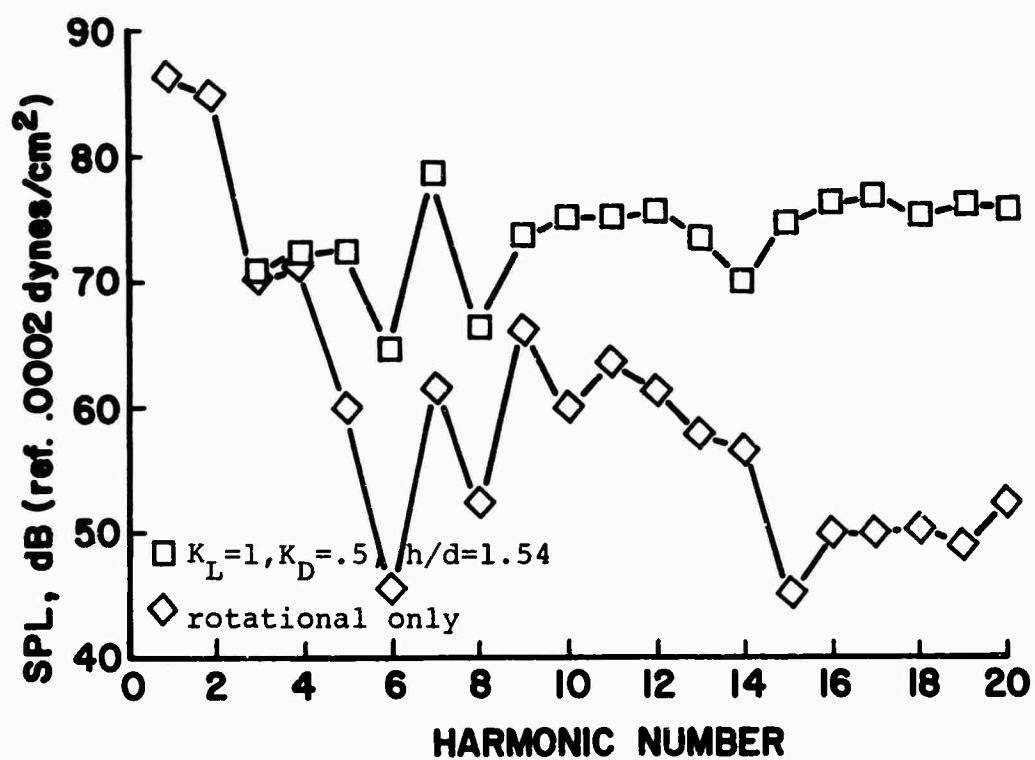


Figure 10. Computed SPL's vs. harmonic number for steep descent. H-34 helicopter, $V \approx 0$, $R_0 \approx 112$ ft., $\psi_0 \approx 90^\circ$, $Z_0 \approx -56$ ft.

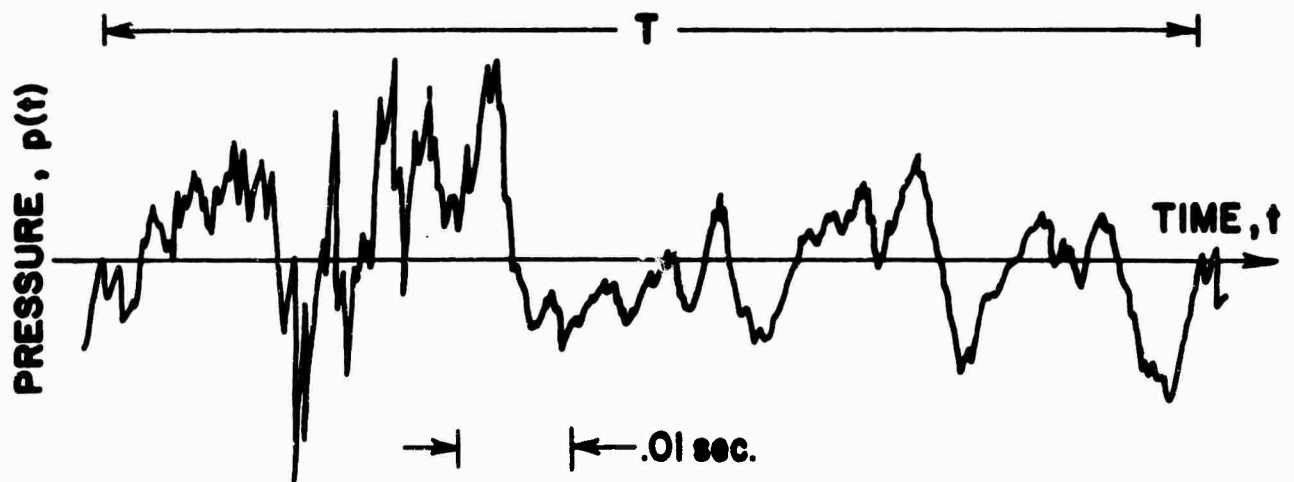


Figure 11. Measured pressure time history for
HU-1A helicopter in hover,
 $R_0=200$ ft., $\psi_0=210^\circ$, $Z_0=-11.4$ ft.

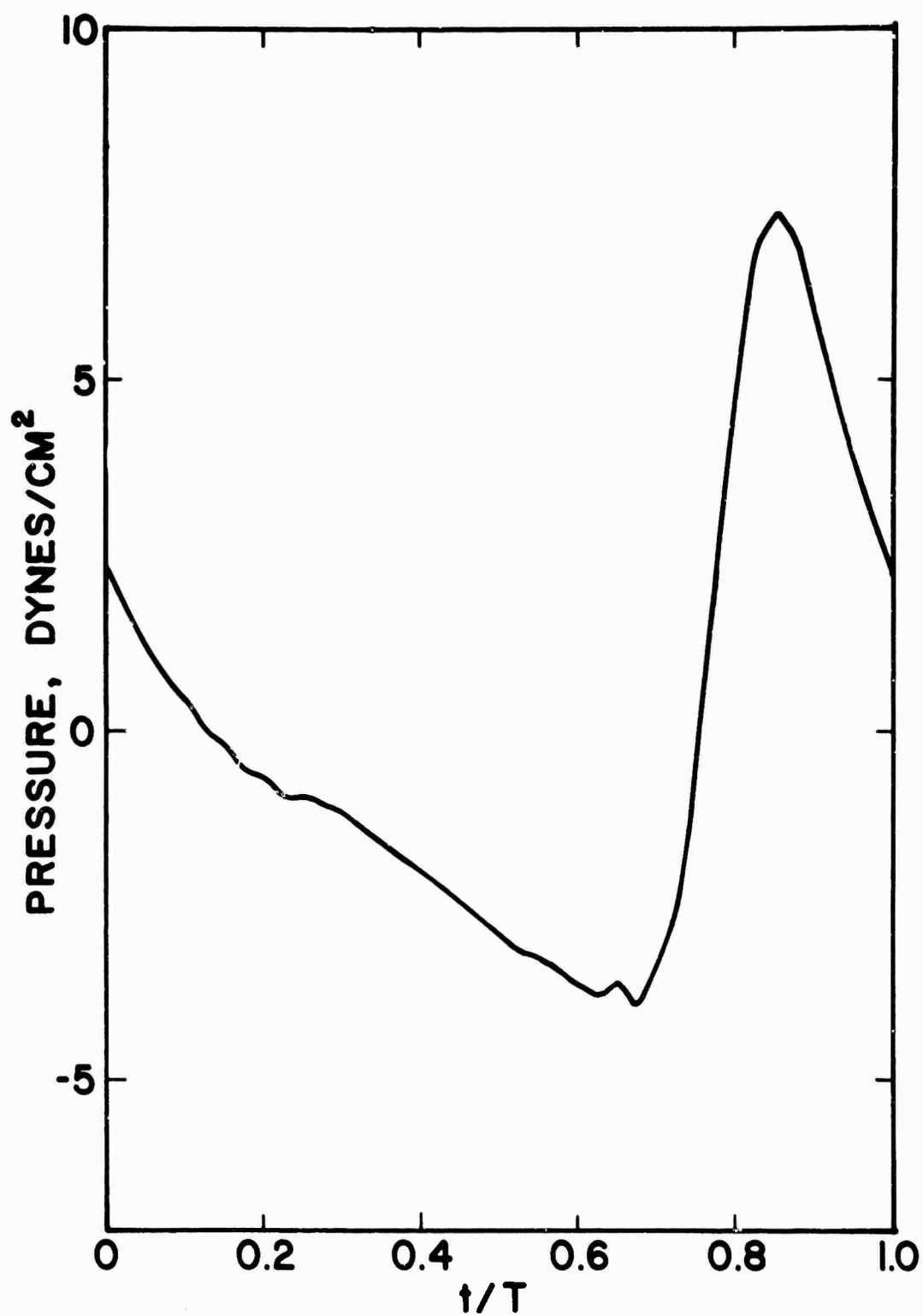


Figure 12. Computed pressure time history with rotational noise only for HU-1A helicopter in hover, $R_0=200$ ft., $\psi_0=210^\circ$, $Z_0=-11.4$ ft.

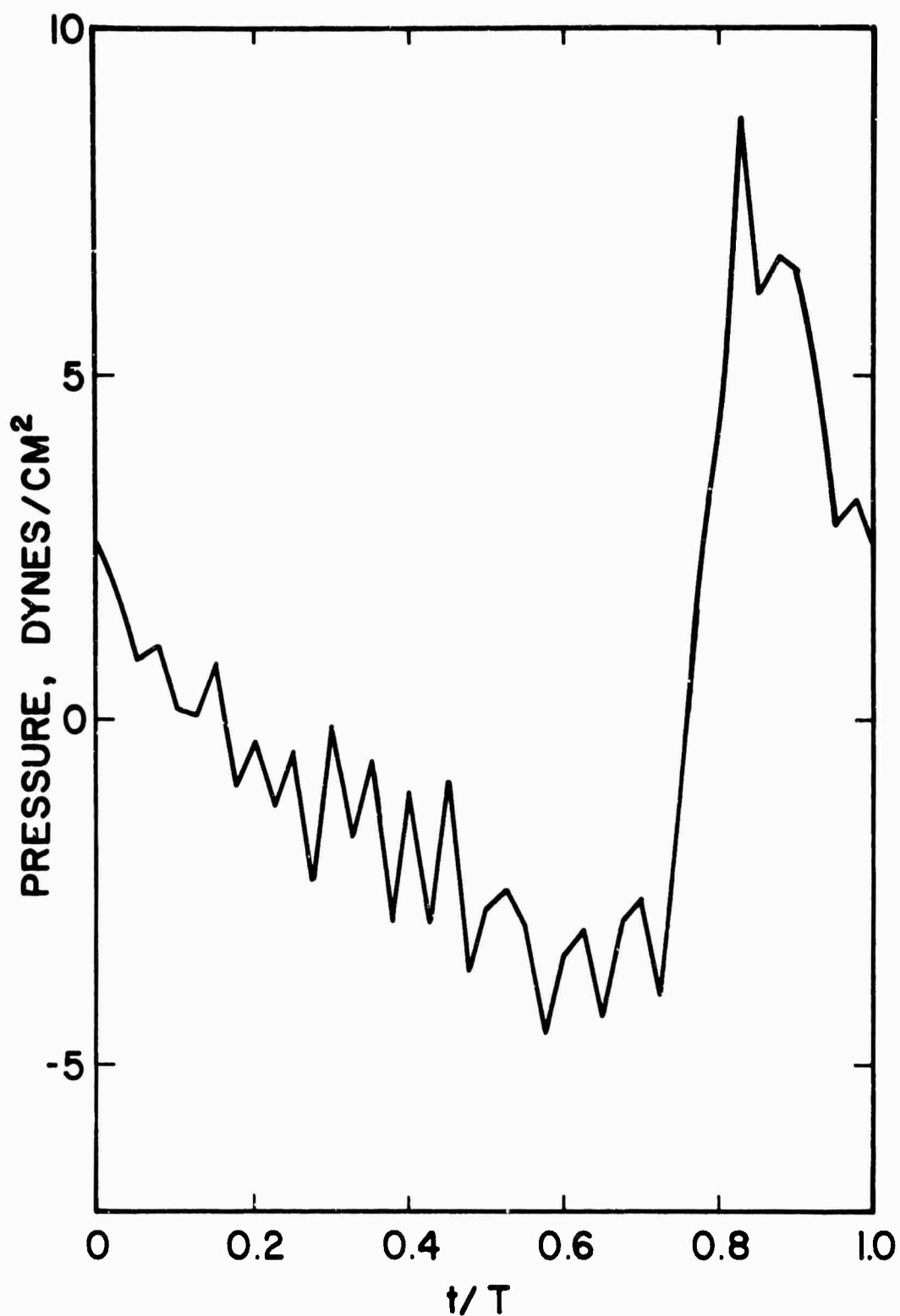


Figure 13. Computed pressure time history with rotational and vortex noise for HU-1A helicopter in hover, $K_L=1.0$, $K_D=0.5$, $R_0=200$ ft., $\psi_0=210^\circ$, $Z_0=-11.4$ ft.

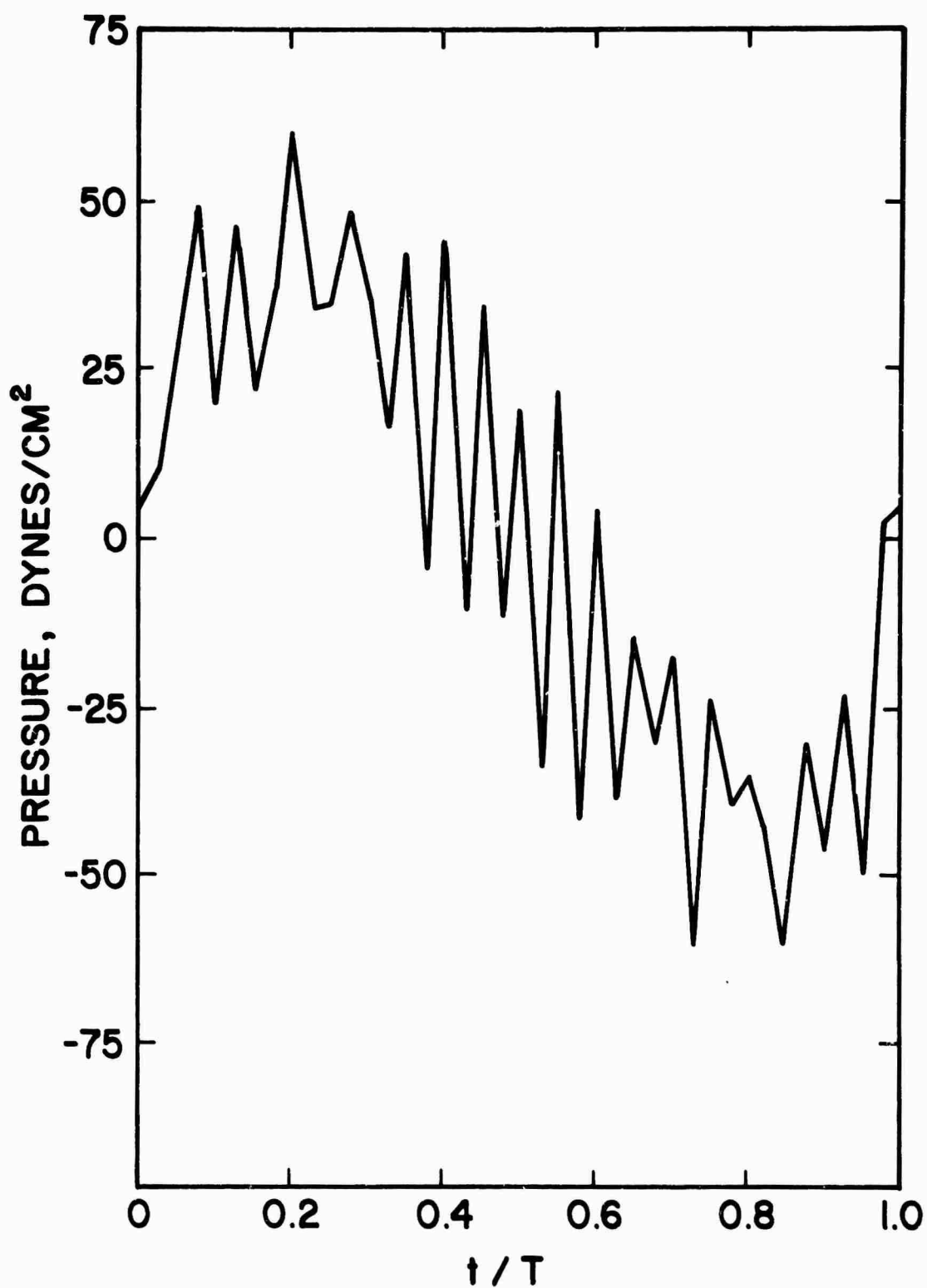


Figure 14. Computed pressure time history from unmodified ASL's for H-34 helicopter. $K_L=1.0$, $K_D=0.5$, $V=115$ knots, $R_0=112$ ft., $\psi_0=90^\circ$, $Z_0=-56$ ft.

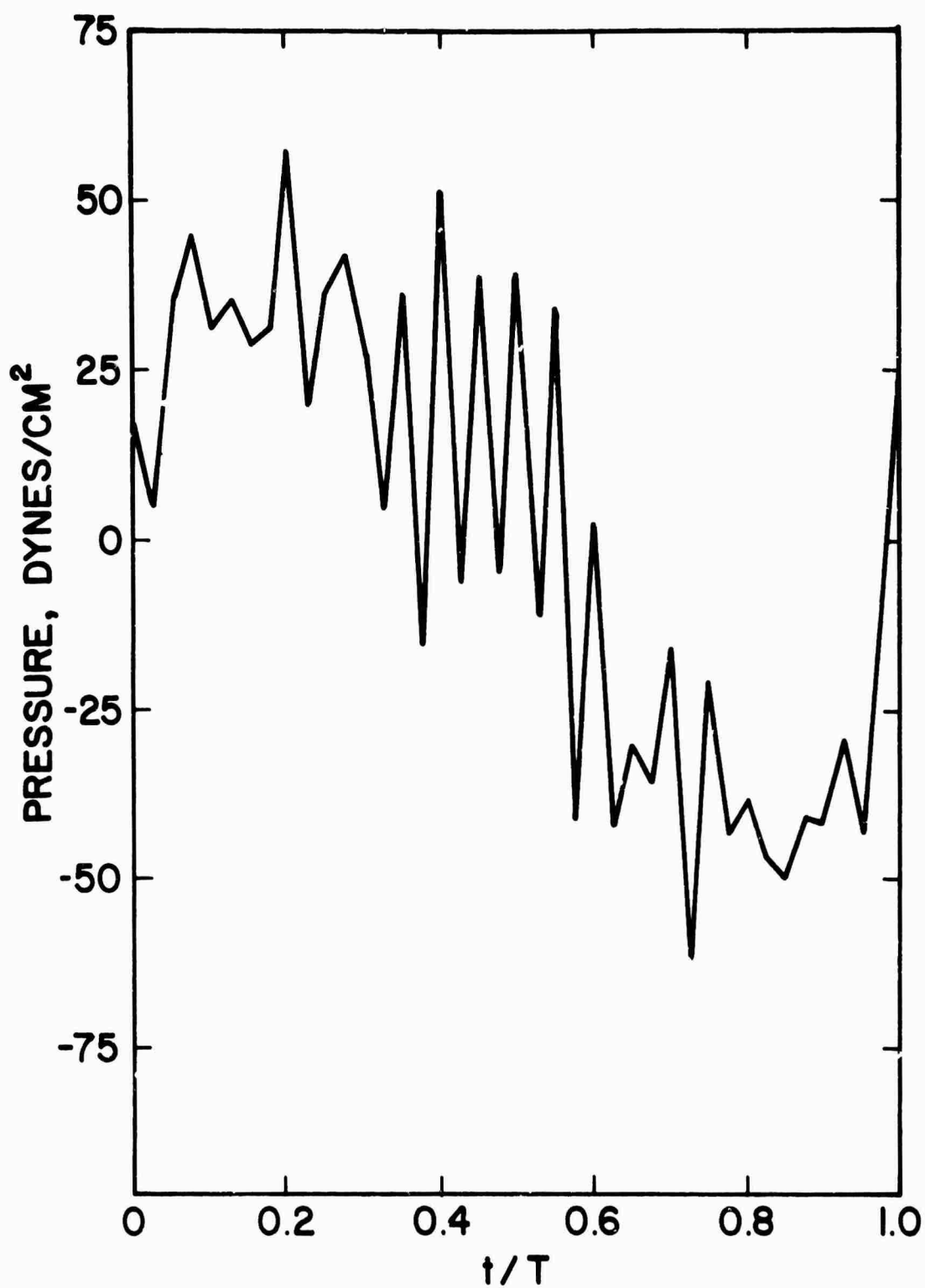


Figure 15. Computed pressure time history from modified ASL's for H-34 helicopter. $K_L=1.0$, $K_D=0.5$, $V=115$ knots, $R_0=112$ ft., $\psi_0=90^\circ$, $Z_0=-56$ ft.

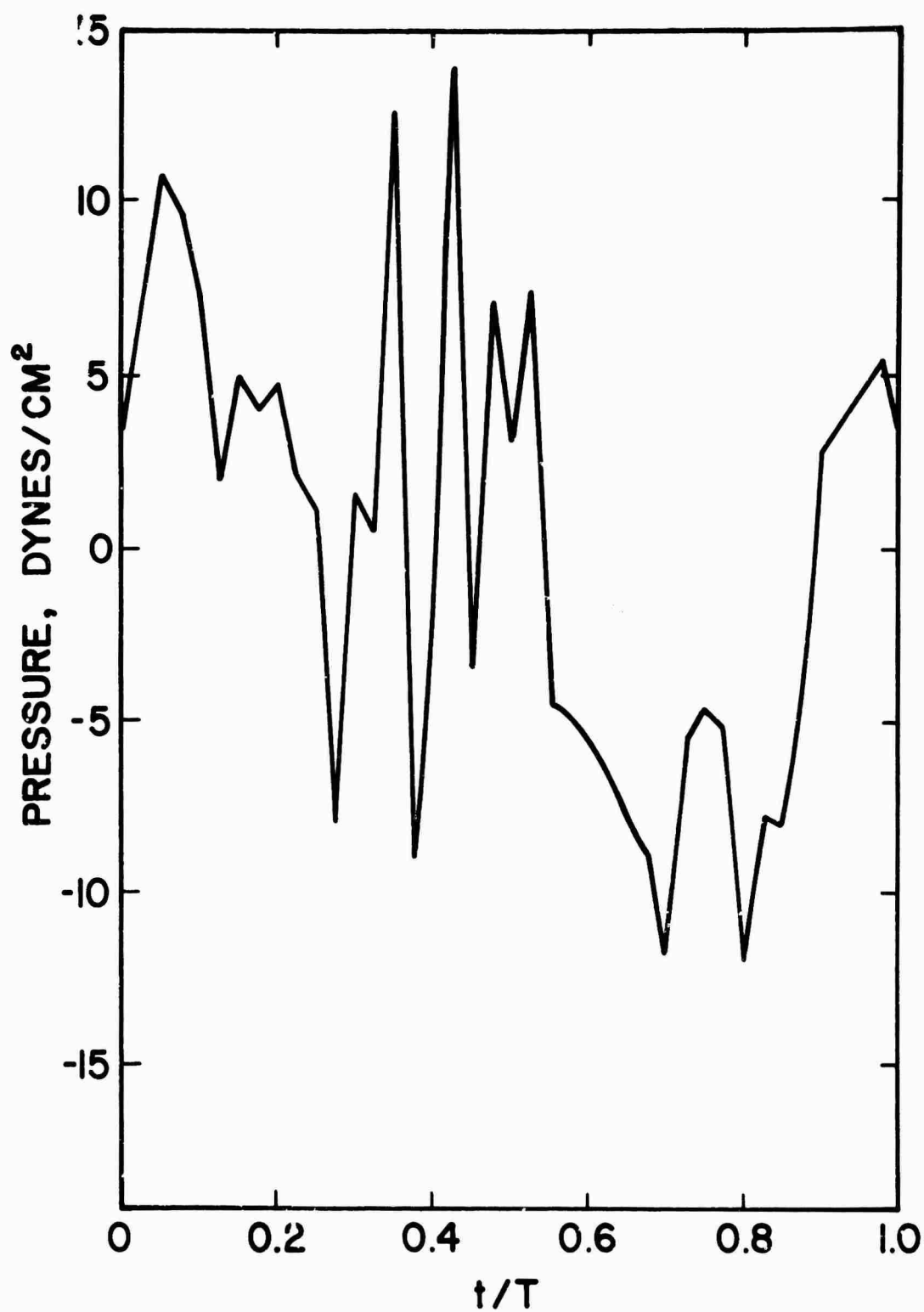


Figure 16. Computed pressure time history from steep descent ASL's for H-34 helicopter. $K_L=1.0$, $K_D=0.5$, $V \approx 0$, $R_0=112$ ft., $\psi_0=90^\circ$, $Z_0=-56$ ft.

PREDICTION METHODS AND TRENDS FOR HELICOPTER ROTOR NOISE

by

ROBERT J. KING & RONALD G. SCHLEGEL

Sikorsky Aircraft
Division of United Aircraft Corporation
Stratford, Connecticut, U.S.A.

© Sikorsky Aircraft, Division of United Aircraft Corporation, U.S.A., 1969 All rights reserved."

INTRODUCTION

Helicopter rotor noise is comprised of what is commonly referred to as rotational noise and vortex noise. Although some serious questions have been raised as to the basic difference in these noise types, there is considerable evidence to support treating them separately, as is done here. Several solutions to the rotational noise problem have been derived over the past five years. They represent a quantum step in the understanding and prediction of rotational noise generation since the first workable solution was derived by Gatin (Reference 1) in 1936. Several of these more recent solutions are discussed in light of their relative merits. These solutions are shown to be comparable in accuracy despite widely varying assumptions and degrees of simplification. Vortex noise, and its relationship to rotational noise is discussed briefly and current empirical prediction methods are presented. Theoretically derived and empirically substantiated trend studies are presented for both rotational and vortex noise in terms of the basic parameters of tip speed, thrust, blade area, diameter and number of blades. These trend charts have proven to be valuable at Sikorsky Aircraft in developing preliminary design data over a limited range of parameter values and typical helicopter rotor Reynolds Numbers. Finally, some examples of rotor noise trending application to both detection and annoyance situations are discussed.

METHODS

Rotational Noise

Rotational noise is the type of rotor system noise normally described as ordered or discrete frequency which appears at multiples of the blade passing frequency. The solution for rotational noise was first analytically derived by Gutin (Reference 1). Gutin used a simple uniform loading case and assumed a concentrated load from aerodynamic loading at the 0.7 radius point. He assumed non time varying rotor loads and, in so doing, was able to attain a closed form solution to the rotational noise problem. Figure 1 shows the rotor-measurement position layout. Equation 1 of Figure 2 shows Gutin's solution which amounts to a phased acoustic array in a flat disk. The rotational noise generated in this case was merely a doppler shift effect of moving sources. This closed form solution made it easy to calculate trends. There is a basic problem with this solution however, in that it is not accurate beyond the first harmonic, or fundamental frequency of rotational noise at tip Mach numbers below the transonic range. In the higher tip Mach numbers approaching the transonic region, Gutin's prediction method becomes fairly accurate for even the higher harmonics.

A second solution to the rotational noise problem which was published in 1966 by Sikorsky Aircraft under USAAVLABS sponsorship (Reference 10) was a digitally integrated solution which accounted for non-uniform spanwise pressure distribution on the blade and pressure varying with time. This solution, although it could not be accomplished in closed form, was programmed on a digital computer using measured blade airloads for input data. The solution is shown in integral form as Equation 2 of Figure 2. The use of the spanwise pressure distribution in addition to the fluctuating blade pressure resulted in much better noise harmonic correlation than was available using Gutin's solution. It was found that in order to predict accurately the m th harmonic of rotor noise, the $m(n-1)$ loading harmonic was required, n being the number of blades. Note

that the m th harmonic of noise and the $m(n-1)$ harmonic of blade loading are at nearly the same frequency. This relationship seems reasonable, in that the frequency of the m th harmonic of noise, $mn \Omega$, in the fixed coordinate system is influenced most by the harmonic of pressure in the rotating system whose frequency $m \Omega (n-1)$, differs from it only by the frequency of rotation. Although this solution requires a digital computer, it is easily used for trending. Sikorsky has therefore used it for most of its trending studies. This solution was followed at Sikorsky Aircraft by a second generation digital solution, also under AVLABS contract (Reference 9). This solution differed from the initial digital integrated solution in that the actual chordal pressure distribution was used as input. Using this particular solution, less azimuthal pressure (blade loading) harmonics were required to describe the rotational noise harmonics accurately than were required on the original program. This solution is currently being modified to add coning and one per rev flapping to this solution to better describe the sound field and to further improve accuracy. The basic limitation with both of these solutions is the fact that it is not possible at present to calculate blade loading harmonics beyond the third with any degree of accuracy. Because this program requires blade chordal loading data which is difficult to obtain, it is not quite as widely used as the original simple rectangular chordwise loading solution. It is used, however, when measured chordal data is available.

The next form of rotational noise solution which shall be discussed here is derived in Reference 7 by Martin Lowson and John Ollerhead of Wyle Laboratories. This is a closed form solution somewhat similar to that of Gutin, only with significantly more detail. This solution derives rotational noise from rotor thrust, drag and radial components of blade loading, and includes the effects of forward speed and blade motion. An assumption is made in this analysis that the rotor loading harmonics decay in a prescribed manner. Al-

though the program is capable of loading any assumed fall-off, it is generally assumed by its authors that the loading harmonics decrease as the inverse square of the loading harmonic number. In addition, the phase between these harmonics has been randomized to simplify the calculation procedure. It has also been assumed in this analysis that the chordwise loading for all flight conditions can be approximated by a Dirac delta function, i.e., a point chordwise loading pulse of infinitely short duration and unit area.

Sikorsky experience does not, in general, support the implied accuracy of many of these assumptions. Studies show that the phasing of the first several loading harmonics has a significant effect on rotational noise. The assumed phasing of the higher loading harmonics has been shown, however, to be relatively unimportant in predicting the harmonics of noise. Although the data of Reference 6 shows an inverse square decay of harmonic level with harmonic number, more recent data on the Sikorsky S-61⁷, experimental compound helicopter, has shown a blade loading harmonic order decay of $1/n^{1.4}$ to $1/n^{1.6}$ for most of the flight regimes from hover thru 140 knots (n = airload harmonic order). This decay results in approximately a 10 dB drop in the noise harmonic level per 10 harmonics of noise. At 50 knots, where known blade vortex intersections exist, the harmonic drop-off-reduced to $1/n^{0.6}$. It is interesting to note that main rotor test stand data during clean in-flow conditions approximates the $1/n^2$ law assumed by Lowson, resulting in a 20 dB drop in the noise harmonics level per 10 harmonics of noise. For conditions where the inflow was not as clean, the blade loading harmonic order decay again approached the $1/n^{1.5}$ level achieved in flight. Another assumption which should be briefly discussed is that of the concentrated chordal load. This concentrated load (single radial station) assumption should restrict this closed form solution to conditions with relatively clean inflow and minimal vortex interference. Blade vortex intersections can occur almost anywhere along the span with significant effects

on the acoust. signature. Experience with measured S-61F data of a recent USAAVLABS contract study (Reference 9) reflects the authors' position on the importance of an accurate definition of the chordwise loading distribution. Closer correlation was achieved between the predicted and measured first four noise harmonics of a 5 bladed rotor using only the first 16 measured loading harmonics with the measured chordwise loading distribution than was achieved using 30 measured loading harmonics with a rectangular chordwise loading distribution. When only 8 loading harmonics were used a rectangular chordal loading assumption predicted the fourth noise harmonic to be 15 dB lower than the value predicted with the measured chordal loading distribution was used.

In spite of the seeming uncertainties introduced into the Lowson/Ollerhead analysis by the approximations used in its formulation, the solution will be later shown to provide reasonable correlation with measured data and does, in fact, provide a useful tool for trending studies.

The analysis performed by Loewy & Sutton (Reference 4) results in an open form digitally integrated solution which accounts for steady and periodic blade loading, spanwise blade pressure distribution, a typical chordal pressure distribution, rotor coning, flapping and pitching motion and radial as well as thrust and drag components of blade loading. As for any other open form solution, detailed blade loading information is required for accurate results. No attempt has been made to include scaled harmonic to steady blade loading values into the final equations for trending. However judging by the form of the solution, this could be accomplished here rather easily.

The rotational noise analysis of S. E. Wright (Reference 12) yields a far field sound pressure relation which is based on both steady and fluctuating thrust and torque values. Although no data is given, it is presumed that correlation with measured data will be significantly better than that attainable with Gutin's solution. Because blade loading is concentrated at one radial

position, correlation should not be as good, however, as those analyses which distribute blade loading radially. It should be noted here that Lowson and Ollerhead in their study of Reference 6 concluded that with randomized blade loading the loss of accuracy due to the point spanwise loading assumption may be only of the order of 2 dB. To the authors' knowledge, sufficient empirical data has yet to be studied to correlate this finding. The presentation of Wright's analysis does provide an excellent insight into the modal development of rotational noise and a good feel for the mechanism of noise generation due to a rotating pressure field.

The ultimate test as to the worth of an analysis is its ability to correlate with measured data. Fortunately, rotational noise data calculated by several of the procedures described above is available along with corresponding measured data for the Sikorsky S-58 (CH-34) helicopter. Figure 3 indicates that the analyses of Loewy and Sutton (Reference 4), Lowson and Ollerhead (Reference 7), and Schlegel, King and Mull (Reference 10) yield comparable correlation with measured data up to the fourth harmonic for the hover case. As expected, the Gutin solution (Reference 1) loses accuracy rapidly after the first harmonic because of its reliance on steady blade loading only. Note that all of the analyses calculate low for the level of the fourth harmonic. This is to be expected from the Reference 4 and 10 results because the blade loading from Reference 8 used in each of these analyses was recorded only up to the tenth harmonic with questionable accuracy for the last 4 or 5 harmonics. For a four bladed rotor, blade loadings up to at least the twelfth are required to capture the peak contributor to the fourth noise harmonic. Another possible contributor to the discrepancy may lie in the fact that noise and blade pressure measurements were made on two different ships at two different times. Differences in the ships' rigging, in ambient winds, or in the ships' angle into the wind could make for blade loading and noise changes. The fact that the measured fourth

harmonic level is higher than the third indicates that high amplitude high harmonic blade loadings prevailed during the noise measurement test. This would cause the blade loading harmonic drop-off to be other than the smooth inverse square function assumed by Lowson & Ollerhead (Reference 7) and would in turn explain their lack of correlation.

Figures 4 and 5 show 80 and 110 knot data for the S-58. Correlation is similar to the hover case with the above comments regarding measured air-load and noise data holding true here also.

It can be concluded then that several valid analytical solutions to helicopter rotational noise are available. They vary in degree of difficulty of usage and quantity of input data required, but all are uniformly accurate for at least the first three harmonics of rotational noise under normal rotor operating conditions. It is the conclusion of the authors that until such time as better prediction methods are available for blade loadings, any of the above mentioned analyses should give reasonably accurate results for the first few harmonics. As current work concludes on improved wake and blade loading prediction methods, however, it would appear that the digital solutions would give better results for higher harmonic noise.

Vortex Noise

In calculating vortex noise, empirical solutions have been used primarily in the past. The equation shown below from the Sikorsky study of Reference 10 has been used widely in predicting rotor vortex noise.

$$\text{SPL} = 10 \left[2 \log (V_{0.7}) + 2 \log (T) - \log (A_B) - 3.57 \right]$$

$$V_{0.7} = \text{Velocity at } 0.7 \text{ radius (Ft/sec)}$$

$$T = \text{Thrust (lb)}$$

$$A_B = \text{Blade area (ft}^2\text{)}$$

This equation was derived for a field point which is located 17° from

the plane of the rotor away from the direction of thrust. For field points at different directions from the rotor plane, the change in level due to directivity can be achieved by assuming a dipole radiation pattern, symmetrical about the plane of the rotor. This relationship assumes maximum S.P.L. on the axis of the rotor and a $-20 \log \sec \theta$ relationship down to a minimum of no radiation ($-\infty$ dB) in the plane of the rotor, where θ is the angle between the rotor axis and the field point. To the authors' knowledge, the problem of vortex noise directivity variation with rotational and translational Mach number has not been treated very thoroughly either theoretically or empirically and more work is needed in this area. This vortex equation has been corroborated by several investigators and has shown excellent accuracy for the particular directional point to which it was derived. Agreement with this solution is not universal, however. Stuckey and Goddard, Reference 11, have developed a slightly different solution which seems to agree well with their measured data, indicating the probable dependence of blade design and uniformity of inflow on vortex noise generation.

The Reynolds number for which this data is applicable is in the range of 10^6 . The nominal center frequency of the vortex spectrum can be calculated by multiplying the velocity at the 0.7 radius point divided by the projected blade dimension times the Strouhal constant which is .28 for a rotor in this Reynolds number region.

For several years it has been generally assumed that the vortex noise generated by a rotor was the summation of the noise generated at the various blade stations due to the shedding of wakes at each station. The cumulative sound power generated by a blade from root to tip is shown relative to the total at the tip in Figure 6. Tests run by Sikorsky Aircraft on a trapezoidal tipped rotor blade have shown that spreading the tip vortex yields up to a 7 dB noise reduction in the vortex frequency range. According to Figure 6 there is nothing

that can be done to the outer 10 percent of the blade to yield anywhere near this type of noise reduction. Even complete removal of the outer 10 percent of the blade yields less than 1.5 dB. This fact raises serious doubts as to the dependence of vortex noise on trailing edge vortex shedding. It has been suggested that the noise is not generated at the tips but rather by the trailing vortex intersecting a trailing blade. This intersection of the tip vortex with the trailing blade has been seen on test stands for multi-bladed rotors. It is not clear, however, whether this effect is actually the one which is causing the bulk of the vortex noise. This suggestion is illustrated in Figure 7 which shows two rotors with thickened and standard coretip wakes intercepting the rotor.

There is a definite link between rotational and vortex noise. As mentioned above, rotational noise is usually considered to be the discrete frequency noise at rather low frequencies in the spectrum and vortex noise is assumed to be the middle frequency random or broadband noise. The fact is that they are both caused by oscillating blade pressures and that they just fall into different frequency ranges. Rotational noise is caused by more ordered blade loading effects and the vortex noise is caused by more random higher frequency pressure loadings. Some investigators (Reference 2 and 5) have seen discrete frequencies of the main rotor blade passage noise up to frequencies of 400 Hertz where random vortex noise is normally assumed to be present. For now in any case, it is convenient to treat rotational and vortex noise separately and calculate their effects separately because they do appear to behave differently. The trend studies will be presented with these effects treated independently.

TRENDS

Rotational Noise

The basic rotational noise trends as used at Sikorsky Aircraft are listed in Figure 8. They were developed using a simpler of the two digital rotational noise prediction methods per Reference 10. Only a steady loading was

used to determine the levels of the rectangular chordal pressure, and the distributed steady loading is all that is required for calculation of the fundamental noise harmonic level. The trends were run on untwisted blades and do not include the effects of blade pitch change.

Figure 9 shows the effect of tip velocity on the fundamental harmonic of blade passage noise. The tip speed effect is strongly influenced by the number of blades in the rotor. Blade numbers of 4, 5, and 6 are shown; however the second equation of Figure 8 will serve to extend this range.

Figure 10 describes the effect of thrust and radius on the fundamental frequency rotational noise. The curves are based on the relationships that (a) 20 times the common log of the thrust ratio gives the thrust S.P.L. difference, with the higher thrust holding the higher S.P.L., and (b) 8.5 times the common log of the radius ratio gives the radius S.P.L. difference, with the larger radius yielding the lower S.P.L.

The final trending parameter considered here is number of blades. Figure 11 presents number of blades versus S.P.L. as a function of tip Mach number. A linear inverse relationship between number of blades and S.P.L. is seen to exist. Here the tip Mach number affects the slope of the sound pressure level blade number curve, according to the first equation of Figure 8.

Vortex Noise

The vortex noise trends are simply represented by the equation shown below.

$$\Delta \text{SPL} = 20 \log \frac{V_2}{V_1} + 20 \log \frac{T_2}{T_1} + 10 \log \frac{A_{B1}}{A_{B2}}$$

The parameters affecting vortex noise are blade area, rotor thrust, and rotor tip speed. Figure 12 shows the variation of these parameters graphically. Increasing thrust increases the sound pressure level at a rate of 20 times the common log of the thrust ratio. The same relationship is true of the

tip speed ratio. The blade area is a ten log relationship for sound pressure level. The rotors used to empirically derive these numbers had Reynolds numbers in the vicinity of 10^6 .

General Comments on Trending

The trending relationships given above have been found to be useful for determining the rotational and vortex noise impact of small variations in rotor physical and operational parameters. The rather large parameter ratios are not meant to imply fractional dB accuracy over these ranges. Rotor noise predictions are normally made by both trending from the best available measured data and by the use of analytical methods.

IMPACT OF TRENDS

General

Rotor noise trending is useful in providing tradeoff information for particular problems. Two of the common uses for the acoustic trending relations are in aural detection and perceived noisiness calculations. In military situations where detection distance is to be kept to a minimum, the aircraft is flown in the nap of the earth to take advantage of terrain for both visual cover and acoustic absorption. At altitudes in the 100 foot range, aural detection is normally controlled by low frequency rotor rotational noise because the mid and high frequency noise is attenuated quickly by the terrain in addition to the standard atmospheric absorption mechanisms.

For civil application of VTOL aircraft the primary external noise concern is for the perceived noisiness levels transmitted to inhabited areas. The calculation of perceived noisiness places emphasis on mid and high frequency noise. In a helicopter, the noise in this frequency range is either rotor vortex or engine generated noise. It is generally less expensive to treat a turbine engine than it is to change main rotor operational and physical parameters to attain a given noise reduction. After the engine noise level has been reduced

to well below that of the main rotor, however, vortex noise trending may be used for further noise reduction.

Detectability

The effects of these trends on the detectability problem can be best shown by use of example. The detection criteria used here is that of Reference 3 by R. Lowey. Figure 13 shows acoustic detection criteria for aircraft cruising at 50 ft. altitude over sparse-jungle terrain. The ordinate is the sound pressure level generated 200 ft. directly in front of the aircraft at ground level. The abscissa is the detection distance in feet. One curve is drawn for each of the first three octave bands. Matching the sound pressure level of the aircraft by octave band to these curves gives a detection distance for each octave. The largest number for detection distance, or the furthest distance away from the observer at which the aircraft is detected in any one octave determines the actual detection distance. To evaluate the tradeoff of helicopter noise versus detection distance, consider the simplified case of a single rotor helicopter, in which first octave rotational noise controls detection. Let the level be 70 dB in front of the aircraft in the first octave at a 200 ft. distance. Also assume a 0.7 tip Mach number for the aircraft. Figure 14 shows the effect of trading off this tip speed on detection distance. This curve is obtained by following the tip speed trending and the first octave detection criteria. It is obvious from Figure 14 that tip speed is a powerful function for the control of rotational noise levels and hence detection distance.

Annoyance

A popular way of describing acoustic annoyance is perceived noisiness which is expressed in PNdB (perceived noisiness decibels). PNdB is a single number method of expressing annoyance level and is obtained from the octave band sound spectrum and the Noy tables. The Noy tables relate sound pressure level of noise to the ear's sensitivity by frequency. The ear is most sensitive in

the mid-frequencies, and these frequencies are the most important in determining the annoyance level.

As far as the single articulated rotor helicopter is concerned, mid-frequency noise is controlled by the engine and by main rotor vortex noise. If the engine is excluded as a significant source in this trending study, main rotor vortex noise alone is the determining factor in this frequency range. Using the trending study for determining vortex noise level, a chart such as shown in Figure 15 may be constructed. This figure shows annoyance level versus tip speed ratio. The aircraft operates initially at a tip speed of 700 ft. per second. Vortex noise is reduced according to the trends, maintaining constant thrust and C_T/σ . Note that to attain the reductions noted in Figure 15, substantial performance penalties must be tolerated. The requirement for constant thrust and C_T/σ means that blade area must be increased as the inverse square of the tip Mach number reduction. One obvious implication here is that vortex noise reduction is extremely expensive in weight when simple parametric trending is used. Less costly reductions may be obtained only after more is known and understood about the basic physical mechanism of vortex noise generation.

Consumed Horsepower - PNdB Trend

To take a short look at overall helicopter and STOL noise trends, Figure 16 was constructed. Trend lines are drawn for conventional helicopters, STOL aircraft, and for a quiet helicopter series. This quiet helicopter series consists now of only two vehicles. Notice that there are not only differences in magnitude separating these groups of vehicles but differences in slope. It is found that the slope of conventional V/STOL vehicle trend curve is approximately 23 times the log of the consumed horsepower ratio, while the slope of the quiet helicopter series is 13 times the log of the consumed horsepower ratio. The higher slope and magnitude of the conventional V/STOL trend is explained by the fact that the conventional helicopter annoyance is controlled largely by

engine and auxiliary rotor noise and the STOL is controlled by highly loaded propellers operating at high tip speeds. The noise trend slope of the quiet helicopter is controlled by main rotor vortex noise which is a 20 log thrust relationship, which is equivalent to a 13 log horsepower relationship when the ideal propeller law (i.e. horsepower proportional to thrust $3/2$) is utilized. The quiet helicopter can be realized only when sources other than the main rotor (engines and tail rotor) are silenced significantly compared to current practice. Silencing of these auxiliary sources is less costly in both weight and direct operating cost (DOC) than changing the main rotor.

CONCLUSIONS

Several procedures are currently available for calculating up to the first three harmonics of rotor rotational noise accurately. The single most important improvement in these procedures over Gutin's original solution is the addition of noise generated by unsteady airloads. The steady airload solution is still considered a valid indicator of fundamental frequency rotational noise, however, for harmonic airload amplitude - frequency distributions seen on helicopter rotors.

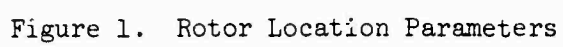
Trend studies for both rotational and vortex noise indicate that tip speed is the most powerful function to use in reducing levels. For rotational noise the tip speed and number of blade effects interact, with more blades yielding the greater noise-tip speed dependence. The trending studies presented are in terms of parameters which allow noise to be traded off against weight and aerodynamic performance. The impact of noise reduction changes on direct operating cost can be evaluated with minimum effort by the use of these simple trends.

REFERENCES

- (1) Gutin, L., "On the Sound Field of a Rotating Propeller", NACA TM-1195, October, 1948.
- (2) Leverton, J.W., "Helicopter Noise", Institute of Sound and Vibration Research, University of Southampton, England
- (3) Loewy, R.G., "Aural Detection of Helicopters in Tactical Situations", Part II, Institute For Defense Analysis Research Paper P-25, AD409535, Alexandria, Virginia, May, 1963.
- (4) Loewy, R.G., and Sutton, L.R., "A Theory For Predicting the Rotational Noise of Lifting Rotors in Forward Flight, Including a Comparison with Experiment", USAAVLABS Technical Report 65-82, January, 1966.
- (5) Lowson, M.V., "Thoughts on Broad Band Noise Radiation By a Helicopter", Wyle Laboratories - Research Staff Report WR 68-20.
- (6) Lowson, M.V., and Ollerhead, J.B., "Studies of Helicopter Rotor Noise", USAAVLABS Contract DAAJ02-67-C-0023.
- (7) Ollerhead, J.B., and Lowson, M.V., "Problems of Helicopter Noise Estimation and Reduction", AIAA, February, 1969.
- (8) Schieman, James, "A Tabulation of Helicopter Rotor Blade Differential Pressures, Stresses, and Motions as Measured in Flight", NASA TM X-952, Langley Station, Hampton, Virginia, March, 1964.
- (9) Schlegel, R.G., Bausch, W.E., "Helicopter Rotor Rotational Noise Prediction and Correlation", USAAVLABS Contract DA 44-177-AMC-448(T), (Not yet published)
- (10) Schlegel, R.G., King, R.J., and Mull, H.R., "Helicopter Rotor Noise Generation and Propagation", USAAVLABS Technical Report 66-4, October, 1966.
- (11) Stuckey, T.J. and Goddard, J.O., "Investigation and Prediction of Helicopter Rotor Noise", Journal of Sound and Vibration, Vol. 5, No. 1,

January, 1967.

- (12) Wright, S.E., "Sound Radiation From a Lifting Rotor Generated by Asymmetric Disc Loading", University of Southampton Institute of Sound and Vibration Research, I.S.V.R. Technical Report No. 5, April, 1968.



$$(1) \quad P = \frac{m\omega_1}{2\pi cR} \left[-P \cos \sigma + \frac{ncM}{\omega r^2} \right] J_{mn}(Kr \sin \sigma)$$

$$(2) \quad P = \frac{R}{2\sqrt{2\pi^2 a}} \left[(P_{re'})^2 + (P_{im'})^2 \right]^{\frac{1}{2}}$$

$$P_{re'} = \int_0^{2\pi} \int_0^r \frac{L(r, \psi)}{mS^2} \sin\left(\frac{mn\psi}{2r}\right) \left\{ \frac{mn\Omega}{c} \sin u + \frac{\cos u}{S} \right\} \\ \left\{ \sin \beta \cos \sigma \sin(\psi - \theta) + \cos \beta \sin \sigma \right\} r dr d\psi$$

$$P_{im'} = \int_0^{2\pi} \int_0^r \frac{L(r, \psi)}{mS^2} \sin\left(\frac{mn\psi}{2r}\right) \left\{ \frac{mn\Omega}{c} \cos u - \frac{\sin u}{S} \right\} \\ \left\{ \sin \beta \cos \sigma \sin(\psi - \theta) + \cos \beta \sin \sigma \right\} r dr d\psi$$

$$u = mn \left[\frac{2S}{c} + \frac{a}{2r} + \psi \right]$$

m = Harmonic Number

ω = Blade Passing Frequency ($b\Omega$)

Ω = Rotor Rotational Speed

b = Number of Blades

c = Speed of Sound

P = Rotor Thrust

M = Rotor Torque

$K = \omega/c$

a = Blade Chord

$S = \sqrt{R^2 + r^2 - 2rR \cos \sigma \cos(\theta - \psi)}$

β = Blade Pitch Angle

$L(r, \psi)$ = Blade Section Loading

Figure 2. Rotational Noise Solutions

□ GUTIN
 ○ SCHLEGEL, KING & MULL
 △ LOWSON & OLLERHEAD
 × LOWEY & SUTTON
 I MEASURED RANGE

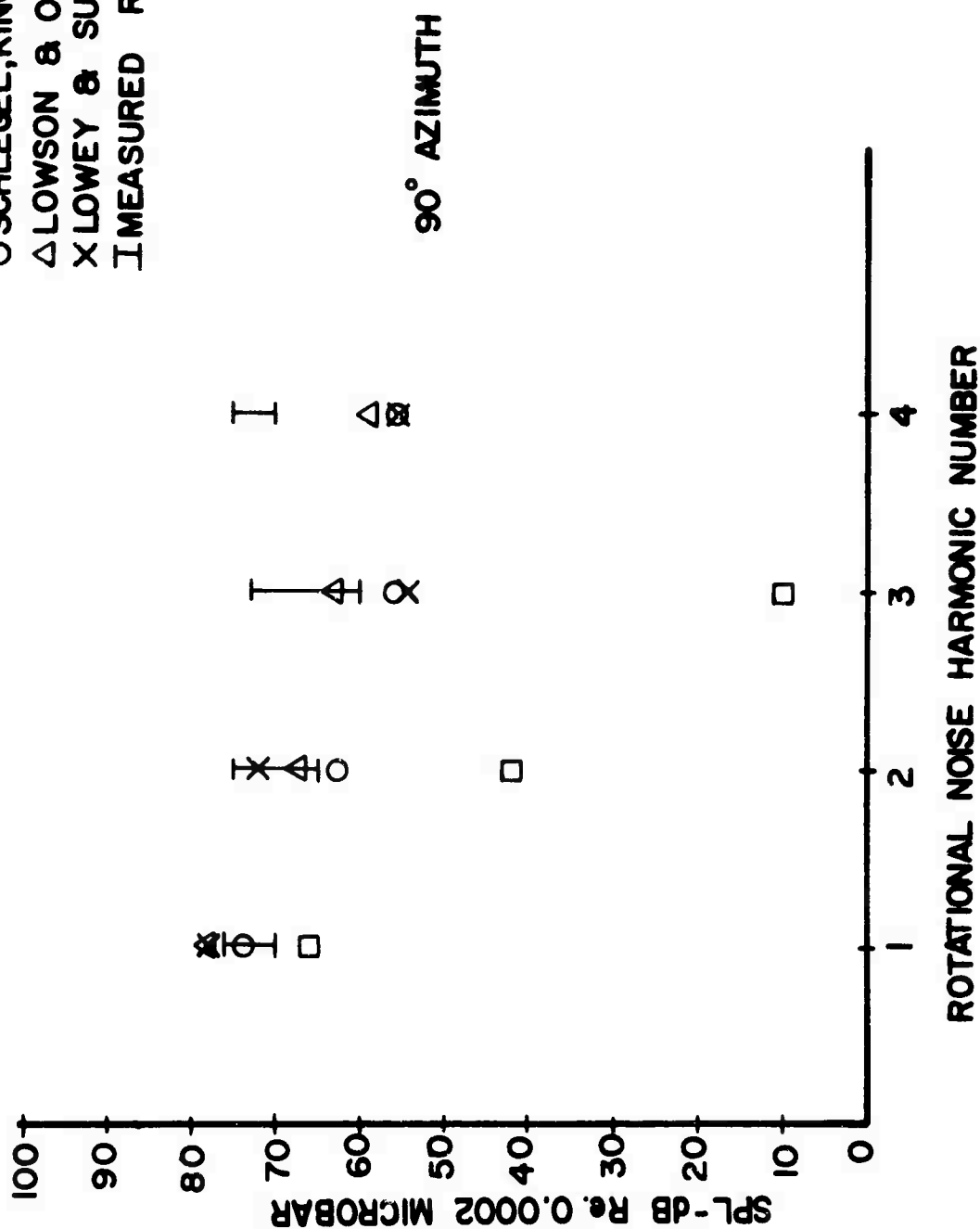


Figure 3. Rotational Noise Correlation For The S-58 Helicopter in Hover

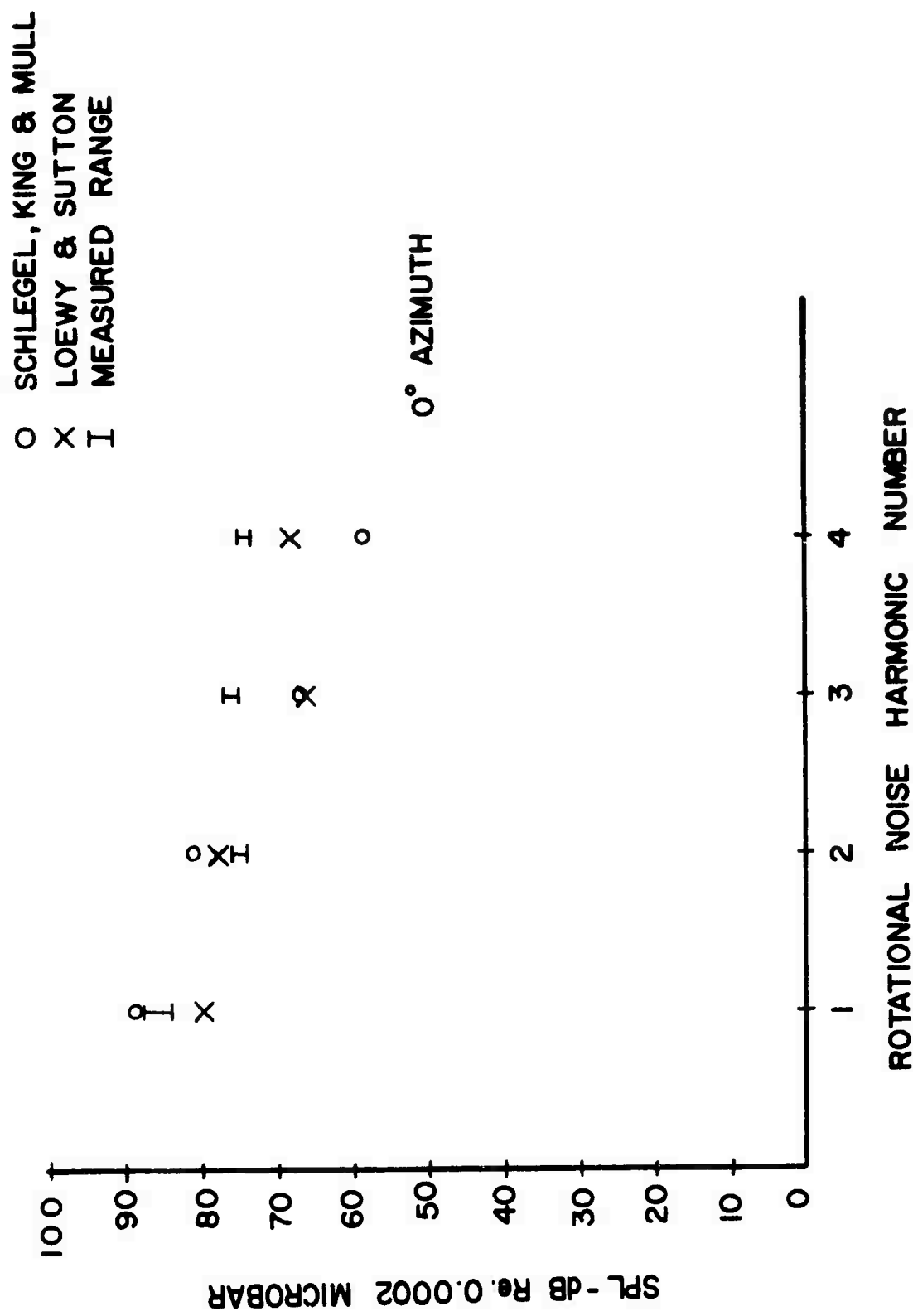


Figure 4. Rotational Noise Correlation For the S-58 Helicopter at 80 Knots

O SCHLEGEL, KING & MULL
 X LOEWY & SUTTON
 I MEASURED RANGE

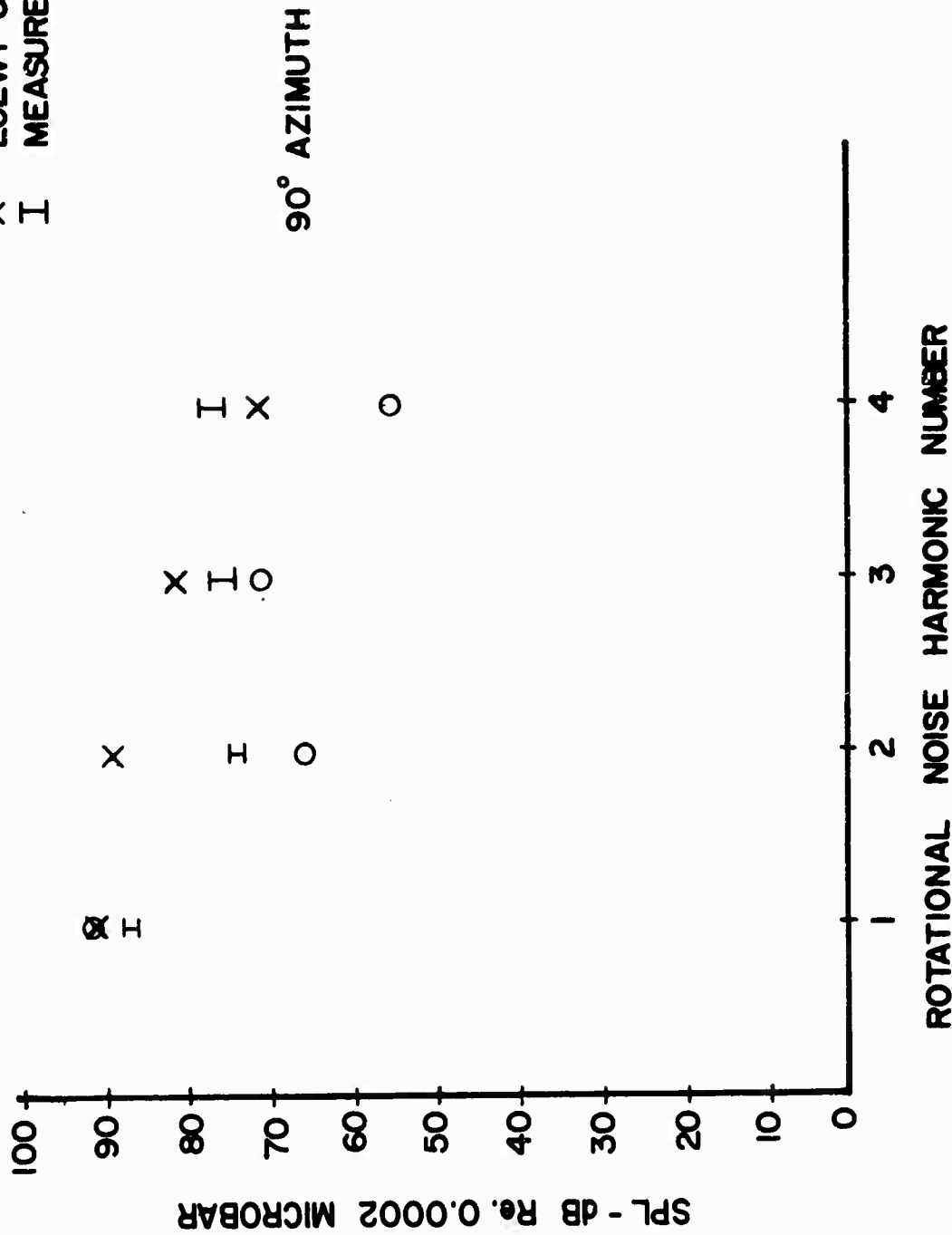


Figure 5. Rotational Noise Correlation For The S-58 Helicopter at 110 Knots

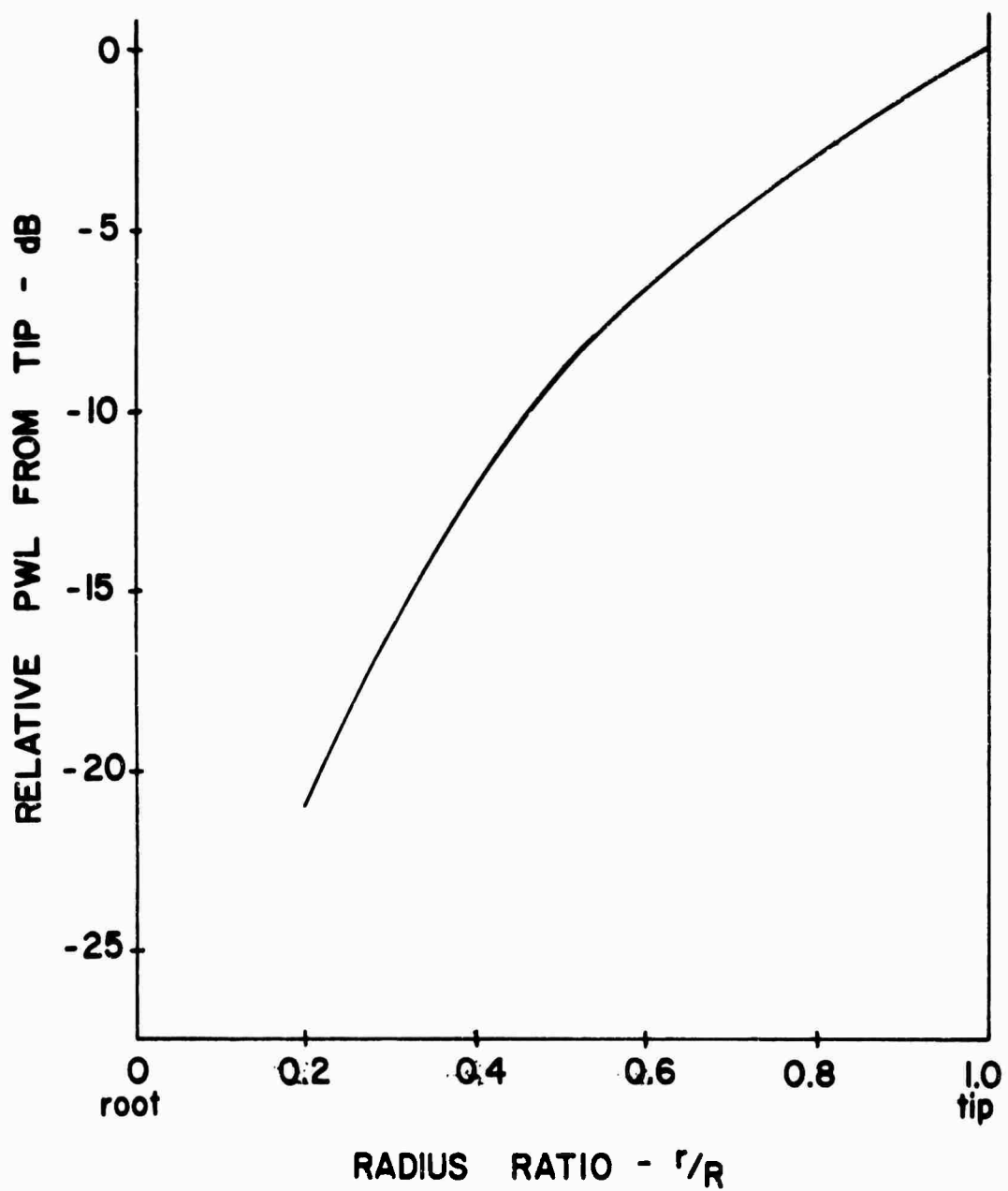


Figure 6. Cumulative Vortex Noise Generation By Trailing
Edge Shedding

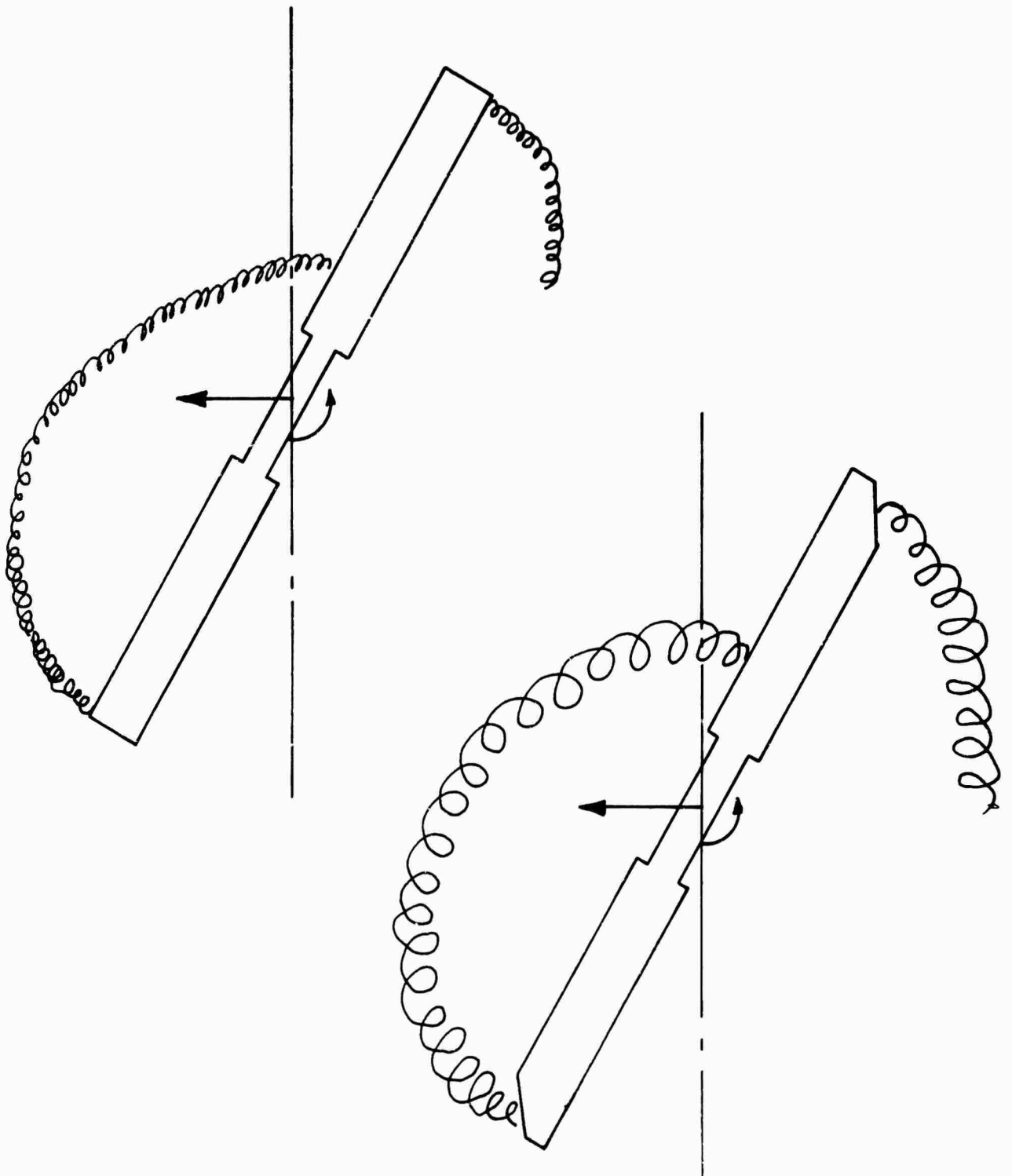


Figure 7. Vortex Noise Generation By Interaction of Tip Wakes

NOMENCLATURE

B = NUMBER OF BLADES
M = TIP MACH NUMBER
R = ROTOR RADIUS
T = ROTOR THRUST
Δ = DIFFERENCE

<u>PARAMETER</u>	<u>SOUND PRESSURE LEVEL RELATION</u>	<u>INDEPENDENT PARAMETERS</u>
B *	$\Delta \text{SPL}_B = - \Delta B \left[\frac{1.46}{M^2} \right]$	R, T
M *	$\Delta \text{SPL}_M = (17B + 22) \log_{10} \left(\frac{M_2}{M_1} \right)$	R, T
R	$\Delta \text{SPL}_R = - 8.5 \log_{10} \left(\frac{R_2}{R_1} \right)$	B, M, T
T	$\Delta \text{SPL}_T = 20 \log_{10} \left(\frac{T_2}{T_1} \right)$	B, R, M

*** For changes in both M and B, either parameter change may be made first**

Figure 8. Expressions for Rotational Noise Trending

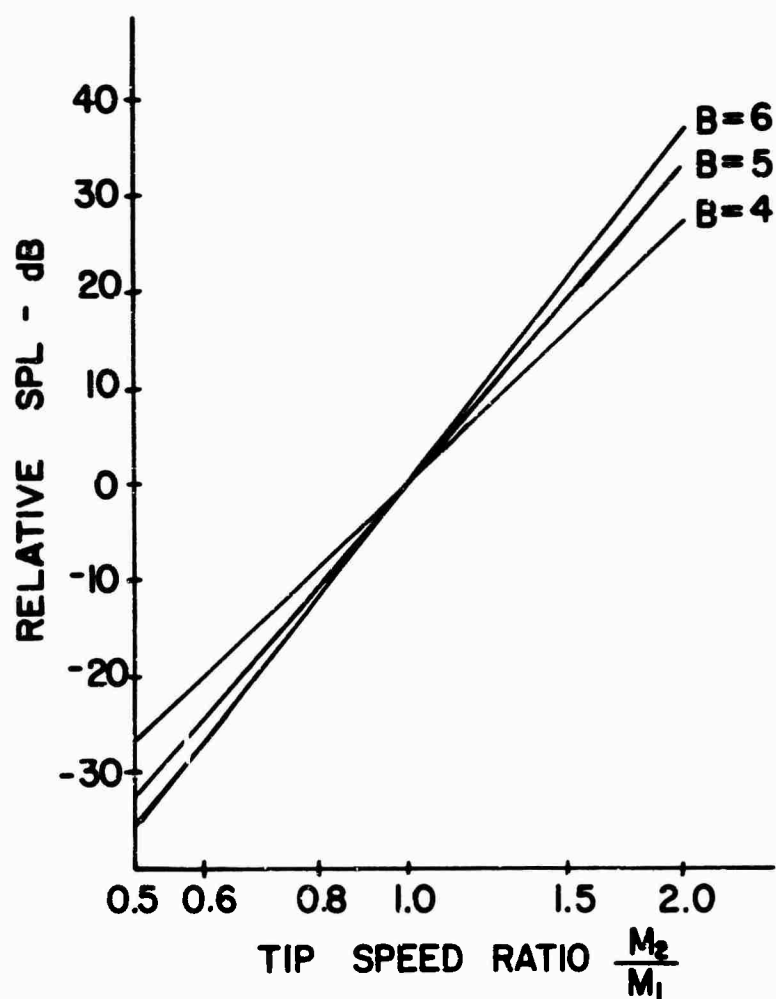


Figure 9. Relative Level of Rotational Noise Fundamental With
Change in Tip Speed

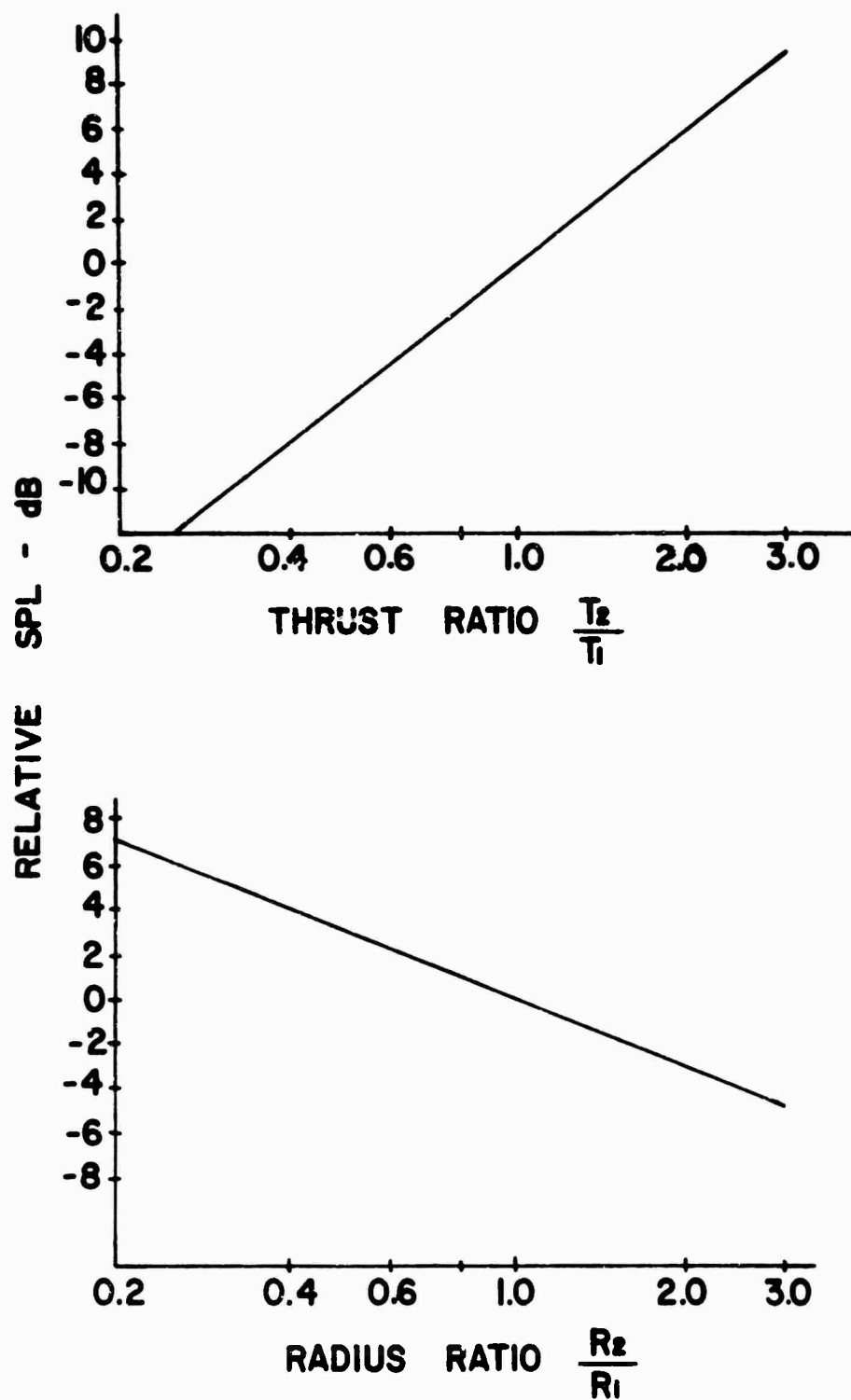


Figure 10. Relative Level of Rotational Noise Fundamental With
Change in Thrust and Radius

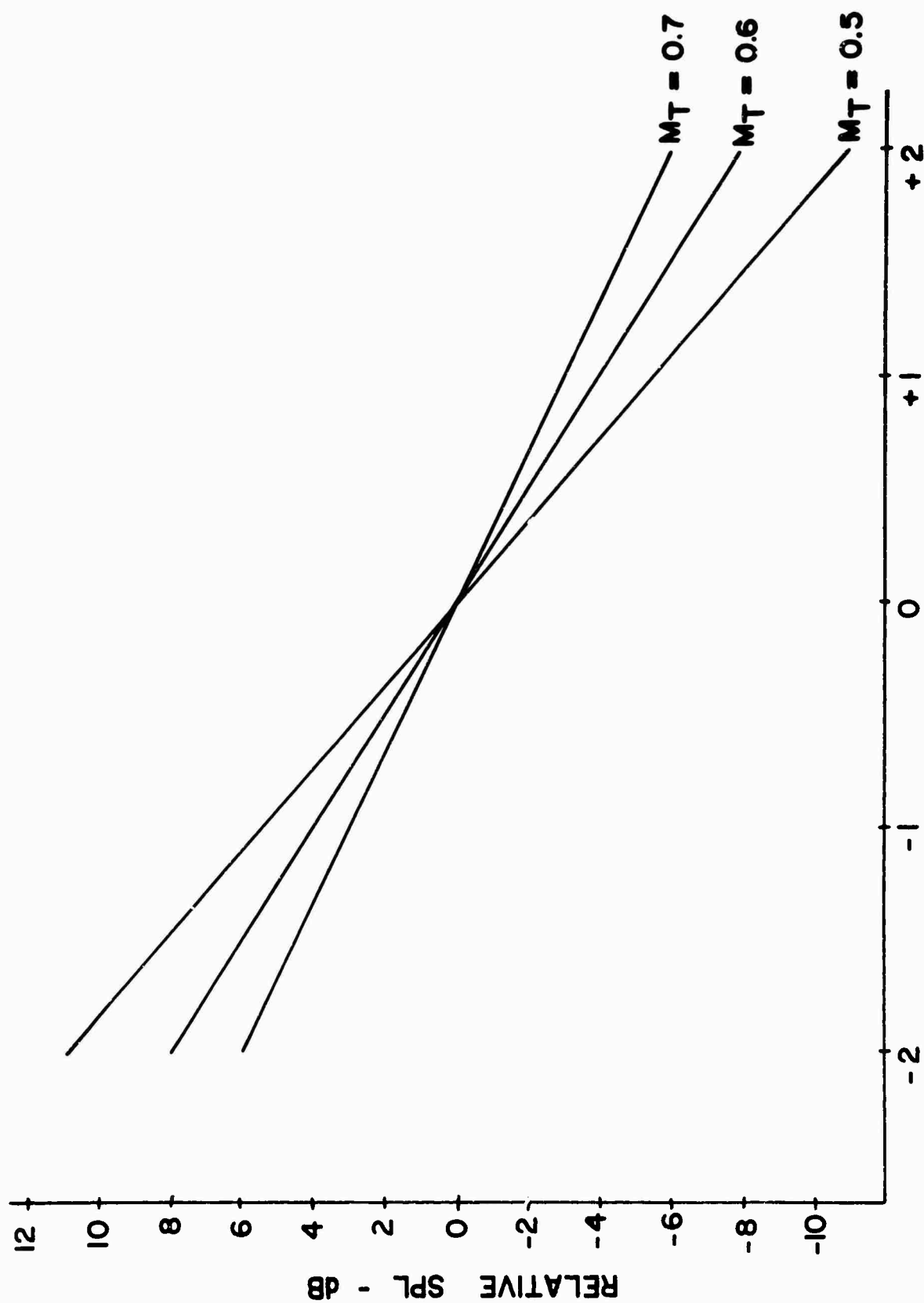


Figure 11. Relative Level of Rotational Noise Fundamental With Change in Number of Blades

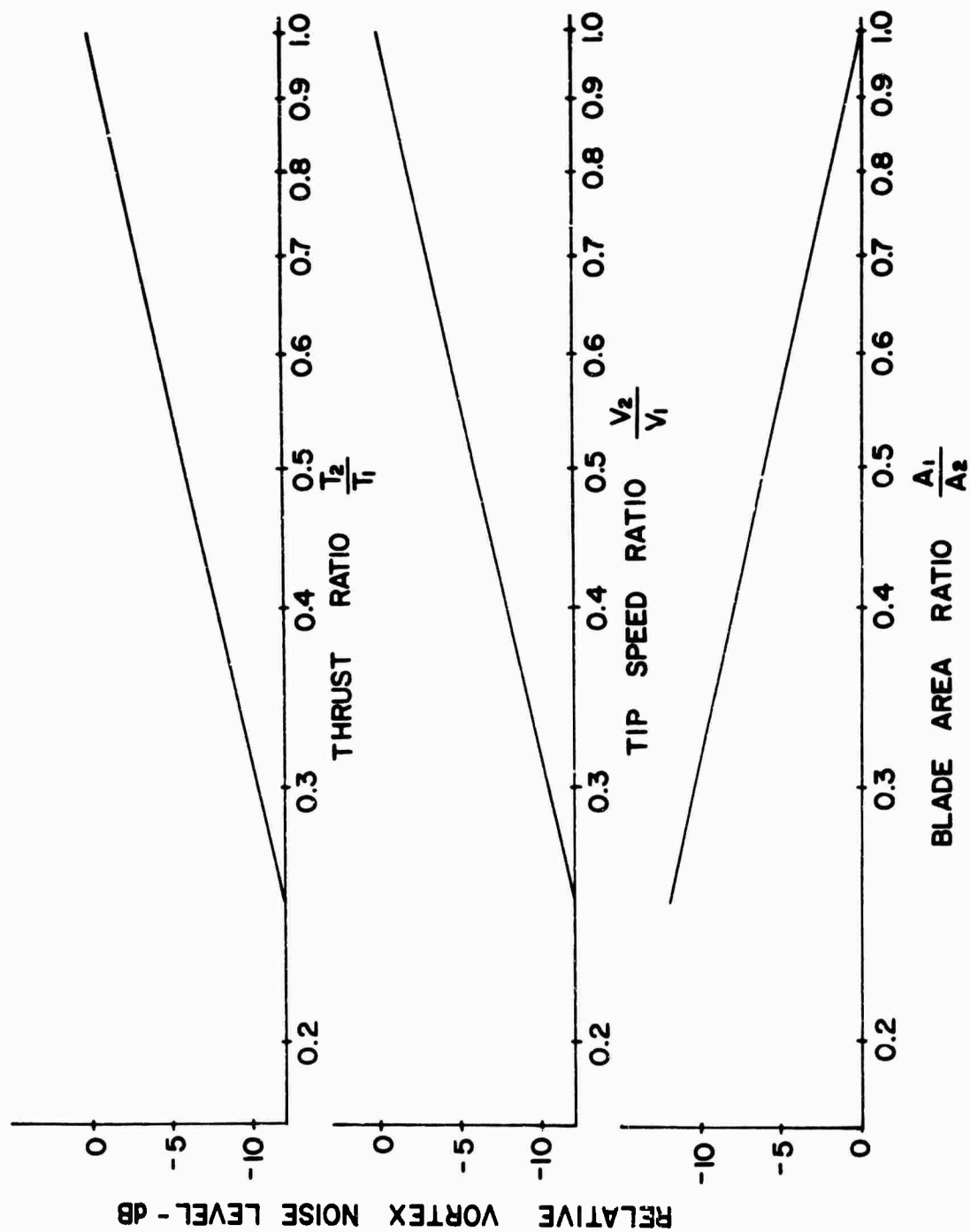


Figure 12. Vortex Noise Trends

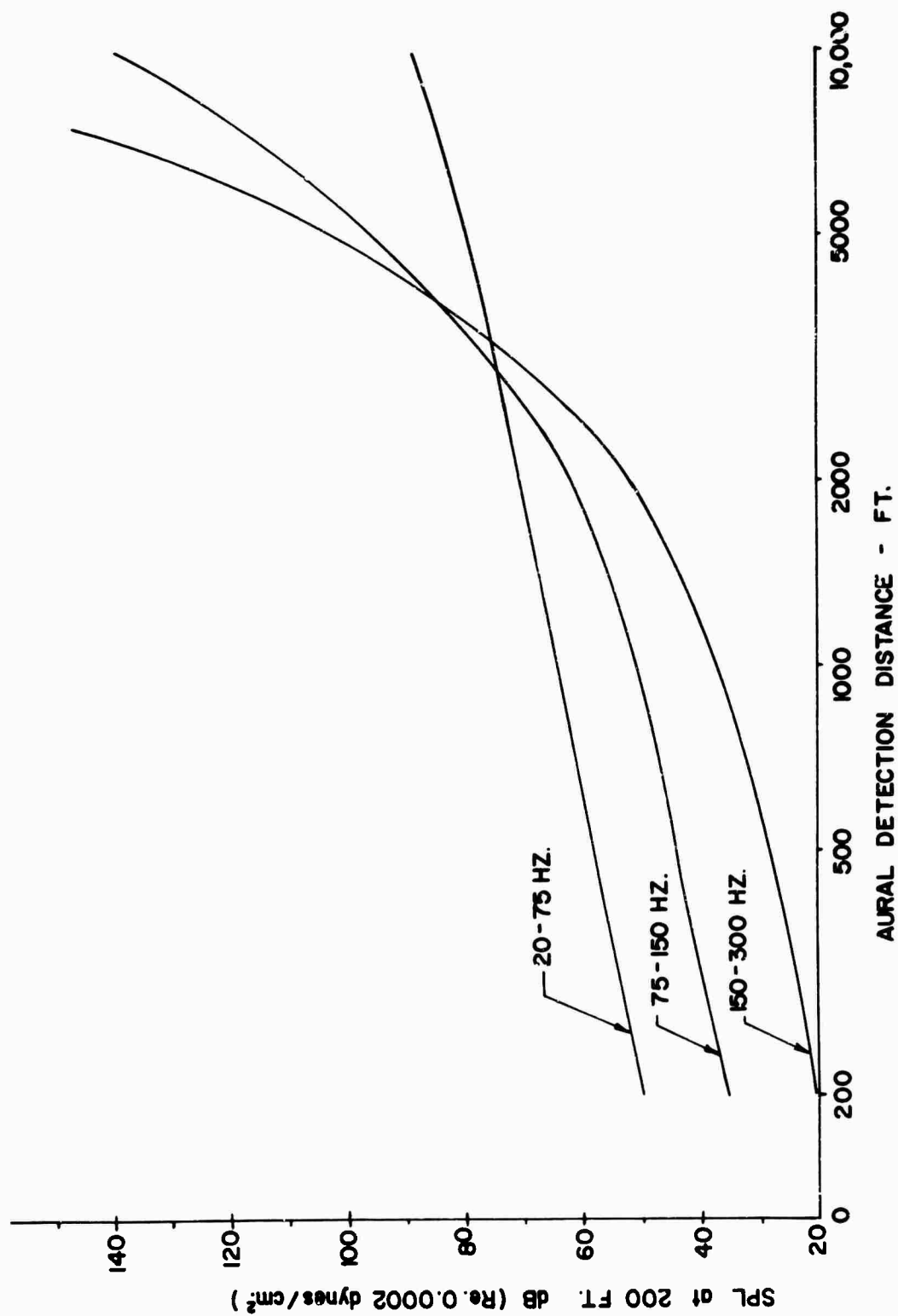


Figure 13. Aural Detection Criteria For 50 Foot Altitude Flight Over Sparse Jungle Terrain

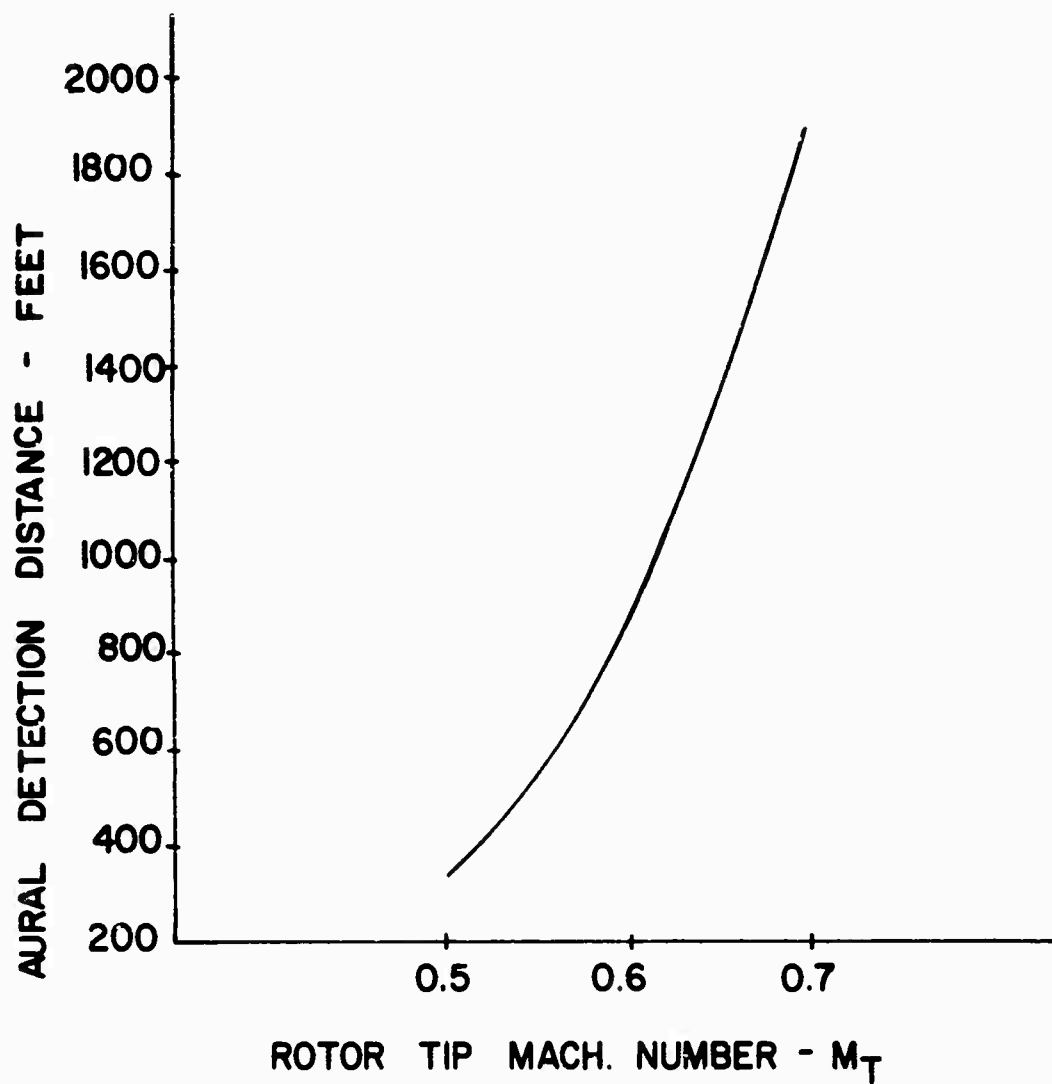


Figure 14. Effect of Main Rotor Tip Speed on Detection Distance
For First Octave Rotational Noise Controlled Detection

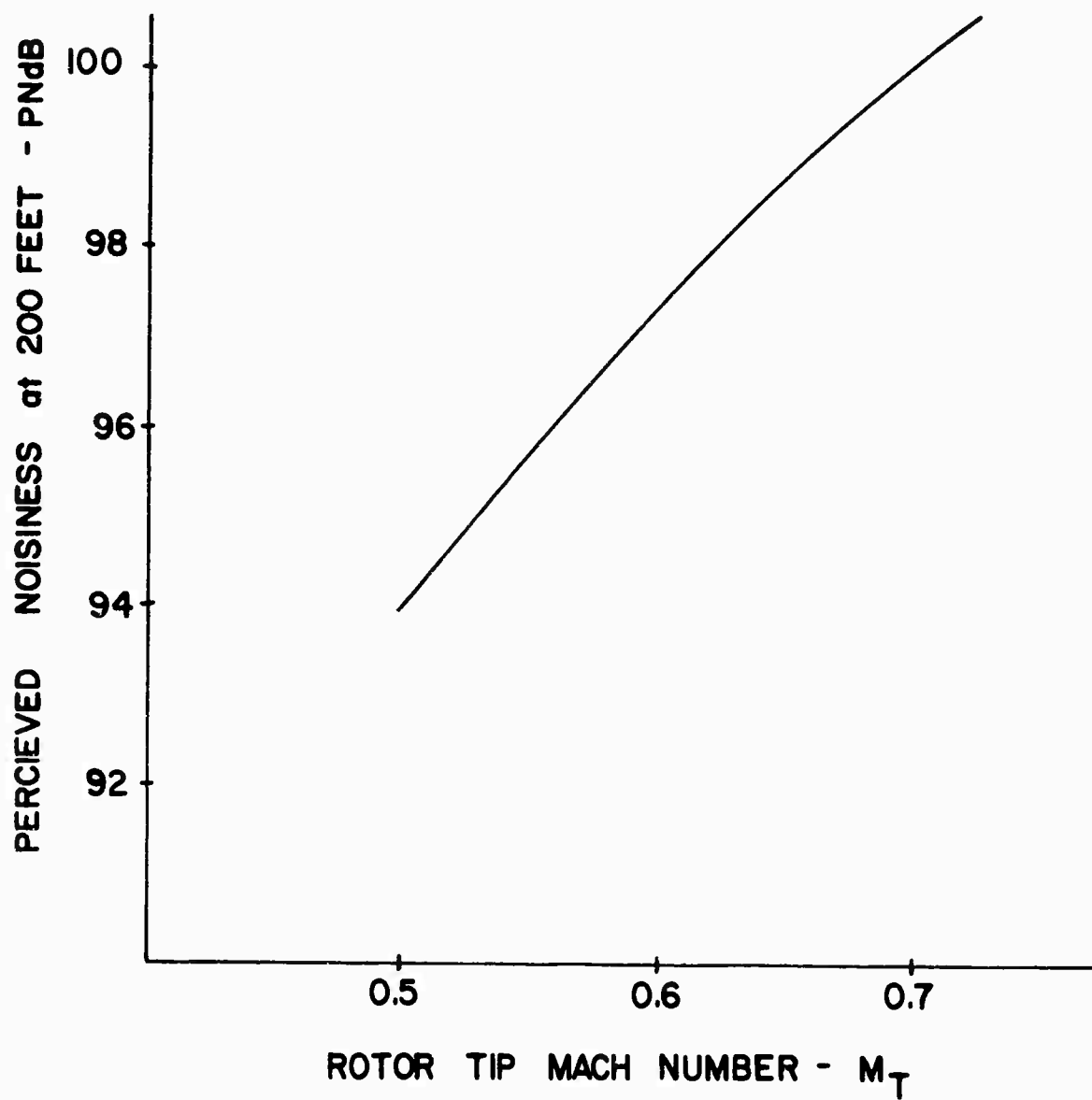


Figure 15. Effect of Main Rotor Tip Speed on Perceived Noisiness
For Constant Thrust and C_T / σ

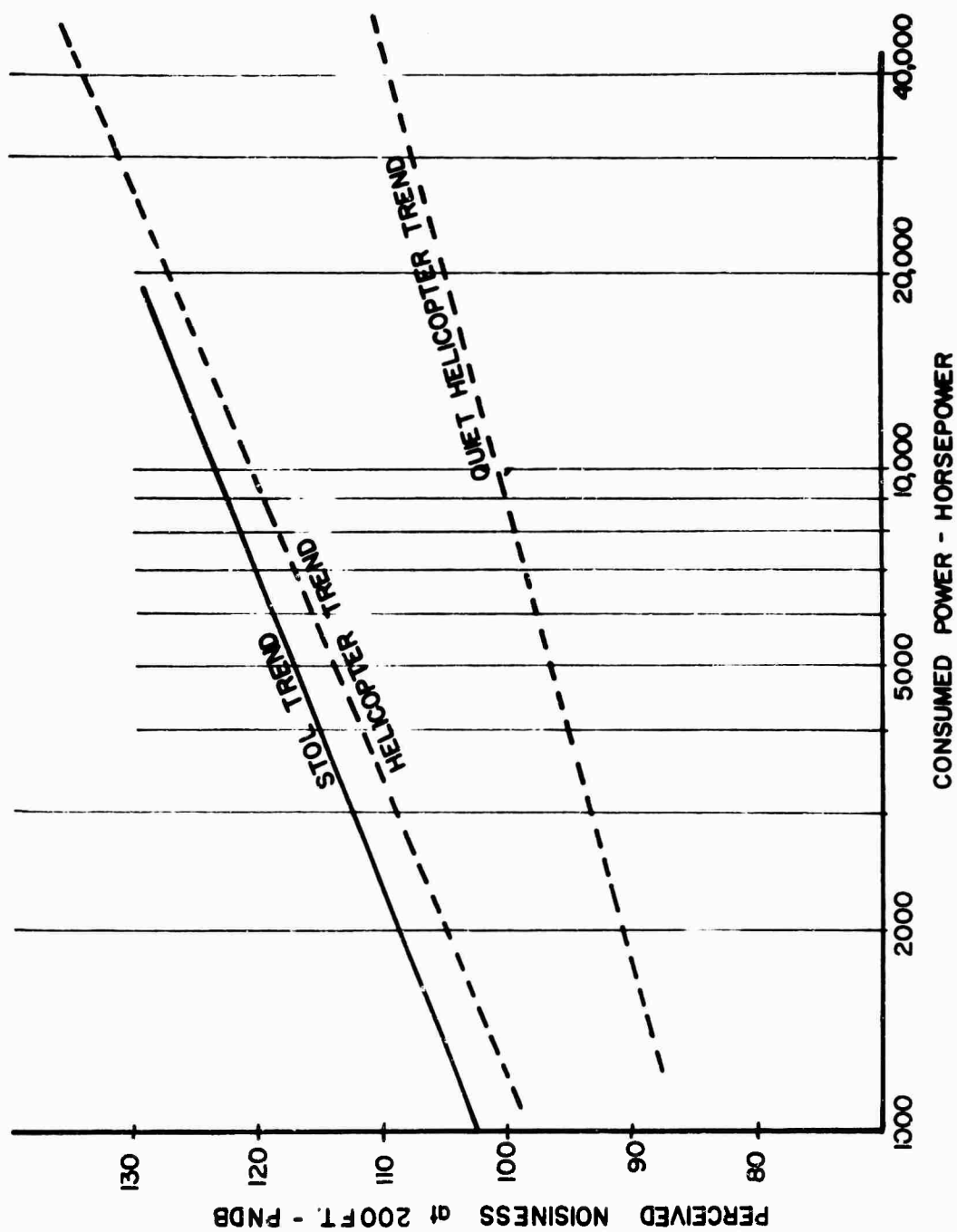


Figure 16. Consumed Power - Perceived Noisiness Trend

ROTOR NOISE MEASUREMENTS IN WIND TUNNELS

by

C. R. COX

Bell Helicopter Company
Fort Worth, Texas, USA

SUMMARY

This paper presents the forward-flight noise characteristics of helicopter rotors, as they were determined in wind-tunnel tests of a model and two full-scale rotors. It describes the effects on rotor noise of advancing-tip Mach number and blade-tip shape. Tunnel noise is defined, and its masking effects on rotor noise are shown to be negligible for most operating conditions. Rotor noise measured in the wind tunnel is compared with that measured during a flyover. The source frequencies of blade slap are defined for advancing-tip Mach numbers up to 1.024. The noise of a model is compared with that of full-scale rotors, and the similarities are discussed. The azimuthal variation of noise, the effects of tip shapes, and the sound directed forward from the model rotor are described.

The advancing-tip Mach number is shown to determine the noise characteristics of a rotor in forward flight. The abrupt increase in noise at advancing-tip Mach numbers between 0.70 and 0.80 is believed to be caused by the onset of compressible flow. This noise, commonly called blade slap, can be reduced by 5 to 8 db by thinning the profile of the blade's tip. The effects of thrust are shown to be negligible at advancing-tip Mach numbers

greater than about 0.85. The source frequencies of blade slap are primarily high-harmonic rotational-noise components, which exceed the low harmonics by 20 db at an advancing-tip Mach number of 1.00. These are believed to be caused by high-order, fluctuating drag forces associated with compressibility.

The noise of model rotors can also be measured in wind tunnels. The abrupt increase of high harmonics at high Mach numbers is similar to that for full-scale rotors. This is evidence that the basic generating mechanism of blade slap is present in the model rotor. Exploratory measurements show the noise of the advancing blade to be higher than that of the retreating blade. The low harmonics peak in the aft quadrant of the advancing side, and the high harmonics, in the forward portion of the disc. The low harmonics are directed above and below the rotor plane, but the high harmonics are at their maxima in the plane. Thinning the profile of the blade tips reduces the model rotor's noise by 3 to 4 db. Sweeping the leading edge, in combination with the profile thinning, lowers it by 7 to 8 db.

LIST OF SYMBOLS

DB, db	Decibel, sound-pressure level referenced to $0.0002 \text{ dynes/cm}^2$
Hertz	Frequency, 1 Hz = 1 cycle per second
$M_{(1.0, 90.)}$	Advancing-tip Mach number, $\Omega R + V$
M	Order of sound harmonic, based on blade-passage frequency
PNdb	Perceived noise level

R	Blade radius
V	Tunnel velocity
μ	Advance ratio, $V/\Omega R$
ψ	Rotor-blade azimuth
Ω	Rotational speed

FULL-SCALE-ROTOR NOISE MEASUREMENTS

The noise of two helicopter rotors was measured in the NASA Ames 40- by 80-Foot Wind Tunnel.* The purpose of these tests was to determine if such measurements were possible, and if so, to define the characteristics of the noise at high advancing-tip Mach numbers and the effects of modifying the shapes of the blade tip. Noise measurements in wind tunnels offer distinct advantages over whirl-tower and inflight measurements: operating conditions can be accurately controlled, and the forward-flight aerodynamics of rotors can be preserved without having to compensate for the effects of relative motion between a fixed microphone and a moving sound source.

Test Description

Figure 1 illustrates the location of the microphone in the test section, and the acoustic-data-acquisition system. The microphone was mounted 68 feet forward of the rotor-mast

*Cox, C. R., Full-Scale Helicopter Rotor Noise Measurements in Ames 40- By 80-Foot Wind Tunnel, Bell Helicopter Company Report 576-099-052, July 1967.

centerline and 14.5 feet below the hub. A faired nosecone over the microphone minimized wind noise. This microphone system is omnidirectional to within ± 0.5 db. The microphone wind noise peaks at frequencies greater than about 5000 Hz, well above the principal source frequencies of rotor noise. All acoustic data were recorded on magnetic tape and later reduced to overall, octave-band and 6-percent narrow-bandwidth sound-pressure levels.

The test envelope included variations in advance ratio, advancing-tip Mach number, rotor-plane inclination, and collective pitch. Two 48-foot-diameter, 21-inch-chord UH-1D/H main rotors were tested. One had standard, square blade tips and the tips of the other, referred to as thin-tip, were tapered in profile thickness at the tip. The latter was tested at advancing-tip Mach numbers up to 1.024.

Tunnel-Noise Characteristics

Wind tunnels are not the ideal environment for acoustic measurements. The fans and powerplants are noisy, and standing waves and reflective surfaces in the enclosure can amplify or deaden sounds. Useful acoustic data can be obtained only if the levels of all the source frequencies to be measured are above those of the tunnel.

Before the rotors were installed, the tunnel's noise characteristics were defined under various operating conditions. The noise measured with the rotors operating is compared with tunnel noise in Figure 2. For the majority of the run conditions,

rotor noise was 10 db or more above that of the tunnel. Tunnel noise adds less than 0.5 db to the measured levels. The measurements must be corrected, however, for certain combinations of Mach number and advance ratio. In the range between Mach 0.80 and Mach 0.87, and for advance ratios higher than 0.20, from 1 to 7 db must be subtracted from the measured levels. The first three octaves require correction by less than 4 db, but the higher octaves require up to 7 db.

The amplification of the enclosure at various microphone locations has been determined.* The resulting corrections of the measured data, to obtain free-field levels, are:

<u>Frequency Band, Hz</u>	<u>Correction, db</u>
20 - 75	--
75 - 150	-7
150 - 300	-9.5
300 - 600	-6
600 - 1200	-7
1200 - 2400	-4
2400 - 4800	-3
4800 - 10,000	0

*Hartman, J. R. and Soderman, P. T., Determination of the Acoustical Properties of the NASA Ames 40- By 80-Foot Wind Tunnel, Preliminary information furnished by Ames Research Center, August 1967. (A random-noise source was used to determine the sound amplification. Additional corrections may be needed for pure-tone sources.)

Wall effects are negligible at all microphone locations farther than about 5 feet from a wall. No obvious resonances or echoes have been observed in the monitoring or the playback of the data.

Variation With Mach Number

The advancing-tip Mach number determines, to a large extent, a rotor's noise characteristics--particularly its acoustic signature at high forward airspeeds. The effects of Mach number on rotor noise are shown in Figure 3. The noise of both rotors is at its minimum at advancing-tip Mach numbers between 0.70 and 0.80, but it increases abruptly at higher speeds--at a rate of 15 to 20 db per Mach 0.10. This abrupt increase is believed to be caused by the onset of compressible flow on the advancing blade.

The rotational-noise harmonics in the first octave increase during low-speed flight up to $M_{(1.0, 90.)} = 0.80$, decrease slightly at 0.85, and then increase rapidly. The harmonics in the second octave are affected by compressibility at Mach numbers as low as 0.73, and thereafter they increase at a constant high rate. They generate the maximum sound-pressure level of those measured. The third and fourth octaves contain the harmonics above the sixteenth and the random-phase (vortex) noise component. They vary with Mach number much as the second octave does. Compressibility affects these components when $M_{(1.0, 90.)} = 0.80$ to 0.85. The effect is most pronounced on the standard rotor: the levels of these components increase quite rapidly in a relatively small range of Mach numbers. The same

effect exists in the fifth and sixth octaves. Components in these octaves contribute little to the total noise, but they do affect perceived noise levels at high Mach numbers, and they contribute to the qualitative intensity of rotor noise described as "slapping", "popping", "banging" and "cracking".

Effects of Tip Shapes

Figure 3 illustrates also the effects on full-scale rotor noise of blade tip shapes. The noise of the thin-tip rotor is 5 to 8 db lower than that of the standard rotor. The amount of noise reduction by octave bands varies, however, as a function of Mach number. The overall sound pressure level is reduced by 5 db. Levels in the first two octaves are reduced by 5 db and, in the high octaves, by 5 to 8 db. These reductions are realized primarily at $M_{(1.0, 90.)} = 0.90$, the highest Mach number for which comparable data are available. Since the noise of the thin-tip rotor apparently increases less rapidly with increasing Mach number than that of the standard rotor, even greater reductions are indicated at higher Mach numbers.

Effects of Other Parameters

The effects of thrust on noise are negligible at Mach numbers greater than about 0.85. Variations from 2000 to 10,000 pounds result in changes of 2 db or less. Thrust is an important parameter when $M_{(1.0, 90.)} < 0.85$. The effects of thrust on rotor noise are summarized below:

<u>M_(1.0, 90.)</u>	<u>Variations in Rotor Noise For Thrusts from 2000 to 10,000 Pounds</u>
0.70 - 0.80	10 - 15 db (high frequencies) 4 - 10 db (low frequencies)
0.80 - 0.85	2 - 4 db
> 0.85	0 - 2 db

Variations in the advance ratio of 0.13 to 0.40 do not affect appreciably rotor noise. Greater variation than that tested may make more change in noise however, especially in hover and in low-speed flight.

Comparison With Free-Field Data

Wind-tunnel measurements of rotor noise can be used to predict free-field levels. Figure 4 compares the rotor noise recorded in the wind tunnel with that measured during a flyover. The operating conditions for the main rotor were similar in both cases: thrust = 10,000 pounds, and $M_{(1.0, 90.)} = .85$. The tunnel data are shown uncorrected and corrected for distance and enclosure amplification. The levels measured in the tunnel are within 2 to 3 db of those measured in the open, except in the frequency ranges known to contain tail-rotor and drive-system noise.

Source Frequencies of Blade Slap

Frequency spectra for the two test rotors at various Mach numbers are given in Figure 5. These spectra are from 6-percent

bandwidth analyses. Rotational noise harmonics are shown in the left portion of each graph. The most notable change in the spectra is the rapid increase with Mach number of the rotational noise components--above the seventh harmonic for the standard rotor, and above the fifth for the thin-tip rotor. These components are the primary source frequencies of blade slap. They are believed to be caused by high-order, fluctuating drag forces, particularly on the tip of the advancing blade.

Noise components at frequencies greater than 200 Hertz also increase rapidly with Mach number. Rotational-noise harmonics higher than the sixteenth are believed to be the primary sources. The random-phase (vortex) noise component is also in this frequency range, but its contribution to blade slap is believed to be small.

Two findings that are as yet unexplained are the relatively low level of the standard rotor's seventh harmonic, and the harmonically unrelated peaks in the spectrum. Their contribution to blade slap and to the rotor's noise signature is not known.

MODEL-ROTOR NOISE MEASUREMENTS

Noise was measured in the Ling-Temco-Vought 7- by 10-Foot Wind Tunnel, to determine the feasibility of using small-scale rotors for basic noise research. A 1/7-scale model rotor, aerodynamically scaled to correspond to the full-scale rotors tested in the Ames tunnel, was fitted with three tip configurations.

Noise measurements were made 9.7 feet forward of the mast centerline, one seventh the distance of the Ames' full-scale tests. In addition, exploratory measurements near the rotor tips were made.

It was found that the noise of scaled rotors can be measured, with negligible masking by and interference from tunnel noise. At low Mach numbers, however, flow recirculated in the test section, resulting in a "rough-running" condition, with correspondingly higher noise levels. This condition disappeared as tunnel velocity increased. No attempt was made to define the amplification of noise by the enclosure.

Comparison of Model and Full-Scale Rotor Noise

The noise components of a model rotor are at higher frequencies than those of a full-scale rotor because of the model's higher rpm. They can be compared with those of a full-scale rotor, however, since the frequencies of the rotational-noise harmonics and the random-phase (vortex) noise component are functions of scaled parameters--blade-passage frequency and profile thickness, respectively.

The noise of the model rotor is compared with that of the full-scale, thin-tip rotor in Figure 6. Data are shown for three advancing-tip Mach numbers. The rotational-noise components above the fourth harmonic are in general agreement, both in level and in variation with Mach number. The most important similarity

is the abrupt increase in these high harmonics at high Mach numbers, which is evidence that the basic generating mechanism of blade slap is present in the model. It is also interesting to note that the harmonics fall off not as a straight-line function, but apparently as a series of peaks that are unrelated to blade-passage frequency. These peaks are evident in the full-scale data (Figure 5), and they extend out to the higher frequencies as the Mach number increases.

There are obvious dissimilarities of full-scale and model rotor noise. For example, the model's low harmonics are higher than those of the full-scale rotor, particularly at high Mach numbers. These harmonics are of little practical significance for main rotors, since most are inaudible and are below the response of AM recording systems. They are primary sources of tail rotor noise, however.

Noise Characteristics Near Rotor Tips

Acoustic data recorded 12 inches from the blade tips provide an insight into the azimuthal variation of rotor noise. The noise emitted near the advancing and retreating sides of the rotor disc is compared in Figure 7. Sound-pressure levels for the 600 to 1200-Hertz band are shown versus advancing-tip Mach number. This octave contains the eighth through the sixteenth rotational-noise harmonics. For a given Mach number, the noise emitted by the advancing blade exceeds that of the retreating

blade. This is the first experimental evidence that rotor noise in forward flight comes primarily from the advancing blade, particularly at the high Mach numbers that are associated with blade slap.

The noise levels measured at each 10 degrees of azimuth (ψ) on the advancing and retreating sides of the rotor are given in Figure 8. The second through the fourth and the eighth through the sixteenth harmonics are shown for an advancing-tip Mach number of 0.94. The low harmonics reach a maximum while $\psi < 90$ degrees, whereas the high harmonics peak in the forward portion of the disc on the advancing side ($\psi > 90$ degrees). Hence, the aerodynamic loading producing the low-order rotational noise harmonics is different from that producing the high-order harmonics. This loading varies with azimuth and along the span.

Sound Directivity

The directivity of the sound forward of the model rotor is shown in Figure 9. The low harmonics are at their maxima above and below the rotor plane, and at a minimum very near the plane. The high harmonics, however, do not exhibit this directivity. They are at their maxima in the plane of rotation. This is additional evidence that high-order fluctuating drag forces produce blade slap. Because of this inplane directivity forward of the rotor, high-speed blade slap can be heard as a

helicopter approaches but not after it has passed overhead. In addition, the crew cannot hear the slap produced at high speeds and is not aware of the often intense acoustic signal emitted by the rotor.

Tip Shapes

The objective in the design of a blade's tip shape is to improve the rotor's performance while reducing its noise. The operating conditions, for which benefits are desired, dictate the proper design. For high advancing-tip Mach numbers, the tip's profile should be thin and the leading edge should be swept to increase the lifting efficiency of the tip and to delay the effects of compressibility.

The effects of tip shapes on the model rotor's noise are illustrated in Figure 10. Noise levels of a standard square-tip, a thin tip and a thin double-swept-tip are shown. The abrupt increase in noise caused by compressibility is delayed by altering the tip shape. The high harmonics are reduced by 3 to 4 db by thinning the profile, and by 7 to 8 db by also sweeping the leading edge. The rate at which the noise increases after the onset of compressibility effects does not appear to be affected by these tip shapes.

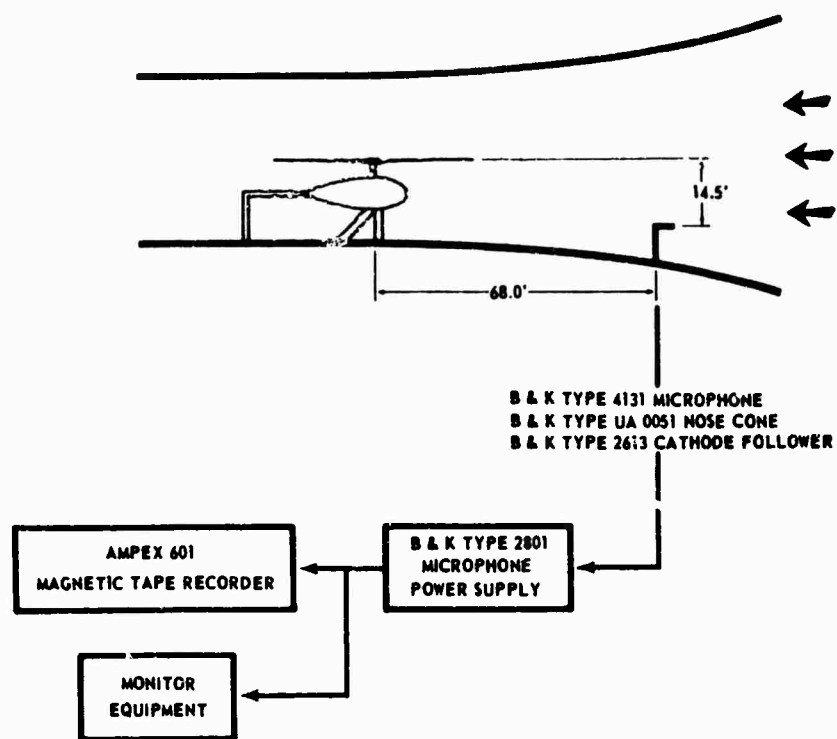


Figure 1. Acoustic Data Acquisition System Used in NASA Ames 40-By 80-Foot Wind Tunnel.

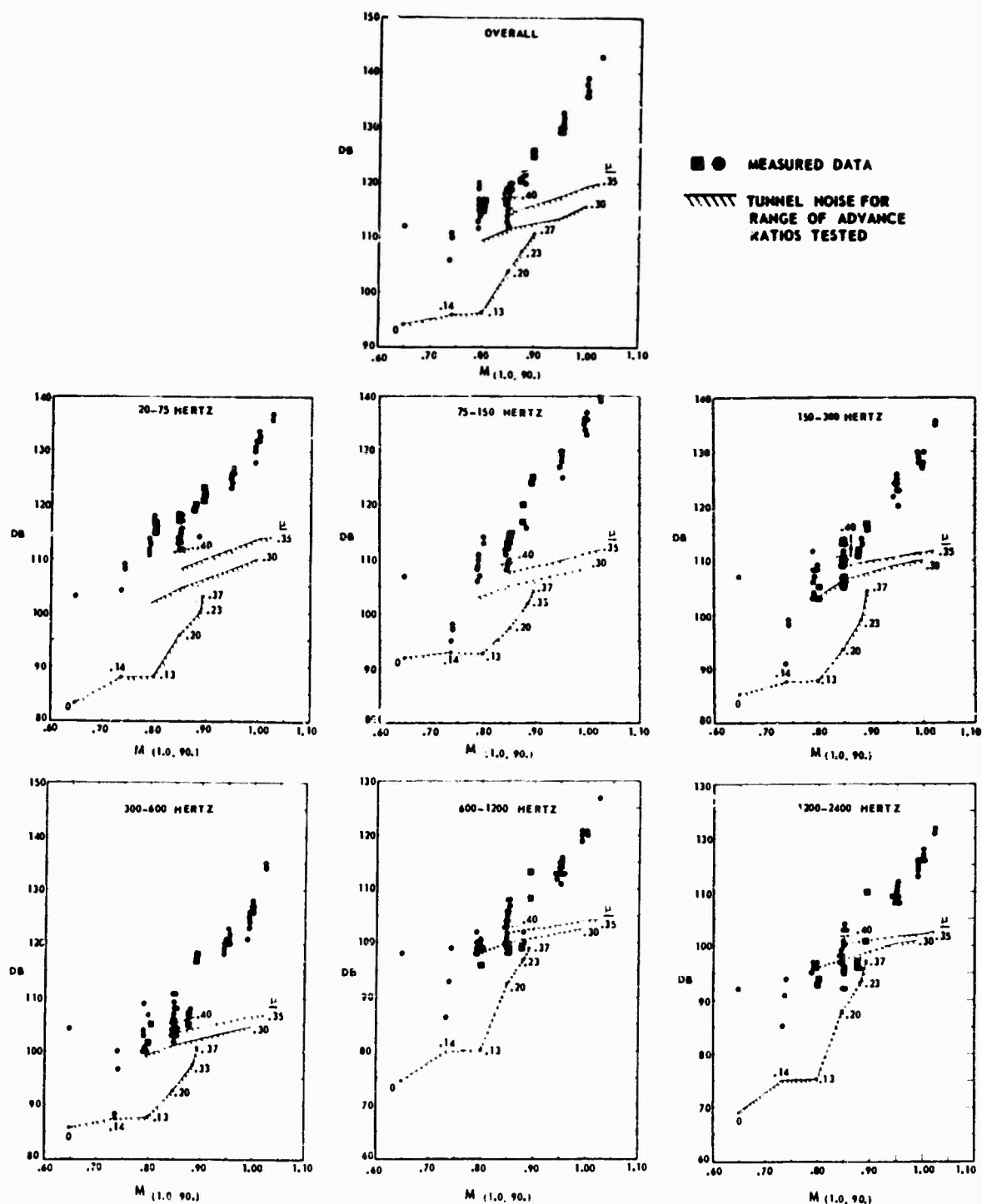


Figure 2. Level of Rotor Noise Above Tunnel Noise.

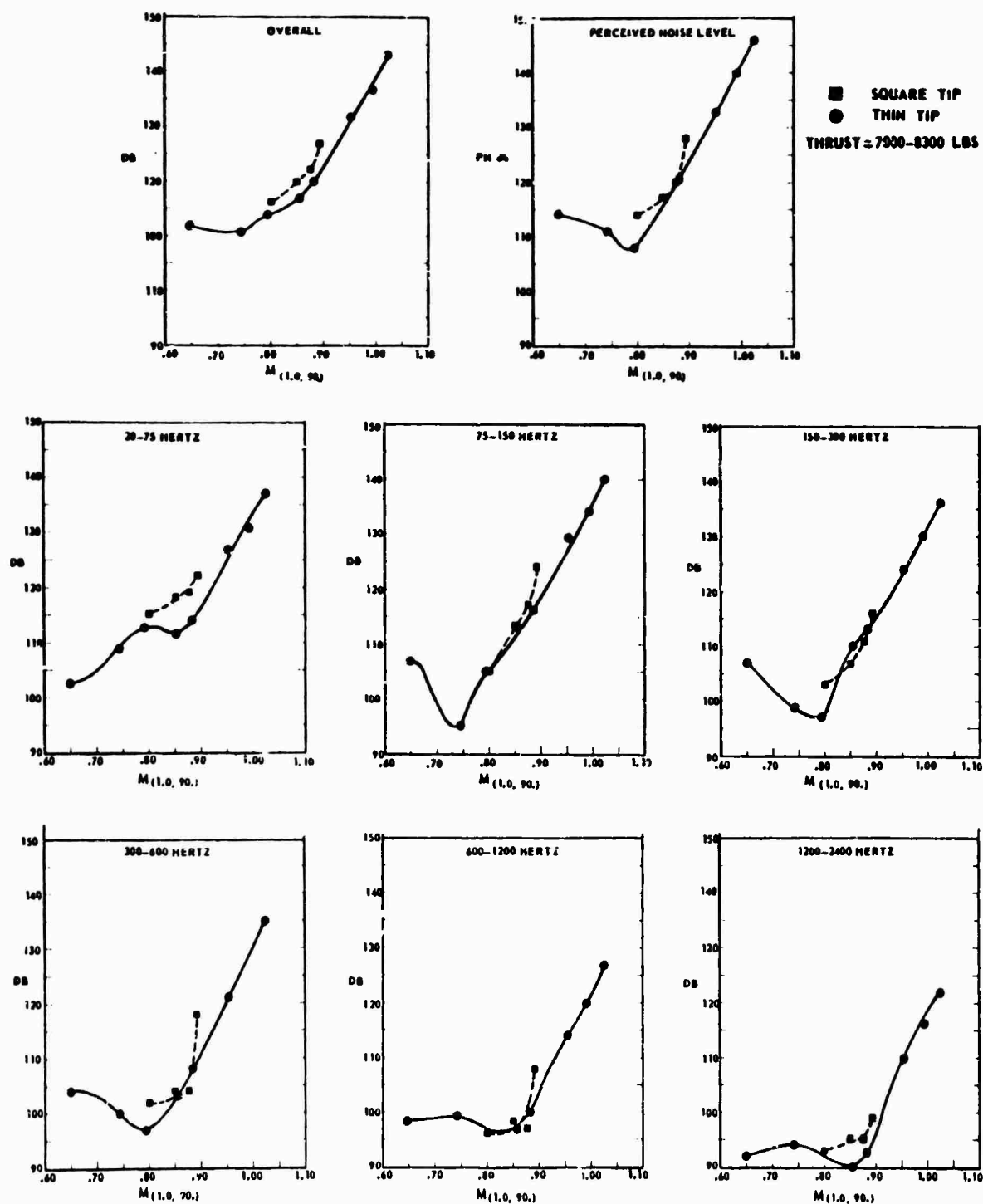


Figure 3. Variation of Rotor Noise with Advancing Tip Mach Number.

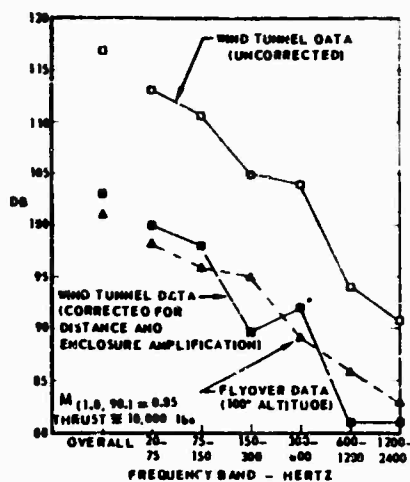


Figure 4. Comparison of Rotor Noise Measured in the NASA Ames Wind Tunnel and During Flyover.

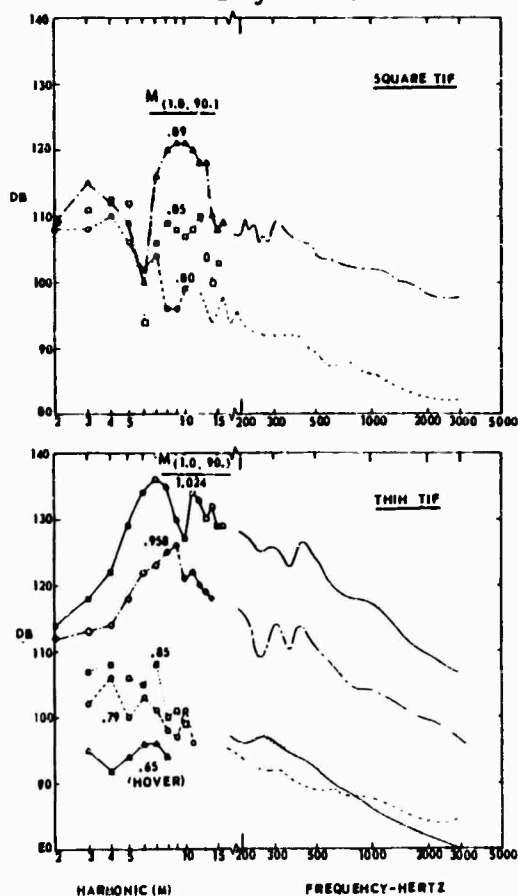


Figure 5. Frequency Spectra of Rotor Noise at Various Advancing Tip Mach Numbers.

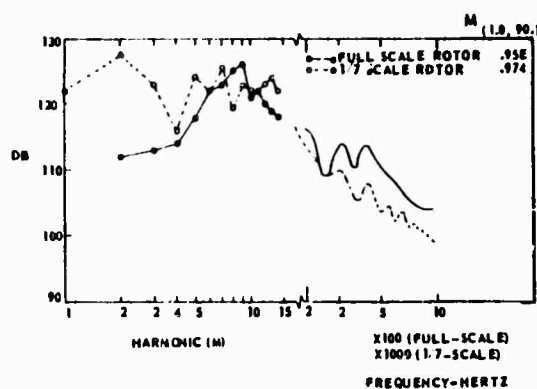
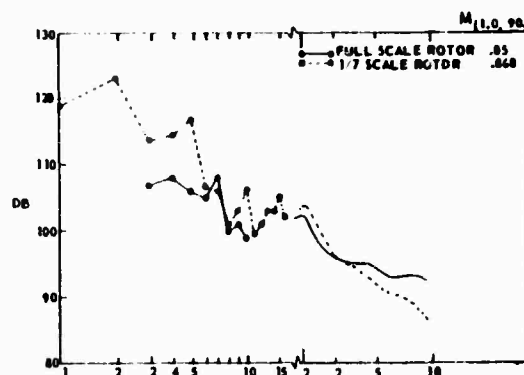
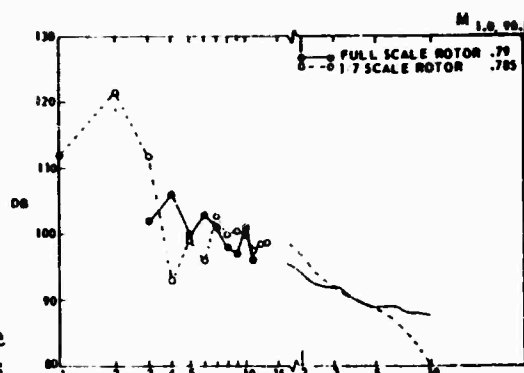


Figure 6. Comparison Between Model and Full-Scale Rotor Noise Spectra.

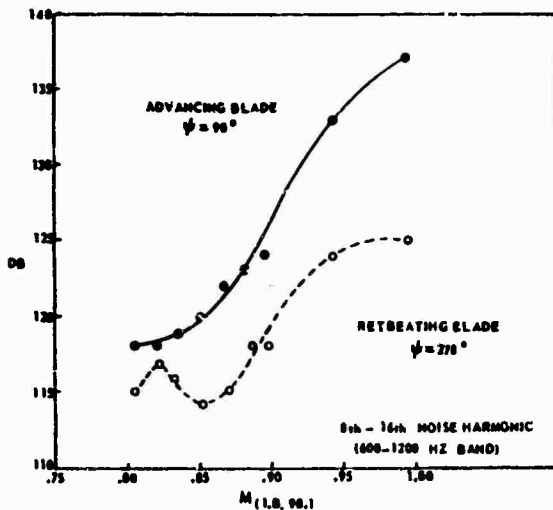


Figure 7. Model Rotor Noise Near Advancing and Retreating Blades.

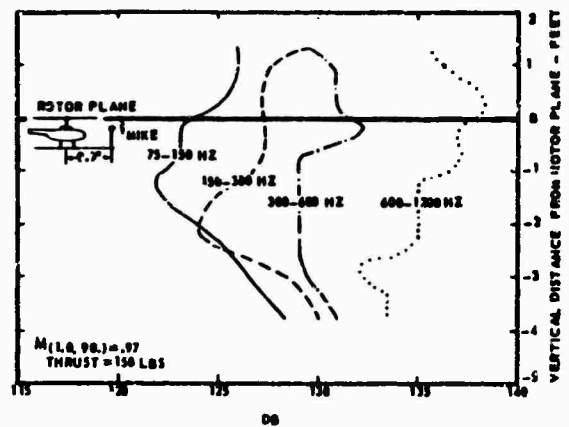


Figure 9. Sound Directivity Forward of Model Rotor.

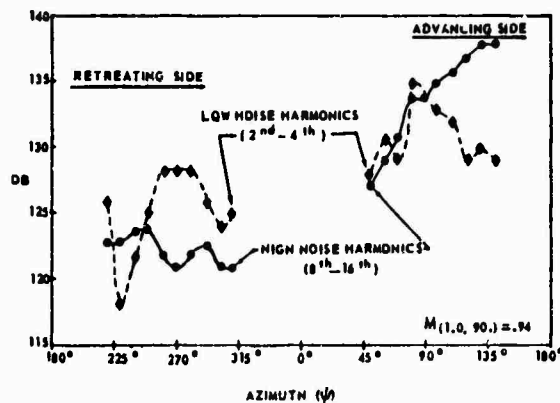


Figure 8. Azimuth Variation of Model Rotor Noise.

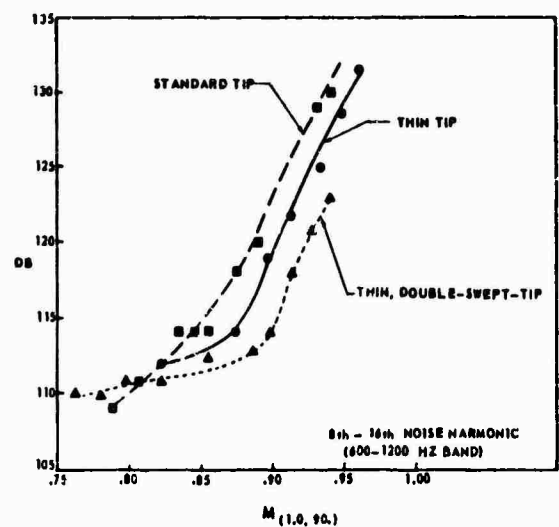


Figure 10. Effects of Tip Shape on Model Rotor Noise.